

Marquette University

e-Publications@Marquette

Dissertations (1934 -)

Dissertations, Theses, and Professional
Projects

Coordination Chemistry of Tetra(Pyrazolyl)-Lutidine Ligands and Derivatives

Tyler James Morin
Marquette University

Follow this and additional works at: https://epublications.marquette.edu/dissertations_mu

 Part of the [Chemistry Commons](#)

Recommended Citation

Morin, Tyler James, "Coordination Chemistry of Tetra(Pyrazolyl)-Lutidine Ligands and Derivatives" (2010). *Dissertations (1934 -)*. 47.
https://epublications.marquette.edu/dissertations_mu/47

COORDINATION CHEMISTRY OF TETRA(PYRAZOLYL)-LUTIDINE
LIGANDS AND DERIVATIVES

by

Tyler J. Morin, B.S.

A Dissertation submitted to the Faculty of the Graduate School,
Marquette University,
in Partial Fulfillment of the Requirements for
the Degree of Doctor of Philosophy

Milwaukee, Wisconsin

May 2010

ABSTRACT
COORDINATION CHEMISTRY OF TETRA(PYRAZOLYL)-LUTIDINE
LIGANDS AND DERIVATIVES

Tyler J. Morin

Marquette University, 2010

There is current interest in the coordination chemistry of simple AE_4 pentadentate ligands that occupy one axial (A) and four equatorial (E) positions about a given transition metal center considering that systems capable of mediating spectacular organic transformations such as alkane oxidation have been identified. The discovery of new systems will improve understanding of C-H bond activation processes which is critical to help make more efficient use of the currently diminishing fossil fuel supplies. As such, a new pentadentate ligand $\alpha,\alpha,\alpha',\alpha'$ -tetra(pyrazolyl)lutidine (**pz₄lut**) and its derivatives **pz⁴₄lut**, (pz⁴ = 4-methylpyrazole); **pz^{*}₄lut**, (pz^{*} = 3,5-dimethylpyrazole); **pz^{DIP}₄lut**, (pz^{DIP} = 3,5-diisopropylpyrazole) have been synthesized and their coordination chemistry towards a host of main group and transition metals has been investigated.

Divalent first row transition metals were used to establish the binding mode(s) (both κ^5 and $\kappa^2\text{-}\mu$ are observed) of the newly synthesized, unsubstituted **pz₄lut** ligand. Substitution along the pyrazolyl periphery with various alkyl groups (4-methyl, 3,5-dimethyl, 3,5-diisopropyl) provided a way to examine the effects of substitution on

binding behavior with transition metals. Cobalt(II) complexes tend to be thermo and solvatochromic giving both pink κ^5 octahedral complexes as well as blue κ^2 tetrahedral complexes for all ligands except **pz^{DIP}₄lut** owing to the steric demands of the isopropyl group. Substitution along the pyrazolyl periphery also allowed for investigation into supramolecular studies of self assembly using silver(I) salts of the newly synthesized ligands. It was found that the silver(I) complexes display unique solution behavior in which the solid state structure is not retained.

Finally, given the importance of oxyferryl species in mediating C-H bond oxidation reactions; the chemistry of iron(II) complexes of the newly synthesized ligands was explored. The reaction between 2 equivalents of *m*-chloroperoxybenzoic acid and the iron(II) complex [Fe(Cl)(pz₄lut)](BAR₄^f) at -30 °C gives a solution with the characteristic green color of iron(IV) oxo species. Due to the highly reactive nature and short lifetime of these species it has not been further characterized. Further efforts have been directed at the synthesis of ligands capable of stabilizing such reactive species, such as the pz^{Et}₄lut ligand; which is substituted at the methyne carbon blocking a potential decomposition pathway.

ACKNOWLEDGMENTS

Tyler J. Morin, B.S.

I would first like to thank my advisor Dr. James Gardinier for all of his advice and guidance throughout my graduate studies. I would also like to acknowledge my committee members Dr. Chae Yi and Dr. James Kincaid for their support and time taken to be on my committee. There are several supporting members who have made invaluable contributions to this work and without them this would not be possible. In no particular order I would like to thank Dr. Sergey Lindeman for X-ray diffraction studies, Dr. Gary Long for the collection of Mössbauer data and Dr. Brian Bennett for all of his assistance in EPR data collection as well as valuable conversations and insight. All of the above have contributed to the success of this work and for that I thank you. I would like to thank the Marquette University Chemistry department for the teaching assistantship that made my graduate studies possible and the National Science Foundation for additional funding in my last semester of graduate study.

Secondly, I would like to thank my family and my friends. My parents have always wished me the best and supported my endeavors. My brothers have always provided support and are invaluable friends. Without them, this would not have been possible and for that I thank them. Andrew Olson, Dr. Tonya Zecycki, Terry Neumann, Dr. Piotr Mak, Irena Mejack, Felipe Macedo have been close friends who have always lent an ear when needed or words of encouragement and understanding. They have helped keep me sane throughout this process and provided many moments of outside enjoyment when they are needed the most. Thank you. My friend Adam Goehner has been a constant source of entertainment and just a great friend who has supported me throughout this process. My group members past and present, Brendan Liddle, Chengeto Gwengo, Felipe Macedo and Sarath Wanniarachichi have all provided assistance and valuable conversations at various points throughout my time here and have contributed to my success.

Last and certainly not least I would like to thank Jill. Jill is the love of my life and has consistently supported me like no one ever has before. Words cannot express what she means to me and what the support she has given me over the past two years has meant. This dissertation is dedicated to her; I love you Jill.

TABLE OF CONTENTS

ACKNOWLEDGMENTS.....	i
Chapter	
I. BREAKING THE CYCLE: IMPACT OF STERICALLY-TAILORED TETRA(PYRAZOLYL)LUTIDINES ON THE SELF-ASSEMBLY OF SILVER(I) COMPLEXES.....	1
II. FIRST ROW TRANSITION METAL COMPLEXES OF $\alpha, \alpha, \alpha', \alpha'$ - TETRA(PYRAZOLYL)LUTIDINE.....	20
III. COORDINATION CHEMISTRY OF COBALT(II) COMPLEXES OF $\alpha, \alpha,$ α', α' -TETRA(PYRAZOLYL)LUTIDINE AND ITS DERIVATIVES.....	52
IV. SYNTHESIS AND CHARACTERIZATION OF PZ ₄ LUT, PZ ⁴ ₄ LUT AND PZ [*] ₄ LUT IRON(II) COMPLEXES.....	85
V. REACTIVITY OF IRON(II) COMPLEXES OF PZ ₄ LUT AND ITS DERIVATIVES.....	102
VI. BORON COMPLEXES OF 2,6-DIPYRAZOLYL-4-X- ANILINES.....	118
VII. NICKEL COMPLEXES OF A NEW NNN Pincer LIGAND.....	145

Chapter 1: Breaking the Cycle: Impact of Sterically-Tailored Tetra(pyrazolyl)lutidines on the Self-Assembly of Silver(I) Complexes

Introduction. There is current interest in the coordination chemistry of simple AE_4 pentadentate ligands capable of occupying one axial (A) and four equatorial (E) positions about a given transition metal center¹ considering that systems capable of mediating spectacular organic transformations such as alkane oxidation have been identified.² For some of these studies, silver(I) complexes of pentadentate ligands could serve as useful reagents for metathesis reactions and possibly for oxidation chemistry.³ For the former purpose, the chemistry of two silver(I) **PY5-R** derivatives (**Figure 1.1**) was recently reported by Huang and co-workers.⁴ Two complexes of the type

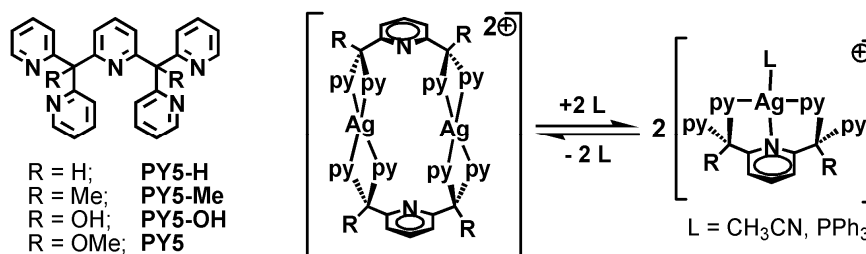


Figure 1.1. **PY5-R** Pentadentate Ligand Scaffolds and Representative Silver(I) complexes.

$[\text{Ag}(\text{PY5 or PY5-OMe})](\text{p-CH}_3\text{C}_6\text{H}_4\text{SO}_3)$ were found by a combination of NMR studies, ESI(+) mass spectral data, to be involved in a solution equilibrium (right of **Figure 1.1**) where the limiting structures, the cyclic bimetallic dication or the κ^3 -monocation (depending on whether or not PPh_3 was added prior to crystallization), were verified by

single crystal X-ray diffraction. We recently communicated ⁵ an initial survey of first-row transition metal coordination chemistry of the pentadentate ligand, $\alpha,\alpha,\alpha',\alpha'$ -tetra(pyrazolyl)lutidine (**pz₄lut**, **Figure 1.2**). During the course of our continuing investigations, we found that some silver(I) complexes of **pz₄lut** (with non-coordinating

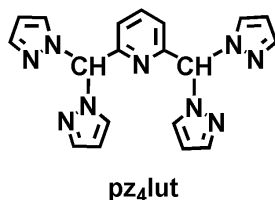
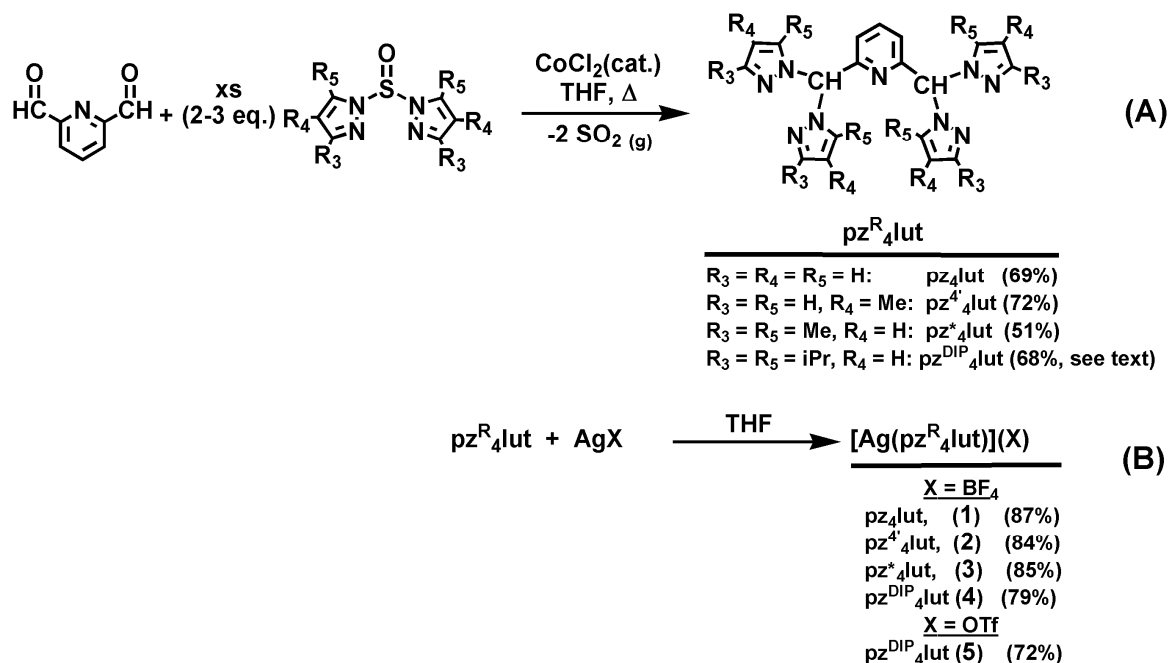


Figure 1.2. The pz₄lut pentadentate ligand.

tetrafluoroborate or triflate counterions) exhibited surprisingly low solubility in polar solvents such as CH₃OH and CH₃CN, solvents in which most silver(I) complexes (including the **PY5-R** derivatives) are soluble. This observation and the interesting results reported for **PY5** derivatives prompted us to more carefully examine the properties of this silver(I) **pz₄lut** complex and some alkyl-substituted derivatives. Herein we report on an improved preparation of **pz₄lut**, the syntheses of three new alkylpyrazolyl-substituted derivatives **pz^{4'}₄lut** (pz^{4'} = 4-methylpyrazolyl), **pz^{*}₄lut** (pz^{*} = 3,5-dimethylpyrazolyl), and **pz^{DIP}₄lut** (pz^{DIP} = 3,5-diisopropylpyrazolyl), as well as the properties of their silver(I) complexes. Future reports will document the use of these ligands and silver complexes in transition metal chemistry.

Syntheses. The pz^R₄lut ligands were prepared using a variation of the CoCl₂-catalyzed Peterson rearrangement reactions^{6a-c} between the appropriate di(pyrazolyl^R)sulfone and 2,6-pyridinedicarboxaldehyde as in **Scheme 1.1A**. We found that the use of an excess of di(pyrazolyl)sulfone (ca 3:1 mol ratio versus the di-aldehyde)

lead to a dramatic improvement in the yield of **pz₄lut** (69%) compared to the previously reported stoichiometric (2:1) conditions (26%).⁵ Three other new ligands **pz^{4'}₄lut**, **pz^{*}₄lut**, and **pz^{DIP}₄lut** were prepared in good yields by adopting a similar strategy. However, it is noted that the sterically demanding **pz^{DIP}₄lut** derivative required an



Scheme 1.1a,b. Preparation of **pz^R₄lut** ligands and AgBF₄ coordination complexes.

additional step for purification, as the product is typically contaminated with variable amounts of 2-(pz^{DIP}₂CH)-6-[CH(O)]-C₆H₃N (mono-carboxaldehyde) that cannot be separated by crystallization or chromatographic separation. Instead, the mono-carboxaldehyde impurity is removed by condensation with 8-aminoquinoline to afford the much less soluble imine derivative which is then easily separated from the desired **pz^{DIP}₄lut** by column chromatography. The reaction between AgBF₄ and each of the **pz^R₄lut** ligands (**Scheme 1.1B**) in THF proceeds to give high yields of the complexes, [Ag(pz^R₄lut)](BF₄) (**1** for R= H; **2** for R= 4-Me, **3** for R = 3,5-Me₂), as hygroscopic solids

indicated by elemental analyses. Once dried under vacuum, **1-3** are insoluble in hydrocarbons, ethereal, and halogenated solvents. The complexes, especially **1**, exhibit surprisingly low solubilities in polar solvents such as acetone, CH₃CN, and MeOH. For instance, their molar solubilities in acetonitrile increase in the order **1** (ca. 7 mM) < **3** (ca. 20 mM) < **2** (ca. 30 mM). The complexes are soluble in highly polar solvents such as DMF or DMSO in which they are expected to be fully dissociated. In contrast, [Ag(**pz**^{DIP}**₄lut**)](X) (X = BF₄ (**4**), OTf (**5**)) are soluble in chlorinated solvents, acetone, CH₃CN, and MeOH. As with **1-3**, complexes **4** and **5** are insoluble in hydrocarbons and ethereal solvents.

Solid State Structures. Single crystals suitable for X-ray diffraction of the ligands **pz₄lut** and **pz*₄lut** were grown by layering acetone solutions with hexanes and allowing solvents to diffuse. The structural details (included here for completeness and for future reference) are provided in **Table 1.1a,b** but will not be further discussed. The silver complexes of the **pz**^{4'}**₄lut** and **pz*₄lut** ligands (**2**·CH₃CN and **3**·CH₃CN, respectively) were obtained by vapor diffusion of THF into dilute (ca. 10 mM) CH₃CN solutions. The silver complex of **pz₄lut** is too insoluble to afford X-ray quality crystals by this methodology, rapid precipitation affords only microcrystalline powder even from dilute solutions (vide infra). However, layering a methanol solution of AgBF₄ onto a CH₂Cl₂ solution of **pz₄lut** and allowing diffusion over 3d was sufficient to obtain high quality crystals of unsolvated [Ag(**pz₄lut**)](BF₄) (**1**). Finally, we were not able to obtain high quality crystals of [Ag(**pz**^{DIP}**₄lut**)](BF₄) (**4**) despite exhaustive attempts as either microcrystalline needles or, in one case with THF:CH₃CN, tiny blocks were obtained where all crystals exhibited birefringence under polarized light and did not hold their

Compound	pz ₄ lut	pz* ₄ lut	1
Formula	C ₁₉ H ₁₇ N ₉	C ₂₇ H ₃₃ N ₉	C ₃₈ H ₃₄ Ag ₂ B ₂ F ₈ N ₁₈
Formula weight	371.42	483.62	1132.19
Crystal system	Orthorhombic	Triclinic	Monoclinic
Space group	P 2 ₁ 2 ₁ 2 ₁	P -1	P 2 ₁ /c
Temp. [K]	100(2)	100(2)	100(2)
<i>a</i> [Å]	7.30230(10)	9.5143(2)	10.17430(10)
<i>b</i> [Å]	16.4433(2)	9.6633(2)	13.7155(2)
<i>c</i> [Å]	45.2477(6)	14.0229(2)	15.9977(2)
α [°]	90	88.9340(10)	90
β [°]	90	83.6710(10)	102.5170(10)
γ [°]	90	89.6990(10)	90
<i>V</i> [Å ³]	5433.07(12)	1281.17(4)	2179.35(5)
<i>Z</i>	12	2	2
<i>D</i> _{calcd.} [gcm ⁻³]	1.362	1.254	1.725
λ [Å] (Cu K α)	1.54178	1.54178	1.54178
μ [mm ⁻¹]	0.724	0.625	7.986
Abs. Correction	multi-scan	multi-scan	numerical
<i>F</i> (000)	2328	516	1128
θ range [°]	2.86 to 68.13	3.17 to 67.27	5.50 to 68.20
Reflections collected	46051	10663	18195
Independent reflections	5569 (<i>R</i> _{int} 0.0260)	4227 (<i>R</i> _{int} 0.0230)	3877 (<i>R</i> _{int} 0.0117)
T _{min} /max	0.8808/0.9511	0.7410/0.9176	0.1203/0.3438
Data/restraints/parameters	5569/0/757	4227/0/471	3877/0/307
Goodness-of-fit on <i>F</i> ²	1.022	1.045	1.041
<i>R</i> 1/ <i>wR</i> 2 [<i>I</i> > 2 σ (<i>I</i>)] ^a	0.0343/0.0809	0.0357/0.0867	0.0205/0.0520
<i>R</i> 1/ <i>wR</i> 2 (all data) ^a	0.0400/0.0833	0.0425/0.0902	0.0206/0.0521

^a $R1 = \Sigma ||F_o| - |F_c|| / \Sigma |F_o|$ $wR2 = [\Sigma w(|F_o| - |F_c|)^2 / \Sigma w|F_o|^2]^{1/2}$.

Table 1.1a. Crystallographic data collection and structure refinement for pz₄lut, pz*₄lut, [Ag₂(μ -pz₄lut)₂](BF₄)₂ (1).

Compound	2·2CH₃CN	3·2CH₃CN	5·CH₃CN·0.5Et₂O
Formula	C ₅₀ H ₅₆ Ag ₂ B ₂ F ₈ N ₂₀	C ₅₈ H ₇₂ Ag ₂ B ₂ F ₈ N ₂₀	C ₄₈ H ₆₈ AgF ₃ N ₁₀ O _{3.5} S
Formula weight	1326.51	1438.72	1038.05
Crystal system	Monoclinic	Triclinic	Monoclinic
Space group	P 2 ₁ /n	P -1	Cc
Temp. [K]	100(2)	100(2)	100(2)
<i>a</i> [Å]	10.6907(2)	11.0965(4)	16.1224(6)
<i>b</i> [Å]	20.7716(4)	12.8261(2)	29.4322(10)
<i>c</i> [Å]	13.5676(3)	13.1776(2)	23.6489(8)
α [°]	90	118.0520(10)	90
β [°]	103.5190(10)	103.8740(10)	108.111(2)
γ [°]	90	92.6180(10)	90
<i>V</i> [Å ³]	2929.38(10)	1579.16(7)	10665.8(6)
<i>Z</i>	2	1	8
<i>D</i> _{calcd.} [gcm ⁻³]	1.504	1.513	1.293
λ [Å] (Cu K α)	1.54178	1.54178	1.54178
μ [mm ⁻¹]	6.039	5.648	3.887
Abs. Correction	numerical	numerical	multi-scan
<i>F</i> (000)	1344	736	4352
θ range [°]	3.97 to 67.99	3.97 to 67.06	3.00 to 68.11
Reflections collected	24254	13173	53558
Independent reflections	5164 (R _{int} 0.0122)	5190 (R _{int} 0.0181)	40241 (R _{int} 0.0546)
T _{min} /max	0.1962/0.2826	0.2734/0.5755	0.4864/0.7462
Data/restraints/parameters	5164/0/472	5190/0/550	40241/21/1270
Goodness-of-fit on <i>F</i> ²	0.999	1.025	1.032
<i>R</i> 1/ <i>wR</i> 2 [<i>I</i> > 2 σ (<i>I</i>)] ^a	0.0218/0.0598	0.0227/0.0577	0.0606/0.1545
<i>R</i> 1/ <i>wR</i> 2 (all data) ^a	0.0219/0.0599	0.0234/0.0581	0.0658/0.1596

^a $R1 = \sum ||F_o| - |F_c|| / \sum |F_o|$ $wR2 = [\sum w(|F_o| - |F_c|)^2 / \sum w|F_o|^2]^{1/2}$.

Table 1.1b. Crystallographic data collection and structure refinement for (**2·2CH₃CN**), and [Ag₂(-pz*₄lut)₂](BF₄)₂·2CH₃CN (**3·2CH₃CN**) and [Ag(pz^{DIP}₄lut)](OTf)·CH₃CN·0.5Et₂O (**5·CH₃CN·0.5Et₂O**).

integrity when removed from solution. On the other hand, small twinned colorless prisms of $[[\text{Ag}(\text{pz}^{\text{DIP}}_4\text{lut})](\text{OTf})\cdot\text{CH}_3\text{CN}\cdot 0.5\text{Et}_2\text{O} (\mathbf{5}\cdot\text{CH}_3\text{CN}\cdot 0.5\text{Et}_2\text{O})$ were obtained by vapor diffusion of Et_2O into a CH_3CN solution. The small, twinned nature of the crystals and the disorder of solvents and anions contribute to the rather low quality of the structure, but the results are sufficient to establish the connectivity. The structures of the cations in **1**, **2**· CH_3CN and **3**· CH_3CN are provided in **Figures 1.3 and 1.4** while that of **5**· $\text{CH}_3\text{CN}\cdot 0.5\text{Et}_2\text{O}$ is found in **Figure 1.5**. Selected intra- cation bond distances and angles are collected in **Table 1.2**.

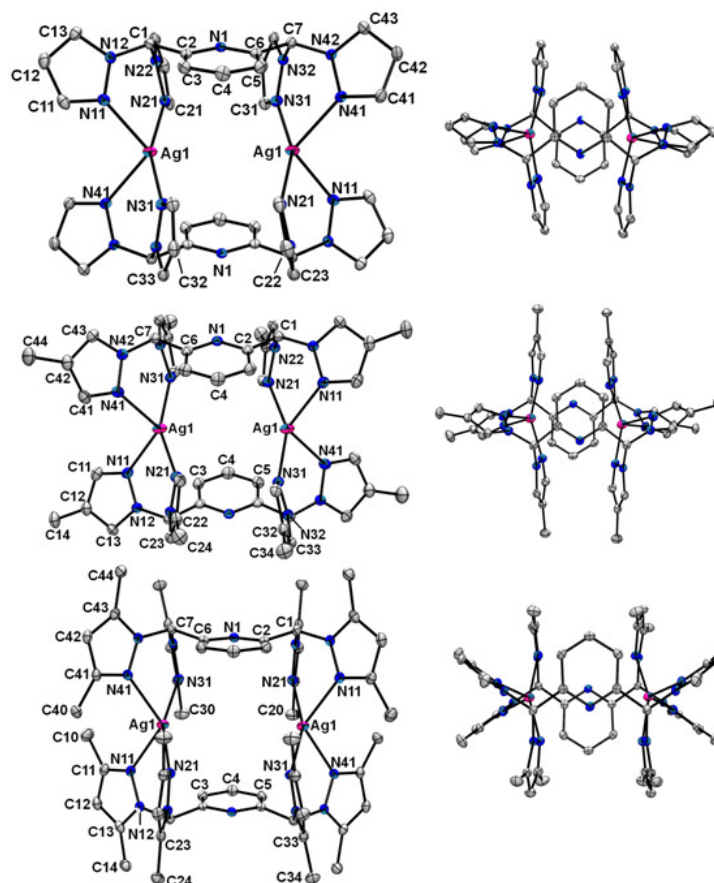


Figure 1.3. Views of the cyclic dications in $[\text{Ag}(\text{pz}_4\text{lut})](\text{BF}_4)$ (**1**), top; $[\text{Ag}(\text{pz}^{4'}_4\text{lut})](\text{BF}_4) \text{CH}_3\text{CN}$, **2**· CH_3CN , middle; and $[\text{Ag}(\text{pz}^*_4\text{lut})](\text{BF}_4) \text{CH}_3\text{CN}$, **3**· CH_3CN , bottom; Left, perspective view; Right, view normal to pyridyl plane. Each with thermal ellipsoids shown at 50% probability and with hydrogens removed for clarity.

Distances (Å)	1	2 ·CH ₃ CN	3 ·CH ₃ CN	5 ·CH ₃ CN·0.5Et ₂ O
Ag1-N11	2.4284(15)	2.4121(15)	2.3855(17)	2.373
Ag1-N21	2.2154(15)	2.2617(14)	2.3030(16)	2.238
Ag1-N31	2.2139(16)	2.2485(15)	2.3002(16)	2.249
Ag1-N41	2.4329(16)	2.4106(16)	2.3894(16)	2.356
Ag...Ag	4.767(2)	4.956(2)	5.391(2)	8.628, 8.610
Angles (°)				
N11-Ag1-N21	85.76(5)	84.91(5)	79.92(6)	86.98
N31-Ag1-N41	83.10(5)	85.09(5)	81.09(6)	86.14
N11-Ag1-N41	103.32(5)	106.23(5)	114.27(5)	91.93
N21-Ag1-N31	155.99(6)	151.77(5)	157.89(6)	155.23
N11-Ag1-N31	107.45(5)	116.07(5)	113.39(6)	110.49
N21-Ag1-N41	113.94(5)	107.98(5)	110.38(6)	111.49
Torsions (°)				
Ag1N11-N12C1	18.3(2)	9.8(2)	0.2(2)	21.77
Ag1N21-N22C1	-23.8(2)	-28.8(2)	-15.8(2)	-49.83
Ag1N31-N32C7	-16.6(2)	-24.9 (2)	-28.6(2)	-44.39
Ag1N41-N42C7	9.3(2)	12.2(2)	0.8(2)	20.99
H1C1-C2N1	71.9(2)	-64.8	-75.6(2)	67.95
H7C7-C6N1	-70.8(2)	71.5	72.3	70.37

Table 1.2. Selected interatomic bond distances (Å), bond angles (°), and bond torsions (°) for [Ag(**pz₄lut**)](BF₄) (**1**), [Ag(**pz^{4'}****lut**)](BF₄) CH₃CN, **2**·CH₃CN, [Ag(**pz*****lut**)](BF₄) CH₃CN, **3**·CH₃CN, and [Ag(**pz^{DIP}****lut**)](OTf)·CH₃CN·0.5Et₂O (**5**·CH₃CN·0.5Et₂O).

As can be seen in **Figure 1.3**, complexes **1-3** each contain a cyclic bimetallic dication (of nearly ideal C_{2h} symmetry) that is located on an inversion center. In each dication, the two silver centers are well-separated (4.77 - 5.39 Å) by the bridging, chelating ligand. Each silver center possesses a slightly distorted see-saw geometry imposed by disparate

bonding to pyrazolyl nitrogens that occupy either pseudo-axial or pseudo-equatorial positions (the central pyridyl remains unbound) about the metal. Thus, there are two shorter, nearly collinear (pseudo-axial) Ag-N bonds, Ag1-N21 and Ag1-N31, that average 2.215 Å for **1**, 2.244 Å for **2**·CH₃CN, and 2.256 Å for **3**·CH₃CN with N21-Ag1-N31 of 156° for **1**, 152° for **2**·CH₃CN, and 158° for **3**·CH₃CN. The other two (pseudo-equatorial) Ag-N bonds Ag-N11 and Ag1-N41 are longer (averaging 2.412 Å for **1**, 2.374 Å for **2**·CH₃CN, and 2.431 Å for **3**·CH₃CN) than the pseudo-axial bonds and the corresponding N11-Ag-N41 bond angles are more acute (103° for **1**, 106° for **2**·CH₃CN, and 114° for **3**·CH₃CN) than the pseudoaxial N21-Ag1-N31 angle. The average of the four Ag-N distances (2.334 Å for **1**, 2.309 Å for **2**·CH₃CN, and 2.323 Å for **3**·CH₃CN) and ligand bite angles (corresponding to N11-Ag1-N21 and N31-Ag1-N41 which are 84° for **1**, 85° for **2**·CH₃CN, and 80° for **3**·CH₃CN) are all in line with those found in the closely related dications of [Ag₂(μ-*m*-[CH(pz)₂]₂C₆H₄)₂](X)₂ (X = BF₄, PF₆)⁷ or [Ag₂(μ-[CH(pz)₂]₂(CH₂)_n)₂]²⁺ (n = 1-3)⁸ and indicate that the influence of anions, central linker, or, surprisingly, even the addition of methyl groups at the 3- and 5- positions of the pyrazolyls have little influence on the metal's primary coordination geometry. On the other hand, the added steric bulk of 3-methyl groups in **3**·CH₃CN relative to **1** causes van der Waals contacts with the central pyridyl rings (**Figure 1.4**) that distort the cyclic dication by bending the lutidyl methines C1 and C7 in **3**·CH₃CN on average 0.25 Å above the mean plane of the pyridyl rings (**Figure 1.4**, right). For comparison, the C1 and C7 atoms of **1** reside, on average, only 0.07 Å above the mean plane of the pyridyl. Similarly, the corresponding methine atoms in [Ag₂(μ-*m*-[CH(pz)₂]₂C₆H₄)₂]²⁺ are also displaced by 0.07 Å.⁷

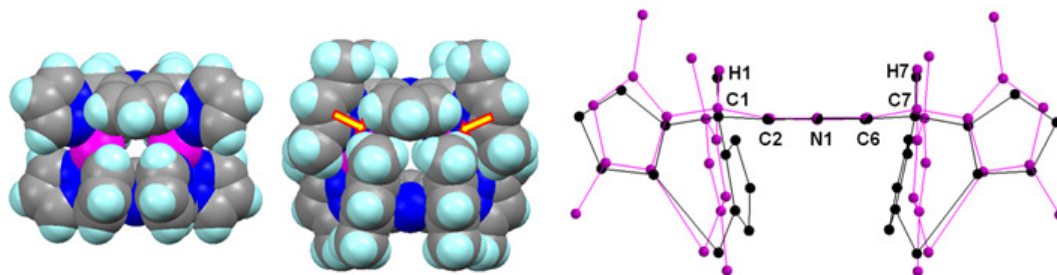


Figure 1.4. Space-filling representations of the crystal structures of cyclic dications of $[\text{Ag}(\text{pz}_4\text{lut})](\text{BF}_4)$, **1** (left), $[\text{Ag}(\text{pz}^*\text{4lut})](\text{BF}_4) \cdot \text{CH}_3\text{CN}$, **3**· CH_3CN (center), emphasizing the steric interactions involving the methyl and pyridyl groups of the latter. An overlay (right) shows greater bending of lutidine methines (C1 and C7) above the mean pyridyl plane containing N1 in **3** (pink) versus **1** (black).

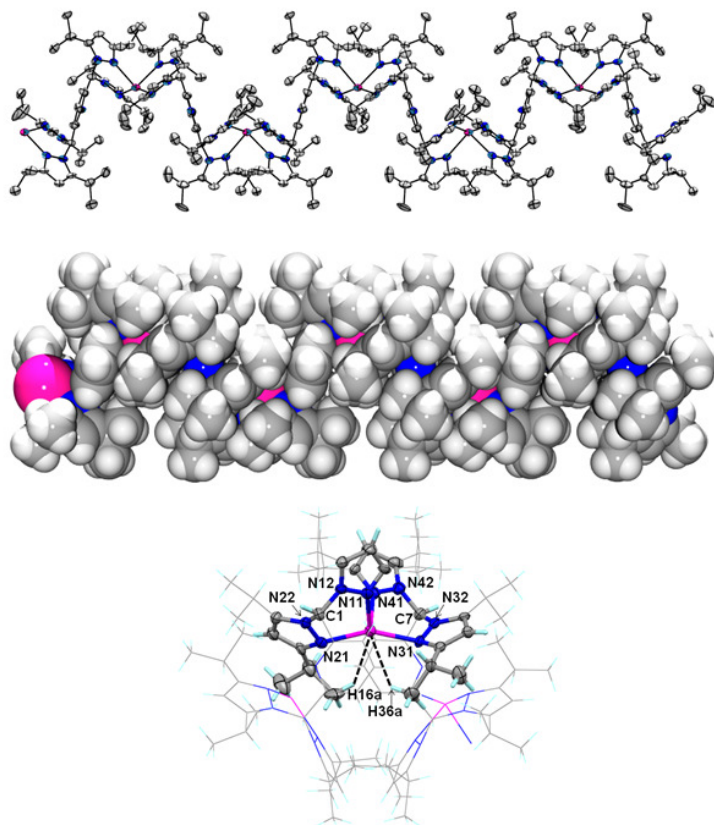


Figure 1.5. Views of the cation in $[\text{Ag}(\text{pz}^{\text{DIP}}\text{4lut})](\text{OTf}) \cdot \text{CH}_3\text{CN} \cdot 0.5\text{Et}_2\text{O}$ (**5**· $\text{CH}_3\text{CN} \cdot 0.5\text{Et}_2\text{O}$). Top: ORTEP drawing (thermal ellipsoids shown at 50% probability and with hydrogens removed for clarity) of a fragment of one polymeric chain that propagates along a -axis. Middle: Space-filling representation of same fragment. Bottom: A view approximately down the a -axis emphasizing the coordination environment about silver.

In light of the steric interactions in **3**, it was anticipated that bulkier groups on the pyrazolyls would break the cyclic motif. Indeed, in complex **5** the cation is no longer cyclic but is organized into polymeric chains that propagate along the crystallographic *a*-axis (**Figure 1.5**). The ligand contains an unbound pyridyl as in **1-3** but, in contrast to the three latter complexes, the silver-bound dipyrazolylmethane units are located on opposite sides of the central pyridyl ring; the H1C1-C2N1 and H7C7-C6N1 torsion angles (**Table 1.2**) have the same sign in **5** but have opposite signs in **1-3**. On first inspection, the distorted see-saw coordination environment about silver in **5** appears similar to those in **1-3** in that the shorter pseudo-axial Ag-N bonds (avg. 2.244 Å), longer pseudo-equatorial Ag-N bonds (avg. 2.365 Å), and average Ag-N bond length of 2.304 Å (indicative of tetracoordinate silver⁹) are similar to those distances found in **1-3**. However, while the pseudo-axial N21-Ag-N31 angle of 155° is in line with those in **1-3**, the pseudo-equatorial N11a-Ag-N41 angle of 92° is more acute than those in **1-3**. Closer inspection of the silver coordination sphere shows that opposite to the N11a-Ag-N41 fragment, there are two rather short Ag...H contacts Ag...H26dC26 (2.603 Å, 138.94°) and Ag...H36aC36 (2.788 Å, 134.26°) that arise from methyls of the 3-isopropylpyrazolyl groups. An additional consequence of the moderate steric profiles of the isopropylpyrazolyl substituents is that there is substantial twisting of pyrazolyl rings defined by the absolute value of the AgN-NC_{methine} torsion angle (**Table 1.5**). Pyrazolyl ring twisting is a common distortion in metal poly(pyrazolyl)methane complexes¹⁰ and provides one measure of the ‘fit’ of these ligands to the metal (and vice versa); ideally this value should be zero. For **5**, the average pyrazolyl ring twist of 34° is much greater than 17°, 19°, and 11° found in **1-3**, respectively, where it is noted that in all cases the pseudo-axial

rings are more twisted than the pseudo-equatorial rings. The greater pyrazolyl ring twisting in **5** likely arises from the several intra-chain van der Waals contacts involving the isopropyl substituents and neighboring pyridyl and pyrazolyl rings.

The highly organized supramolecular structures of **1-3** likely contribute to the low solubilities of the compounds. That is the crystal packing of **1-3** is dominated by numerous non-covalent interactions including CH \cdots F weak hydrogen bonding involving the tetrafluoroborate and acidic hydrogens of pyridyl and pyrazolyl rings as well as various CH- π and π - π stacking interactions involving heterocyclic aromatic groups. In **5**, the isopropyl substituents protect aromatic groups from entering into extensive ‘intermolecular’ non-covalent interactions (being limited only to CH \cdots O weak hydrogen bonding). The relative number of non-covalent interactions identified in each crystal parallels the observed trend in solubility (**1** < **3** < **2** << **5**). It is important to note, however, that aside from **1**, the structures obtained from single crystal X-ray structural determination may not be representative of the bulk crystalline solid. For illustration, the X-ray powder diffraction patterns obtained from various samples of **1** and **3** are given in

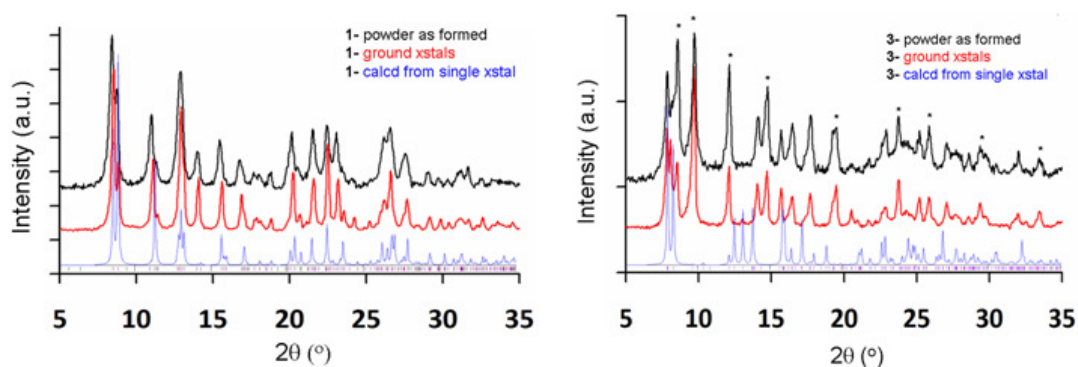


Figure 1.6. X-Ray Powder diffraction patterns of **1** (left) and **3** (right) obtained for initially obtained precipitate of preparative reactions in THF (top, black) and for bulk crystalline samples (middle, red) after drying and grinding. The calculated diffraction patterns based on single crystal diffraction experiments are also given (bottom, blue). For **3**, reflections demarcated with asterisks (*) are not found in the calculated pattern of the solvate **3**·CH₃CN.

Figure 1.6. The structure of **1** obtained by single crystal diffraction did not contain any solvent in the lattice. Accordingly, both the powder initially isolated from the reaction mixture (**Fig 1.6, top left**) in THF and the samples of ground vacuum-dried crystals grown by layering MeOH and CH₂Cl₂ solutions (**Fig 1.6, middle left**) showed identical diffraction patterns that were consistent with the calculated pattern obtained from the single crystal structure determination. On the other hand, the structure of **3** from single crystal X-ray diffraction showed it to be a CH₃CN solvate, but elemental analysis of vacuum dried samples indicated that solvent is absent. The diffraction patterns for as-isolated (dried and ground) powder from the preparative reaction and that of a bulk sample after recrystallization (after vacuum-drying and grinding) were identical. Fittingly, neither pattern was consistent with that calculated for **3**·CH₃CN from the single crystal X-ray diffraction experiment. Thus, desolvation does not result (in this case) in loss of crystallinity but does significantly alter the structure; similar observations hold for **2** and **5**, but desolvation causes loss of crystallinity in the latter case.

Solution Properties. For complexes 1-5, the combined data from electrospray ionization mass spectrometric (ESI-MS) as well as variable temperature and diffusion ¹H NMR spectroscopic measurements suggest that the solid state structures are not maintained in CH₃CN solution. Instead, monometallic cations are most likely the predominant species in the liquid temperature range of CH₃CN. ESI-MS data are thought to accurately reflect the solution structures of coordination complexes and coordination polymers of inert metals.¹¹ For labile silver(I) complexes such as with polytopic di(pyrazolyl)methane ligands linked via various organic spacers^{7,8,10} and of related ligands⁹, ESI-MS data appear to provide reliable measure for distinguishing which

complexes will form metallacycles versus coordination polymers in the solid state. For instance, it has been reported that those complexes that give cyclic dications in the solid state such as either $[\text{Ag}_2(\mu\text{-}m\text{-}[\text{CH}(\text{pz})_2]_2\text{C}_6\text{H}_4)_2](\text{X})_2$ ($\text{X} = \text{BF}_4, \text{PF}_6$)⁷ or $[\text{Ag}_2(\mu\text{-}[\text{CH}(\text{pz})_2]_2(\text{CH}_2)_n)_2]^{2+}$ ($n = 1\text{-}3$)⁸ give a weak peak in their ESI(+) mass spectrum with m/z corresponding to $[\text{Ag}_2\text{L}_2(\text{X})]^+$ ($\text{X} = \text{anion}$) whereas such a peak is absent in cases where the solid state structure is of a coordination polymer. In the latter cases, very weak intensity peaks for higher order species such as $[\text{Ag}_3\text{L}_2(\text{X})_2]^+$ are sometimes observed. In all previously reported cases, the ESI(+) spectrum contains peaks for $[\text{AgL}_2]^+$ and $[\text{AgL}]^+$ (usually the base peak, the pattern is never for $[\text{Ag}_2\text{L}_2]^{2+}$ which is easily distinguishable from a monocation). In many cases, peaks for $[\text{HL}]^+$, $[\text{HL-pz}]^+$, $[\text{AgL}(\text{CH}_3\text{CN})]^+$, and $[\text{Ag}(\text{CH}_3\text{CN})_n]^+$ ($n = 1\text{-}4$) are observed. All of the above observations demonstrate that ambiguity still exists concerning whether the ESI-MS data of silver(I) complexes accurately reflects their solution structures and the current study further probes this issue. The ESI(+)-MS data for 1-5 are in general agreement with findings for the related aryl- or alkylidene linked di(pyrazolyl)methane ligands but some important differences are also observed. First, as in related cases, weak intensity peaks for $[\text{Ag}_2\text{L}_2(\text{X})]^+$ ($\text{X} = \text{BF}_4^-$, and Cl^- from spectrometer) were observed for **1** and **2** (for example, $m/z = 1105$ and 1157 in **Figure 1.7**) which showed cyclic dications in the solid state but were absent in the spectrum of **4** or **5**. Interestingly, the $[\text{Ag}_2\text{L}_2(\text{X})]^+$ peak in the spectrum of **3** was only observed at relatively high concentration even though the solid state structure was also of a cyclic dication. Secondly, very weak intensity peaks for higher-order $[\text{Ag}_2\text{L}_3(\text{X})]^+$ and $[\text{Ag}_2\text{L}_2(\text{X})_2]^+$ ions were observed for **1** and **2** but not for **3-5** which

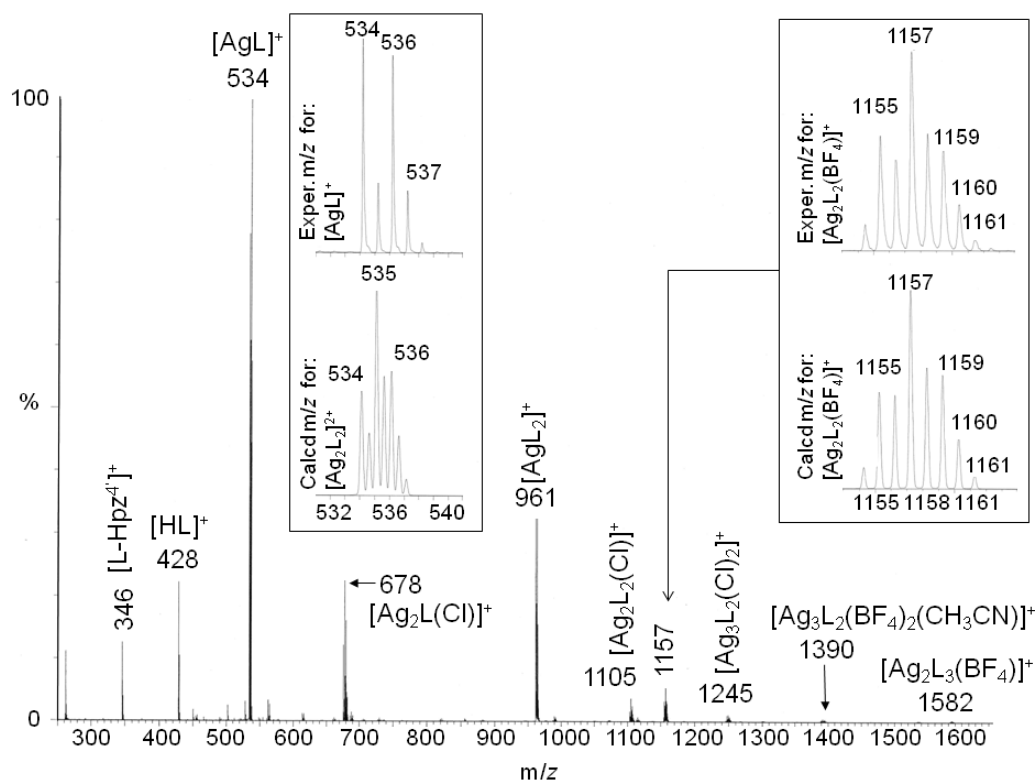


Figure 1.7. ESI(+) mass spectrum of $[\text{Ag}(\text{pz}^4\text{lut})][\text{BF}_4]$, **2** in CH_3CN .

would seem to indicate that **1** and **2** form coordination polymers to some small extent in either in solution or during the desolvation phase of the mass spectrometry experiment. The lack of higher order peaks for **5** (and **4**) is thus rather surprising given the solid state coordination polymer structure. It is also of interest that higher-order ions were not reported for the related $[\text{Ag}_2(\mu\text{-}m\text{-}[\text{CH}(\text{pz})_2]_2\text{C}_6\text{H}_4)_2](\text{X})_2$ ($\text{X} = \text{BF}_4, \text{PF}_6$)⁷. The spectrum for each **1-5** contains peaks for $[\text{AgL}_2]^+$, $[\text{Ag}_2\text{L}(\text{Cl})]^+$, $[\text{AgL}]^+$, $[\text{HL}]^+$, and $[\text{L-Hpz}]^+$ where $[\text{AgL}]^+$ is the base peak for **1** and **2** while $[\text{HL}]^+$ is the base peak for **3-5**. The spectrum for each **1-3** contains a peak for $[\text{AgL}_2]^+$, a species absent in the spectrum of either **4** or **5**. It is noteworthy that in none of the cases here does a peak corresponding to $[\text{AgL}(\text{CH}_3\text{CN})]^+$ appear in the spectrum of **1-5**, such a species was conjectured for **PY5-**

R derivatives. Regardless, the presence of peaks for multiple silver ions with different numbers of **pz^R₄lut** ligands in the corresponding spectrum of each **1-5** would seem to indicate significant dissociation occurs in solution, a conjecture that is supported by NMR spectral data.

Both pulsed field-gradient spin-echo¹² (PFGSE) and variable temperature ¹H NMR spectral data for CD₃CN solutions of **1-5** indicate that these complexes are monomeric in CD₃CN but they do not have static structures. The PFGSE experiment permits the indirect evaluation of molecular size based on applying incrementally larger field gradients during the course of spectra acquisition where differing rates of diffusion cause a corresponding loss of signal intensity which can be used in conjunction with the Stokes-Einstein relation to obtain hydrodynamic radii. Typically, this technique affords hydrodynamic radii that are within approximately 10-15 % of those radii found from X-ray diffraction studies. The results of PFGSE experiments of room temperature CD₃CN solutions of ligands with Ga(acac)₃ added as an internal reference and of individual silver complexes, **1-5**, with [Ru(bpy)₂(CH₃CN)₂](BF₄)₂ added as an internal reference are found in **Table 1.3** and in **Figure 1.8**. For the ligands described here, **Table 1.3** shows the hydrodynamic radii to be slightly smaller but comparable to those radii found crystallographically or those found by using energy-minimized structures from equilibrium geometry calculations (HF 3-21G). For complexes **1-3**, the hydrodynamic radii more closely match calculated values for monomeric cations obtained from semi-empirical (PM3) geometry optimization calculations rather than those values for dimeric dications obtained either from single-crystal X-ray diffraction experiments or by using

molecular modeling. Similarly, the hydrodynamic radii for **4** and **5** are consistent with monomeric $[\text{AgL}]^+$ species rather than with radii for $[\text{AgL}_2]^+$, dimers such as $[\text{Ag}_2\text{L}_2]^{2+}$ or

Compound	D ($\times 10^{-10} \text{ m}^2/\text{s}$)	r_H (Å, PFGSE)	radius ^a (Å, X-ray)	Radius ^b (Å, HF 3-21G or PM3)
solvent			---	
Ga(acac) ₃	18.2	4.84	4.84 ¹³	---
pz ₄ lut	15.7	5.57	6.20	6.23/5.34
pz ⁺ ₄ lut	14.9	5.77	---	7.44/6.10
pz [*] ₄ lut	13.6	6.35	6.73	7.50/6.24
pz ^{DIP} ₄ lut	12.9	8.21	---	8.81/7.30
[Ru(bpy) ₂ (CH ₃ CN) ₂] ²⁺	22.5	5.72	5.72 ¹⁴	5.95
1	17.8	5.76	7.46	6.10 monomer max., 7.40 dimer
2	16.8	5.92	7.77	
3	15.4	6.29	7.89	7.32 monomer max., 7.94 dimer
4	12.4	8.08	---	8.90 AgL, 9.2 AgL ₂
5	12.3	8.88	7.61, 9.70, 10.14 AgL, AgL ₂ , Ag ₂ L ₃	8.90 AgL, 9.2 AgL ₂

a. from largest measured distance, see text.

Table 1.3. Summary of from PFGSE ¹H NMR experiments.

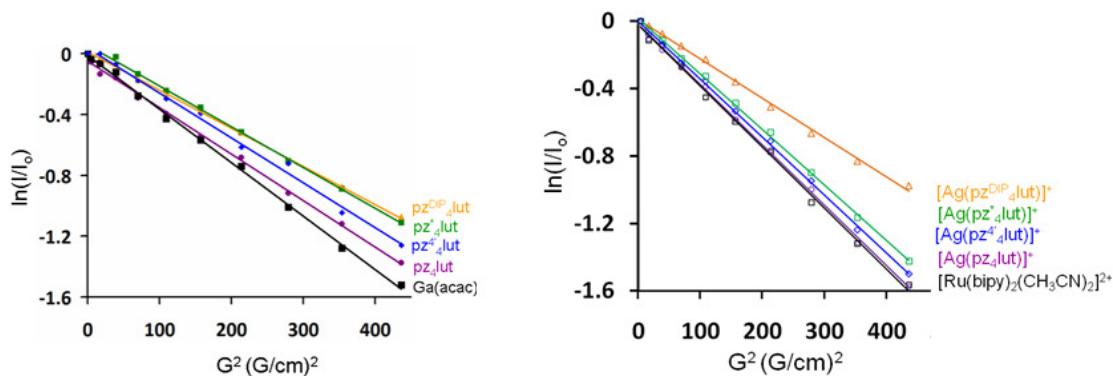


Figure 1.8. Results from PFGSE ¹H NMR Experiments.

even higher-order oligomers such as $[\text{Ag}_2\text{L}_3]^{2+}$ or $[\text{Ag}_3\text{L}_4]^{3+}$ (values that can be extracted from the crystal structure of **5** or from molecular modeling).

The appearance of the ¹H NMR spectrum of each **1-5** in CD₃CN under various conditions is also indicative of monomeric $[\text{AgL}]^+$ ions in solution. For instance, if the solid state structures of **1-3**, and **5** were retained (and if **1-3** had ideal C_{2h} symmetry) in

solution, two sets of resonances for symmetrically distinct (pseudo-axial and pseudo-equatorial) pyrazolyl group hydrogens would be expected but only one set is observed for each complex **1-5** at about ambient temperature or above. For ‘intact’ cyclic dications of **1-3**, a minimum of two Ag-N(pz) bonds would need to be broken concomitant with C-C and C-N bond rotations for pseudo-axial and pseudo-equatorial pyrazolyl groups to give exchange-averaged signals, a highly improbable scenario relative to the processes available to monomeric cations (vide infra). Moreover, addition of excess free ligand to the solutions of **1-5** gives only exchange-averaged signals rather than discrete resonances for each the free ligand and the corresponding silver complex. In solutions of pure **1-5**, the resonances for the metal-bound ligands are distinct from the respective “free” ligand resonances both by their downfield chemical shifts and by their temperature dependence. Over the liquid range of CD₃CN, the number of resonances of **1** and **2** remains constant but the resonances for the *meta*- hydrogens of the pyridyl group experience the greatest change in both chemical shift and in line-broadening with temperature. The resonances for the methine and the 5- hydrogens of the pyrazolyl groups change to a lesser degree than those for the *meta*- pyridyl hydrogens while the remaining resonances are only little affected by changes in temperature. Although coalescence was not reached, line shape analyses based on line broadening of 5-pyrazolyl hydrogen resonances gave energy barriers for exchange of 10.8 ± 0.1 kcal/mol for **1** and 11.3 ± 0.1 kcal/mol for **2**. As exemplified by the spectra for **3** shown in **Figure 1.8**, similar observations hold for complexes **3-5** but the slow exchange limit is attained (calculated to possess identical activation barriers of 14.3 ± 0.1 kcal/mol for **3** and 14.4 ± 0.1 kcal/mol for **4** and **5**) and

evidence for the formation of multiple species is found in each case. That is at high temperature only one set of resonances are observed for ligand hydrogens. In the case of

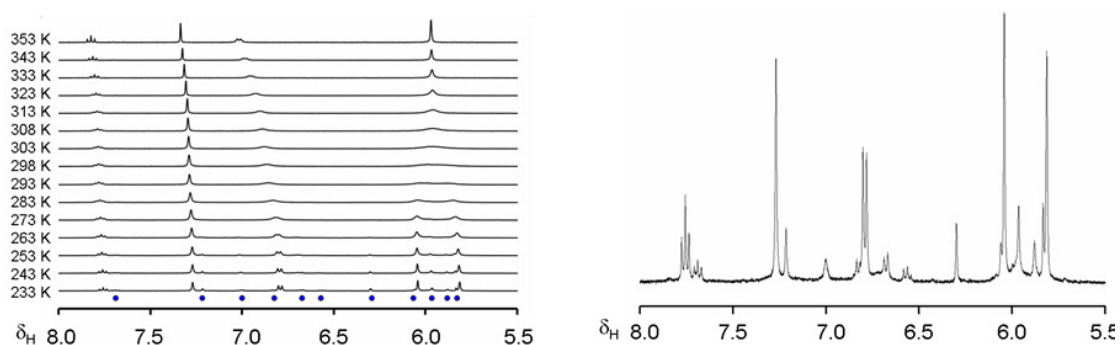


Figure 1.9. Left: The downfield region of the ^1H NMR spectrum of **3** in CD_3CN acquired at different temperatures emphasizing both a dynamic process and the equilibrium formation of a new species at low temperature (blue circles). Right: Magnified view of the 233 K spectrum.

cooling the solution of **3**, the three single resonances for each type of pyrazolyl group hydrogens (4-H, 3-methyl and 5-methyl) broaden and decoalesce near room temperature to give six total resonances (two for each type) that sharpen as exchange is slowed by further lowering temperature. Concomitantly, the pyridyl hydrogen resonances shift upfield, lose and regain coupling features, but do not split into multiple resonances on cooling. However, new sets of ligand resonances appear from the baseline at about 263 K and grow in intensity when the temperature is lowered to 233 K (right of **Figure 1.8**), behavior indicative of the equilibrium formation of multiple species at low temperature. Similar behavior is observed for samples of **4** and **5** but the low temperature spectra are much more complicated owing to the presence of a large number of multiplet resonances.

Disregarding the stereochemistry at the methine carbon atoms, there are thirteen possible coordination modes for the ligand in monomeric $[\text{AgL}]^+$ complexes giving species that span only four different point groups (C_{2v} , C_2 , C_s , and C_1) as illustrated in

Figure 1.10. Thus, even before considering any dynamic behavior, there is intrinsic ambiguity regarding possible solution structures based solely on the number and types of resonances appearing in the NMR spectrum. After contemplating the solution NMR behavior and mass spectral data of **1-5** and of related silver complexes, we favor a

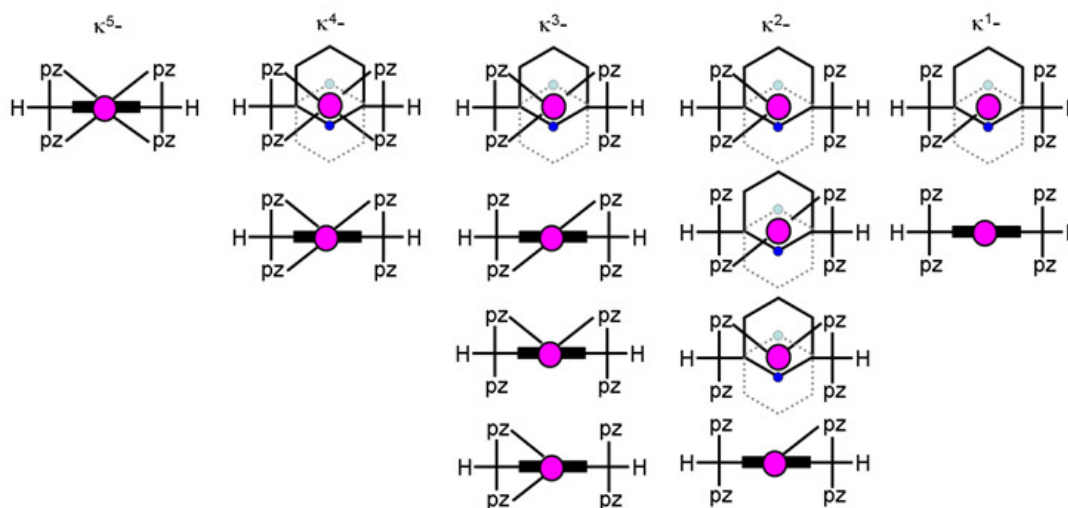


Figure 1.10. Cartoon depictions of coordination modes of ligands in monomeric $[\text{AgL}]^+$ complexes.

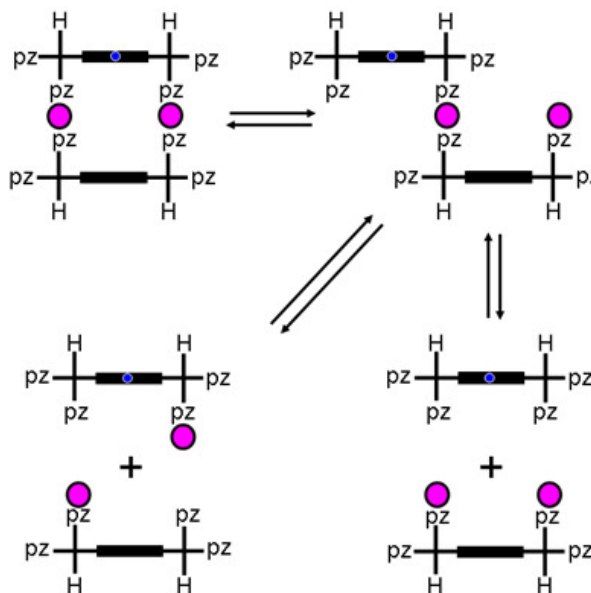


Figure 1.11. Proposed equilibria controlling self-assembly and ligand exchange.

scenario where at high temperature, rapid interchange between κ^1 - and κ^2 - bound ligands (right half of **Figure 1.10**) affords exchange-averaged pyrazolyl group resonances in the dynamic solution process. In this situation, the alkyl-substitution on the pyrazolyls contribute to increasing the activation barrier of such a process by both inductive electronic effects (by strengthening the Ag-N bond) and by restricting C-C and C-N bond rotations involving pyrazolyls and the pyridyl groups around methine carbons via steric interactions (we are neglecting any added effects from silver-bound solvent molecules). At modestly low temperature, the C_s symmetric κ^2 - structure (second from the bottom of **Figure 1.10**) would necessarily predominate giving two sets of pyrazolyl signals. Alternative possibilities such as rapid interchange between κ^5 - and κ^4 - bound ligands (left half of **Figure 1.10**) cannot be excluded but are disfavored considering the preference of silver(I) for low coordination numbers (typically ≤ 4), the relatively high activation energy anticipated for Ag-N(pyridyl) bond dissociation and rotation (while maintaining Ag-N(pz) bonds) compared to the low energy of the observed activation barriers (10-14 kcal/mol), and because these alternatives also fail to account for either the facile ligand exchange process or the disparity in self-assembly with pyrazolyl substitution (**Figure 1.11**). At very low temperature the newly observed peaks in **3-5** could be accounted for by the formation of either cyclic or linear oligomers (as in the top of **Figure 1.11**) or, less satisfactorily from a self-assembly point of view, by the preferential formation of any of the C_1 -symmetric (κ^3 , κ^2 , or κ^1) monomeric cations.

Summary and Conclusions. Three new alkyl pyrazole-substituted derivatives of the ligand $\alpha,\alpha,\alpha',\alpha'$ -tetra(pyrazolyl)lutidine, (**pz₄lut**) been synthesized: **pz⁴₄lut**, **pz^{*}₄lut** and **pz^{DIP}₄lut** along with their silver(I) complexes in order to study the effects of alkyl

substitution along the pyrazole backbone on the coordination chemistry of silver(I) salts. In the solid state silver(I) complexes of pz₄lut, pz⁴₄lut, pz^{*}₄lut all give cyclic dications where each ligand binds the silver through the pyrazolyl nitrogens similar to tetra(pyridyl)lutidine **PY5-R** and tetra(pyrazolyl)-*m*-xylene ligands. While silver(I) complexes of the ligand pz^{DIP}₄lut give structures consisting of infinite polymer chains, which can most likely be attributed to the unfavorable steric interactions between the 3-isopropyl groups and the central pyridyl ring in the cyclic structure.

However, solution studies of the silver complexes show that this cyclic structure is not maintained and the silver complexes become monomeric upon dissolution; concluded on the basis of ESI(+) mass spec, variable temperature ¹H NMR and diffusion (PFGSE) NMR experiments. While some uncertainty remains in assigning the absolute coordination mode of the silver complexes in solution, owing to the fact that there are a limited number and type of resonances appearing in the NMR spectra, we are able to rule out certain possibilities based on energy constraints as well as the favored coordination number for silver(I) complexes (≤ 4). As such, we favor a process in which there is rapid interchange between the κ^1 and κ^2 modes at high temperature giving rise to the exchange averaged pyrazolyl resonances that are observed, while the κ^2 mode is the dominant form at lower temperatures and the formation of cyclic or linear oligomers gives rise to the new peaks observed.

Experimental

General Considerations. The compound 2,6-pyridinedicarboxaldehyde was prepared according to the literature procedure.^{ref} While the preparation of **pz4lut** has been described previously,^{ref} an improved preparation is described below along with additional characterization including the single-crystal X-ray structural determination. All other chemicals were commercially available and were used as received. Solvents were dried by conventional methods and distilled prior to use. The syntheses of the silver complexes were carried out under a nitrogen atmosphere using standard Schlenk techniques and in foil-covered apparatus to protect AgBF₄ or AgOTf from light. After complex formation, no special precautions to avoid light or air were taken.

Midwest MicroLab, LLC, Indianapolis, Indiana 45250, performed all elemental analyses. IR spectra were recorded for samples as KBr pellets in the 4000-500 cm⁻¹ region on a Nicolet Magna-IR 560 spectrometer. ¹H and ¹³C NMR spectra were recorded on a Varian 400 MHz spectrometer. Chemical shifts were referenced to solvent resonances at δ_H 7.26 and δ_C 77.23 for CDCl₃, δ_H 1.96 and δ_C 118.9 for CD₃CN. Details regarding diffusion NMR experiments are found in the Supporting Information. Absorption measurements were recorded on an Agilent 8453 spectrometer. Melting point determinations were made on samples contained in glass capillaries using an Electrothermal 9100 apparatus and are uncorrected. Mass spectrometric measurements recorded in ESI(+) mode were obtained on a Micromass Q-TOF spectrometer whereas those performed by using direct-probe analyses were made on a VG 70S instrument. For the ESI(+) experiments formic acid (approximately 0.1 % v/v) was added to the mobile

phase (CH₃CN). X-ray powder diffraction measurements were performed with a Rigaku MiniFlex II instrument using Cu K α (1.54178 Å) radiation.

General procedure for the syntheses of pz^R₄lut ligands. A solution of a given pyrazole, Hpz^R (6.1 equiv.) in THF (ca. 0.3-0.7 M) was slowly added to a suspension of NaH (6 equiv.) in THF at a rate to control hydrogen evolution. The resulting solution was stirred magnetically at room temperature for 30 min, then neat thionyl chloride (3 equiv.) was slowly added by syringe (dropwise, to control the slightly exothermic reaction) immediately causing the formation of copious colorless precipitate. After the mixture had been stirred at room temperature for 1 h, CoCl₂ (60 mol % of 2,6-pyridinedicarboxaldehyde) and 2,6-pyridinedicarboxaldehyde (1 equiv.) were sequentially added as solids under a nitrogen blanket. The reaction flask was fitted with a condenser and the mixture was heated at reflux 40 h under nitrogen. After cooling to room temperature, 50 mL CH₂Cl₂ and 100 mL of 4 wt% NaHCO₃ and 1 wt% EDTA in water were added to the mixture. The layers were separated and the aqueous phase was washed with three 50 mL portions of CH₂Cl₂. The combined organic layers were washed with two 100 mL portions of water, dried over MgSO₄, and filtered to give viscous pale orange or brown oils after removing solvent by rotary evaporation. The desired product was separated from the oil residue by column chromatography either on neutral alumina or on silica gel, as indicated below.

pz₄lut. The reaction between 3.00 g (22.2 mmol) 2,6-pyridinedicarboxaldehyde, 1.73 g (13.3 mmol) CoCl₂, and 66.6 mmol O=S(pz)₂ in 400 mL THF (formed in-situ from 9.23 g (135 mmol) pyrazole in 300 mL THF, 3.20 g (133 mmol) NaH in 100 mL THF, and 4.84 mL (7.92 g, 66.6 mmol) thionyl chloride) afforded 5.67 g (69 %) of **pz₄lut**

as a colorless solid after aqueous work-up and column chromatography of the oily product mixture on neutral alumina using Et₂O as the eluent and collecting the second band ($R_f = 0.68$ on a Al₂O₃ plate). Crystals suitable for X-ray diffraction were obtained by layering an acetone solution with hexanes and allowing solvents to diffuse 2d. Both the powder and crystals had characterization data consistent with those previously reported.^{ref} Mp, 119-120°C. ¹H NMR (CD₃CN, 293 K): δ 7.87 (t, $J = 8$ Hz, 1H, H₄-py), 7.83 (s, 2H, CH(pz)₂), 7.68 (d, $J = 2$ Hz, 4H, H₃-pz), 7.58 (d, $J = 1$ Hz, 4H, H₅-pz), 7.21 (d, $J = 8$ Hz, 2H, H_{3,5}-py), 6.35 (dd, $J = 1$; 2Hz, 4H, H₄-pz). UV-Vis (CH₃CN) λ_{\max} , nm (ϵ , M⁻¹, cm⁻¹): 228 (33,000), 265 (8,500).

pz^{4'}4lut. The crude product mixture obtained from a reaction between 0.459 g (3.40 mmol) 2,6-pyridinedicarboxyaldehyde, 0.256 g (2.04 mmol) CoCl₂, and 6.80 mmol O=S(pz^{4'})₂ (formed in-situ from 1.11 g (13.5 mmol) 4-methylpyrazole in 50 mL THF, 0.325 g (13.5 mmol) NaH in 50 mL THF, and 0.49 mL (0.81 g, 6.8 mmol) thionyl chloride) was subject to column chromatography on neutral alumina. First, elution with Et₂O removed an unidentified impurity, then elution with ethyl acetate ($R_f = 0.89$, Al₂O₃ plate) afforded 1.05 g (72 %) of **pz^{4'}4lut** as a colorless solid after removing solvent, triturating the oily fraction with Et₂O, and drying under vacuum. Mp, 145-148 °C. Anal. Calcd. (obsd.) for C₂₃H₂₅N₉: C, 64.62 (64.28); H, 5.89 (6.01); N, 29.49 (29.15). ¹H NMR (CDCl₃) δ_H 7.56 (t, $J = 8$ Hz, 1H, H₄-py), 7.36 (s, 2H, CH(pz^{4'})₂), 7.21 (s, 4H, H₃-pz^{4'}), 7.11 (s, 4H, H₅-pz^{4'}), 6.95 (d, $J = 8$ Hz, 2H, H_{3,5}-py), 1.86 (s, 12H, CH₃). ¹H NMR (CD₃CN, 293 K) δ_H 7.82 (t, $J = 8$ Hz, 1H, H₄-py), 7.61 (s, 2H, CH(pz^{4'})₂), 7.42 (s, 4H, H₃-pz^{4'}), 7.35 (s, 4H, H₅-pz^{4'}), 7.18 (d, $J = 8$ Hz, 2H, H_{3,5}-py), 2.03 (s, 12H, CH₃). ¹³C

NMR (CDCl₃) δ_C 154.8, 141.4, 138.6, 128.4, 122.8, 117.2, 78.1, 9.1. UV-Vis (CH₃CN) λ_{\max} , nm (ϵ , M⁻¹, cm⁻¹): 228 (33,000), 265 (8,500).

pz*₄lut. The crude product mixture obtained from a reaction between 3.40 g (25.1 mmol) 2,6-pyridinedicarboxyaldehyde, 0.530 g (4.10 mmol) CoCl₂ and 75.4 mmol O=S(pz*)₂ (formed in-situ from 14.22 g (147.9 mmol) 3,5-dimethylpyrazole in 200 mL THF, 3.55 g (147.9 mmol) NaH in 200 mL THF, and 5.48 mL (8.97 g, 75.4 mmol) thionyl chloride) was subject to column chromatography on neutral alumina. First, elution with Et₂O removed an unidentified impurity, then elution with ethyl acetate (R_f = 0.62, Al₂O₃ plate) afforded 5.44 g (45 %) of **pz*₄lut** as a colorless solid after removing solvent, triturating the oily fraction with Et₂O, and drying under vacuum. Mp, 156-157°C. Anal. Calcd. (obsd.) for C₂₇H₃₃N₉: C, 67.06 (67.27); H, 6.88 (7.02); N, 26.07 (25.88). ¹H NMR (CDCl₃) δ_H 7.65 (t, J = 8 Hz, 1H, H₄-py), 7.41 (s, 2H, CH(pz*)₂), 7.00 (d, J = 8 Hz, 2H, H_{3,5}-py), 5.78 (s, 4H, H₄-pz*), 2.15 (s, 12H, CH₃), 2.05 (s, 12H, CH₃). ¹H NMR (CD₃CN, 293 K) δ_H 7.75 (t, J = 8 Hz, 1H, H₄-py), 7.46 (s, 2H, CH(pz*)₂), 7.02 (d, J = 8 Hz, 2H, H_{3,5}-py), 5.87 (s, 4H, H₄-pz*), 2.10 (s, 12H, CH₃), 2.07 (s, 12H, CH₃). ¹³C NMR (CDCl₃) δ_C 155.1, 148.3, 141.0, 137.7, 122.2, 106.7, 74.5, 13.8, 11.4. UV-Vis (CH₃CN) λ_{\max} , nm (ϵ , M⁻¹ cm⁻¹): 228 (34,000), 267 (10,400).

pz^{DIP}₄lut. After aqueous work-up of the reaction between 1.08 g (25.1 mmol) 2,6-pyridinedicarboxyaldehyde, 1.037 g (7.99 mmol) CoCl₂ and O=S(pz^{DIP})₂ (formed in-situ from 4.98 g (32.7 mmol) 3,5-diisopropylpyrazole in 200 mL THF, 0.790 g (32.7 mmol) NaH in 200 mL THF, and 1.13 mL (1.90 g, 15.9 mmol) thionyl chloride), 5.79 g of brown oil was obtained. The ¹H NMR spectrum of the brown oil was consistent with a mixture of two main species, **pz^{DIP}₄lut** (90 %) and 2-(pz^{DIP}₂CH)-6-[CH(O)]-C₆H₃N (10

%) (see Supporting Information) whose composition is determined using the relative integrations of resonances in the H₄-pz region of the spectrum at δ_{H} 5.86 (desired product) and δ_{H} 5.95 (mono-carboxaldehyde). The comparable high solubilities of components prevented successful separation by column chromatography on either silica gel or alumina, therefore separation was achieved as follows: A 5.76 g (0.85 mmol) sample of the product mixture and 0.123 g (0.85 mmol) 1,8-aminoquinoline in 15 mL methanol was heated at reflux 1 h. This second product mixture was adsorbed onto a short pad of silica gel where elution with 4:1 hexanes:ethyl acetate (R_{f} = 0.64 SiO₂) gave 3.85 g (68 % overall yield based on 2,6-pyridinedicarboxyaldehyde) of **pz^{DIP}4lut** as a tan solid after removing solvent, trituration with Et₂O, and drying under vacuum. Mp, 79-81 °C. Anal. Calcd. (obsd.) for C₄₃H₆₅N₉: C, 72.94 (72.86); H, 9.25 (9.11); N, 17.80 (17.89). ¹H NMR (CDCl₃) δ_{H} 7.66 (t, J = 8 Hz, 1H, H₄-py), 7.63 (s, 2H, CH(pz^{DIP})₂), 7.02 (d, J = 8 Hz, 2H, H_{3,5}-py), 5.86 (s, 4H, H₄- pz^{DIP}), 3.11 (sept, J = 7 Hz, 1H, ⁱPrCH), 2.87 (sept, J = 7 Hz, 1H, ⁱPrCH), 1.16 (d, J = 7 Hz, 24H, ⁱPrCH₃), 0.91 (d, J = 7 Hz, 24 H, ⁱPrCH₃). ¹H NMR (CD₃CN, 293 K) δ_{H} 7.76 (t, J = 8 Hz, 1H, H₄-py), 7.57 (s, 2H, CH(pz^{DIP})₂), 7.06 (d, J = 8 Hz, 2H, H_{3,5}-py), 6.02 (s, 4H, H₄- pz^{DIP}), 3.10 (sept, J = 7 Hz, 1H, ⁱPrCH), 2.81 (sept, J = 7 Hz, 1H, ⁱPrCH), 1.17 (d, J = 7 Hz, 24H, ⁱPrCH₃), 1.03 (d, J = 7 Hz, 12 H, ⁱPrCH₃), 0.97 (d, J = 7 Hz, 12 H, ⁱPrCH₃). ¹³C NMR (CDCl₃) δ_{C} 159.2, 156.5, 152.9, 138.6, 123.4, 100.8, 75.5, 30.8, 28.7, 26.3, 23.7 UV-Vis (CH₃CN) λ_{max} , nm (ϵ , M⁻¹ cm⁻¹), 205 (31,040), 221 (23,618sh), 265 (4941).

[Ag(**pz4lut**)](BF₄), **1**. A solution of 0.500 g (1.35 mmol) **pz4lut** in 20 mL THF was added to a solution of 0.262 g (1.35 mmol) AgBF₄ in 15 mL THF causing immediate precipitation. After the cloudy suspension had been stirred 4h, the precipitate was

isolated by cannula filtration, was washed with three successive 10 mL portions of Et₂O, and was dried under vacuum 12 h to give 0.663 g (87 %) **1** as a colorless powder. Mp, 210–214 °C (dec.) Anal. Calcd. (obsd.) for C₁₉H₁₇N₉AgBF₄: C, 40.31 (40.50); H, 3.03 (3.16); N, 22.27 (22.38). IR (KBr, cm⁻¹), $\nu(\text{BF}_4^-)$ regions: 1084, 1063, 775, 753. ¹H NMR (CD₃CN, 293 K) δ_{H} 7.94 (t, J = 8 Hz, 1H, H₄-py), 7.85 (s, 2H, CH(pz)₂), 7.84 (d, J = 2 Hz, 4H, H₅-pz), 7.61 (d, J = 1 Hz, 4 H, H₃-pz), 7.41 (d, J = 8 Hz, 2H, H_{3,5}-py), 6.36 (dd, J = 2, 1 Hz, 4H, H₄-pz), 2.16 (s, 26H, CH₃CN). ¹H NMR (CD₃CN, 233 K) δ_{H} 7.934 (t, J = 8 Hz, 1H, H₄-py), 7.927 (d, J = 2 Hz, 4H, H₅-pz), 7.85 (br s, 2H, CH(pz)₂), 7.57, (d, J = 1 Hz, 4H, H₃-pz), 7.29 (br s, 2H, H_{3,5}-py), 6.36 (dd, J = 2, 1 Hz, 4H, H₄-pz), 2.39 (s, 26H, CH₃CN). UV-Vis (CH₃CN) λ_{max} , nm (ϵ , M⁻¹ cm⁻¹): 218 (35,500), 263 (7,200). HRMS [ESI(+), m/z] Calcd. (Obs) for C₃₈H₃₄N₁₈Ag₂BF₄, [Ag₂(pz₄lut = L)₂(BF₄)⁺, 1045.1351 (1045.1318). LRMS [ESI(+), m/z] (Int.) [assign.]: 1282 (0.1) [Ag₃L₂(BF₄)₂(CH₃CN)]⁺, 1137 (1) [Ag₃L₂(Cl)₂]⁺, 1045 (0.1) [Ag₂L₂(BF₄)]⁺, 993 (3) [Ag₂L₂(Cl)]⁺, 849 (17) [AgL₂]⁺, 622 (24) [Ag₂L(Cl)]⁺, 480 (100) [AgL]⁺, 394 (31) [NaL]⁺, 372 (35) [HL]⁺, 304 (26) [L-Hpz]⁺. Colorless crystals of unsolvated [Ag(pz₄lut)](BF₄) suitable for X-ray were grown by layering a methanol solution of AgBF₄ onto a CH₂Cl₂ solution of the ligand and allowing solvents to diffuse 3 d.

[Ag(pz^{4'}lut)](BF₄), **2**. A solution of 0.531 g (1.24 mmol) pz^{4'}lut in 10 mL THF was added to a solution of 0.241 g (1.24 mmol) AgBF₄ in 10 mL THF causing immediate precipitation. After the mixture had been stirred 4h, the precipitate was isolated by cannula filtration, was washed with three successive 10 mL portions of Et₂O, and was dried under vacuum 12 h to give 0.648 g (84%) **2** as a colorless powder. Mp, 189–195 °C (dec. to a black solid). Anal. Calcd. (obsd.) for C₂₃H₂₅N₉AgBF₄: C, 44.40 (44.07); H,

4.05 (4.04); N, 20.26 (19.94). IR (KBr, cm^{-1}) $\nu(\text{BF}_4^-)$ regions: 1084, 778. ^1H NMR (CD_3CN , 293 K, see text) δ_{H} 7.94 (t, $J = 8$ Hz, 2H, $\text{H}_4\text{-py}$), 7.68 (br s, 12H, $\text{CH}(\text{pz}^{4'})_2$ and $\text{H}_3\text{-pz}^{4'}$), 7.40 (d, $J = 8$ Hz, 4H, $\text{H}_{3,5}\text{-py}$), 7.39, (s, 8H, $\text{H}_5\text{-pz}$), 2.16 (s, 8H, CH_3CN), 2.04 (s, 24H, pzCH_3). ^1H NMR (CD_3CN , 233 K) δ_{H} 7.97 (t, $J = 8$ Hz, 2H, $\text{H}_4\text{-py}$), 7.75 (br s, 8H, $\text{H}_3\text{-pz}^{4'}$), 7.62 (br s, 4H, $\text{CH}(\text{pz}^{4'})_2$), 7.26, (s, 8H, $\text{H}_5\text{-pz}$), 7.09 (br s, 4H, $\text{H}_{3,5}\text{-py}$), 2.38 (s, 8H, CH_3CN), 2.03 (s, 24H, pzCH_3). UV-Vis (CH_3CN) λ_{max} , nm (ϵ , $\text{M}^{-1} \text{cm}^{-1}$): 227 (36,300), 264 (9,300). HRMS [ESI(+), m/z] Calcd. (Obs) for $\text{C}_{46}\text{H}_{50}\text{N}_{18}\text{Ag}_2\text{BF}_4$, [Ag₂(pz^{4'}₄lut = L)₂(BF₄)]⁺, 1155.2605 (1155.2616). LRMS [ESI(+), m/z] (Int.) [assign.]: 1390 (0.5) [Ag₃L₂(BF₄)₂(CH₃CN)]⁺, 1245 (1) [Ag₃L₂(Cl)₂]⁺, 1157 (6) [Ag₂L₂(BF₄)]⁺, 1105 (4) [Ag₂L₂(Cl)]⁺, 961 (33) [AgL₂]⁺, 678 (22) [Ag₂L(Cl)]⁺, 536 (100) [AgL]⁺, 428 (22) [HL]⁺, 346 (13) [L-Hpz^{4'}]⁺. Colorless crystals were obtained by vapor diffusion of THF into a concentrated CH₃CN solution.

[Ag(pz*₄lut)](BF₄), **3**. A solution of 0.506 g (1.05 mmol) pz*₄lut in 10 mL THF was added to a solution of 0.208 g (1.07 mmol) AgBF₄ in 10 mL THF causing immediate precipitation. After the mixture had been stirred 4h, the precipitate was isolated by cannula filtration, was washed with three successive 10 mL portions of Et₂O, and was dried under vacuum 12 h to give 0.536 g (85 %) **3** as a colorless powder. Mp, 242 – 245 °C (decomp.). Anal. Calcd. (obsd.) for $\text{C}_{27}\text{H}_{33}\text{N}_9\text{AgBF}_4$: C, 47.81 (47.66); H, 4.90 (4.81); N, 18.58 (18.53). IR (KBr, cm^{-1}) $\nu(\text{BF}_4^-)$ regions: 1084, 783. ^1H NMR (CD_3CN , 233 K, see text) δ_{H} 7.75 (t, $J = 8$ Hz, 2H, $\text{H}_4\text{-py}$), 7.27 (s, 4H, $\text{CH}(\text{pz}^*)_2$), 6.79 (d, $J = 8$ Hz, 4H, $\text{H}_{3,5}\text{-py}$), 6.04 (s, 4H, $\text{H}_4\text{-pz}^*$), 5.81 (s, 4H, $\text{H}_4\text{-pz}^*$), 2.41 (s, 36 H, CH_3CN), 2.37 (s, 12H, pz^*CH_3), 2.30 (s, 12H, pz^*CH_3), 1.81 (s, 12H, pz^*CH_3), 1.62 (s, 12H, pz^*CH_3). ^1H NMR (CD_3CN , 293 K) δ_{H} 7.77 (br t, $J = 8$ Hz, 2H, $\text{H}_4\text{-py}$), 7.28 (s, 4H, $\text{CH}(\text{pz}^*)_2$), 6.82 (br s,

4H, H_{3,5}-py), 6.02 (br, 4H, H₄-pz^{*}), 5.84 (br, 4H, H₄-pz^{*}), 2.34 (br, 24H, pz^{*}CH₃), 2.18 (s, 36H, CH₃CN), 1.84 (br, 24H, pz^{*}CH₃) ¹H NMR (CD₃CN, 353 K) δ_{H} 7.83 (t, $J = 8$ Hz, H₄-py), 7.34 (s, 4H, CH(pz^{*})₂), 7.02 (d, $J = 8$ Hz, 4H, H_{3,5}-py), 5.97 (s, 8H, H₄-pz^{*}), 2.34 (s, 24H, pz^{*}CH₃), 1.97 (s, 36H, CH₃CN), 1.92 (s, 24H, pz^{*}CH₃). UV-Vis (CH₃CN) λ_{max} , nm (ϵ , M⁻¹, cm⁻¹): 216 (39,400), 266 (6,600). HRMS [ESI(+), m/z] Calcd. (Obs) for C₅₄H₆₆N₁₈Ag₂BF₄, [Ag₂(pz^{*}₄lut = L)₂(BF₄)]⁺, 1267.3859 (1267.3835). LRMS [ESI(+), m/z] (Int.) [assign.]: 1267 (0.1) [Ag₂L₂(BF₄)]⁺, 1215 (0.4) [Ag₂L₂(Cl)]⁺, 1076 (6) [AgL₂]⁺, 734 (8) [Ag₂L(Cl)]⁺, 592 (38) [AgL]⁺, 546 (7) [Na(CH₃CN)L]⁺, 506 (40) [NaL]⁺, 484 (100) [HL]⁺, 388 (7) [L-Hpz^{*}]⁺. Colorless crystals were obtained by vapor diffusion of THF into a concentrated CH₃CN solution.

[Ag(pz^{DIP}₄lut)](BF₄), **4**. A solution of 0.518 g (0.73 mmol) pz^{DIP}₄lut in 10 mL THF was added to a solution of 0.142 g (0.73 mmol) AgBF₄ in 10 mL THF giving a cloudy solution. The flask was covered in foil and allowed to stir overnight forming a small amount of precipitate. The solution was filtered and was concentrated to give an oily solid residue which was triturated with Et₂O and dried under vacuum to give 0.475 g (72 %) of **4** as a colorless powder. Mp, 165 – 170 °C (decomp.). Anal. Calcd. (obsd.) for C₄₃H₆₅N₉AgBF₄: C, 57.21 (56.91); H, 7.25 (7.45); N, 13.96 (13.78). IR (KBr, cm⁻¹) ν (BF₄⁻) regions: 1083, 708. ¹H NMR (CD₃CN, 233 K, see text) δ_{H} 7.76 (br s 2H, H₄-py), 7.59 (s, 8H, CH(pz^{DIP})₂), 6.99 (br s 4H, H_{3,5}-py), 6.17 (m, 8H), 2.99 (br d, 16H, ⁱPrCH), 2.51 (t, $J = 1$ Hz, 48H, ipr), 0.68 (br m, 48H, ⁱPrCH₃). ¹H NMR (CD₃CN, 293 K) δ_{H} 7.78 (br t, $J = 8$ Hz, 2H, H₄-py), 7.14 (s, 4H, CH(pz^{DIP})₂), 6.33 (br s, 4H, H_{3,5}-py), 6.11 (br s, 8H, H₄-pz^{DIP}), 2.98 (br s, 8H, ⁱPrCH), 2.21 (s, 48H, ⁱPrCH₃), 0.81 (br m, 48H, ⁱPrCH₃). ¹H NMR (CD₃CN, 353 K) δ_{H} 7.83 (t, $J = 8$ Hz, 2H, H₄-py), 7.42 (s, 4H, CH(pz^{DIP})₂),

6.91 (br s, 4H, H_{3,5}-py), 6.13 (s, 8H, H₄-pz), 3.08 (sept, $J = 7$ Hz, 8H ⁱPrCH), 2.66 (br s, 8H, ⁱPrCH), 2.00 (s, 24H, ⁱPrCH₃), 1.18 (d, $J = 7$ Hz, 12H, ⁱPrCH₃), 1.11 (d, $J = 7$ Hz, 12H, ⁱPrCH₃). UV-Vis (CH₃CN) λ_{max} , nm (ϵ , M⁻¹, cm⁻¹): 215 (25,706), 267 (4,948). [ESI(+), m/z] Calcd. (Obs) for C₄₃H₆₅N₉AgBF₄, [Ag(pz^{DIP}₄lut = L)(BF₄)]⁺, LRMS [ESI(+), m/z] (Int.) [assign.]: 958 (0.7) [Ag₂L(Cl)]⁺, 814 (21) [AgL]⁺, 730 (10) [NaL]⁺, 708 (100) [L]⁺, 556 (10) [L-Hpz3,5-diiso]⁺, 355 (17) [Na(CH₃CN)L]⁺, 279 (21) [NaL]⁺, 189 (0.4) [Hpz^{DIP}(Cl)]⁺, 153 (7) [Hpz^{DIP}]⁺.

[Ag(pz^{DIP}₄lut)](SO₃CF₃), **5**. A solution of 0.200 g (0.28 mmol) pz^{DIP}₄lut in 10 mL THF was added to a solution of 0.72 g (0.28 mmol) AgSO₃CF₃ in 10 mL THF giving a cloudy solution. The flask was covered in foil and allowed to stir overnight forming a large amount of white precipitate. The precipitate was collected by filtration, was washed with Et₂O (3 x 10 mL), and was dried under vacuum to give 0.195 g (72 %) of **5** as a colorless powder. Mp, 204 – 208 °C (decomp.). Anal. Calcd. (obsd.) for C₄₄H₆₅N₉AgF₃SO₃: C, 53.75 (54.04); H, 6.82 (6.82); N, 13.12 (12.89). IR (KBr, cm⁻¹) ν (SO₃CF₃⁻) regions: ν [SO₃(E)]: 1267 cm⁻¹; ν [SO₃(A₁)]: 1032 cm⁻¹; ν [CF₃(A₁)]: 1259 cm⁻¹; [CF₃(E)]: 1153 cm⁻¹. ¹H NMR (CD₃CN, 233 K, see text) δ_{H} 7.77 (br s, 2H), 6.99 (br s, 4H), 6.17 (br m, 10H), 2.94 (br d, 8H), 2.44 (s, 48H, ⁱPrCH₃), 0.75 (br m, 48H, ⁱPrCH₃). ¹H NMR (CD₃CN, 293 K) δ_{H} 7.80 (t, $J = 7$ Hz, 2H, H₄-py), 7.11 (s, 4H, CH(pz^{DIP}₂)), 6.34 (br s, 4H, H_{3,5}-py), 6.13 (br, 8H, H₄-pz^{DIP}), 2.96 (br, 4H, H₄-pz^{DIP}), 2.20 (br, 24H, ⁱPrCH₃), 0.80 (br m, 2H ⁱPrCH₃). ¹H NMR (CD₃CN, 353 K) δ_{H} 7.83 (t, $J = 8$ Hz, 2H, H₄-py), 7.37 (s, 4H, CH(pz^{DIP}₂)), 6.80 (d, $J = 8$ Hz, 4H, H_{3,5}-py), 6.13 (s, 8H, H₄-pz^{DIP}), 3.06 (sept, $J = 7$ Hz, 8H, ⁱPrCH), 2.56 (br s, 8H), 2.12 (s, 48H, ⁱPrCH₃), 1.19 (d, $J = 7$ Hz, 24H, ⁱPrCH₃), 1.10 (d, $J = 7$ Hz, 24 H, ⁱPrCH₃). UV-Vis (CH₃CN) λ_{max} , nm (ϵ , M⁻¹,

cm^{-1}), 214 (33 476), 265 (5 719). HRMS [ESI(+), m/z] Calcd. (Obs) for $\text{C}_{43}\text{H}_{65}\text{N}_9\text{Ag}$,
 $[\text{Ag}(\text{pz}^{\text{DIP}}_4\text{lut} = \text{L})]^+$, 814.4414 (814.4430). LRMS [ESI(+), m/z] (Int.) [assign.]: 816
 (0.8) $[\text{AgL}]^+$, 731 (0.3) $[\text{AgHL}]^+$, 708 (100) $[\text{L}]^+$, 556 (0.8) $[\text{L-Hpz}^{\text{DIP}}]^+$, 519 (0.4)
 $[\text{AgL}]^+$, 355 (23) $[\text{Na}(\text{CH}_3\text{CN})\text{L}]^+$, 279 (29) $[\text{NaL}]^+$, 153 (0.9) $[\text{Hpz}^{\text{DIP}}]^+$. Colorless
 crystals were obtained by vapor diffusion of THF into a concentrated CH_3CN solution.

Chapter 2: First Row Transition Metal Complexes of $\alpha, \alpha, \alpha', \alpha'$ -Tetra(pyrazolyl)lutidine.

Introduction. There has been recent interest in tetrapodal pentadentate ligands that bind metals in an MAE₄ (M = Metal; A = Axial; E = Equatorial) fashion for studies in fundamental coordination chemistry especially those involving modeling of the reactivity of biologically important species such as hemes and cobalamins.¹ The continued development of pentadentate ligands has led to the discovery of interesting new nonheme metal complexes capable of facilitating many spectacular organic transformations, highlighted by the oxidation of alkanes.¹⁵ Pentadentate ligands of particular relevance to the current study are those derived from tetrakis(2-pyridyl)-m-lutidine (**Figure 2.1** below). Numerous coordination modes have been observed for each,¹⁶ with the pentadentate mode being more extensively structurally authenticated for **PY5**¹⁷ than for other **PY5-R** derivatives.¹⁸ Transition-metal complexes of pentadentate **PY5** have an unusual structural feature in that the dihedral angle between the axial pyridyl and the equatorial N₄ plane significantly deviates from ideal orthogonality. Such a deformation likely reduces the efficiency of both σ - and π -orbital interactions between the axial heterocycle and the metal d orbitals, a possible factor for influencing the reactivity of the complexes. Molecular models suggest that this unusual arrangement is

enforced by steric interactions about the quaternary carbons specifically between the methoxy and pyridyl groups. While this deformation may not be as pronounced in

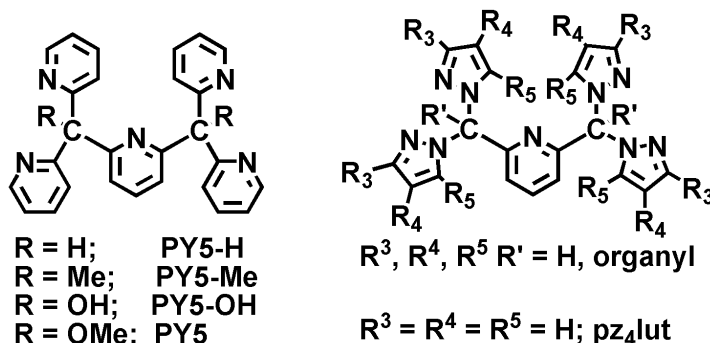
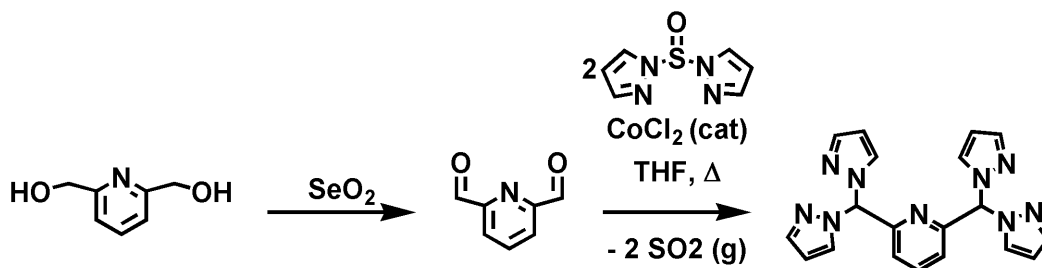


Figure 2.1. Related pentadentate ligand scaffolds.

solution,¹⁹ we conjectured the modification of the pentadentate ligand backbone might provide a key to tuning the properties and chemical reactivity of the resulting metal complexes because, in metal complexes, the cone angle for steric accessibility is larger for ligands with five membered pyrazolyl rings compared to those with similarly substituted six-membered pyridyl rings. To this end, we have developed a new class of pentadentate ligand based on $\alpha, \alpha', \alpha', \alpha'$ -tetra(pyrazolyl)lutidine, pz₄lut scaffold (**Figure 2.1**) and have initiated an investigation into their coordination chemistry. The new ligands offer some advantageous design features that can be exploited for further systematic studies, including (i) the ease of synthesis of pyrazoles with nearly limitless substitution patterns that allow for facile means to control steric and electronic properties of the resulting metal complexes and, by appropriate pyrazolyl substitution, allow for the deliberate construction of supramolecular assemblies²⁰ and (ii) the flexible ligand synthesis permitting ready substitution of the fourth group (R' in **Figure 2.1** above, right) of the sp^3 carbon atoms, which will allow further evaluation of the impact of this substituent on the properties of the resulting metal complex. Herein we report the

synthesis of the new ligand and its coordination complexes with a series of divalent first-row transition-metal halides to probe the coordination mode (the expected κ^5 -) and what structural trends can be observed if any as well as a discussion on the survey of electronic properties.

Synthesis. The synthesis of the new pentadentate ligand, pz₄lut (**Scheme 2.1**) takes advantage of the CoCl₂-catalyzed rearrangement reaction⁶ between 2,6-pyridinecarboxaldehyde²¹ (prepared by SeO₂ oxidation of 2,6-pyridinedimethanol) and the appropriate di(pyrazolyl)-sulfone (prepared in situ by the reaction between NaH, Hpz, and SOCl₂)²² in THF. Typically, the CoCl₂-catalyzed rearrangement reaction with dialdehydes affords high yields (>70%) of product. In the current case, the yield is typically only 40%. Presumably, the relatively higher stability and lower solubility of the cobalt complex of this ligand sequesters the catalyst, lowering its performance. However, more recently we have found that using three equivalents of SOCl₂ instead of two typically leads to higher yields (>60 %). Full experimental details can be found at



Scheme 2.1. Synthesis of new pz₄lut ligand.

the end of this chapter.

X-ray-quality crystals of divalent metal chloride complexes [MCl(κ^5 N-**pz₄lut**)]⁺ were obtained by layering of methanol solutions of the transition-metal salts (except for

Ni, for which ethanol gave better quality crystals) onto CH_2Cl_2 or CHCl_3 solutions of the ligands and allowing the solvents to slowly diffuse over several days.

Solid State Structures. The complexes with $M = \text{Mn, Fe, Co, and Cu}$ contain a chloride anion and methylene chloride solvent molecule. The nickel derivative crystallizes with a chloride anion but as an ethanol solvate, while the zinc derivative contains the $[\text{ZnCl}_3(\text{MeOH})]^-$ anion. The six metal cations prepared in this study share a number of common features. All have MN_5Cl kernels as a result of κ^5 -ligand coordination with pyridyl and chloride axial groups and four pyrazolyl N atoms occupying the equatorial plane of the pseudooctahedral metal center. The average metal-nitrogen(pz) bond distances $\text{Mn}^{\text{II}}\text{-N}$ 2.26 Å (d^5), $\text{Fe}^{\text{II}}\text{-N}$ 2.20 Å (d^6), and $\text{Co}^{\text{II}}\text{-N}$ 2.15 Å (d^7) are indicative of high-spin systems.²³ The structure and metrical parameters are shown below (**Table 2.1**) while the structures of the six cations are shown on the following page (**Figure 2.2**). In the $[\text{MCl}(\text{pz}_4\text{lut})](\text{Cl})$ complexes ($M = \text{Mn, Fe, Co, Ni, Cu, Zn}$) the metal sits above the mean plane of pyrazolyl nitrogens toward the axial chloride group. A closer examination of the geometries of the various $[\text{MCl}(\text{pz}_4\text{lut})]^+$ cations (**Table 2.2, Figures 2.3 & 2.4**) indicates that nickel(II) provides the best “fit” for the new ligands. Relative to other metal centers, nickel is situated closest to (0.165 Å above) the mean plane of equatorial pyrazolyl nitrogens. The metal-bound pyrazolyls experience the least amount of ring-twisting (ideally, this torsion angle should be 0°)¹³ in the Ni^{II} case, defined by the average $\text{MN-NC}(\text{sp}^3)$ torsion angle of 1.76° (compared to MnN-NC of 3.28° in the manganese case, for example). In all cases, there is more ring twisting in the PY5 (9.8° average) complexes than in the pz_4lut cases (1.8° average **Figure 2.5**), with the greatest contribution in the former cases from the axial pyridyl.

Also, the nickel complex exhibits the smallest octahedral volume [Volume of $MN_{4(pz)}N_{(Npy)}Cl = 12.930 \text{ \AA}^3$] and quadratic elongation $(1.010)^{24}$ compared to all other metals in the series. There is a regular variation in bond distances versus the number of d-electrons on traversing the series from manganese (d^5) to nickel (d^8) (**Figure 2.3**). Copper (d^9) represents the break in the trend (**Figure 2.3 top**) of smaller divalent metal cations giving shorter mean bond distances, due to distortion of equatorial Cu-N bonds. The $[CuCl(pz_4lut)]^+$ cation contains two very short Cu-N(pz) (Cu-N5 and Cu-N7, avg. 1.999 \AA) bonds and two long Cu-N(pz) bonds (Cu-N3 and Cu-N9, avg. 2.392 \AA) giving a coordination sphere that approaches square planar (with two long Cu-N(pz) contacts). If these longer axial contacts are ignored, then the Cu-N(pyrazolyl) bonds and the weighted average of all metal-ligand bonds (2.096 \AA)

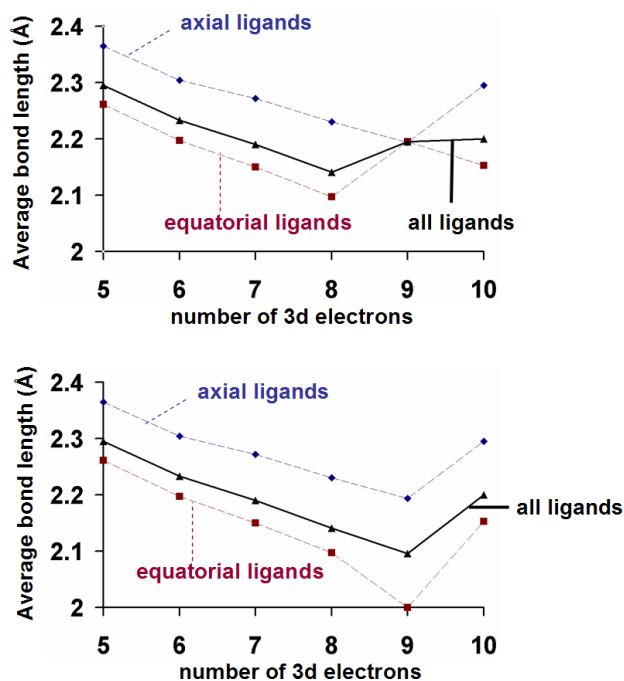


Figure 2.3. Plots of bond distances as a function of d-electron count of metal in $[MCl(pz_4lut)]^+$. Average of all groups of MN_5Cl considered (top). Long Cu-N(pyrazolyl) bond distances ignored (bottom).

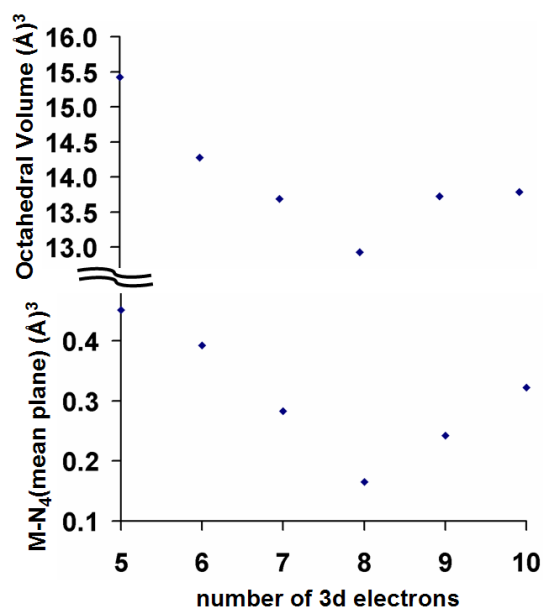


Figure 2.4. Plots of MN_5Cl octahedral volume (top) and deviation of M from equatorial N_4 plane (bottom) versus d-electron count of metal in $[\text{MCl}(\text{pz}_4\text{lut})]^+$ complexes.

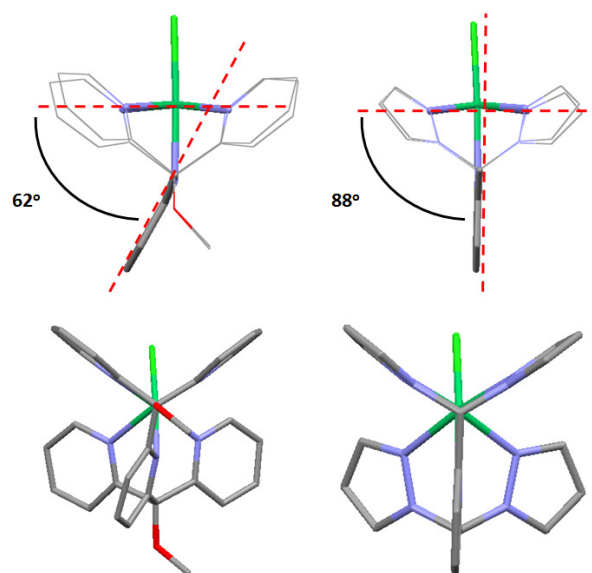


Figure 2.5. Comparison of the structures of related $[\text{NiCl}(\text{L})]^+$ cations ($\text{L} = \text{PY5}$, left; $\text{L} = \text{pz}_4\text{lut}$, right). H atoms are omitted. Top: views orthogonal to the axial pyridyl. Bottom: Views down C – O (PY5) or C – H (pz4lut) bonds.

fall in line with other metals in the series (**Figure 2.3b**). The preference for lower coordination geometries for Cu^{2+} is well-documented and is also observed in the related square-pyramidal $[\text{CuCl}(\kappa^4\text{-PY5})]^+$ cation.²⁵ Usually this coordination preference is attributed to Jahn-Teller distortion due to single occupancy of degenerate e_g^* orbitals. The low symmetry of the complexes in this series was expected to remove such degeneracy and this distortion was unexpected.

Electronic Absorption Spectra. The electronic spectra of the ligand and metal complexes are shown below (**Figure 2.5, 2.6**). For each, there are two rather intense bands near 200 nm ($\epsilon \sim 25\,000\text{ M}^{-1}\text{ cm}^{-1}$) and 260 nm ($\epsilon \sim 5000\text{ M}^{-1}\text{ cm}^{-1}$), assigned to $\pi - \pi^*$ intraligand transitions on the basis of intensity. For all of the metal complexes, an additional shoulder near 300 nm ($\epsilon \sim 50 - 2700\text{ M}^{-1}\text{ cm}^{-1}$) is observed that is absent in the free ligand and is tentatively assigned as metal-to-ligand charge transfer in nature. For Fe^{II} , Co^{II} , Ni^{II} , and Cu^{II} , lower-energy low-intensity ($\epsilon < 50\text{ M}^{-1}\text{ cm}^{-1}$) spin allowed d – d bands are also observed; the spin-forbidden bands in Mn^{II} are not observed. The single d – d band in the spectra of each Fe^{II} and Cu^{II} shows a pronounced shoulder from the expected Jahn – Teller distortions. The crystal field splitting parameters (**Table 2.3**) calculated from the observed d – d bands gave the metal-dependent spectrochemical series $\text{Co}^{\text{II}} > \text{Ni}^{\text{II}} > \text{Fe}^{\text{II}} > \text{Cu}^{\text{II}}$ for the pz_4lut complexes.²⁶ In the cases of Co^{II} and Ni^{II} , where full data are readily available for comparison, the crystal-field splitting parameters for $[\text{MCl}(\text{L})]^+$ ($\text{L} = \text{pz}_4\text{lut}, \text{PY5}$) indicate that the pz_4lut ligand exerts a slightly stronger field ($\text{Co}^{\text{II}}, 10\text{ Dq} = 11\,582\text{ cm}^{-1}$; $\text{Ni}^{\text{II}}, 10\text{ Dq} = 11\,442\text{ cm}^{-1}$) than the related PY5 ligand ($\text{Co}^{\text{II}}, 10\text{ Dq} = 10\,915\text{ cm}^{-1}$; $\text{Ni}^{\text{II}}, 10\text{ Dq} = 10\,707\text{ cm}^{-1}$).⁴ Because pyridyls are generally

stronger field donors than pyrazolyls, this rather surprising observation may be a result of the greater ligand distortions in the PY5 framework compared to the pz₄lut cases. A greater degree of ring twisting in the former may potentially reduce the full σ -donor (and π -accepting) capabilities of the PY5 ligand.

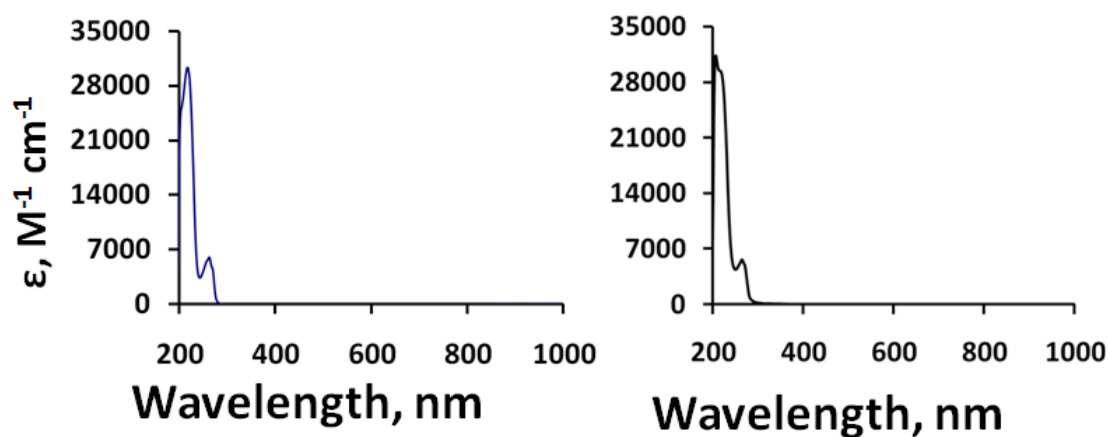


Figure 2.5. UV-Vis absorption spectra of pz₄lut in MeOH (left). Representative metal complex in MeOH ([MnCl(L)](Cl), right).

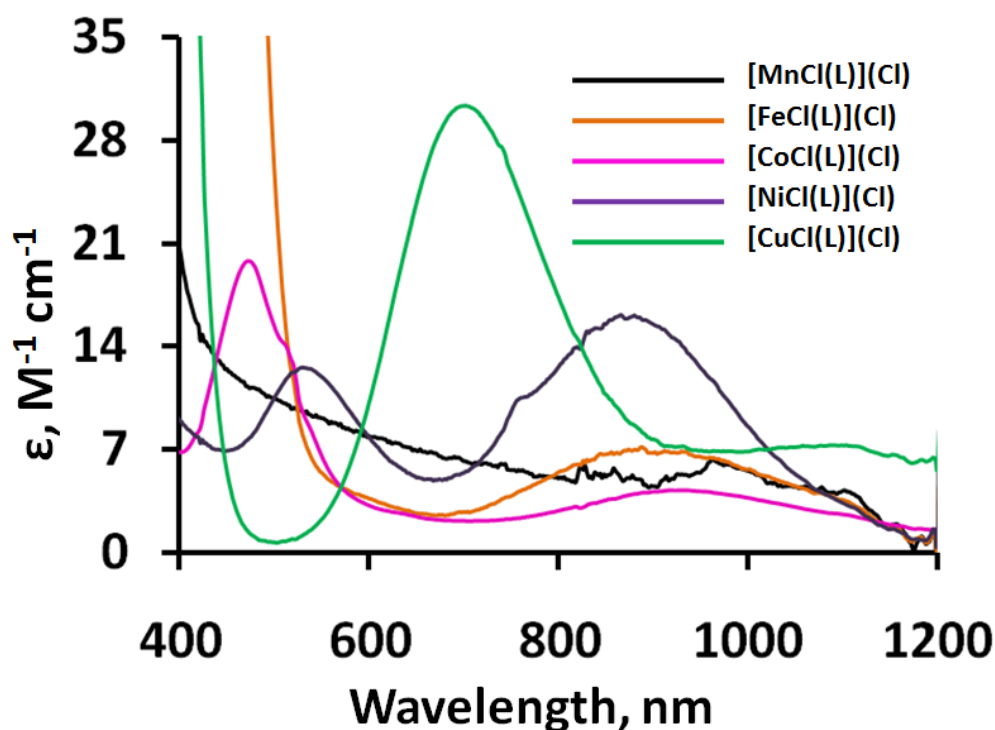


Figure 2.6. Near IR region of metal complexes in MeOH.

Table 2.1. Crystallographic Data and Refinement Parameters for (a) [MnCl(pz₄lut)](Cl)•CH₂Cl₂ (1•CH₂Cl₂); (b) [FeCl(pz₄lut)](Cl)•CH₂Cl₂ (2•CH₂Cl₂); (c) [CoCl(pz₄lut)](Cl)•CH₂Cl₂ (3•CH₂Cl₂); (d) [NiCl(pz₄lut)](Cl)•EtOH (4•EtOH); (e) [CuCl(pz₄lut)](Cl)•0.82CH₂Cl₂ (5•CH₂Cl₂); (f) [ZnCl(pz₄lut)]ZnCl₃(MeOH)]•0.63CH₂Cl₂•0.34 MeOH (6•0.63 CH₂Cl₂•0.34 MeOH).

Compound	1•CH ₂ Cl ₂	2•CH ₂ Cl ₂	3•CH ₂ Cl ₂	4•EtOH	5•0.82 CH ₂ Cl ₂	6•0.63 CH ₂ Cl ₂ •0.34 MeOH
Formula	C ₂₀ H ₁₉ Cl ₄ MnN ₉	C ₂₀ H ₁₉ Cl ₄ FeN ₉	C ₂₀ H ₁₉ Cl ₄ CoN ₉	C ₂₁ H ₂₃ Cl ₂ N ₉ NiO	C _{19.82} H _{18.65} Cl _{3.64} CuN ₉	C _{21.37} H _{25.21} C _{15.26} N ₉ O _{1.74} Zn ₂
Formula Weight	582.18	583.09	586.17	547.09	575.71	753.22
Crystal System	Monoclinic	Monoclinic	Monoclinic	Monoclinic	Monoclinic	Monoclinic
Space Group	P2 ₁ /n	P2 ₁ /c	P2 ₁ /n	C2/c	P2 ₁ /c	P2 ₁ /n
a, Å	10.5304(6)	10.4115(5)	10.2900(2)	21.7305(7)	10.8339(2)	11.52640(10)
b, Å	19.2722(10)	19.2410(9)	19.1675(3)	22.0929(8)	22.2728(3)	13.94720(10)
c, Å	11.9444(6)	12.0005(6)	12.0572(2)	9.7949(4)	9.80290(10)	18.9316(2)
B deg	90.000(2)	90.000(2)	90.0330(10)	90.0000(10)	92.9950(10)	102.3930(10)
V, Å ³	2424.0(2)	1488.9(3)	2378.08(7)	3156.57(6)	2326.22(6)	2972.55(5)
Z	4	4	4	8	4	4
T, K	100(2)	100(2)	100(2)	100(2)	100(2)	100(2)
ρ, calcd, Mg m ³	1.595	1.611	1.637	1.546	1.619	1.683
λ, Å	1.54178	1.54178	1.54178	1.54178	1.54178	1.54178
μ (Cu, Kα) mm ⁻¹	8.734	9.372	10.046	3.573	5.345	6.653
R[I>2σ(I)] ^a (all data)	0.0473(0.0483)	0.0353(0.0387)	0.0411(0.0418)	0.0366(0.0381)	0.0311(0.0410)	0.0237(0.0240)
wR ^b (all data)	0.1102(0.1108)	0.0874(0.0874)	0.1126(0.1131)	0.0930(0.0940)	0.0745(0.0792)	0.0623 (0.0624)

^aR = Σ|F_o| - |F_c|/Σ|F_o|. ^bwR = [Σw(|F_o² - |F_c²||²)/Σw|F_o²|]^{1/2}

Figure 2.2. Views of the cation structures with atom labeling for (A) $[\text{MnCl}(\text{pz}_4\text{lut})](\text{Cl})\cdot\text{CH}_2\text{Cl}_2$ (**1**), (B) $[\text{FeCl}(\text{pz}_4\text{lut})](\text{Cl})\cdot\text{CH}_2\text{Cl}_2$ (**2**), (C) $[\text{CoCl}(\text{pz}_4\text{lut})](\text{Cl})\cdot\text{CH}_2\text{Cl}_2$ (**3**), (D) $[\text{NiCl}(\text{pz}_4\text{lut})](\text{Cl})\cdot 4\text{EtOH}$ (**4**), (E) $[\text{CuCl}(\text{pz}_4\text{lut})](\text{Cl})\cdot 0.82 \text{CH}_2\text{Cl}_2$ (**5**), and (F) $[\text{ZnCl}(\text{pz}_4\text{lut})][\text{ZnCl}_3(\text{MeOH})]\cdot 0.063 \text{CH}_2\text{Cl}_2\cdot 0.34 \text{MeOH}$ (**6**).

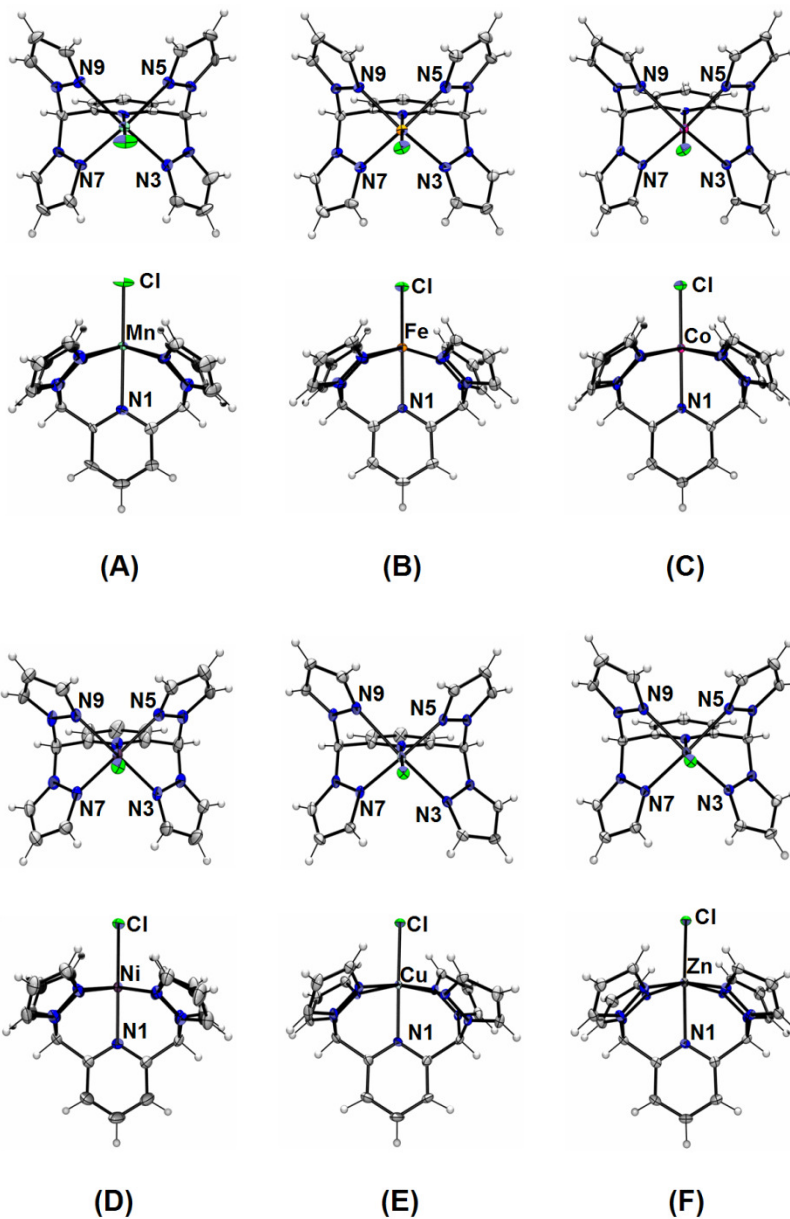


Table 2.2. Intercationic geometric parameters for [MCl(pz₄lut)]⁺ (M = Mn, Fe, Co, Ni, Cu, Zn).

M =	Mn	Fe	Co	Ni	Cu	Zn
M-Cl (Å)	2.365	2.307	2.323	2.360	2.279	2.334
M-N1 _{py} (Å)	2.364	2.300	2.221	2.099	2.109	2.256
M-N3 _{pz} (Å)	2.237	2.179	2.140	2.088	1.999	2.163
M-N5 _{pz} (Å)	2.257	2.187	2.138	2.098	2.376	2.159
M-N7 _{pz} (Å)	2.255	2.198	2.144	2.098	2.408	2.121
M-N9 _{pz} (Å)	2.293	2.222	2.176	2.104	1.998	2.169
Avg. axial (Å)	2.365	2.304	2.272	2.230	2.194	2.295
Avg. Eq. (Å)	2.261	2.197	2.150	2.097	2.195	2.153
Avg. total (Å)	2.295	2.233	2.190	2.141	2.195	2.200
M-N4 _{pl} (Å)	0.451	0.392	0.283	0.165	0.242	0.322
MN3-N2C6 (°)	1.50	1.93	1.22	0.58	3.55	3.27
MN5-N4C6 (°)	3.97	5.08	2.07	4.60	3.65	3.75
MN7-N6C7 (°)	0.85	1.21	4.78	0.90	6.19	1.08
MN9-N8C7 (°)	6.80	7.50	4.70	0.96	2.64	7.14
Avg MN-NC (°)	3.28	3.93	3.19	1.76	4.01	3.81
N1-M-Cl (°)	179.52	179.60	179.97	177.82	177.85	173.76
Oct. Vol (Å) ³	15.421	14.279	13.688	12.930	13.723	13.786
Quad. Elong.	1.034	1.026	1.016	1.010	1.024	1.021
∠_variance (°) ²	114.41	88.46	627.84	25.34	44.24	66.54

Electron Paramagnetic Resonance. The various paramagnetic $[\text{M}^{\text{II}}\text{Cl}(\text{pz}_4\text{lut})]^+$ derivatives as frozen (10 K) glasses in 1 EtOH : 9 MeOH were also subject to X-band (9.6 GHz) electron paramagnetic resonance (EPR) spectroscopic studies to verify spin multiplicities. The data are collected in **Table 2.3** while the EPR spectra are shown below in **Figure 2.7 and 2.8**. The complexes generally displayed axial signals, expected from the solid state geometries. The Mn^{II} and Co^{II} EPR spectra indicated the $S = 5/2$

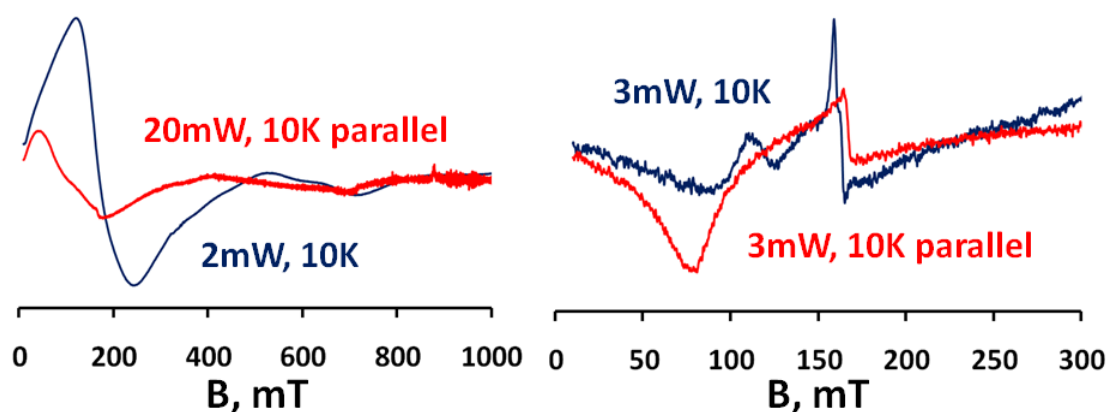


Figure 2.7. Frozen glass EPR of $[\text{MnCl}(\text{pz}_4\text{lut})](\text{Cl})$ (left) and $[\text{FeCl}(\text{pz}_4\text{lut})](\text{Cl})$ (right). For $[\text{MnCl}(\text{pz}_4\text{lut})](\text{Cl})$: transitions at $g_{\text{eff}} \sim 10, 6$, and 2 would be expected for a perfectly axial ($E/D = 0$) system with $7 \text{ cm}^{-1} (10 \text{ K}) > \Delta \gg 0.3 \text{ cm}^{-1}$. The complexity of the spectrum suggests that either the zero-field splitting is not sufficiently large that the Zeeman interaction can be treated as a perturbation (i.e. $\Delta \approx 0.3 \text{ cm}^{-1}$), and/or that there is a significant rhombic zero field splitting term ($E/D > 0$). For $[\text{FeCl}(\text{pz}_4\text{lut})](\text{Cl})$: the parallel mode signal at $g_{\text{eff}} \sim 9$ is due to Fe(II) the dominant species; while the perpendicular mode reveals traces of Fe(III) .

and $S = 3/2$ high-spin configurations, respectively. The zero-field splitting, Δ , was much larger than the Zeeman interaction in both cases. In the case of Mn^{II} , it appears that the excited-state doublets were populated at 10 K (i.e., $7 \text{ cm}^{-1} \leq \Delta \gg 0.3 \text{ cm}^{-1}$), whereas for Co^{II} , $\Delta \gg 7 \text{ cm}^{-1}$. No EPR signal was detected for the Ni(II) complex, typical of a non Kramers ($S = 1$) system with significant zero-field splitting. Interestingly, an EPR signal for the $[\text{Fe}^{\text{II}}\text{Cl}(\text{pz}_4\text{lut})](\text{Cl})$ was

observed at $g_{\text{eff}} \sim 9$ at low temperatures despite a non Kramers ($S = 2$) spin multiplicity owing to some proportion of the zero-field splitting envelop satisfying the condition $\Delta < 0.3 \text{ cm}^{-1}$.²⁷

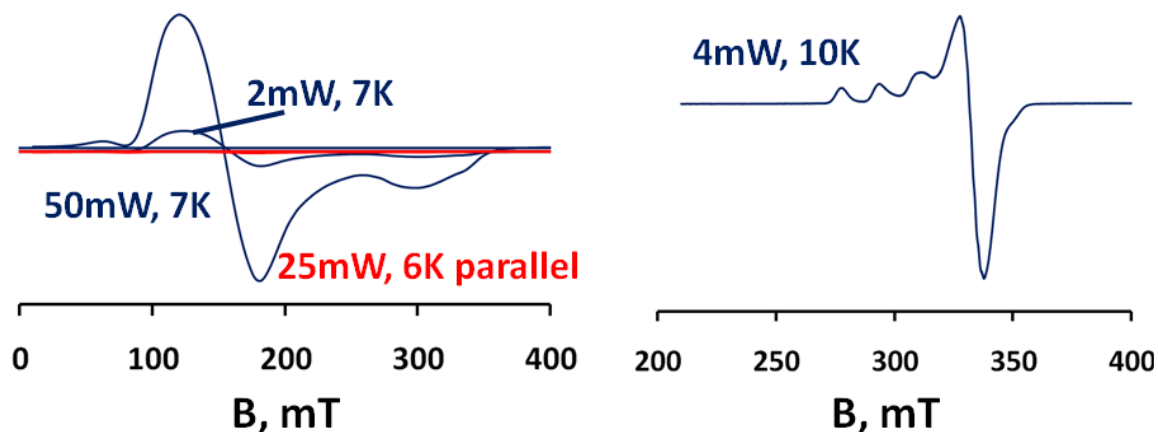


Figure 2.8. Frozen glass EPR of $[\text{CoCl}(\text{pz}_4\text{lut})](\text{Cl})$ (left) and $[\text{CuCl}(\text{pz}_4\text{lut})](\text{Cl})$ (right). For $[\text{CoCl}(\text{pz}_4\text{lut})](\text{Cl})$: the major resonances at $g_{\text{eff}} \sim 4.3$ and 2.3 indicates $S = 3/2$ with $\Delta \gg g\beta BS$ and $M_s = |\pm 1/2\rangle$. The small feature at $g_{\text{eff}} = 11.5$ is likely due to spin-spin interaction between $\text{Co}(\text{II})$ ions ($S = 0, 1, 2, 3$). For $[\text{CuCl}(\text{pz}_4\text{lut})](\text{Cl})$: g_{\parallel} and A_{\parallel} are indicative of nitrogen ligation to $\text{Cu}(\text{II})$. The shoulder to the high field side of the main g_{\perp} peak, and its partner to the low field side, are due to dipolar interactions between adjacent $\text{Cu}(\text{II})$ ions.

Summary & Conclusions. In summary, a new pentadentate ligand, $\alpha, \alpha', \alpha''$ -tetra(pyrazolyl)lutidine, pz_4lut and several coordination complexes with $[\text{MCl}(\text{pz}_4\text{lut})]^+$ ($\text{M} = \text{Mn}, \text{Fe}, \text{Co}, \text{Ni}, \text{Cu}, \text{Zn}$) cations have been prepared. A survey of the structural features of the complexes shows that the ligand binds in the expected $\kappa^5\text{N}$ mode with the axial pyridyl group nearly orthogonal to the equatorial N_4 plane. Analysis of ligand distortions in related $[\text{MCl}(\text{L})]^+$ ($\text{L} = \text{pz}_4\text{lut}, \text{PY5}$) complexes indicated a lower degree of ring twisting in the current system relative to the **PY5** complexes. This feature might be responsible for the rather surprising electronic properties because pz_4lut is a slightly stronger field

ligand to Co^{II} and Ni^{II} compared to the all-pyridyl-based **PY5** ligand, contrary to initial expectations. The simple synthesis of the new ligand architecture combined with ready modifications using numerous available substituted pyrazolylys permits easy access to derivatives with variable sterics and electronic properties, chemical reactivity and ligand denticity.

complex	$\mu_{\text{eff}}, \mu_{\text{B}}$	$\lambda_{\text{max}}, \text{nm} (\epsilon, \text{M}^{-1} \text{cm}^{-1}), \text{MeOH}$	10 Dq, cm^{-1}	EPR X-band (9.6 GHz), g_{eff}
$[\text{MnCl}(\text{pz}_4\text{lut})]^+$	5.9	215 (29 404), 264 (5614), 342 sh (5)		$g_{\perp} 4.05, g_{\parallel} 0.99$
$[\text{FeCl}(\text{pz}_4\text{lut})]^+$	5.2	263 (8762), 300 sh (2677), 428 (282), 888 (19), 1050 sh (5)	10 393	$g_{\text{eff}} \sim 9$
$[\text{CoCl}(\text{pz}_4\text{lut})]^+$	3.6	264 (4936), 300 sh (608), 472 (20), 934 (4)	11 582	$g_{\perp} 4.32, g_{\parallel} 2.30 (g_{\text{real}} \sim 2.2)$
$[\text{NiCl}(\text{pz}_4\text{lut})]^+$	2.3	268 (3455), 300 sh (188), 536 (25), 764 sh (7), 874 (13)	11 442	
$[\text{CuCl}(\text{pz}_4\text{lut})]^+$	1.8	270 (3611), 424 (278), 700 (43), 1150 SH (12)	$\sim 9\,820$	$g_{\perp} 2.07, g_{\parallel} 2.28 (A_{\parallel} = 17 \text{ mT})$

Table 2.3. Summary of the Electronic Properties of Transition-Metal Complexes of **pz₄lut**.

Experimental Details. Pyrazole, thionyl chloride, NaH, and all transition metal halides were obtained commercially and were used as received. The compound 2,6-pyridinecarboxaldehyde was prepared according to a literature method and the synthesis of pz₄lut is described in **Chapter 1**. Solvents were dried by conventional procedures and distilled prior to use, except where noted. Midwest MicroLab, LLZC, Indianapolis, Indiana 45250, performed all elemental analyses. melting point determinations were made on samples contained in glass capillaries using an Electrothermal 9100 apparatus and are uncorrected. ¹H and ¹³C NMR spectra were recorded on a Varian 300 MHz spectrometer. Chemical shifts were referenced to solvent resonances at δ_{H} 7.27 and δ_{C} 77.23 for CDCl₃, δ_{H} 3.31 and δ_{C} 49.15 for methanol-d₄. UV-visible and NIR spectra were recorded using Shimadzu UV-1600/1700 or Jasco V-570 instruments. Solid-state magnetic measurements were made at room temperature using an MK1 magnetic susceptibility balance. EPR spectral measurements were obtained using a Bruker ELEXSYS E600 equipped with an ER4116DM cavity resonating at 9.63 GHz, an Oxford Instruments ITC503 temperatures controller and ESR-900 helium flow cryostat. The ESR spectra were recorded with 100 kHz field modulation.

[MnCl(pz₄lut)](Cl)•CH₂Cl₂, 1•CH₂Cl₂. A Solution of 0.191 g (0.514 mmol) of pz₄lut in 8.5 mL dichloromethane was layered with a methanol solution (8.5 mL) of 0.108 g (0.546 mmol) MnCl₂•4H₂O. After 3 days, 0.176 g (59 %) of X-ray quality colorless blocks of **1•CH₂Cl₂** were collected after filtration, washing with Et₂O and drying under vacuum. Mp, 190-195 °C, dec. Anal. Calcd. (obsd.) for C₂₀H₁₉C₁₄MnN₉: C, 41.26 (41.22); H, 3.29 (3.46); N, 21.65 (21.96). μ_{eff} (Evans) (CD₃OD, 298 K) 5.9 μ_{B} . UV-Vis (MeOH) λ_{max} , nm (ϵ , M⁻¹, cm⁻¹), 215 (29 404), 264 (5614), 342 (53).

[FeCl(pz₄lut)](Cl)•CH₂Cl₂, 2•CH₂Cl₂. A solution of 0.100 g (0.789 mmol) of FeCl₂ in 8.5 mL of MeOH was layered onto a solution of 0.293 g (0.789 mmol) pz₄lut in 8.5 mL of CH₂Cl₂. After 3 days, 0.450 g (98 %) of orange X-ray quality crystals of **2•CH₂Cl₂** were collected as above. Mp, 247-257 °C dec. Anal. Calcd. (obsd.) for C₂₀H₁₉Cl₄FeN₉: C, 41.20 (41.59); 3.28 (3.50); 21.62 (21.68). μ_{eff} (Evans) (CD₃OD, 298 K) 5.2 μ_{B} . UV-Vis (MeOH) λ_{max} , nm (ϵ , M⁻¹, cm⁻¹), 263 (8462), 300 (2677), 428 (282), 888 (19), 1050sh (10).

[CoCl(pz₄lut)](Cl)•CH₂Cl₂, 3•CH₂Cl₂. A Solution of 0.286 g (0.770 mmol) pz₄lut in 8.5 mL of CH₂Cl₂ was layered with a solution of 0.105 g (0.809 mmol) CoCl₂ in 8.5 mL MeOH and solvents were allowed to slowly diffuse over 3 days. A 0.405 g (90 %) sample of **3•CH₂Cl₂** as pink X-ray quality crystals was collected and dried under vacuum. Mp, 282-285 °C dec. Anal. (obsd) for C₂₀H₁₉Cl₄CoN₉; C, 40.98 (40.95); H, 3.27 (3.29); N, 21.51 (21.49). μ_{eff} (Evans) (CD₃OD, 298 K) 3.6 μ_{B} . UV-Vis (MeOH) λ_{max} , nm (ϵ , M⁻¹, cm⁻¹), 264 (4936), 300sh (608), 472 (20), 934 (4).

[NiCl(pz₄lut)](Cl), 4. A chloroform (8.5 mL) solution 0.161 g (0.433 mmol) pz₄lut was layered with a ethanol (8.5 mL) solution of 0.106 g (0.446 mmol) of NiCl₂•6H₂O. After the solvents were allowed to diffuse for 3 d, 0.243 g (98 %) of violet microcrystalline **4**, was isolated after filtration and drying under vacuum. Mp, 200-203 oC, dec. anal. Calcd. (obsd.) for C₁₉H₁₇Cl₂N₉Ni: C, 45.55 (45.31); H, 3.42 (3.24); N, 25.16 (25.04). μ_{eff} (Evans) (CD₃OD, 298 K) 3.6 μ_{B} . UV-Vis (MeOH) λ_{max} , nm (ϵ , M⁻¹, cm⁻¹), 268 (3455), 300sh (188), 563 (25), 764sh (7), 874 (13). X-ray quality crystals of a solvate (**4•EtOH**) are obtained before drying. The solvent is readily removed by vacuum.

[CuCl(pz₄lut)](Cl), 5. A solution containing 0.169 g (0.45 mmol) pz₄lut in 8.5 mL CH₂Cl₂ was layered with a methanol (8.5 mL) solution of 0.063 g (0.47 mmol) CuCl₂ and solvents were allowed to diffuse over 3 days. A 0.216 g (95 %) sample of **5** as a green microcrystalline powder was collected by filtration and dried under vacuum. Mp, 267-270 °C, dec. Anal. Calcd. (obsd.) for C₁₉H₁₇Cl₂CuN₉: C, 45.11 (45.85); H, 3.39 (3.00); N, 24.92 (24.56). μ_{eff} (Evans) (CD₃OD, 298 K) 3.6 μ_{B} . UV-Vis (MeOH) λ_{max} , nm (ϵ , M⁻¹ cm⁻¹), 270 (3611), 424 (278), 700 (43), 1150sh (12). X-ray quality crystals of a solvate (**5**•0.82 CH₂Cl₂) are obtained before drying. The solvent is readily removed by vacuum.

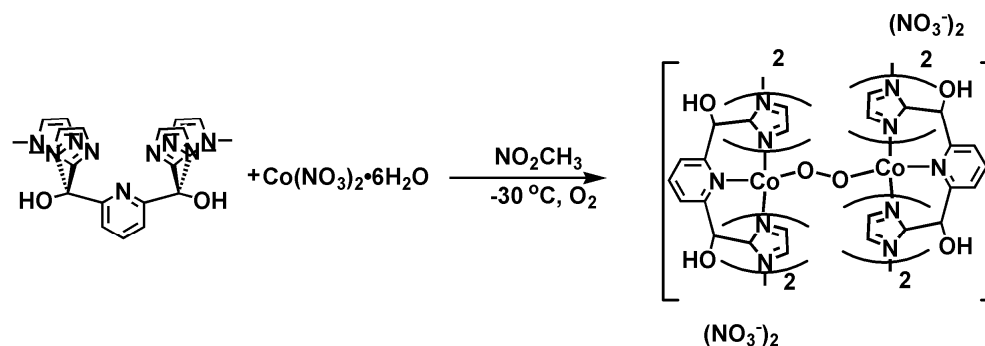
[ZnCl(pz₄lut)][ZnCl₃(MeOH)] 6. A dichloromethane (8.5 mL) solution containing 0.276 g (0.743 mmol) pz₄lut was layered with a methanol (8.5 mL) solution containing 0.109 g (0.800 mmol) of ZnCl₂. After allowing the solvents to diffuse over 4 days, 0.253 g (89 % based on ZnCl₂) of **6** were collected by filtration and dried under vacuum. Mp, 284-290 °C, dec. Anal. Calcd. (obsd.) for C₂₀H₂₁Cl₄N₉OZn₂: C, 35.53 (35.15); H, 3.13 (3.43); N, 18.65 (18.28). This compound is surprisingly less soluble in CD₃OD, than in CH₃OH in which the complex has sparing solubility (it is also insoluble in all other typical organi solvents), so ¹H NMR were recorded as a saturated solution in 10 vol-% D₂O in CD₃OD while ¹³C NMR spectral data could not be recorded in a reasonable amount of acquisition time. ¹H NMR (CD₃OD/10 vol-% D₂O) δ_{H} 8.32 (br s, 4H), 8.27-8.23 (br m, 6H), 8.09 (br m, 3H), 6.57 (s, 4H, H₄-pz). X-ray quality crystals of a solvate (**6**•0.63 CH₂Cl₂•0.34 MeOH) are obtained before drying. The solvent is readily removed by vacuum. UV-Vis (MeOH) λ_{max} , nm (ϵ , M⁻¹ cm⁻¹), 216 (25 271), 264 (5 736), 300sh (1008).

Chapter 3: Coordination Chemistry of Cobalt(II)

Complexes of $\alpha, \alpha, \alpha', \alpha'$ -Tetra(pyrazolyl)lutidine and its Derivatives

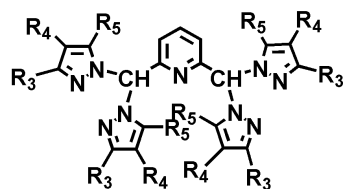
Introduction. Cobalt plays an integral role in bio-inorganic chemistry in form of cobalamin complexes.²⁸ In cobalamin complexes the cobalt is five-coordinate with a sixth coordination spot that can be occupied by any number of ligands (CN, Me, H₂O, adenosyl) with cyano being the most commonly isolated derivative.²⁹ Cobalt has also been substituted for iron in complexes as models for other biologically active oxygen carriers such as hemoglobin, hemerythrin and hemocyanin due to the fact that cobalt gives rise to more easily interpreted electronic spectra (EPR, absorption spectroscopy) than that of iron or copper.³⁰ As such, it has become relevant to design pentadentate ligands which bind in the MAE₄ (M = metal; A = Axial; E = equatorial) fashion; giving a sixth axial position capable of binding different ligands as to “mimic” these biologically relevant systems.

One of the first MAE₄ synthetic systems was designed by Tagaki & co-workers in 1979 shown in **Scheme 3.1**. When reacted with cobalt(II) at -30 °C in a oxygen saturated solution they obtained a bridged cobalt peroxo species that was deep red in color.³¹ Since then, several other pentdenate ligands have been synthesized and reacted with a variety of transition metals as reviewed by Grohman in 2004.¹ We recently reported the $\alpha, \alpha, \alpha', \alpha'$ -Tetra(pyrazolyl)lutidine ligand and its complexes with divalent first row transition



Scheme 3.1. Cobalt bridged peroxo complex proposed by Tagaki and co-workers, 1979.

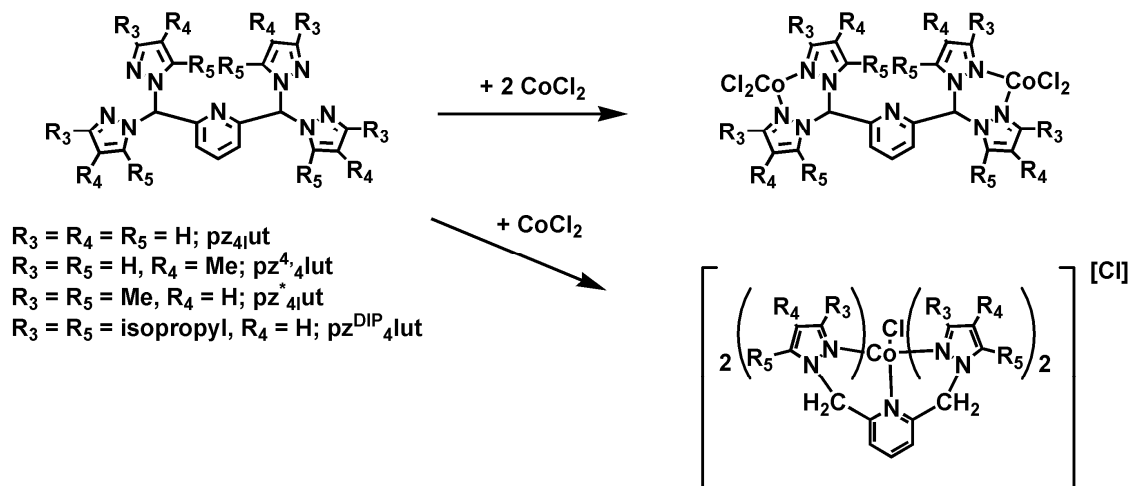
metals which established κ^5 binding mode of the pz₄lut ligand.⁵ By using pyrazoles as the nitrogen donor it allows for seemingly limitless substitution patterns along the pyrazolyl periphery. In doing so, we were able to synthesize several new alkyl substituted pentadentate ligands using 4-methylpyrazole, 3,5-dimethylpyrazole, or 3,5-diisopropylpyrazole (**Figure 3.1**). This enabled the study of steric effects as well as electronic effects of substitution along the pyrazole backbone. Cobalt(II) complexes displayed both κ^5 (pink) and κ^2 - μ (blue) coordination modes. However, in the case of the pz^{DIP}₄lut only the κ^2 - μ coordination mode was observed. Intrigued by this observation we set out to further explore the chemistry of the cobalt(II) complexes and the results are reported herein.



$R_3 = R_4 = R_5 = H$: pz₄lut
 $R_3 = R_5 = H, R_4 = Me$: pz_{4,4}lut
 $R_3 = R_5 = Me, R_4 = H$: pz^{*}₄lut
 $R_3 = R_5 = iPr, R_4 = H$: pz^{DIP}₄lut

Figure 3.1. Ligands used for Cobalt(II) complexes.

Synthesis. The synthesis of the new pentadentate ligands and their coordination chemistry with cobalt(II) chloride is summarized below in **Scheme 3.2**. The ligands were prepared as described previously. Briefly, the CoCl_2 -catalyzed rearrangement reaction⁶ between 2,6-pyridine dicarboxaldehyde (prepared by SeO_2 oxidation of 2,6-pyridine dimethanol⁹) and the appropriate di(pyrazolyl)sulfone (prepared in situ by the reaction between NaH , Hpz , and SOCl_2)⁶ in THF affords the desired ligands in good yield. As seen in Scheme 3.2, by controlling stoichiometry and solvents (vide infra) it is possible to isolate blue bimetallic complexes of all ligands or pink monometallic complexes with pseudo octahedral cobalt(II) for all ligands except for $\text{pz}^{\text{DIP}}_4\text{lut}$. cobalt complexes based on the parent unsubstituted pyrazolyl are far less soluble than their methyl substituted counterparts, which hinders solution characterization, especially of the $[\text{CoCl}(\text{pz}_4\text{lut})]^+$.



Scheme 3.2. Synthesis of cobalt(II) complexes.

All compounds exhibit solution magnetic moments in accord with high spin cobalt(II) centers with magnetic moments corresponding to about $4.2\text{--}4.8 \mu_{\text{B}}$ per tetrahedral cobalt and $3.5\text{--}3.7 \mu_{\text{B}}$ for the pseudo-octahedral complexes. These values differ from the the

spin-only moment ($3.87 \mu_B$) due to substantial orbital contribution, expected for high-spin cobalt(II) derivatives.

The structures of the ligand pz^*_4lut , three pink monometallic solvates $[CoCl(\kappa^5-pz_4lut)][Cl] \cdot CH_2Cl_2$ (**1**•**CH₂Cl₂**), $[CoCl(\kappa^5-pz^*_4lut)][Cl] \cdot MeOH$ (**2**•**MeOH**), $[CoCl(\kappa^5-pz^*_4lut)][Cl] \cdot 2MeOH$ (**3**•**2MeOH**) and two blue bimetallic complexes $(CoCl_2)_2(\mu-\kappa^2, \kappa^2-pz^*_4lut)$ (**4**), $(CoCl_2)_2(\mu-\kappa^2, \kappa^2-pz^{DIP}_4lut)$ (**5**•**MeOH**) have been determined by single crystal X-ray diffraction (**Table 3.1**), as shown in **Figure 3.2**. By comparison with related cobalt(II) derivatives, the bond lengths in the current cobalt complexes are indicative of high-spin cobalt(II).²⁵ The $[CoCl(\kappa^5-pz^*_4lut)][Cl]$ solvates along with $[(PY5)CoCl][Cl]$ ²⁵ ($PY5 = \alpha, \alpha, \alpha', \alpha'$, -tetrakis(2-pyridyl)- α, α' -dimethoxy-m-lutidine) are some of the few structurally characterized examples of pseudooctahedral cobalt(II) complexes with a tetapodal pentadentate (N_5) ligand; to our knowledge all structurally characterized derivatives with an N_5Co (halide) core contain trivalent cobalt.²⁵ Thus, the bond distances and angles of the N_5CoCl kernel in $[CoCl(\kappa^5-pz^*_4lut)][Cl]$ ($X = H, 4-Me, 3,5-Me_2$) are more compatible with those in $[(PY5)CoCl][Cl]$ than in related cobalt(III) complexes of pentadentate N_5 donors such as $[(DAMPP)CoCl][Cl][ClO_4] \cdot H_2O$ ($DAMPP = 2,6$ -bis(1',3'-diamino-2'-methylprop-2'-yl)pyridine)³² or the purely aliphatic $[(ditame)CoCl][ZnCl_4]$ ($ditame = 2,2,6,6$ -tetrakis(aminomethyl)-4-azaheptane).³³

Specifically, the average Co-N and Co-Cl bond distances (**Table 3.2**) for the common N(pyridyl)-Co-Cl axis in the three derivatives **1**•**CH₂Cl₂** (Co-N(axial), 2.221 Å; Co-Cl, 2.323 Å), **2**•**MeOH** (Co-N(axial), 2.185 Å, 2.337 Å), **3**•**2MeOH** (Co-N(axial)

2.154 Å, 2.325 Å) are similar to those in [(PY5)CoCl]⁺ (Co-N(axial), 2.127 Å, Co-Cl 2.265 Å) but are significantly longer than those in [(DAMPP)CoCl]²⁺ (Co-N(axial), 1.951 Å; Co-Cl, 2.265 Å) as might be expected. The average equatorial Co-N(pz) bond

Compound	1 •CH ₂ Cl ₂	2 •MeOH	3 •2MeOH	6	7 •MeOH
Formula	C ₂₀ H ₁₉ Cl ₄ CoN ₉	C _{24.85} H _{32.10} Cl _{2.30} CoN ₉ O _{1.70}	C ₂₉ H ₄₁ Cl ₂ CoN ₉ O ₂	C ₂₇ H ₃₃ Cl ₄ N ₉ Co ₂ N ₉	C ₄₅ H ₆₉ Cl ₄ Co ₂ N ₉ O _{2.4}
Formula Weight	586.17	624.56	677.54	743.28	1034.79
Crystal System	Monoclinic	Monoclinic	Orthorhombic	Monoclinic	Monoclinic
Space Group	P2 ₁ /n	P2 ₁ /n	Pnma	P2 ₁ /c	C2/c
a, Å	10.2900(2)	13.0101(2)	14.2736(2)	8.5289(2)	39.1841(1)
b, Å	19.1675(3)	16.0538(4)	12.8759(1)	12.3132(4)	13.9057(4)
c, Å	12.0572(2)	14.1792(4)	17.1753(2)	30.6427(9)	22.1028(5)
B deg	90.0330(10)	90.000(2)	90.000(2)	91.8810 (1)	116.2930(1)
V, Å ³	2378.08(7)	2844.00(1)	3156.57(6)	3216.30(2)	10797.40(5)
Z	4	4	4	4	8
T, K	100(2)	100(2)	100(2)	100(2)	100(2)
ρ, calcd, Mg m ⁻³	1.637	1.459	1.426	1.535	1.273
λ, Å	1.54178	1.54178	1.5417	1.54178	1.54178
μ (Cu, Kα) mm ⁻¹	10.046	7.044	6.169	11.413	6.976
R[I>2σ(I)] ^a (all data)	0.0411(0.0418)	0.0408(0.0494)	0.0318(0.0324)	0.0484(0.0706)	0.0453(0.0573)
wR ^b (all data)	0.1126(0.1131)	0.0921(0.0948)	0.0767(0.0770)	0.1042(0.1117)	0.1063(0.1143)

^aR = Σ|F_o| - |F_c|/Σ|F_o|. ^bwR = [Σw(|F_o² - |F_c²)|²/Σw|F_o²|]^{1/2}

Table 3.1. Crystallographic data collection and structure refinement for **1**•CH₂Cl₂, **2**•MeOH, **3**•2MeOH, **4**, **5**•MeOH.

distance in [CoCl(κ⁵-pz₄lut)][Cl] (2.249 Å) is longer than in **2**•MeOH (2.131 Å) and **1**•CH₂Cl₂ (2.149 Å), presumably due to the steric interactions between the 3-methylpyrazolyl substituents and the chloride in the former (**Figure 3.3**). As such, the axial N_{py}-Co-Cl angle in **3**•2MeOH (177 °) experiences a greater deviation from linearity (180 °) than in both **2**•MeOH and **1**•CH₂Cl₂. In addition, the pyrazolyl rings **3**•2MeOH are more twisted (CoN-NC(H)=5.8 °) than those in **2**•MeOH (CoN-NC(H)=2.87 °)

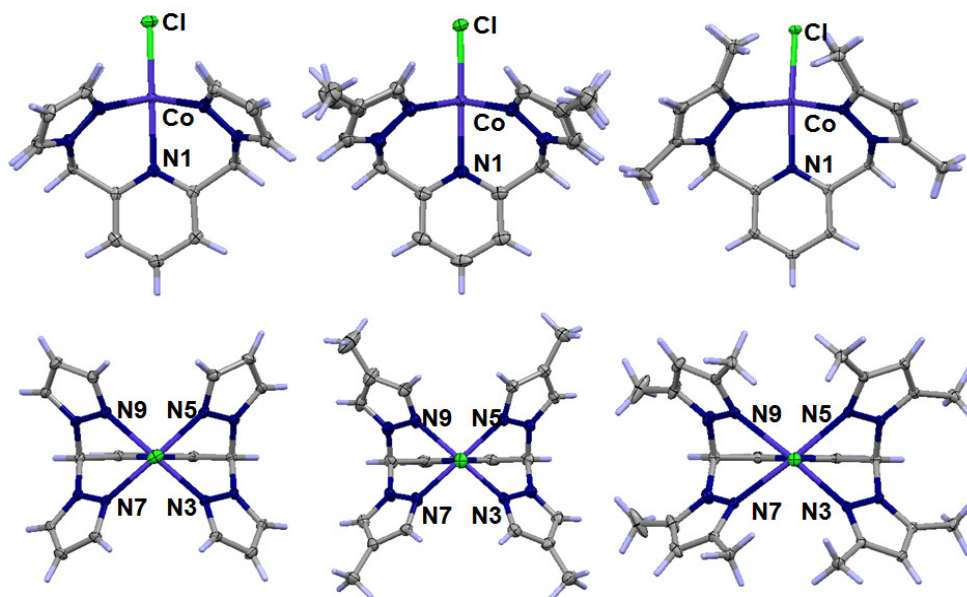


Figure 3.2. X-ray Crystal Structures of **1**•CH₂Cl₂ (left), **2**•MeOH (middle) and **3**•2MeOH (right) cations; ellipsoids drawn at 50 % probability level.

	[CoCl(κ ⁵ - pz ₄ lut)][Cl]•CH ₂ Cl ₂	[CoCl(κ ⁵ - pz ⁴ ₄ lut)][Cl]•MeOH•Et ₂ O	[CoCl(κ ⁵ - pz* ₄ lut)][Cl]•2MeOH
Co-N(pz)	2.138(3), 2.140(3), 2.144(3), 2.175(3)	2.118(2), 2.132(2), 2.133(3), 2.143(2)	2.222(7), 2.276(1), 2.222(7), 2.276(1)
Co-N(pz) Avg	2.149(3)	2.131(2)	2.249(4)
Co-N(py)	2.221(3)	2.185(2)	2.154(1)
Co-Cl	2.322(8)	2.337(5)	2.325(3)
Co-N ₄	0.283	0.257	0.218
N(py)-Co-Cl	179.97	178.53	177.04
Co-N-N-C(H)	2.07, 1.27, 4.78, 4.70 avg. 3.20°	0.29, 3.09, 3.70, 4.43, avg. 2.87 °	0.09, 11.44, 0.09 11.44 avg. 5.77°

Table 3.2. Selected Bond Distances and Angles for **1**•CH₂Cl₂, **2**•MeOH & **3**•2MeOH

and in **1**•CH₂Cl₂ (CoN-NC(H)=3.20 °), but are much less distorted than those in the pseudotetrahedral derivatives (**4**, **5**•MeOH) discussed below.

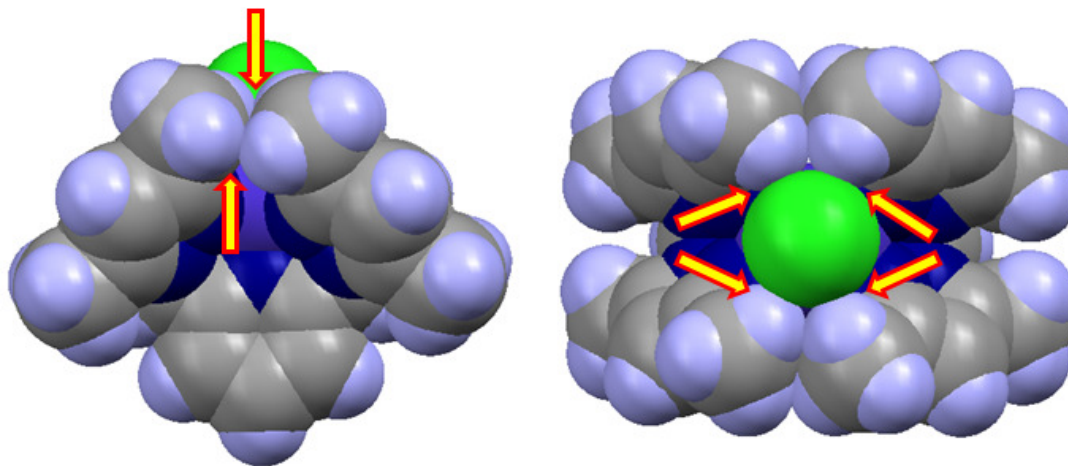


Figure 3.3. Space filling model of **3**•2MeOH showing steric interactions between methyl groups and chloride.

The structures for bimetallic, (CoCl₂)₂(μ-κ²,κ²-pz^{*₄}lut) and (CoCl₂)₂(μ-κ²,κ²-pz^{DIP₄}lut) (**Figure 3.4**). The average Co-N (pyrazolyl) and Co-Cl bond lengths (**Table 3.3**) of 2.024 Å and 2.230 Å in (**4**) and 2.028 Å and 2.237 Å for (**5**•MeOH) compare favorably with other pseudo-tetrahedral CoCl₂ complexes such as; the complex [κ²N-*o*-(HO)C₆H₄CH(pz^{3iPR})₂]CoCl₂; (Co-N, 2.027 Å; Co-Cl, 2.222 Å, synthesized by Carrano & Co-workers).³⁴ Other examples of complexes containing pseudotetrahedral include (pz^x)₂Co^{II}Cl₂ cores such as [PhN(CH₂pz^{*})₂]CoCl₂ (Co-Cl_{avg}, 2.250 Å),³⁵ [2,2'-pz₂(biphenyl)]CoCl₂ (Co-N_{avg}, 2.028 Å; Co-Cl_{avg}, 2.250 Å),³⁶ [(CoCl₂)(μ-pz^{*}₂CH₂)]₂ (Co-N_{avg}, 2.014 Å; Co-Cl_{avg}, 2.239 Å),¹⁴ [CoCl₂(μ-α,α'-pz₂-*m*-xylyl)]_n (Co-N_{avg}, 2.02 Å, Co-Cl_{avg}, 2.240 Å).³⁷ [CoCl₂(μ-α,α'-pz₂-*m*-xylyl)]_n (Co-N_{avg}, 2.02 Å, Co-Cl_{avg}, 2.240 Å).³⁷

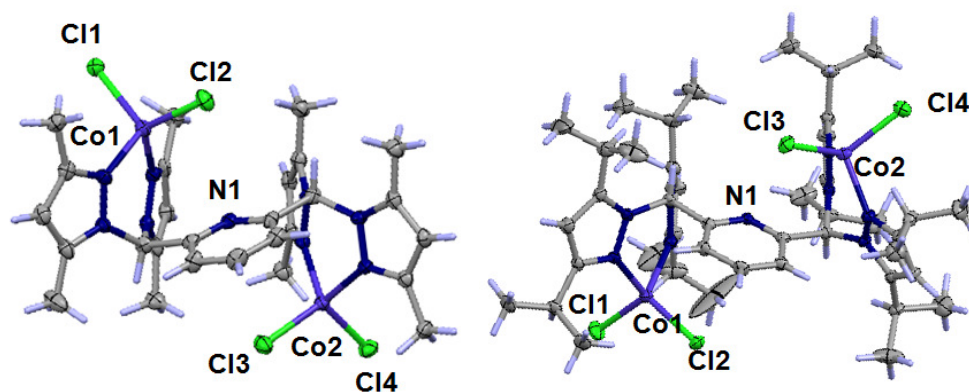


Figure 3.4. X-ray Crystal Structures of **4** (left) and **5•MeOH** (right) ellipsoids drawn at 50 % probability level.

	6	7•MeOH
Co-N(pz)	2.017(3), 2.031(3) 2.019(3), 2.029(3)	2.023(2), 2.027(2), 2.027(2), 2.041(2)
Co-N(pz) Avg	2.024(3)	2.028(2)
Co-N(py)	---	---
Co-Cl	2.230(1) avg.	2.237(8) avg.
Co-N ₄	---	---
N(py)-Co-Cl	---	---
CoN-NC(H) ^o	17.32, 18.47, 14.32, 25.21 avg. 18.83 ^o	12.48, 18.91, 23.30, 31.08 avg. 21.44 ^o

Table 3.3. Selected bond distances and angles for **4** and **5•MeOH**.

EPR. The X-band (9.6 GHz) EPR spectral data for the complexes as frozen (10 K) glasses are consistent with high spin cobalt(II) in all cases. The spectra for newly reported complexes are found in **Figure 3.5 & 3.6a&b** while full spectral parameters for all of the complexes are given in **Table 3.4**.

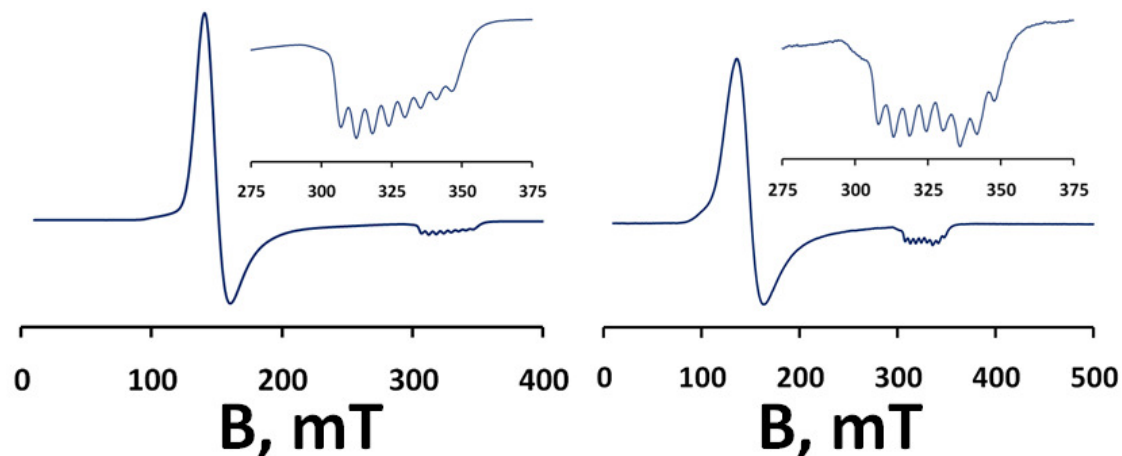


Figure 3.5. X-band EPR spectra of **2•MeOH** (left) and **3•2MeOH** (right); inset: 275 to 375 mT region showing coupling to the ^{59}Co nucleus obtained as frozen (10 K) glasses in 9:1 MeOH:EtOH.

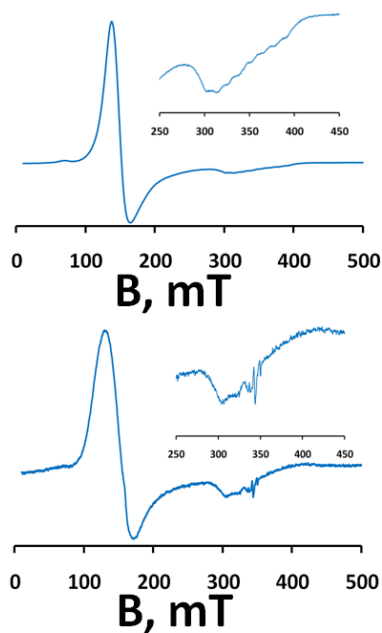


Figure 3.6a. EPR Spectra of of $(\text{CoCl}_2)_2(\mu\text{-pz}_4^{\text{X}}\text{lut})$; (X = H, top, **4**); (X = 4-Me, 2nd, **5**).

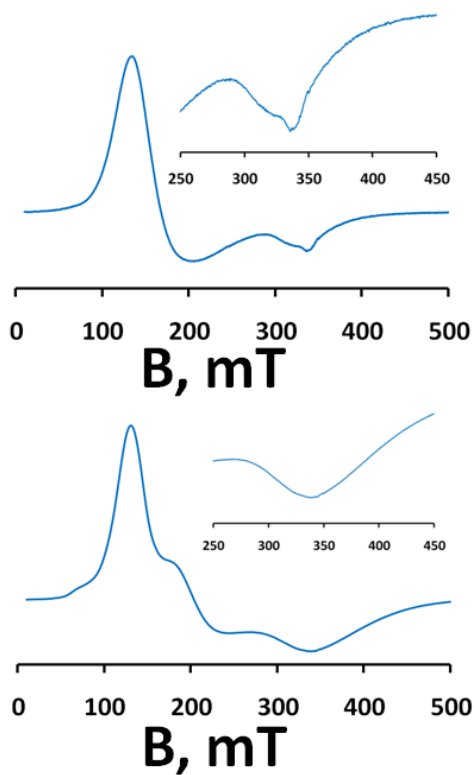


Figure 3.6b. EPR Spectra of of $(\text{CoCl}_2)_2(\mu\text{-pz}_4^{\text{X}}\text{lut})$; (X = 3,5-dimethyl, top, **6**); (X = 3,5-DIP, Bottom, **7**) as Frozen Glass Solutions in Acetonitrile:Toluene.

Compound	$g_{\text{eff}\perp}$	$g_{\text{real}\perp}^a$	g_{\parallel}	$A_{\perp} (\text{cm}^{-1})$	$A_{\parallel} (\text{cm}^{-1})$
$[\text{CoCl}(\text{pz}_4\text{lut})][\text{Cl}]$	4.32	2.20	2.30	nr	nr
$[\text{CoCl}(\text{pz}_4^4\text{lut})][\text{Cl}]$	4.55	2.27	2.10	nr	0.0060
$[\text{CoCl}(\text{pz}_4^*\text{lut})][\text{Cl}]$	4.06	2.30	2.12	nr	0.0055
$(\text{CoCl}_2)_2(\mu\text{-pz}_4\text{lut})$	4.53	2.17	2.20	nr	nr
$(\text{CoCl}_2)_2(\mu\text{-pz}_4^4\text{lut})$	4.43	2.21	2.19	nr	nr
$(\text{CoCl}_2)_2(\mu\text{-pz}_4^*\text{lut})$	4.16	2.08	2.05	nr	nr
$(\text{CoCl}_2)_2(\mu\text{-pz}_4^{\text{DIP}}\text{lut})$	4.35	2.17	2.03	nr	nr

^a $a = g_{\text{eff}\perp} / 2$ (for g_x, g_y), nr = not resolved.

Table 3.4. EPR Spectral Parameters for Cobalt Complexes Prepared in this Work.

As the local symmetry around cobalt is at best either C_{4v} ($\text{CoN}_4^{\text{eq}}\text{N}^{\text{ax}}\text{Cl}$) or C_{2v} (CoN_2Cl_2), the EPR signals are axial with highly anisotropic g -values with $g_{\perp} > 4.1$ ($g_{\text{real}} \approx 2.2$) and $g_{\parallel} > 2.1$, values typical of other axially distorted high-spin cobalt(II) complexes and are consistent with a smaller orbital reduction factor (increased covalency of the Co^{2+} $3d$ orbitals) in the case of pz^4_4lut for the octahedral symmetry.³⁸ The fine structure due to coupling with the ^{59}Co ($I = 7/2$) nucleus is observed in both **2•MeOH** and **3•2MeOH**; however, hyperfine coupling to the nitrogens of the ligands is not observed in any case. The g_{\parallel} values decrease with increasing field strength of the ligand as expected and agree well with the increased covalency factor.³⁸ The deviation from the trend in g -values of the $[\text{CoCl}(\text{pz}_4\text{lut})][\text{Cl}]$ complex (compared to **2•MeOH**, **3•2MeOH**) can be attributed to the different medium used (silicone oil versus a frozen glass of MeOH:EtOH). This in turn can have an effect on the resonance position of g_{\parallel} and therefore will be re-acquired in a frozen glass of MeOH:EtOH to confirm the trend.

The EPR spectra of the pseudotetrahedral derivatives also display highly axial signals. Only the complex $(\text{CoCl}_2)_2(\mu\text{-pz}^{\text{DIP}}_4\text{lut})$ displays distinct signals for g_x , g_y , and g_z due to the reduced symmetry about the cobalt(II) center caused by the isopropyl groups. All of the other pseudotetrahedral derivatives display signals for g_{\perp} and g_{\parallel} owing to the higher degree of symmetry about the cobalt(II) center. However, no fine structure or hyperfine structure for coupling of the electron with the ^{59}Co nucleus or ^{14}N of the ligands is observed in any of the spectra. The values of g_{\parallel} decrease in the expected order with the increased field strength of the ligands owing to the fact that all of the complexes have a similar local symmetry about the cobalt(II) center.

Electronic Absorption Spectra. The electronic absorption spectral data for the various ligands and cobalt complexes are collected in **Table 3.5** while representative spectra for the complexes are shown in **Figures 3.7** and **3.8**. The spectra of each pink monometallic complexes (**1**•CH₂Cl₂, **2**•MeOH, **3**•2MeOH) in methanol and the blue bimetallic complexes (**4**, **5**•MeOH) in acetonitrile are clearly different than for the solvated CoCl₂ (in MeOH, CH₃CN), indicating that ligand dissociation is not extensive in these solvents (*vide infra*). The pink monometallic spectra consist of high-intensity ($\epsilon > 20,000 \text{ M}^{-1}\text{cm}^{-1}$), high energy bands ($> 18,000 \text{ cm}^{-1}$) that can be attributed to ligand-based transitions. The low intensity, lower energy bands are typical for d-d transitions of high spin cobalt(II) and their assignments can be in accordance with standard methodology.³⁹

In the ligand field region, the higher energy band near 515 nm (ca. $19,500 \text{ cm}^{-1}$) is characteristic for the ${}^4T_1(P) \leftarrow {}^4T_1(F)$ transition but contains some fine structure due to the perturbation caused by the axial symmetry of the complexes (which is more pronounced in the **2**•MeOH than **1**•CH₂Cl₂).

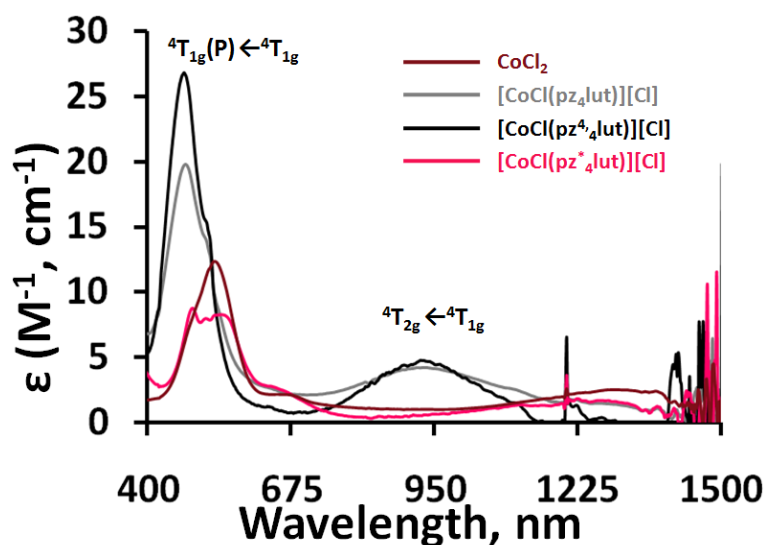


Figure 3.7. UV-visible and Near-IR Absorption Spectra for d-d Transitions in MeOH solutions of **1**•CH₂Cl₂ (gray), **2**•MeOH (black), **3**•2MeOH (pink) and CoCl₂ (brick red).

The band for the spin-forbidden ${}^2T_{1,2}(G) \leftarrow {}^4T_1(F)$ transition. The low energy band (between 8,000-10,000) can be unequivocally assigned to the ${}^4T_2(F) \leftarrow {}^4T_1(F)$ transition. The calculated ligand field parameters further support the notion that the pz^*_4lut is a weaker-field ligand ($\Delta_o \sim 9,000\text{ cm}^{-1}$) than the unsubstituted pz_4lut ($11,764\text{ cm}^{-1}$) or the pz^4_4lut ($12,000\text{ cm}^{-1}$) derivative. Although counter-intuitive, this finding is in accord with other poly(pyrazolyl)methyl or poly(pyrazolyl)borate systems which will be discussed in further detail below. $\{Fe[HC(pz)_3]_2^{2+}\}^{40}$ or $Fe[HB(pz)_3]_2^{40}$ which contain low-spin octahedral iron(II) versus $\{Fe[HC(pz^*)_3]_2^{2+}\}^{40}$ or $Fe[HB(pz^*)_3]_2^{40}$ which contain high spin iron(II). In these latter cases steric interactions involving the 3-methyl groups (proximal to the metal) favor the longer Fe-N bonds of the high spin state, effectively making these ligands weaker field than their methylated analogues. A similar argument could be invoked for the current cobalt(II) systems where the steric interactions between 3-methyl groups on the pyrazolyls and the chlorides may presumably induce longer (and weaker) Co-N bonds. Indeed, comparison of structures establish that the methyl derivative indeed has longer Co-N distances and more distorted pyrazolyl rings compared to the unsubstituted derivative, consistent with expectations for a weaker field ligand. This observation is also in accord with the observed nephelauxetic parameter β ($\beta = B_{\text{complex}} / B_{\text{freeion}}$). The parameter β provides an indication of covalency where ionic bonding would give values close to unity while more covalent giving less. In this case the strongest field ligand pz^4_4lut gives 0.590, while pz_4lut gives 0.617 and pz^*_4lut gives 0.858 which reflects a lower effective charge experienced by the metal's d-electrons in the former. It is noted that 4-methyl substituted pz^4_4lut and unsubstituted pz_4lut appear to be stronger field ligands than PY5 to cobalt as Δ_o was found to be $10,900\text{ cm}^{-1}$.

The spectra of the pseudo-tetrahedral derivatives (**Figure 3.8a,b**) contain structured high energy bands near 620 nm (ca. 16,000 cm^{-1} , $\epsilon \approx 350 \text{ M}^{-1}\text{cm}^{-1}$) for the $^4\text{T}_1(\text{P}) \leftarrow ^4\text{A}_2$ d \leftarrow d transition and a low-intensity ($\epsilon < 100 \text{ M}^{-1}\text{cm}^{-1}$), low-energy $^4\text{T}_1(\text{F}) \leftarrow ^4\text{A}_2$ d \leftarrow d transition (which occurs as a triplet, owing to spin-orbit coupling for the pz^*_4lut case) centered near 1250 nm (8,000 cm^{-1}). The ligand field parameters Δ_t and B' (effective Racah parameter) calculated by standard methods³⁹ (**Table 2.4**) indicate that the pz^*_4lut ($\Delta_t \sim 4,993 \text{ cm}^{-1}$) is a stronger field ligand than pz_4lut ($\Delta_t \sim 4,124 \text{ cm}^{-1}$) and pz^4_4lut ($\Delta_t \sim 4,720 \text{ cm}^{-1}$) but weaker than $\text{pz}^{\text{DIP}}_4\text{lut}$ ($\Delta_t \sim 5,058 \text{ cm}^{-1}$) as expected due to the eight electron donating methyl groups versus the eight electron donating isopropyl groups. It should be noted that Δ_t in $(\text{CoCl}_2)_2(\mu\text{-pz}^*_4\text{lut})$ is larger but similar to those values calculated for the monometallic derivatives $\text{CoCl}_2[\text{pz}^{**}_2\text{CH}_2]$ ($\Delta_t \sim 2,127 \text{ cm}^{-1}$) and $\text{CoCl}_2[\text{pz}^{3\text{Me}}_2\text{CH}_2]$ ($\Delta_t \sim 2,392 \text{ cm}^{-1}$).⁴¹

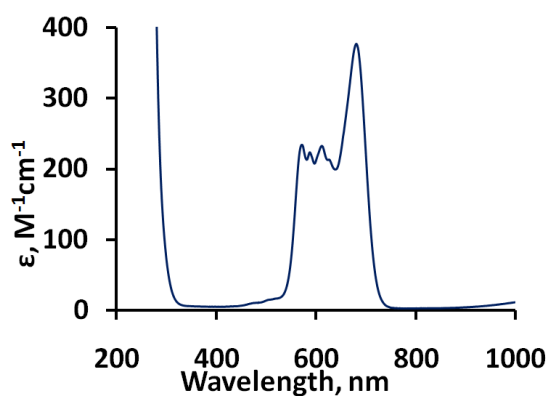


Figure 3.8a. Absorption Spectrum of CoCl_2 in Acetonitrile.

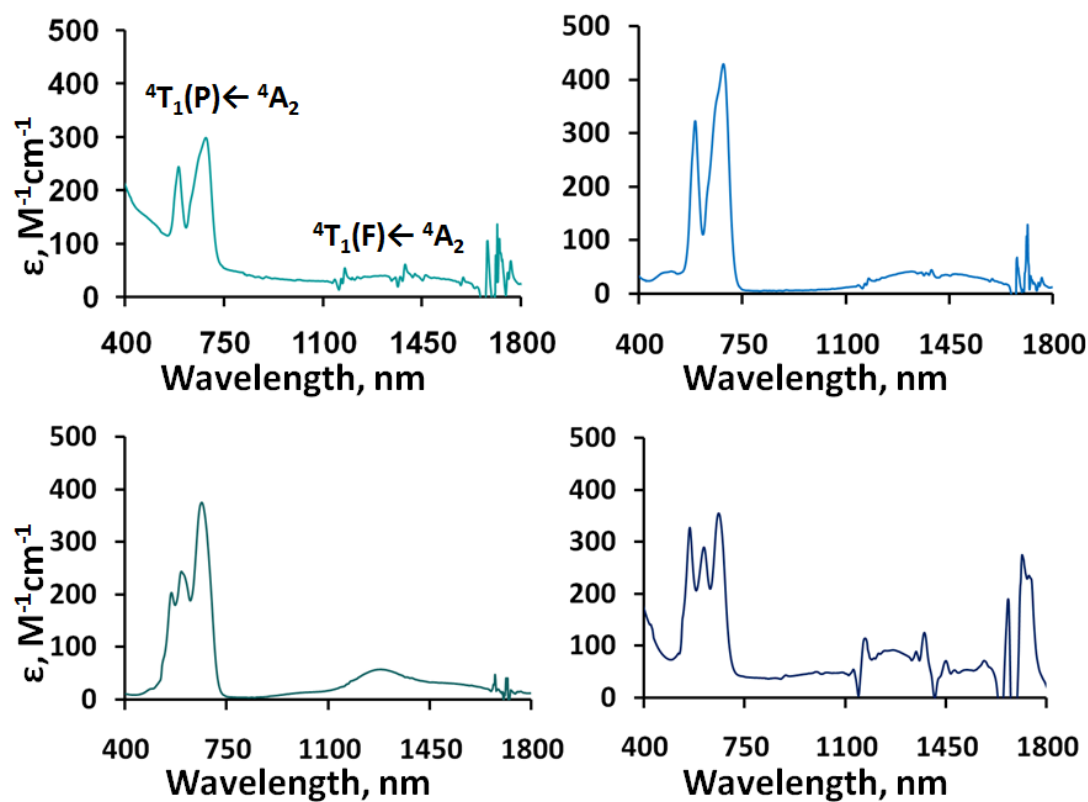
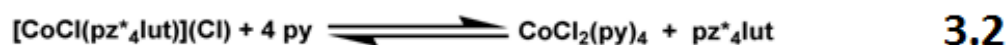
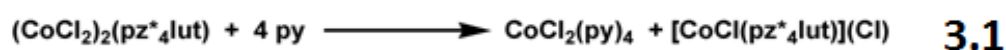


Figure 3.8b. Absorption Spectra of $(\text{CoCl}_2)_2(\mu\text{-pz}_4\text{lut})$ (**4**, top left), $(\text{CoCl}_2)_2(\mu\text{-pz}^4_4\text{lut})$ (**5**, top right), $(\text{CoCl}_2)_2(\mu\text{-pz}^*_4\text{lut})$ (**6**, bottom left), $(\text{CoCl}_2)_2(\mu\text{-pz}^{\text{DIP}}_4\text{lut})$ (**7**, bottom right) in Acetonitrile.

Compound	Solvent	λ_{\max} , cm^{-1} (ϵ , $\text{M}^{-1}\text{cm}^{-1}$)	$10\text{Dq}(\text{cm}^{-1})^{\text{a,b}}$	$B(\text{cm}^{-1})^{\text{a,b}}$	B'	Ref.
CoCl_2	CH_3CN	17,483(230), 16,949(202), 16,340(236), 15,974(210), 14,663(360), 7,692(34)	4,500 ^{d,e,f}	691	---	f
$\text{CoCl}_2[\text{pz}_2\text{CMe}_2]$	acetone	16,181(262), 15,290(379), 15,151(365) NIR nr	---	---	---	41c
$\text{CoCl}_2[\text{pz}^{4\text{Me}}_2\text{CMe}_2]$	CH_3CN	16,892(130), 15,337(150), 14,749(180), 9,580 (nr)	---	---	---	41b
$\text{CoCl}_2[\text{pz}^{**}_2\text{CMe}_2]^{\text{c}}$	CH_3CN	17,668(340), 16,340(360), 14,970(410), 9350(nr), 7500(nr), 5970(nr)	4,700 ^{d,e}	686	---	41b
$\text{CoCl}_2[\text{pz}^{3\text{Me}}_2\text{CH}_2]$	acetone	16,700(nr), 15,400(nr), 9,600(nr), 7,600(nr), 6200(nr)	4,400 ^{d,e}	734	---	41a
$(\text{CoCl}_2)_2(\mu\text{-pz}_4\text{lut})$	CH_3CN	17,007(352), 14,620(430), 13,175sh(73), 7102(62)	4,100 ^{d,e}	703	0.627	f
$(\text{CoCl}_2)_2(\mu\text{-pz}^4_4\text{lut})$	CH_3CN	17,007(323), 14,620(430), 8,169(31), 7,564(42), 6,793(38)	4,700 ^{d,e}	669	0.597	f
$(\text{CoCl}_2)_2(\mu\text{-pz}^*_4\text{lut})$	CH_3CN	17,921(298), 16,502(316), 15,106(471), 9,747(53), 7,849(101), 6,720(67)	5,000 ^{d,e}	666	0.594	f
$(\text{CoCl}_2)_2(\mu\text{-pz}^{\text{DIP}}_4\text{lut})$	CH_3CN	17,924(328), 16,447(290), 15,198(356), 10,000(51), 7,911(93), 6,562(55)	5,100 ^{d,e}	660	0.589	f
CoCl_2	MeOH	18,939 (12), 14,925 (2), 7,716 (3)	8,620 ^f	862	---	f
$[\text{CoCl}(\text{pz}_4\text{lut})](\text{Cl})$	MeOH	21,186(20), 19,608sh(14), 18,727sh(12), 15,974sh(3), 10,706(4)	11,764 ^d	695	0.617	f
$[\text{CoCl}(\text{pz}^4_4\text{lut})][\text{Cl}]$	MeOH	21,277(27), 19,231(14), 10,822(5), 9,025(2)	12,075 ^d	667	0.590	f
$[\text{CoCl}(\text{pz}^*_4\text{lut})][\text{Cl}]$	MeOH	20,576(19), 19,608(17), 18,382(18), 15,532(8), 7,899(4)	9,000 ^d	849	0.858	f
$[\text{CoCl}(\text{PY5})][\text{Cl}]$	MeOH	21,598 (25), 19,157 (20), 18,349 (15), 10,320 (7)	10,915 ^d	658	0.665	9

Table 3.5. UV-Vis & Near IR absorption data and parameters for various high spin cobalt(II) complexes in various solvents at or near 295 K. ^a tetrahedral derivatives calculated as in reference 39A, ^b octahedral calculated as in ref 39b. ^c pz** = 3,4,5-trimethylpyrazole. ^d mean value for high energy bands used; ^e spin-orbit weighted. f = this work

Solution Studies. The cobalt(II) complexes of pz^*_4lut exhibit a range of solvatochromic behavior that provoked further investigation. Pyridine solutions of either $(\text{CoCl}_2)_2(\mu\text{-pz}^*_4\text{lut})$ or $[\text{CoCl}(\text{pz}^*_4\text{lut})][\text{Cl}]\cdot 2\text{CH}_3\text{OH}$ were thermochromic (pink at low temperature, blue at high temperature) because pyridine displaces the heteroscorpionate ligand (**Eqs. 3.1 & 3.2**) to form thermochromic $\text{CoCl}_2(\text{py})_4$ ⁴² as confirmed by titration studies (**Figure 3.9**) and by comparison of the properties of the resulting of the



solutions with independently prepared pyridine solutions of CoCl_2 as pyridyls are stronger donors than pyrazoles and have higher increased lewis base character. It has previously been shown that $\text{CoCl}_2(\text{py})_4$ (pink) exists in solution in equilibrium with $\text{CoCl}_2(\text{py})_2$ (blue) and two equivalents of free pyridine with the pink form favored at low temperature and the blue form favored at high temperature.⁴²

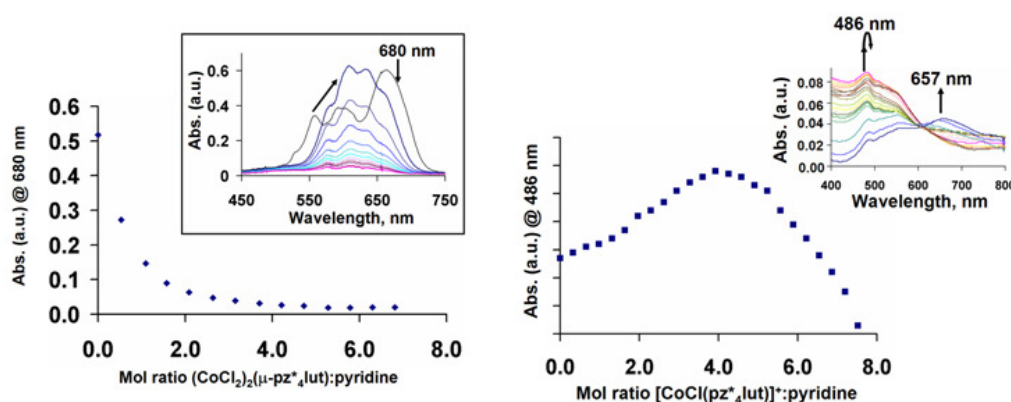


Figure 3.9. Titration of pyridine into solutions of $(\text{CoCl}_2)_2(\mu\text{-pz}^*_4\text{lut})$ in CH_3CN (left) and of $[\text{CoCl}(\text{pz}^*_4\text{lut})][\text{Cl}]$ in MeOH (right).

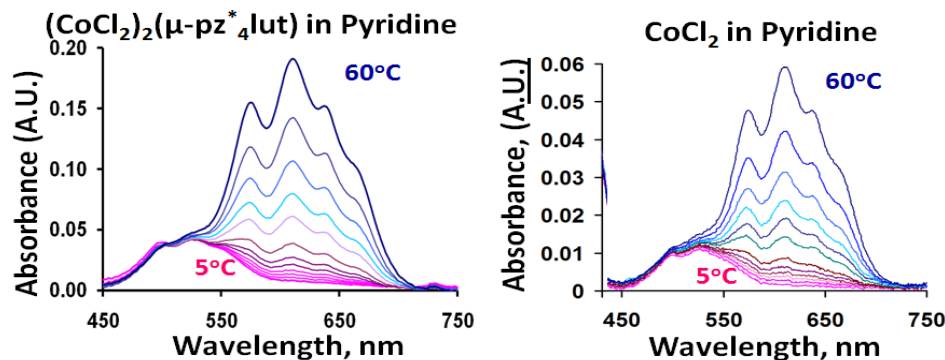


Figure 3.10. Variable temperature absorption spectra in pyridine of $(\text{CoCl}_2)_2(\mu\text{-pz}^*_4\text{lut})$ (left) and CoCl_2 (right).

In solvents less donating than pyridine, such as methanol the $[\text{Co}(\text{Cl})(\text{pz}^*_4\text{lut})]^+$ cation is well behaved as shown by both the titration data of pz^*_4lut in methanol added to CoCl_2 in methanol as well as the Job's plot in methanol (**Figure 3.11**) which confirm the stoichiometry to be that of 1:1. Of interest is the fact that the reaction between $\text{pz}^{\text{DIP}}_4\text{lut}$ and CoCl_2 in methanol on the bulk scale gives a blue, presumably tetrahedral cobalt(II) complex; most likely due to the steric demands of the isopropyl groups on pyraozole.

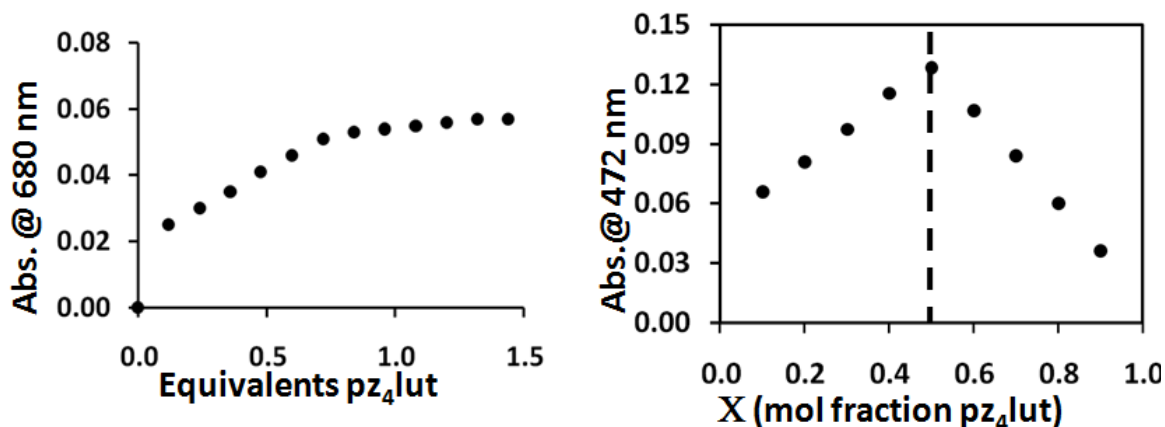


Figure 3.11. Titration of pz^*_4lut (in MeOH) into a methanol solution of CoCl_2 (left) and Job's plot in MeOH of pz_4lut .

However, when blue $(\text{CoCl}_2)_2(\mu\text{-pz}^*_4\text{lut})$ is dissolved in MeOH a pink solution with electronic spectra containing bands characteristic of the $[\text{CoCl}(\text{pz}^*_4\text{lut})]^+$ cation (**Figure 3.12**) are observed. Furthermore, when MeOH was added into a blue acetonitrile solution of $(\text{CoCl}_2)_2(\mu\text{-pz}^*_4\text{lut})$ (**Figure 3.12**), the color changed to pink as a result of the formation of octahedral cobalt either in the form of $[\text{CoCl}(\text{pz}^*_4\text{lut})]^+$ cation and, presumably, $\text{CoCl}_2(\text{MeOH})_4$ likely via $[\text{CoCl}_2(\text{HOMe})_2]_2(\mu\text{-pz}^*_4\text{lut})$. This behavior in methanol can best be summarized by equations 3.3-3.5 shown below.

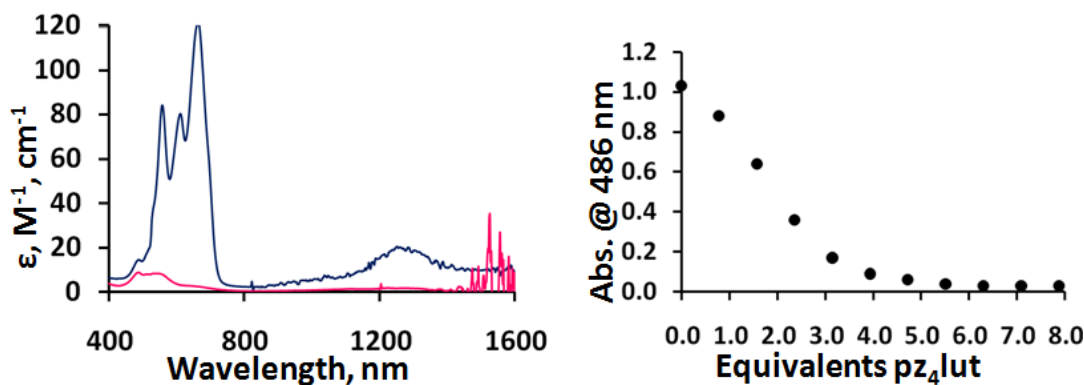
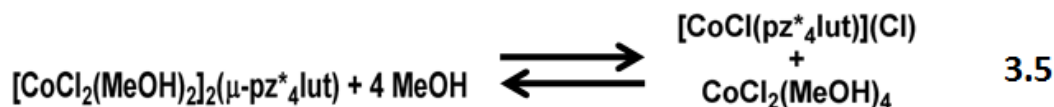
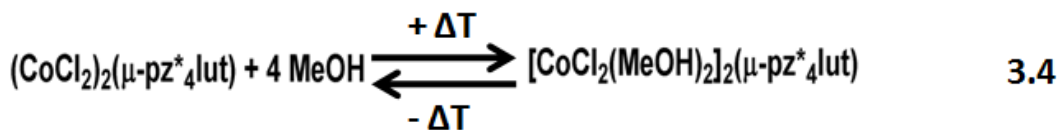
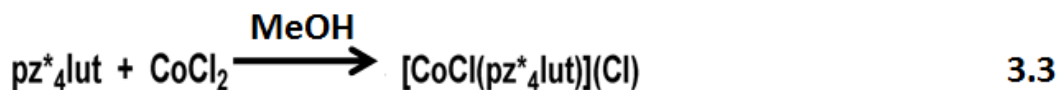


Figure 3.11. Blue $(\text{CoCl}_2)_2(\mu\text{-pz}^*_4\text{lut})$ dissolved in MeOH (left) and addition of MeOH to a $(\text{CoCl}_2)_2(\mu\text{-pz}^*_4\text{lut})$ in CH_3CN (right).



The titration pz^*_4lut in acetonitrile into cobalt(II) chloride in acetonitrile indicate that both bimetallic $(\text{CoCl}_2)_2(\mu\text{-pz}^*_4\text{lut})$ and a monometallic species, presumably, $(\text{CoCl}_2)(\kappa^2\text{-pz}^*_4\text{lut})$, are formed (**Figure 3.12**) depending on the stoichiometry of reagents (Equations 3.6 & 3.7). Unfortunately, attempts to isolate the monometallic $(\text{CoCl}_2)(\kappa^2\text{-pz}^*_4\text{lut})$ have been unsuccessful, as the pink $[\text{CoCl}(\text{pz}^*_4\text{lut})][\text{Cl}]$ is formed as an insoluble solid on removing solvent from the preparative reaction. When pink

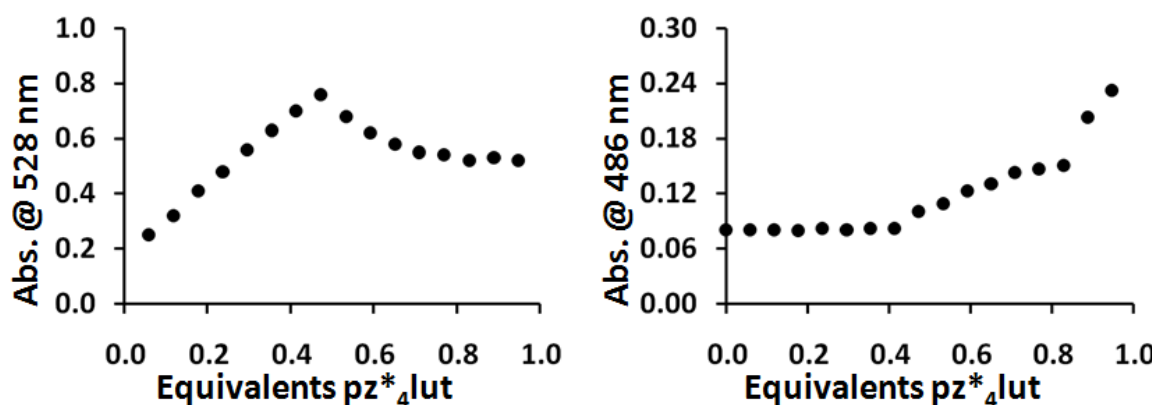
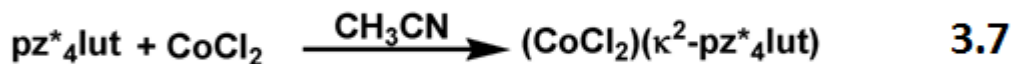
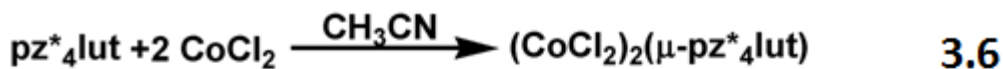


Figure 3.12. Titration of pz^*_4lut in CH_3CN into CoCl_2 in CH_3CN at 528 nm (left) and 486 nm (right).



$[\text{CoCl}(\text{pz}^*_4\text{lut})][\text{Cl}]$ is treated with CH_3CN , a blue solution is formed initially in which the absorption spectra (**Figure 3.11, left**) appears to be comprised of bands for each $[\text{CoCl}(\text{pz}^*_4\text{lut})]^+$ and $(\text{CoCl}_2)_2(\mu\text{-pz}^*_4\text{lut})$. Stoichiometric considerations would favor the latter, as in equation 3.8. Especially since, after a period of several minutes of dissolving $[\text{CoCl}(\text{pz}^*_4\text{lut})][\text{Cl}]$ in CH_3CN to give a blue solution, insoluble $[\text{CoCl}(\text{pz}^*_4\text{lut})][\text{Cl}]$ re-precipitates. Solutions of pink $[\text{CoCl}(\text{pz}^*_4\text{lut})][\text{Cl}]$ in either CH_2Cl_2 , DMF, or DMSO are also blue and the spectra exhibit bands for both tetrahedral and octahedral cobalt(II), however it has not been possible to structurally verify the blue species, presumably $(\text{CoCl}_2)(\kappa^2\text{-pz}^*_4\text{lut})$, for the reason described in the acetonitrile case.

$\text{pz}^{\text{DIP}}_4\text{lut}$ Ligand Solution Behavior. The stoichiometry of the $(\text{CoCl}_2)\text{-}(\mu\text{-pz}^{\text{DIP}}_4\text{lut})$ complex in dichloromethane/acetonitrile is confirmed both by titration of a dichloromethane solution of $\text{pz}^{\text{DIP}}_4\text{lut}$ into an acetonitrile solution of cobalt(II) chloride as well as by Job's method in dichloromethane/acetonitrile (both, **Figure 3.13**). By

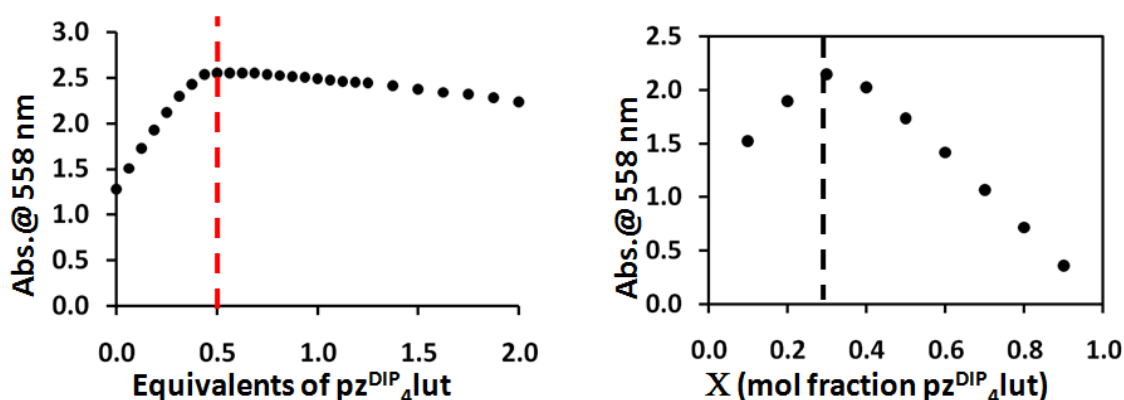


Figure 3.13. Titration of $\text{pz}^{\text{DIP}}_4\text{lut}$ solution (CH_2Cl_2) into a CoCl_2 solution (CH_3CN , left). Job's plot of $\text{pz}^{\text{DIP}}_4\text{lut}$ and CoCl_2 in acetonitrile and dichloromethane showing 1:2 stoichiometry.

monitoring the absorbance at 558 nm; the addition of $\text{pz}^{\text{DIP}}_4\text{lut}$ to cobalt(II) chloride shows a sharp break at 0.5 equivalents and then subsequent leveling of the absorbance all

way up to two equivalents of $\text{pz}^{\text{DIP}}_4\text{lut}$ while the Job's plot displays maximum absorbance when the stoichiometry is one ligand to two cobalt(II) chloride.

Despite obtaining a blue solid upon reaction in methanol on the bulk scale, the dilute solution behavior of $\text{pz}^{\text{DIP}}_4\text{lut}$ and cobalt(II) chloride is significantly different. Solutions of $(\text{CoCl}_2)_2-(\mu\text{-pz}^{\text{DIP}}_4\text{lut})$ in methanol at low concentrations (< 1 mmolar) gives a solution that is purple in color as can be seen from (**Figure 3.14.**). Furthermore, methanol solutions are thermochromic in nature giving increasingly blue solutions upon warming while giving pink solutions upon cooling. The pink color is indicative of the six-coordinate monometallic species; however, due to the steric demands of the isopropyl groups it is not possible for the $\text{pz}^{\text{DIP}}_4\text{lut}$ to be coordinated to the cobalt(II) in a κ^5 fashion. Therefore, this observation required further investigation in order to fully understand the solution behavior in methanol.

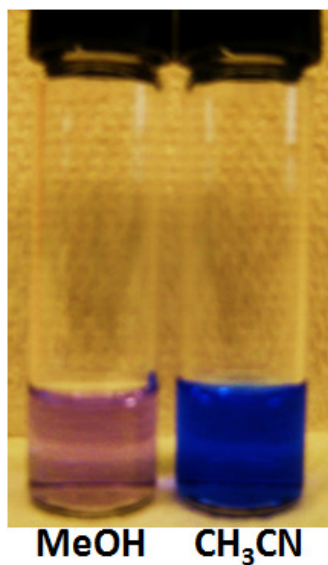


Figure 3.14. Picture of $(\text{CoCl}_2)_2-(\mu\text{-pz}^{\text{DIP}}_4\text{lut})$ in MeOH (left) and CH_3CN (right).

Furthermore, methanol solutions are thermochromic in nature giving increasingly blue solutions upon warming while giving pink solutions upon cooling. While the pink color is indicative of the six-coordinate monometallic species; however, due to the steric demands of the isopropyl groups it is not possible for the $\text{pz}^{\text{DIP}}_4\text{lut}$ to be coordinated to the cobalt(II) in a κ^5 fashion.

Shown below in **Figure 3.15** is the absorption spectra of $(\text{CoCl}_2)_2-(\mu\text{-pz}^{\text{DIP}}_4\text{lut})$ in methanol and in acetonitrile. Upon inspection, the absorption spectra appears to contain peaks for two species as the peak at 487 nm is indicative of a six-coordinate cobalt(II) species (based on previous cobalt(II) complexes discussed above); while the absorbances at 558 nm, 601 nm and 654 nm as well as the shoulder at 526 nm are indicative a tetrahedral species.

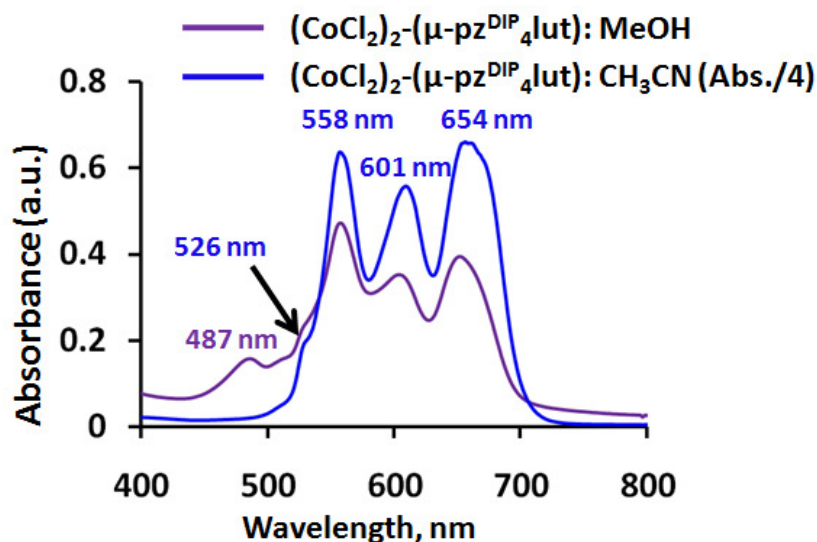


Figure 3.15. Absorption spectra of $(\text{CoCl}_2)_2-(\mu\text{-pz}^{\text{DIP}}_4\text{lut})$ $8.33 \times 10^{-3} \text{ M}^{-1}$ in methanol (purple) and $4.54 \times 10^{-3} \text{ M}^{-1}$ in acetonitrile (blue).

The Job's plot in methanol does not provide any further clarity as monitoring of two different wavelengths gives the same results as shown below in **Figure 3.16**.

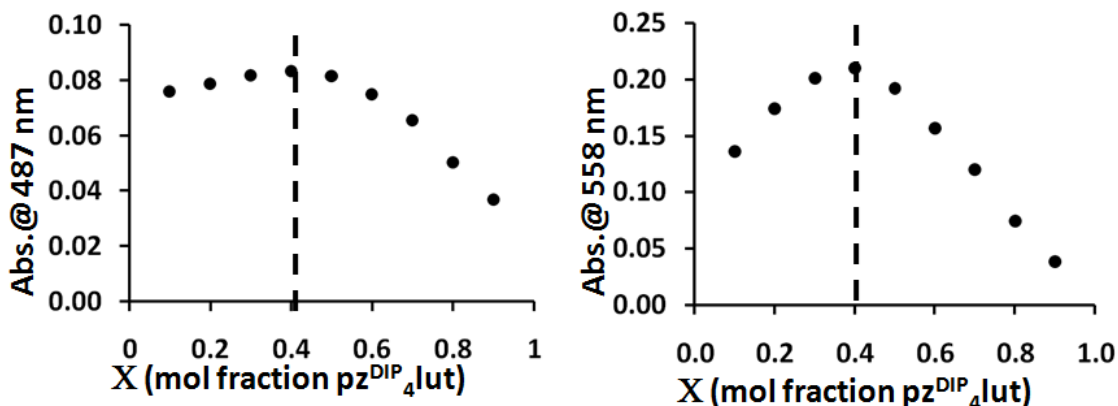


Figure 3.16. Job's plot of $\text{pz}^{\text{DIP}}_4\text{lut}$ and CoCl_2 in methanol; 487 nm (left) and 558 nm (right).

Both the plot at 487 nm (characteristic of pink monometallic species) as well as the plot at 558 nm (characteristic of blue tetrahedral species) display maximum absorbance when at a stoichiometry of 2:3 (two ligands:three cobalt). One possible explanation for these results; is that the system is involved in an equilibrium (vide infra). Further insight was gained by performing titrations where $\text{pz}^{\text{DIP}}_4\text{lut}$ in methanol was added to cobalt(II) chloride in methanol were performed as discussed below.

The addition of $\text{pz}^{\text{DIP}}_4\text{lut}$ ligand in methanol to a methanol solution of cobalt(II) chloride monitored at 487 nm and 558 nm is shown below in **Figure 3.17**. The plot for

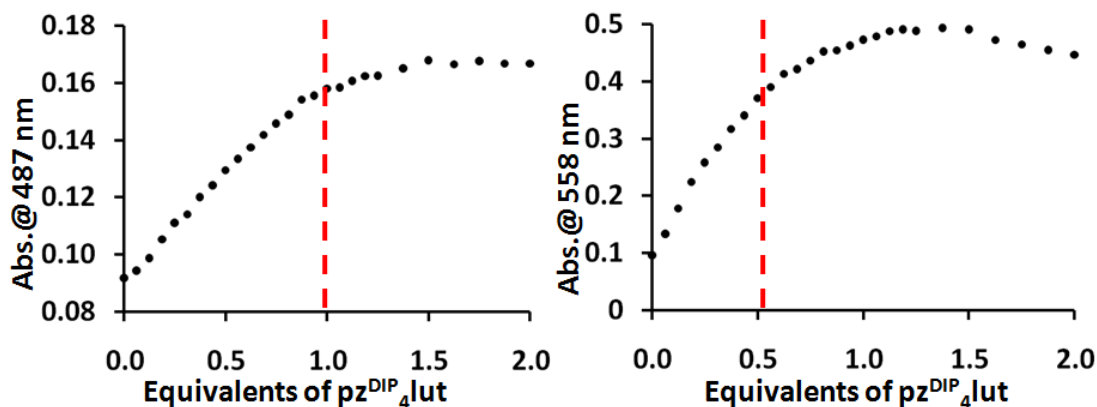


Figure X.18. Titration of $\text{pz}^{\text{DIP}}_4\text{lut}$ in methanol added to cobalt(II) chloride in methanol at 487 nm and 558 nm.

487 nm clearly shows an increase in absorbance until 1.0 equivalents at which point the absorbance begins to level off up until two equivalents have been added. However, the plot for 558 nm is not as clearly defined. There appears to be a sharper slope to 0.5 equivalents indicating the formation of a tetrahedral complex with 1:2 stoichiometry (1 ligand to 2 cobalts) however the absorption does not really begin to level off until after 1 equivalent of $\text{pz}^{\text{DIP}}_4\text{lut}$ has been added. plots are obtained in both cases which show increases in absorbance until 1.0 equivalents of ligand have been added at which point the absorbance values begin to level off. Both plots indicate the formation of complexes that have stoichiometry of 1:1. As stated previously the steric demands of the isopropyl groups prevent it from being coordinated in a κ^5 fashion and therefore must be a lower coordination mode.

Finally, the thermochromic behavior of the solutions was explored by using Job's method at both a high temperature (50 °C) and a low temperature (0 °C) in methanol to determine the stoichiometry. Shown below in **Figure 3.18** is the variable temperature absorption spectra in methanol at 0 °C, 23 °C and 50 °C. Methanol solutions at low

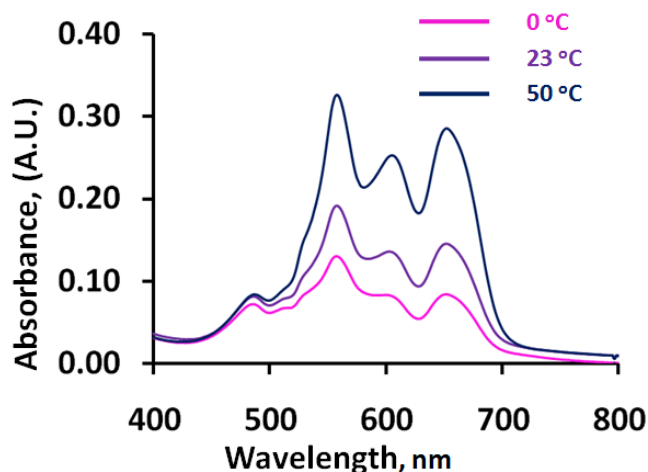


Figure 3.18. Absorption spectra of $(\text{CoCl}_2)_2-(\mu\text{-pz}^{\text{DIP}}_4\text{lut})$ in methanol, 0 °C (pink), 23 °C (purple), 50 °C (blue).

temperature were increasingly pink in color while at high temperature solutions were increasingly blue in color. Plots for 487 nm at 0 °C and 558 nm at 50 °C are shown below in **Figure 3.19**. The plot for 487 nm at 0 °C shows maximum absorbance when the stoichiometry is 1:1 while the plot for 558 nm at 50 °C shows maximum absorbance when the stoichiometry is one ligand for every two cobalts.

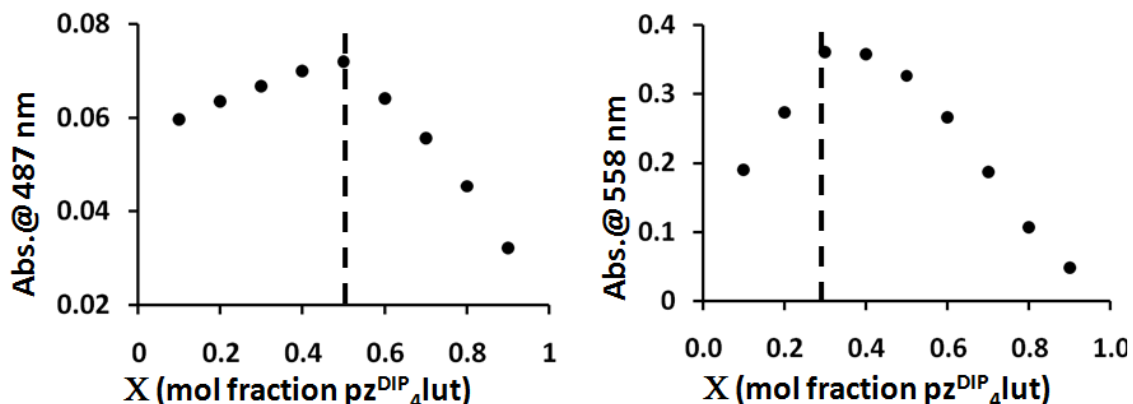


Figure 3.19. Job's plots for 487 nm, 0 °C (left) and 558 nm, 50 °C (right).

An equilibrium between a complex that has 1:1 stoichiometry and that of 1:2 stoichiometry (one ligand:two cobalt) appears to be the most likely cause of the purple solution obtained in methanol. X-ray quality crystals were obtained from by vapor diffusion of Et_2O into a concentrated methanol solution (that started out purple) over the course of approximately one week; giving both blue blocks of the complex as well as a colorless precipitate presumed to be free ligand. Both Job's plots at 487 nm and 558 nm show maximum absorbance at 0.4 eq of $\text{pz}^{\text{DIP}}_4\text{lut}$ ligand. This ratio happens to be between the exact ratios of 1:1 and 1:2 at room temperature and indicates both complexes are likely to exist in solution. The titration data at room temperature in methanol shows the formation of both a 1:1 complex by monitoring of the band growing in at 487 nm as well as the formation of a 1:2 complex as shown by the growth of the band at 558 nm.

Further evidence supporting this equilibrium is the fact that a color change is observed upon heating (blue) and cooling (pink) of the solutions. While the 1:2 complex is known to be that of the tetrahedral species shown earlier the nature of the 1:1 complex remains unknown for reasons discussed in more detail below.

The $\text{pz}^{\text{x}}_4\text{lut}$ ligand scaffold has shown the ability to display multiple coordination modes as shown above and earlier with silver(I) complexes; as such there remains ambiguity in assigning the exact nature of the 1:1 complex. In addition to the multiple coordination modes, there is no way to distinguish between one six coordinate complex or another, as they are all pink in color and display characteristic absorptions in the 480 nm range. Shown below in **Figures 3.20 & 3.21** are two potential equilibrium processes taking place at room temperature. However, upon changing the temperature the equilibrium is shifted to left favoring the six-coordinate complexes at low temperatures and blue four-coordinate complex at high temperatures while room temperature contains a mixture of the two species.

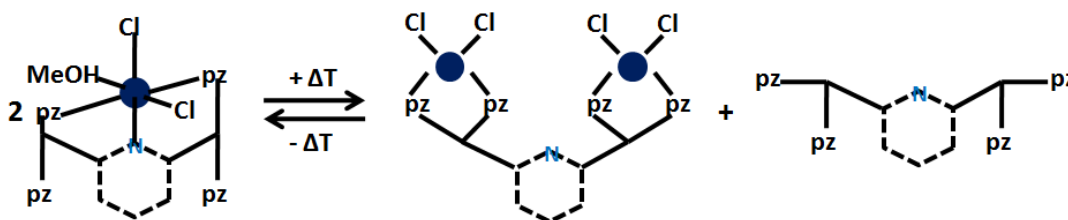


Figure 3.20. Potential equilibrium process of $(\text{CoCl}_2)_2-(\mu\text{-pz}^{\text{DIP}}_4\text{lut})$ in methanol at room temperature.

Summary and Conclusions. Six new high spin cobalt(II) complexes have been synthesised: two pink monometallic species with a κ^5 coordination mode and four blue bimetallic species with a κ^2 - μ coordination mode. The $\text{pz}^4_{4\text{lut}}$ and $\text{pz}^*_{4\text{lut}}$ ligands exhibit both coordination modes depending on solvent choice while the $\text{pz}^{\text{DIP}}_{4\text{lut}}$ ligand exhibits the κ^2 - μ mode exclusively (confirmed by Job's method) regardless of solvent; owing to the steric bulk of the isopropyl groups. The complexes exhibit solvato- and thermochromic behavior in strongly Lewis basic solvents such as acetonitrile and pyridine; they are stronger donors than the newly synthesized $\text{pz}^{\text{R}}_{4\text{lut}}$ ligand. The $(\text{CoCl}_2)_2(\mu\text{-}\kappa^2, \kappa^2\text{-}\text{pz}^{\text{DIP}}_{4\text{lut}})$ complex provides a unique opportunity to explore the reactivity of these complexes; as it displays significantly increased solubility over the other derivatives in

organic solvents such as THF and CH_2Cl_2 and only displays a single coordination mode due to the isopropyl groups except in methanol or pyridine in which case the solvent can displace the ligand.

The substitution of alkyl groups along the pyrazole periphery has both steric as well as electronic consequences. In the case of the pink complexes, pz^4_4lut exhibits the strongest ligand followed by pz_4lut and pz^*_4lut . While this is counter intuitive since pz^*_4lut has eight sigma donating methyl groups, this results agrees well with the previously reported high spin iron(II) complexes as well as other iron(II) pyrazole borate complexes owing to the steric interactions of the 3-methyl groups. In the case of the blue $\kappa^2\text{-}\mu$ complexes the trend follows as expected in terms of ligand field strength: $\text{pz}^{\text{DIP}}_4\text{lut} > \text{pz}^*_4\text{lut} > \text{pz}^4_4\text{lut} > \text{pz}_4\text{lut}$ as there steric interactions between the alkyl groups are removed since each cobalt is only four coordinate.

The reaction between on the bulk scale between $\text{pz}^{\text{DIP}}_4\text{lut}$ and cobalt(II) chloride gives a blue complex characterized in the solid state as well as acetonitrile or dichloromethane as $(\text{CoCl}_2)_2\text{-(}\mu\text{-pz}^{\text{DIP}}_4\text{lut)}$. Titration data shows that both a complex that is thought to be six coordinate cobalt(II) and has 1:1 stoichiometry is formed as well as that of a blue tetrahedral species with 1:2 stoichiometry. In methanol an equilibrium process that shifts at low and high temperatures giving both the monometallic pink species and blue bimetallic species is favored. The low solubility of octahedral pz_4lut and pz^4_4lut preclude further reactivity study unless new anions are explored.

Experimental Section

General Information. All transition metals were obtained commercially and used as received. The synthesis of ligands pz_4lut , pz^4_4lut , pz^*_4lut and $\text{pz}^{\text{DIP}}_4\text{lut}$ can be found in **Chapter 2**. Solvents were dried by conventional procedures and distilled prior to use, except where noted. Job's method was performed using solutions with a total concentration of $1.0 \times 10^{-4} \text{ M}^{-1}$. Titrations were performed by transferring 2 mL of a $1.0 \times 10^{-2} \text{ M}^{-1}$ solution to a cuvette and titrating in a $0.5 \times 10^{-1} \text{ M}^{-1}$ solution of ligand in 25 μL increments, until 2 equivalents of ligand have been added. Midwest Microlab, LLC, Indianapolis, Indiana 45250, performed all elemental analyses. Melting point determinations were made on samples contained in glass capillaries using an Electrothermal 9100 apparatus and are uncorrected. ^1H and ^{13}C NMR spectra were recorded on a Varian 300 MHz spectrometer. Chemical shifts were referenced to solvent resonances at δ_{H} 3.31 and δ_{C} 49.15 for methanol- d_4 . UV-visible and NIR spectra were recorded using Shimadzu UV-1600/1700 or Jasco V-570 instruments. Solid-state magnetic measurements were made at room temperature using an MK1 susceptibility balance. EPR spectral measurements were obtained using a Bruker ELEXSYS E600 equipped with ER4116DM cavity resonating at 9.63 GHz, an Oxford instruments ITC503 temperature controller and ESR-900 helium flow cryostat. The EPR spectra were recorded with 100 kHz field modulation.

[CoCl(pz⁴₄lut)][Cl]•MeOH, 2•MeOH. A solution of 0.100 g (0.38 mmol) pz⁴₄lut in 8.5 mL of CH₂Cl₂ was layered with a solution of 0.050 g (0.38 mmol) of CoCl₂ in 8.5 mL of MeOH and the solvents were allowed to slowly diffuse over 3 days. A 0.218 g (90 %) sample of **2•MeOH** as pink X-ray quality crystals was collected and dried under vacuum. Mp, 250-255 °C decomp. UV-Vis (MeOH) λ_{max} , nm (ϵ , M⁻¹cm⁻¹), 558(27), 520(14), 924(5), 1108(2)

[CoCl(pz⁴₄lut)][Cl]•MeOH, 3•2MeOH. A solution of 0.404 g (0.77 mmol) pz⁴₄lut in 8.5 mL of MeOH was layered with a solution of 0.100 g (0.78 mmol) of CoCl₂ in 8.5 mL of MeOH and the solvents were allowed to slowly diffuse over 3 days and then the mixture was allowed to slowly evaporate to give magenta X-ray quality crystals. A 0.503 g (100 %) sample of **3•2MeOH** collected and dried under vacuum. Mp, 278 – 282 °C decomp. Anal. Calcd. (obsd.) for C₂₇H₃₄Cl₂CoN₉2: C, 52.10 (52.12); H, 5.78 (5.75); 19.57 (16.61). μ_{eff} (Solid) 3.52 μ_{B} . UV-Vis (MeOH) λ_{max} , nm (ϵ , M⁻¹cm⁻¹), 486(19), 509(17), 544(18), 643(8), 1265(4).

(CoCl₂)₂(μ -pz₄lut), 4. A Solution of 0.206 g (0.55 mmol) pz₄lut in 25 mL of CH₃CN was added to a stirred solution of 0.143 g (1.10 mmol) CoCl₂ in 25 mL of CH₃CN. A green/blue precipitate immediately formed and was collected by filtration, washed with CH₃CN (1 x 10 mL) and dried under vacuum to give 0.297 g (84 %) of (CoCl₂)₂(μ -pz₄lut). X-ray quality crystals could not be grown despite multiple attempts giving at best microcrystalline needles from diffusion of Et₂O into a concentrated CH₃CN solution. Mp, > 350 °C. Anal. Calcd. (Obsd.) for C₁₉H₁₈Cl₄Co₂N₉: C, 36.10 (35.99); H, 2.87 (2.79); N, 19.94 (20.05). μ_{eff} (Solid) 6.65 μ_{B} (3.33 μ_{B} per Co). UV-Vis (CH₃CN) λ_{max} , nm (ϵ , M⁻¹cm⁻¹), 588(284), 684(376), 1058(15), 1240(32), 1506(32).

(CoCl₂)₂(μ-pz⁴₄lut), 5. A solution of 0.100 g (0.23 mmol) pz⁴₄lut in 15 mL of CH₃CN was added to a stirred solution of 0.060 g (0.46 mmol) CoCl₂ in 15 mL of CH₃CN to immediately produce a green/blue precipitate. The precipitate was collected by filtration, washed with additional CH₃CN (1 x 10 mL) and dried under vacuum to give 0.143 g (91 %) of (CoCl₂)₂(μ-pz⁴₄lut) as a green/blue solid. Mp, 280-286 °C decomp. Anal. Calcd. (Obsd.) for C₂₃H₂₅Cl₄Co₂N₉: C, 40.20 (37.20); H, 3.67 (4.30); N, 18.34 (16.48). UV-Vis (CH₃CN) λ_{max}, nm (ε, M⁻¹cm⁻¹), 587(323), 683(430), 1224(31), 1322(42), 1484(38).

(CoCl₂)₂(μ-pz^{*}₄lut), 6. A solution of 0.504 g (1.04 mmol) of pz^{*}₄lut in 25 mL of CH₃CN was added to a stirred solution of 0.270 g (2.08 mmol) CoCl₂ in 25 mL of CH₃CN to immediately produce a green/blue precipitate. The precipitate was collected by filtration, washed with additional CH₃CN (1 x 10 mL) and dried under vacuum to give 0.680 g (95 %) of **4**. Fine blue crystalline needles suitable for X-ray diffraction were grown by vapor diffusion of Et₂O into a concentrated solution of 1:1 CH₃CN:THF. Mp, 298-300 °C decomp. Anal. Calcd. (obsd) for C₂₇H₃₃Cl₄Co₂N₉: C, 43.63 (44.04); H, 4.47 (4.47); N, 16.96 (17.03). μ_{eff} (Solid) 8.44 μ_B (4.22 μ_B per Co). UV-Vis (CH₃CN) λ_{max}, nm (ε, M⁻¹cm⁻¹), 558(298), 665(316), 661(471), 1026(53), 1267(93), 1524(55).

(CoCl₂)₂(μ-pz^{DIP}₄lut)•MeOH, 7•MeOH. A solution of 0.200 g (0.28 mmol) of pz^{DIP}₄lut in 10 mL of CH₃CN was added to a stirred solution of 0.073 g of CoCl₂ in 30 mL of CH₃CN. Upon addition of the pz^{DIP}₄lut solution the reaction mixture turned deep blue/purple in color. The reaction was allowed to stir for one hour and the solvent was removed by vacuum to leave a blue/purple solid. The solid was washed with Et₂O (3 x 10 mL) and collected by filtration and allowed to dry under vacuum to give 0.248 g (91

%) of 5 as a purple solid. Crystals suitable for X-ray diffraction were grown by vapor diffusion of Et₂O into a concentrated MeOH solution. Mp, 280-290 °C. decomp. Anal. Calcd. (Obsd.) for C₄₃H₆₅Cl₄Co₂N₉: C, 53.27 (52.15); H, 6.77 (6.55); N, 13.03 (12.13). μ_{eff} (Evan's, CD₃CN, 295 K) 9.62 μ_B (4.86 μ_B per Co). UV-Vis (CH₃CN) λ_{max} , nm (ϵ , M⁻¹cm⁻¹), 558(328), 608(290), 658(356), 1000(51), 1264(93), 1524(55).

Chapter 4: Synthesis and Characterization of Iron(II) complexes of pz₄lut, pz⁴₄lut & pz^{*}₄lut.

Introduction. Investigations into the coordination chemistry of simple abiotic AE₄ pentadentate ligands¹ capable of occupying one axial (A) and four equatorial (E) positions about pseudo-octahedral transition metal complexes has given rise to important advances in understanding of bonding, electronic structure, and chemical reactivity in complex biological systems. Moreover, the lessons learned from model MAE₄ complexes have also served as the foundation for contemporary discoveries of systems capable of mediating spectacular organic transformations such as alkane oxidation.⁴³ We recently communicated our initial foray into the field with a survey of some first-row divalent transition metal coordination chemistry of $\alpha,\alpha,\alpha',\alpha'$ -tetra(pyrazolyl)lutidine (**pz₄lut**, left of **Figure 4.1**).⁵ The **pz₄lut** ligand, a relative of the more intensively studied tetra(pyridyl)lutidine **PY5-R** derivatives (right of **Figure 4.1**) exhibited many similar characteristics to the latter in terms of metal binding behavior but

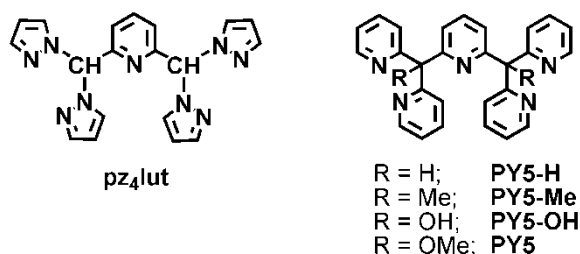


Figure 4.1. Pentadentate Ligand Scaffolds.

the change in equatorial groups from six-member pyridyl rings to the five-member pyrazolyl rings lead to intriguing changes in the properties of the resulting complexes. For instance, the copper(II) complexes $[\text{CuCl}(\kappa^4\text{-PY5})]^+$ and $[\text{CuCl}(\kappa^5\text{-pz}_4\text{lut})]^+$ exhibit different coordination modes. Also, based on absorption spectra of Ni^{2+} and Co^{2+} complexes, the **pz₄lut** ligand was found to be stronger field donor than **PY5**, a surprising feature that was attributed to greater ligand distortions in PY5 complexes that potentially reduce the full σ -donor (and π -acceptor) capabilities of the ligand. In the work reported below; we detail our investigation into the structural and electronic effects (**Figure 4.2**) substituting pyrazol hydrogens with methyl groups. Included in this work are reports on solid state (X-Ray structural analysis, Mössbauer and, Electron Paramagnetic Resonance Spectroscopy) and solution and electronic behavior (Absorption Spectroscopy) behavior.

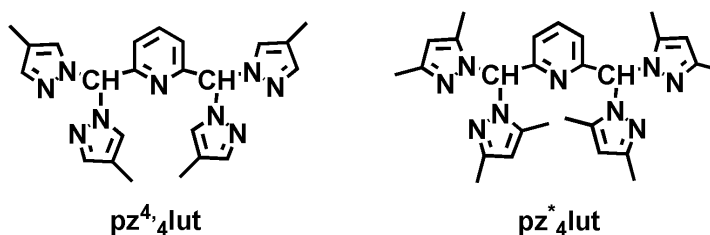


Figure 4.2. $\text{pz}^{4,4}\text{lut}$ and $\text{pz}^*_{4}\text{lut}$ ligands used in this study.

Solid State. The metal complexes of $\text{pz}^{\text{R}}_4\text{lut}$ ligands are prepared in nearly by mixing equimolar amounts of FeCl_2 and ligand. X-ray quality crystals of all three complexes of $[\text{FeCl}(\text{pz}_4\text{lut})][\text{Cl}]$ (**1**), $[\text{FeCl}(\text{pz}^{4,4}\text{lut})][\text{Cl}]$ (**2**), and $[\text{FeCl}(\text{pz}^*_{4}\text{lut})][\text{Cl}]$ (**3**) were obtained either by layering a dichloromethane solution of anhydrous iron(II) chloride and allowing the layers to diffuse for two days or by slow evaporation of the diffused solution. The complexes crystallized as a solvates: **1**• CH_2Cl_2 , **2**• MeOH • Et_2O , **3a**• 2MeOH and **3b**• MeOH . The structural and metrical parameters are shown below (**Tables 4.1& 4.2**) while a comparison of structural cations is shown in **Figure 4.3**. The

Compound	1•CH ₂ Cl ₂	2•MeOH•Et ₂ O	3a•MeOH	3b•2MeOH
Formula	C ₂₀ H ₁₉ Cl ₄ FeN ₉	C _{25.4} H _{32.5} Cl ₂ FeN ₉ O _{0.4}	C ₂₈ H ₃₇ Br _{0.11} Cl _{1.89} FeN ₉ O	C ₂₉ H ₄₁ Cl ₂ FeN ₉ O ₂
Formula Weight	583.09	597.04	647.31	674.46
Crystal System	Monoclinic	Monoclinic	Triclinic	Orthorhombic
Space Group	P2 ₁ /c	P2 ₁ /n	P1	Pnma
a, Å	10.4115(5)	12.9870(2)	8.7842(2)	14.3222(2)
b, Å	19.2410(9)	16.2105(2)	12.5916(4)	12.9169(2)
c, Å	12.0005(6)	14.3844(2)	13.7985(4)	17.1494(2)
B deg	90.000(2)	106.2600(1)	84.392(2)	90.000(2)
V, Å ³	2404.0(2)	2907.2(7)	1488.9(3)	3172.6(1)
Z	4	4	2	4
T, K	100(2)	100(2)	100(2)	100(2)
ρ, calcd, Mg m ³	1.611	1.399	1.444	1.412
λ, Å	1.54178	1.54178	1.54178	1.54178
μ (Cu, Kα) mm ⁻¹	9.372	6.157	6.111	5.709
R[I>2σ(I)] ^a (all data)	0.0353(0.0387)	0.0349(0.0406)	0.041090.0562)	0.0352(0.0393)
wR ^b (all data)	0.0862(0.0874)	0.0869(0.0349)	0.0886(0.0930)	0.0775(0.0790)
^a R = Σ F _o - F _c /Σ F _o . ^b wR = [Σw(F _o ² - F _c ²) ² /Σw F _o ²] ^{1/2}				

Table 4.1. Summary of single crystal x-ray diffraction data collection and refinement parameters.

Complex	1•CH ₂ Cl ₂	2•MeOH•Et ₂ O	3a•MeOH	3b•2MeOH
M-Cl (Å)	2.307(3)	2.323(6)	2.345(2)	2.328(2)
M-N1 _{py} (Å)	2.300(3)	2.268(2)	2.210(2)	2.218(3)
M-N3 _{pz} (Å)	2.179(3)	2.184(2)	2.290(2)	2.245(3)
M-N5 _{pz} (Å)	2.187(3)	2.169(2)	2.273(2)	2.245(3)
M-N7 _{pz} (Å)	2.198(3)	2.174(2)	2.252(2)	2.317(7)
M-N9 _{pz} (Å)	2.222(3)	2.182(2)	2.259(2)	2.317(7)
Avg. axial (Å)	2.304(3)	2.295(2)	2.302(2)	2.273(2)
Avg. Eq. (Å)	2.197(3)	2.177(2)	2.268(7)	2.281(4)
Avg. total (Å)	2.233(3)	2.216(2)	2.271(7)	2.330(1)
M-N4 _{pl} (Å)	0.392	0.365	0.250	0.293
MN3-N2C6 (°)	1.93	6.21	6.68	10.65
MN5-N4C6 (°)	5.08	3.37	1.73	10.65
MN7-N6C7 (°)	1.21	4.67	2.53	2.55
MN9-N8C7 (°)	7.50	4.14	14.80	2.55
Avg MN-NC(°)	3.93	4.59	6.44	6.60
N1-M-Cl (°)	179.60	177.98	179.70	176.81
Oct. Vol (Å) ³	14.279	14.054	15.134	15.236
Quad. Elong.	1.026	1.023	1.022	1.024
∠_variance (°) ²	88.46	76.99	76.17	81.48

Table 4.2. Structural parameters for compounds **1**, **2**, **3a** & **3b**.

state structures for all three reveal a six coordinate iron(II) center deviating from ideal local C_{4v} symmetry. For each complex the Fe-N(pz) bond lengths are characteristic of high spin iron(II) species⁴⁴ with an average Fe-N(pz) bond length of 2.196 Å for **1**•CH₂Cl₂, 2.177 Å for **2**•MeOH•Et₂O, 2.268 Å for **3a**•2MeOH, and 2.259 Å for **3b**•MeOH; for reference low spin on average < 2.000 Å.⁴⁵ High spin iron(II) is also accounted from examining the average axial (Fe-N(py) and Fe-Cl) bond lengths of each complex: 2.303 Å for **1**•CH₂Cl₂, 2.295 Å for **2**•MeOH•Et₂O, 2.277 Å for **3a**•2MeOH, and 2.273 Å for **3b**•MeOH again for low spin iron(II) complexes typically are less than 2.000 Å. Despite having eight electron donating methyl groups and what is anticipated to be the stronger field ligand the complexes **3a**•2MeOH and **3b**•MeOH contain not only the longest average bond distances but also the highest amount of ligand distortions which can be quantified by the FeN-NC(H) torsion angles (vide infra).

Shown in **Figure 4.3** is an overlay of structures showing the differences in FeN-NC(H) torsion angles of the four complexes. As can be seen **1**•CH₂Cl₂ experiences the least amount of twisting with an average FeN-NC(H) angle of 3.93 °, while **3a**•2MeOH and **3b**•MeOH experience the most twisting at 6.44 ° and 6.60 °. As expected the complex **2**•MeOH•Et₂O represents a case with intermediate distortion with 4.6 ° of ring twisting. Ideally, this torsion angle would approach zero and the pyrazoles would experience no distortions.⁴⁶ Presumably, the eight methyl groups adjust to have a maximum distance from the chloride group and steric interaction from the 3-methyl, 3-methyl groups, giving rise to the longer average bond lengths and higher torsions angles seen in both **3a**•2MeOH and **3b**•MeOH (highlighted in **Figure 4.4** below).

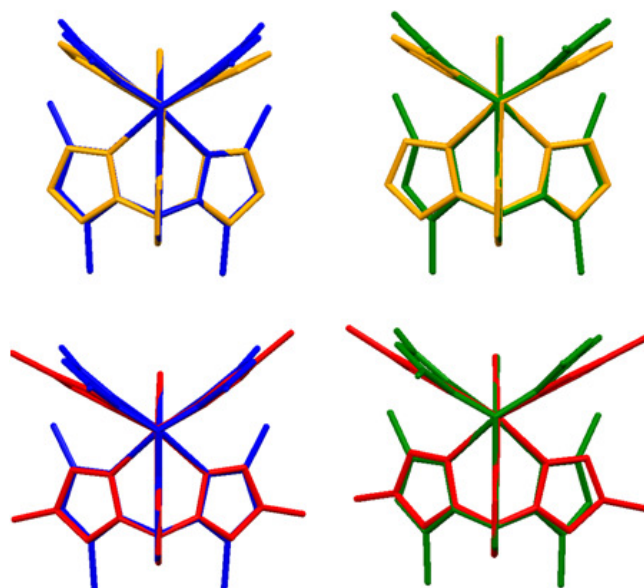


Figure 4.3. Structural overlay of $1 \cdot \text{CH}_2\text{Cl}_2$ (gold) & $3\text{a} \cdot 2\text{MeOH}$ (blue) (top left), $1 \cdot \text{CH}_2\text{Cl}_2$ & $3\text{b} \cdot \text{MeOH}$ (green) (top left), $2 \cdot \text{MeOH} \cdot \text{Et}_2\text{O}$ (red) & $3\text{a} \cdot 2\text{MeOH}$ (bottom left), and $2 \cdot \text{MeOH} \cdot \text{Et}_2\text{O}$ & $3\text{b} \cdot \text{MeOH}$ (bottom right).

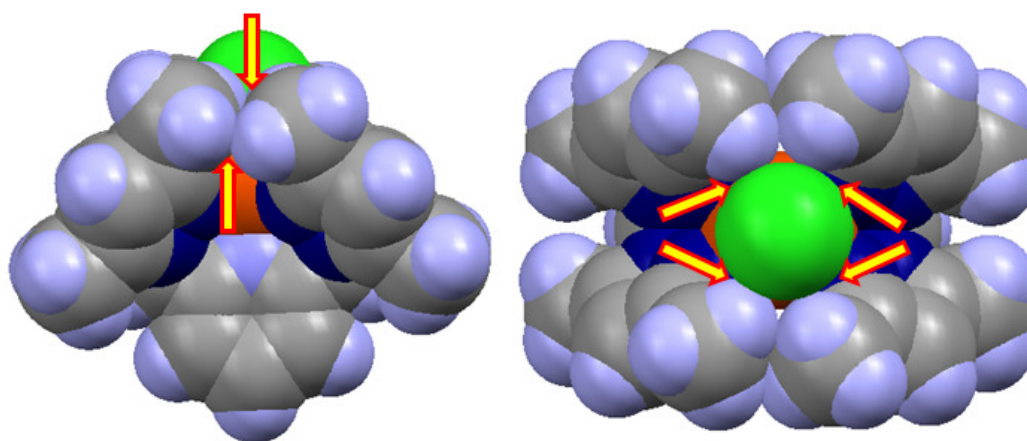


Figure 4.4. Space-filling model of $3\text{a} \cdot 2\text{MeOH}$ highlighting the steric interactions between methyls (left) and between methyls and chloride groups (right).

Mössbauer Spectroscopy. The Mössbauer spectra of $[\text{FeCl}(\text{pz}_4\text{lut})]\text{Cl}\cdot\text{CH}_2\text{Cl}_2$, $\mathbf{1}\cdot\text{CH}_2\text{Cl}_2$, obtained at 85 and 295 K are shown in **Figure 4.5**; the 155 and 225 K spectra are virtually identical to those shown in this figure. These spectra have been fit with a symmetric quadrupole doublet and the resulting parameters are given in **Table 4.3**. The 85 to 295 K spectra of $\mathbf{1}\cdot\text{CH}_2\text{Cl}_2$, are fully consistent⁴⁷ with the presence of high-spin iron(II) in a distorted octahedral coordination environment; there is no indication of the presence of any iron(III) or iron(II) in a different coordination environment. The observed isomer shift is typical of iron(II) in an FeN_4Cl_2 coordination environment. The temperature dependence of the isomer shift, δ , of $\mathbf{1}\cdot\text{CH}_2\text{Cl}_2$, (**Figure 4.6**) is well fit with the Debye model⁴⁸ for the second-order Doppler shift with a characteristic Mössbauer

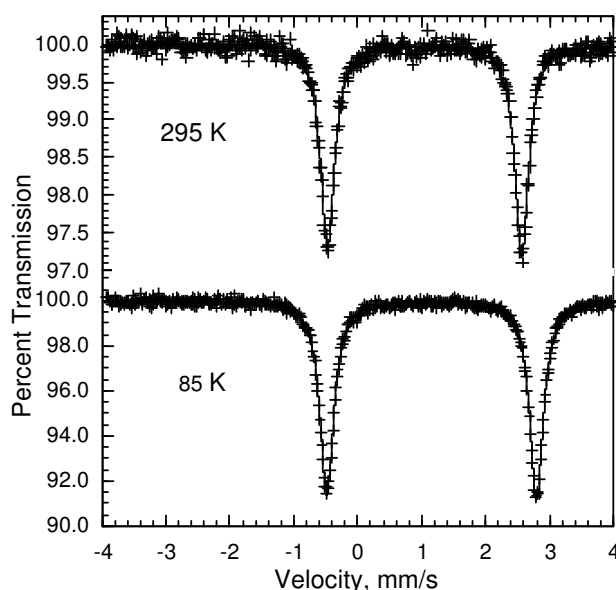


Figure 4.5 Mössbauer spectrum of $\mathbf{1}\cdot\text{CH}_2\text{Cl}_2$ at 295 K and 85 K.

complexes indicate that Θ_M^δ is often at least twice as large as Θ_M^δ , i.e., the isomer shift is more sensitive to higher energy phonons. The isomer shift of $\mathbf{1}\cdot\text{CH}_2\text{Cl}_2$, see **Figure 4.5**,

decreases by only 0.110 mm/s between 85 and 295 K, a decrease which is typical for this type of complex.⁴⁹

The 3.04 mm/s quadrupole splitting observed at 295 K for **1** is typical⁷ of that expected for iron(II) in a pseudooctahedral FeN_4Cl_2 coordination environment. In contrast and unexpectedly, there is little change in this rather large quadrupole splitting with temperature; between 85 and 295 K the splitting decreases by only 0.24 mm/s, albeit in an almost linear fashion, (See **Figure 4.6**). As is also shown in this figure, an attempt

$[\text{FeCl}(\text{pz}_4\text{lut})](\text{Cl})$	T , K	δ , mm/s ^a	ΔE_Q , mm/s	I , mm/s	Area, (% ϵ)(mm/s)
	295	1.047	3.04	0.26	2.198
	85	1.157	3.28	0.26	6.944
$[\text{FeCl}(\text{pz}^*_4\text{lut})](\text{Cl})$	295	1.093	1.32	0.28	41.2
	85	1.226	1.99	0.31	36.3

Table 4.3. Mössbauer parameters obtained for **1**• CH_2Cl_2 and **3a**•2MeOH.

to fit the temperature dependence of the quadrupole splitting of **1** with the Ingalls model⁵⁰ in terms of the low-symmetry crystal field splitting, Δ , of the t_{2g} orbitals fails; the “best fit” yields a splitting of 725 cm^{-1} a not unreasonable value for the splitting. Apparently there is a small temperature dependence to Δ which invalidates the Ingalls model.

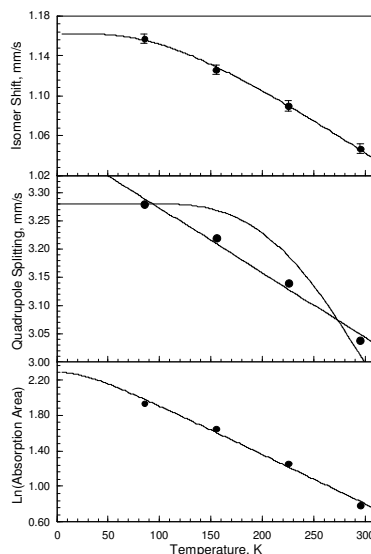


Figure 4.6. The temperature dependence of the isomer shifts, upper, the quadrupole splittings, center, and the logarithm of the spectral absorption areas, lower, of **1•CH₂Cl₂**. The isomer shifts and the logarithm of the spectral absorption areas have been fit with the Debye model for a solid and the quadrupole splittings have been fit with a linear dependence on temperature; an attempted fit with the Ingalls model, the curved line, is also shown.

Solution. All of the $[\text{Fe}(\text{Cl})\text{pz}^{\text{R}}_4\text{lut}]$ complexes are sparingly soluble in methanol to give orange (**1**) or yellow (**2**) solutions but are completely insoluble in other organic solvents. Paramagnetic ^1H NMR spectra indicate high spin iron(II) paramagnetic with magnetic moments (Evans, CD_3OD , 298 K): $5.45 \mu_{\text{B}}$ for **1•CH₂Cl₂**, $4.41 \mu_{\text{B}}$ for **2•MeOH•Et₂O** and $6.40 \mu_{\text{B}}$ for **3a•MeOH**. The electronic absorption spectrum for each **1•CH₂Cl₂**, **2•MeOH•Et₂O** and **3a•2MeOH** is shown below in **Figure 4.7**. Each spectrum consist of two main bands: one low energy, low intensity band ($\sim 800\text{-}1000 \text{ nm}$, $\epsilon < 10$) and one higher energy, higher intensity band ($\sim 400 \text{ nm}$, $\epsilon > 100$). The low energy bands can be assigned to the expected $^5\text{E} \leftarrow ^5\text{T}_2$ d \leftarrow d transition for high spin d^6 compounds while the higher energy bands can be assigned to either a $\pi^* \leftarrow \text{n}$ or charge transfer; with the low intensity suggestive of the former. Since there is only one expected

d-d transition for high spin d^6 complexes the energy of this transition directly corresponds to the crystal field parameter Δ_o for each complex. The Δ_o values are $10,400\text{ cm}^{-1}$ for **1**• CH_2Cl_2 , $10,612\text{ cm}^{-1}$ for **2**• MeOH • Et_2O and $8,950\text{ cm}^{-1}$ for **3a**• 2MeOH . While these results are initially surprising, they fall in line with other high spin iron(II) poly(pyrazole)methane complexes and will be discussed in further detail later on (vide infra).

Stoichiometry. The stoichiometry of the complexes was confirmed by using Job's plot analysis.⁵¹ By monitoring the absorbance at 424 nm (**1**), 438 nm (**2**) and 403 nm (**3**) in methanol the expected complexation ratio of 1:1 was confirmed. The plots below (**Figure 4.8**) all show that the absorbances for the respective wavelengths are at a maximum when the ratio of ligand to metal is at 1:1. Information about the strength of the formation constant can also be obtained from the appearance of the plots. Only complexes that have large formation constants give plots that are triangular in shape.⁵²

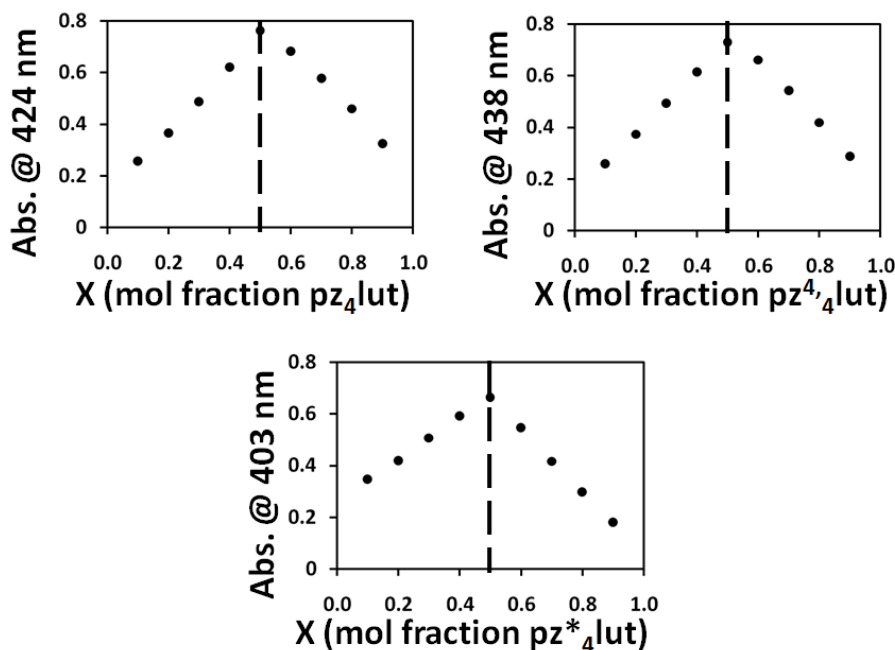


Figure X.8. Job's plots of **1**, **2** and **3** in methanol.

Electrochemistry. The cyclic voltammograms of complexes **1**•CH₂Cl₂, **2**•MeOH•Et₂O and **3a**•2MeOH was recorded in methanol at a scan rate of 100 mVs with n-butyl ammonium hydrogen sulfate as the supporting electrolyte (**Figure 4.9**). Both **1**•CH₂Cl₂ and **2**•MeOH•Et₂O displayed quasi reversible oxidation waves: $E_{1/2} = 0.76$ V for **1**•CH₂Cl₂ and 0.65 V for **2**•MeOH•Et₂O versus Ag/AgCl. However, the complex **3a**•2MeOH only displayed an irreversible oxidation centered at 0.96 V. As the ligand is redox innocent under these conditions. In all complexes, this oxidation wave corresponds to the one electron oxidation of Fe^{II} to Fe^{III}. The closest related species [FeCl(PY5)][Cl]

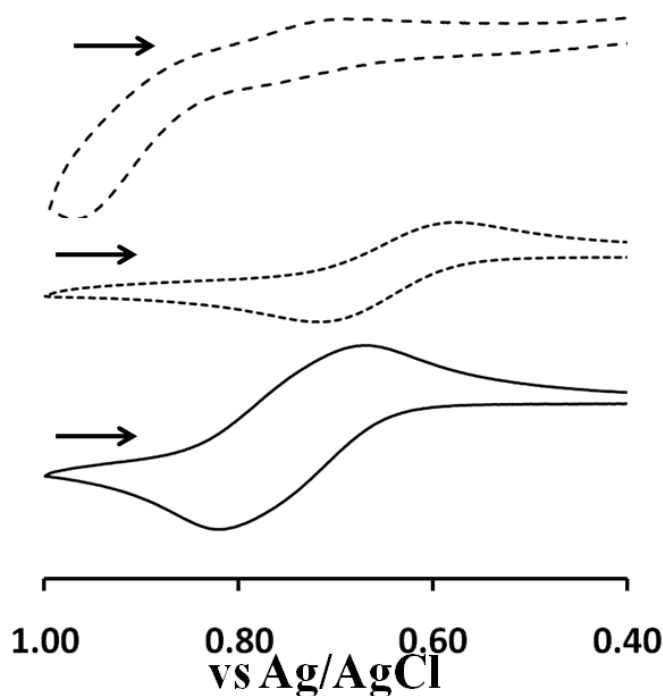


Figure 4.9. Cyclic voltammograms of **1**•CH₂Cl₂ (bottom), **2**•MeOH•Et₂O (middle) and **3a**•2MeOH (top) in methanol (1 mM) with 0.1 mM [NBu₄][HSO₄]. Scan rate = 100 mvs.

has a reversible oxidation wave at 0.40 V^{13a} while [Fe(bztpen)Cl][Cl] has a reversible oxidation potential of 0.22 V.^{53b}

Electron Paramagnetic Resonance. The X-band (9.6 GHz) electron paramagnetic resonance spectra for **1**, **2** and **3** was recorded at 10 K in 9:1 MeOH:EtOH as shown in (Figure 4.10). All three species are rare examples of non-Kramer's systems ($S = 2$) that give detectable EPR signals owing to some proportion of the zero-field splitting envelope satisfying the condition $\Delta < 0.3 \text{ cm}^{-1}$; however, no hyperfine coupling to any of the nitrogens is observed.⁵⁴

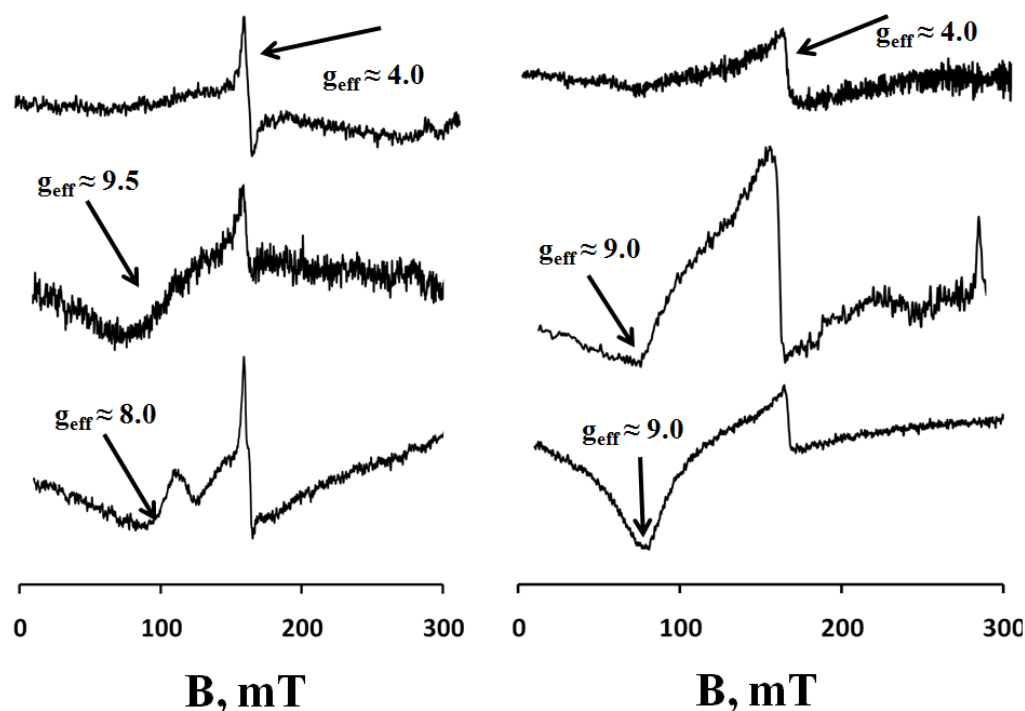


Figure 4.10. Perpendicular mode (left) and parallel mode (right) X-band EPR of **1**•CH₂Cl₂ (bottom), **2**•MeOH•Et₂O (middle) and **3a**•2MeOH (top) at 3 mW and 10 K.

The signals for the main iron(II) species are observed at $g_{\text{eff}} \approx 8.0$ for **1**•CH₂Cl₂, $g_{\text{eff}} \approx 9.5$ for **2**•MeOH•Et₂O and $g_{\text{eff}} \approx 4.0$ for **3a**•2MeOH. The signals at $g_{\text{eff}} \approx 4.0$ in **1**•CH₂Cl₂ and **2**•MeOH•Et₂O are attributed to the minor species (iron(III) impurity). Parallel mode confirms the presence of the high spin iron(II) signals.

Discussion. Three new iron(II) complexes of $\text{pz}^{\text{R}}_4\text{lut}$ have been synthesized in high yield. All three complexes show a iron(II) center, slightly deviated from ideal local C_{4v} symmetry because of various differences in the equatorial M-N bond distances and associated angles imposed in part by pyrazole methyl substitution. The complex **3a•2MeOH** was expected to have the shorter bond distances due to eight electron donating methyl groups. From examination of bond distances and angles it was found that 3,5-dimethyl substitution causes significant Fe-N(pz) bond lengthening and pyrazolyl ring twisting relative to the complexes without these pyrazolyl substitutions. The steric interactions between methyls and methyls and axial chloride serve to lengthen and presumably weaken the bonds. This observation falls in line with other high spin iron(II) complexes bound to methyl substituted pyrazoles. For example, the complexes $\{\text{Fe}[\text{HC}(\text{pz}_3)_2]^{2+}\}$ and $\text{Fe}[\text{HB}(\text{pz})_3]_2$ are low-spin while $\{\text{Fe}[\text{HC}(\text{pz}^*)_3]_2^{2+}\}$ and $\text{Fe}[\text{HB}(\text{pz}^*)_3]_2$ are high spin.⁴⁰ In the latter cases, it is believed that the steric interactions involving the 3-methyl groups (proximal to the metal) favor the longer Fe-N bonds of the high spin state, effectively making the 3,5-dimethyl pyrazole derivative weaker field ligands than the unsubstituted analogues. While, in the present case, all complexes are high spin but differences between **3c** and complexes without 3-methyl substitution are significant.

Furthermore the structural trends that are observed can also be observed through other solid state measurements such as Mössbauer spectroscopy. The isomer shifts for **1•CH₂Cl₂** and **3a•2MeOH** obtained at both 295 K and 85 K are consistent with high spin iron(II) in a distorted tetrahedral environment. The values for the isomer shift also are consistent with the above observation of the pz^*_4lut being the weaker field ligand.

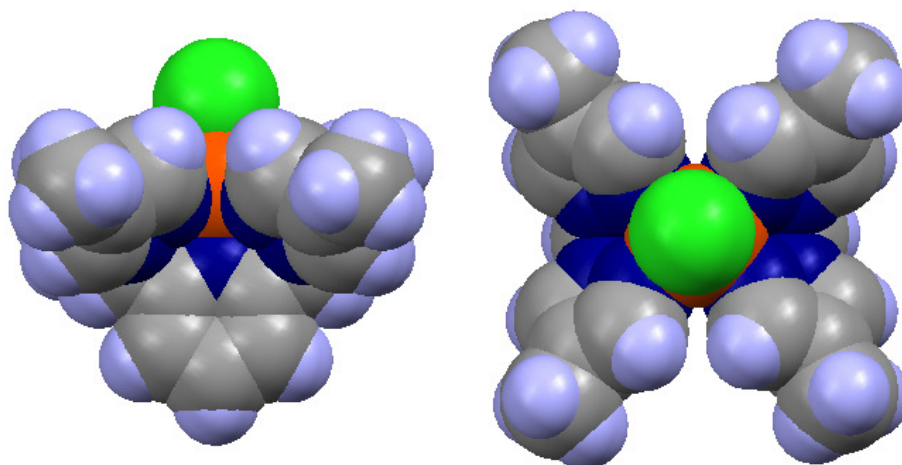


Figure 4.11. Spacefilling model of the cation of **2•MeOH•Et₂O** showing the lack of steric interactions.

These can be accounted for by the nephelauxetic series.⁵⁴ As the degree of covalency between the iron center and the ligand increases an expansion of the *3d*-orbitals occurs. As the *d*-orbitals expand they in turn become further away from the nucleus and are thus less able to screen the *s*-orbitals from nuclear charge. Therefore, a higher *s*-electron density at the nucleus provides for a less positive isomer shift in the spectra which is what is observed (at both temperatures, **Table 4.3**) in the above complexes: $\delta = 1.047$ mm/s for **1•CH₂Cl₂** and 1.093 mm/s at 295 K for **3a•MeOH•Et₂O**.

The solution properties of the three newly prepared high spin iron(II) complexes matches well with the solid state data. The stoichiometry was found to be 1:1 for each iron complex as determined by Job's method. By looking at the shape of the Job's plots it can be inferred that the strength and formation constant are both very large, as they will give triangular shaped plots.¹² As such, these constants cannot be determined via standard methods and were not able to be determined. The high binding constant is also

inferred by electrochemical and spectroscopic data which give distinct features from each other or FeCl_2 .

By calculating the ligand field parameters from the average energy of the main band and shoulder,⁵⁵ the values for Δ_o were found to be $10,612\text{ cm}^{-1}$ for pz^4_4lut , $10,400\text{ cm}^{-1}$ for pz_4lut and $8,950\text{ cm}^{-1}$ for pz^*_4lut . These values are fully consistent with the bond length data as well as the mössbauer data obtained above; with pz^*_4lut being the weaker field ligand despite having eight electron donating methyl groups. Furthermore, these trends can also be observed in the EPR as well as electrochemical data. As ligand field strength increases so does the g-value, as seen by the g-values obtained from the EPR experiments ~ 9.5 for $\mathbf{2} \cdot \text{MeOH} \cdot \text{Et}_2\text{O}$, ~ 8.0 for $\mathbf{1} \cdot \text{CH}_2\text{Cl}_2$ and ~ 4.0 for $\mathbf{3a} \cdot 2\text{MeOH}$.

Conclusion. Due to the favoring of the longer and weaker bond lengths by the pz^*_4lut ligand, it has been shown to be a weaker field ligand despite possessing the eight electron donating methyl groups. From the data shown the trend in ligand field strength is as follows $\text{pz}^4_4\text{lut} > \text{pz}_4\text{lut} > \text{pz}^*_4\text{lut}$ which agrees well with previously studied iron(II) pyrazole complexes. We will shortly disseminate our findings with regard to investigation of methods to increase solubility of the complexes and the capacity of these or related derivatives to undergo chemical transformations.

Experimental Section

General Information. All transition metals were obtained commercially and used as received. For ligand syntheses, please see **Chapter 1** and **1•CH₂Cl₂** see **Chapter 2**. Solvents were dried by conventional procedures and distilled prior to use, except where noted. Midwest Microlab, LLC, Indianapolis, Indiana 45250, performed all elemental analyses. Melting point determinations were made on samples contained in glass capillaries using an Electrothermal 9100 apparatus and are uncorrected. ¹H and ¹³C NMR spectra were recorded on a Varian 300 MHz spectrometer. Chemical shifts were referenced to solvent resonances at δ_{H} 7.27 and δ_{C} 77.23 for CDCl₃ and δ_{H} 3.31 and δ_{C} 49.15 for methanol-d₄. UV-visible and NIR spectra were recorded using Shimadzu UV-1600/1700 or Jasco V-570 instruments. The stoichiometry for pz₄lut, pz⁴₄lut and pz^{*}₄lut complexation was established by Job's plot analysis using electronic absorption, with a total solution concentration of 10.0×10^{-4} M. Solid-state magnetic measurements were made at room temperature using an MK1 susceptibility balance. Electrochemical measurements were obtained using a BASi CV-50V instrument for ca. 2.0 mM MeOH solutions of the complexes with 0.05 M NBu₄PF₆ as the supporting electrolyte. EPR spectral measurements were obtained using a Bruker ELEXSYS E600 equipped with ER4116DM cavity resonating at 9.63 GHz, an Oxford instruments ITC503 temperature controller and ESR-900 helium flow cryostat. The EPR spectra were recorded with 100 kHz field modulation.

[FeCl(pz⁴lut)](Cl)•MeOH•Et₂O, 2•MeOH•Et₂O. A solution of 0.074 g (0.58 mmol) of FeCl₂ in 8.5 mL of MeOH was layered onto a solution of 0.250 g (0.58 mmol) of pz⁴lut ligand in 8.5 mL of CH₂Cl₂. After allowing the solution to diffuse over several days, the solvent was allowed to slowly evaporate and after several days **2•MeOH•Et₂O** orange x-ray quality crystals were collected after filtration, washing with Et₂O and drying under vacuum. Mp, 275-280 °C decomp. ¹H NMR (CD₃OD) δ_H μ_{eff} (evans) (CD₃OD, 298 K) 4.41 μ_B. UV-Vis (MeOH) λ_{max}, nm (ε, M⁻¹, cm⁻¹), 268 (5874), 314 (1136), 438 (97), 868 (7).

[FeCl(pz⁴*lut)](Cl)•2MeOH, 3a•2MeOH. A solution of 0.126 g (0.99 mmol) of FeCl₂ in 8.5 mL of MeOH was layered onto a solution of 0.503 g (0.99 mmol) of pz⁴*lut ligand in 8.5 mL CH₂Cl₂. After allowing the solution to diffuse, the solvent was allowed to slowly evaporate and after several days 0.653 g (100 %) of **3a•2MeOH** yellow x-ray quality crystals were collected after filtration, washing with Et₂O and drying under vacuum. Mp, 230-242 °C decomp. Anal. Calcd. (Obsd.) for C₂₉H₄₁Cl₂FeN₉O₂: C, 51.64 (50.94), H, 6.13 (6.17), N, 18.69 (18.29). μ_{eff} (evans) (CD₃OD, 298 K) 6.40 μ_B ± 0.3 μ_B. UV-Vis (MeOH) λ_{max}, nm (ε, M⁻¹, cm⁻¹), 264(7290), 321 (1354), 970 (2).

Chapter 5: Reactivity of Iron(II) Complexes of pz₄lut and its Derivatives.

Introduction. Given the importance of oxoferryl species in bio-inorganic chemistry and their ability to mediate difficult organic transformations such as C-H bond activation it is of interest to synthetically generate these highly reactive species to deepen the understanding of such processes⁵⁷ which can help to make more efficient use of the world's diminishing fossil fuel supplies. Given the several recent reports of MAE₄ type pentadentate ligands that stabilize highly reactive intermediates such as oxos, superoxos, alkyl peroxos and hydroxyls (**Figure 5.1**)⁵⁸ we sought to investigate the reaction chemistry of the newly reported pz₄lut ligand system as well as its ability to stabilize highly reactive intermediate species such as iron(IV) oxos.

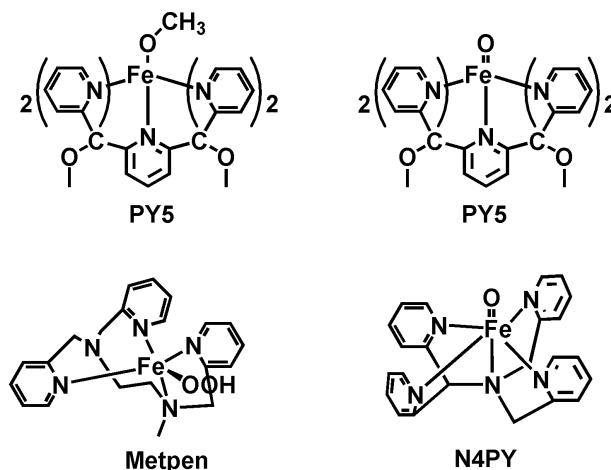
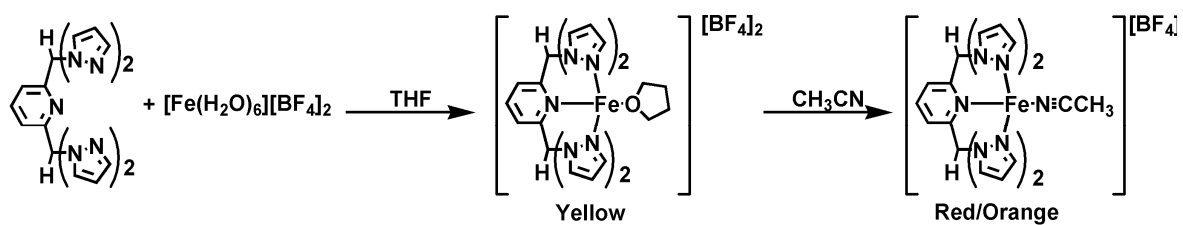


Figure 5.1. Some highly reactive intermediates of some pentadentate ligands.

The previously synthesized complexes of $[\text{Fe}(\text{Cl})\text{pz}_4^{\text{R}}\text{lut}][\text{Cl}]$ ($\text{R} = \text{H}$, 4-methyl, 3,5-dimethyl) exhibit very low solubility in most organic solvents. Therefore various means to increase the solubility of the iron(II) complexes were explored such as the use of non-coordinating anions via the use of $[\text{Fe}(\text{H}_2\text{O})_6][\text{BF}_4]_2$ as a precursor or anion exchange reactions between $[\text{Na}][\text{BAr}_4^{\text{f}}]$ and $[\text{FeCl}(\text{pz}_4^{\text{R}}\text{lut})][\text{Cl}]$. The reactivity of these complexes toward simple axial substitution reactions including reactions with strong nucleophilic to potentially generate rare alkyl or alkoxy derivatives were explored. Finally, in attempt to generate highly reactive intermediate species, several different iron(II) complexes were exposed to various chemical oxidants as well as oxygen atom transfer reagents in an effort to identify key reactive intermediate species. The results of these investigations are disseminated herein.

Synthesis. When pz_4lut is reacted with $[\text{Fe}(\text{H}_2\text{O})_6][\text{BF}_4]_2$ (**Scheme 5.1**) in THF at room temperature $[\text{Fe}(\text{THF})\text{pz}_4\text{lut}][\text{BF}_4]_2$ (**1**) as a yellow precipitate (characterized by elemental analysis) is immediately formed. Complex **1** displays low solubility as it is only soluble in solvents with which it reacts. For example, when acetonitrile is added to the yellow THF solvate a deep red orange solution is immediately obtained. Upon removal of the solvent $[\text{Fe}(\text{CH}_3\text{CN})(\text{pz}_4\text{lut})][\text{BF}_4]_2$ (**2**) as a red/orange solid is obtained in high yield (85 %) (**Scheme 5.1**). This complex red has been characterized both crystallographically and spectroscopically (UV-Vis, ^1H NMR) as a diamagnetic low spin iron(II) species (**Figure 5.2**).



Scheme 5.1. Synthesis of $[\text{Fe}(\text{THF})(\text{pz}_4\text{lut})][\text{BF}_4]_2$ (**1**) and $[\text{Fe}(\text{CH}_3\text{CN})(\text{pz}_4\text{lut})][\text{BF}_4]_2$ (**2**).

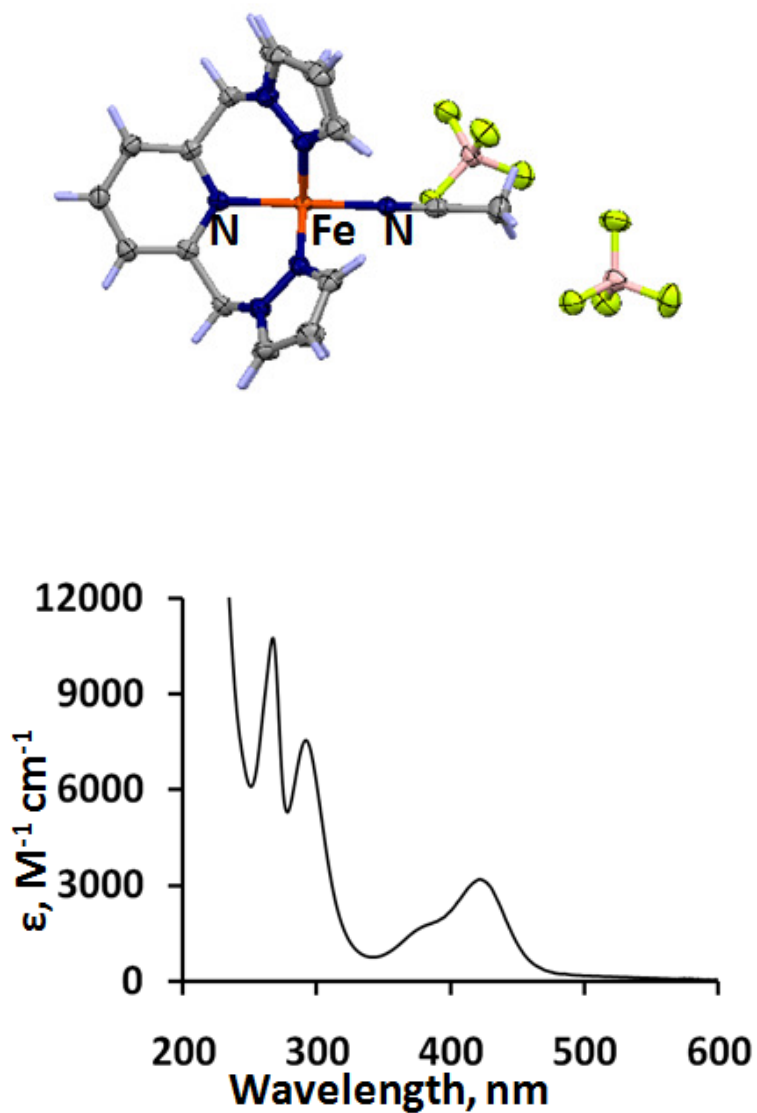


Figure 5.2. X-ray crystal structure of **2**, ellipsoids drawn at 50 % probability level (top); absorption spectra of **2** in acetonitrile (bottom).

Crystallographically the iron(II) complex (**2**) displays an average Fe-N(pz) bond distance of 1.978(3) Å while giving the Fe-N(py) bond distance is 1.947(3) Å, typical of low spin iron(II) complexes; high spin iron(II) complexes typically have Fe-N bond distances closer to 2.10 Å.⁵ The absorption spectrum of **2** in acetonitrile displays charge transfer bands at 380 nm and 420 nm in the visible region which offers a useful means for the monitoring of reactions by absorption spectroscopy. However, d←d transitions are likely obscured by ligand transitions. It is worth noting, that in contrast to **1** the reaction between pz^{*}₄lut and [Fe(H₂O)₆][BF₄]₂ immediately produces [Fe(H₂O)(pz^{*}₄lut)][BF₄]₂ (**3**) as a yellow precipitate with water rather than THF in the axial position (elemental analysis). Furthermore, no color change is observed when yellow **3** is dissolved in acetonitrile; most likely owing to the steric interactions of the 3-methyl groups that prevent axial substitution reactions with this ligand.

It was found that (**2**) was susceptible to anation with [NEt₃Bz][Cl] by monitoring the reaction by electronic absorption spectroscopy at 420 nm. The reaction stoichiometry was confirmed to be 1:1 as shown by **Figure 5.3** below. Several attempts to grow crystals of [Fe(Cl)(pz₄lut)][BF₄] (**4**) were not successful; but, the complex has been characterized using elemental analysis and spectroscopy.

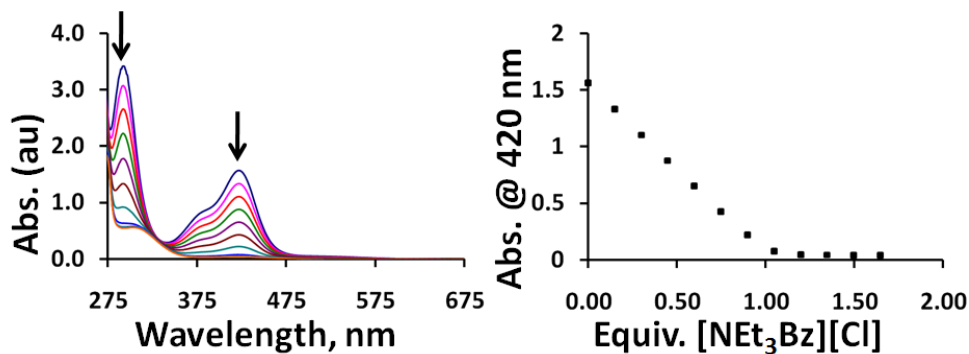
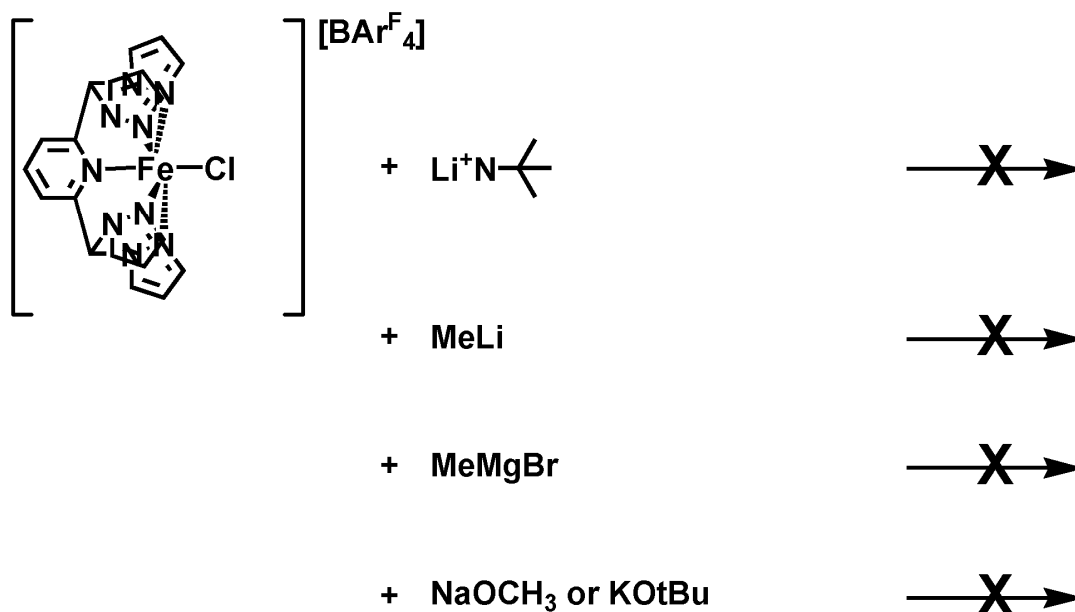


Figure 5.3. Addition of [NEt₃Bz][Cl] to **2** in acetonitrile: absorption spectra (left) and plot of absorbance versus equivalents of [NEt₃Bz][Cl] (right).

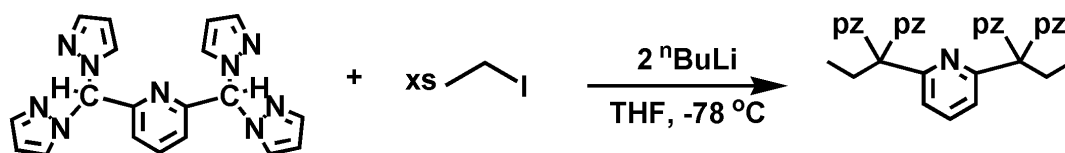
Attempts were made to prepare more unusual alkyl, amido or alkoxy complexes via strongly nucleophilic bases such as those shown in **Scheme 5.2**. Due to the fact that the tetrafluoroborate salt is only soluble in solvents with which it reacts and the low solubility of the $[\text{FeCl}(\text{pz}_4\text{lut})][\text{Cl}]$ complex (only soluble in MeOH) we performed an anion exchange reaction between $[\text{Na}][\text{BAr}^{\text{F}}_4]$ and $[\text{FeCl}(\text{pz}_4\text{lut})][\text{Cl}]$ in dichloromethane/methanol to give the complex $[\text{FeCl}(\text{pz}_4\text{lut})][\text{BAr}^{\text{F}}_4]$ (**5**). The $[\text{BAr}^{\text{F}}_4]$ complex displays increased solubility in a wide variety of organic solvents therefore allowing a wide variety of potential reactions. Shown below in **Scheme 5.2** is a reaction summary between several strong bases and the $[\text{FeCl}(\text{pz}_4\text{lut})][\text{BAr}^{\text{F}}_4]$ complex.



Scheme 5.2. Reaction summary of several strong bases with $[\text{FeCl}(\text{pz}_4\text{lut})][\text{BAr}^{\text{F}}_4]$. Unfortunately brown decomposition products that were insoluble in any organic solvent were obtained as the result of these reactions and left them uncharacterizable. A potential explanation for these undesirable products may be decomposition via methyne deprotonation. Previous work on related poly pyrazolylalkanes,⁵⁹ indicated that the

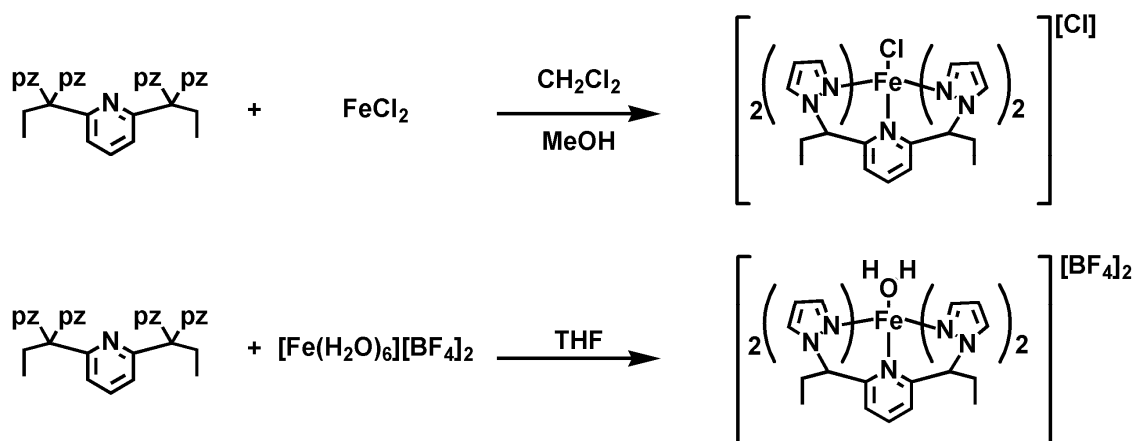
acidic methyne and or protons along the heterocycle periphery are susceptible to nucleophilic attack and subsequent derivitization with electrophiles.

As proof of principle, and as a means to remove this potential decomposition pathway, the synthesis of a methyne-protected derivative $\text{pz}_4\text{Et}_2\text{lut}$, is show in **Scheme 5.3**. The reaction of pz_4lut with 2 equivalents of $^n\text{BuLi}$ at -78°C in THF afforded a deep brown solution which after reaction with excess ethyl iodide, gave good yields of $\text{pz}_4\text{Et}_2\text{lut}$.



Scheme 5.3. Synthesis of $\text{pz}_4\text{Et}_2\text{lut}$ ligand.

Both the iron(II) chloride and iron(II) tetrafluoroborate complexes of pz_4Et_2 have been synthesized as shown in **Scheme 5.4**. Both complexes are obtained in high yield



Scheme 5.4. Syntheses of $[\text{Fe}(\text{Cl})(\text{pz}_4\text{Et}_2\text{lut})][\text{Cl}]$ (**6**) and $[\text{Fe}(\text{H}_2\text{O})(\text{pz}_4\text{Et}_2\text{lut})][\text{BF}_4]_2$ (**7**) complexes.

While crystals suitable for x-ray diffraction for either compound have not been obtained, both complexes have been characterized by elemental analyses (experimental details), diamagnetic NMR and absorption spectroscopy (*vide infra*) and display characteristics consistent with low spin iron(II).

Solution Studies. Both complexes **6** & **7** display a significant increase in solubility over the parent complexes $[\text{FeCl}(\text{pz}_4\text{lut})][\text{Cl}]$ (slightly soluble only in methanol) and $[\text{Fe}(\text{THF})(\text{pz}_4\text{lut})][\text{BF}_4]_2$ (**1**) (soluble only in solvents with which it reacts) in organic solvents such as methanol, acetonitrile and acetone. The absorption spectra for both complexes is shown below in **Figure 5.4** and display characteristic bands in the

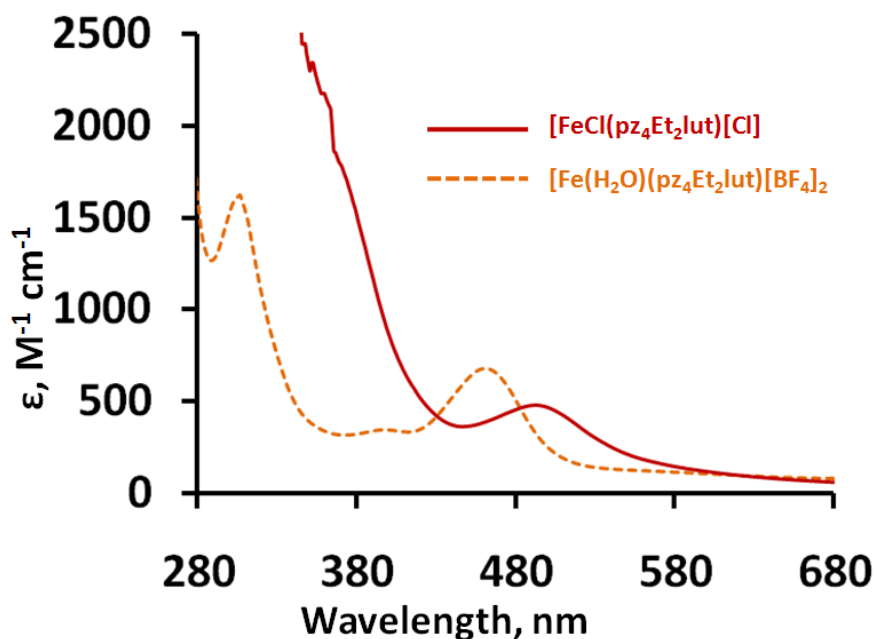


Figure 5.4. Absorption spectra of $[\text{FeCl}(\text{pz}_4\text{Et}_2\text{lut})][\text{Cl}]$ in CH_2Cl_2 (brick red) and $[\text{Fe}(\text{Sol})(\text{pz}_4\text{Et}_2\text{lut})][\text{BF}_4]_2$ in MeOH (orange).

visible region that again can be used for monitoring reaction chemistry by absorption spectroscopy.

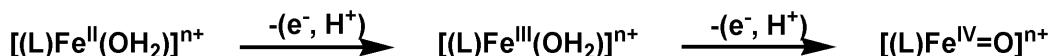
Attempts at Oxoferryl Generation. The generation of other iron(IV) oxo species has been achieved both chemically as well as electrochemically as summarized in **Scheme 5.5**. With other ligands iron(IV) oxo species have been reported as green complexes with a characteristic absorption band of $\lambda_{\text{max}} \sim 700 \text{ nm}$.⁵⁸

Single oxygen atom donors, [O]



[O] = PhIO, *m*-CPBA, peracetic acid, KHSO₅, O₃, NaOCl

Electrochemical



Scheme 5.5. Methods for the generation iron(IV) oxo species.

Four iron(II) complexes (**1**, **3**, **6**, & **7**) were each subjected to numerous chemical oxidants in an effort to obtain iron(IV) oxo species. When two equivalents of *m*-CPBA are reacted with [FeCl(pz₄lut)][BAR₄^f] at -30 °C in acetonitrile a green color ($\lambda_{\text{max}} \sim 700 \text{ nm}$) similar to other iron(IV) oxo species is observed by absorption spectroscopy (**Figure 5.5**).³ The lifetime of this reactive green species is very short ($t_{1/2} < 5 \text{ minutes}$) at -30 °C and, upon warming, of the solution the green color disappears. Re-cooling of the solution or the addition of further quantities of *m*-CPBA does not restore the green color and the final reaction solution appears orange/yellow. Interestingly, the reactive green intermediate was capable of converting tri(phenyl)methane to tri(phenyl)methanol (~15 % based on GC-MS). Furthermore, this conversion does not happen without the metal complex present. Further supporting an intermediate is the fact that upon addition of triphenyl methane ~ 15 % is converted to triphenyl methanol (based on GC- MS).

Numerous attempts to grow crystals of the reactive intermediate species failed; including the layering of oxidant on top of solutions of iron(II) complex even at low temperature. Similarly, no crystals were obtained of the decomposition product from the yellow/orange solution despite numerous attempts. It should be noted that attempts to generate the iron(IV) oxo species with other oxidants (Solid PhIO, excess 30 % H_2O_2 , Me_3NO) were unsuccessful.

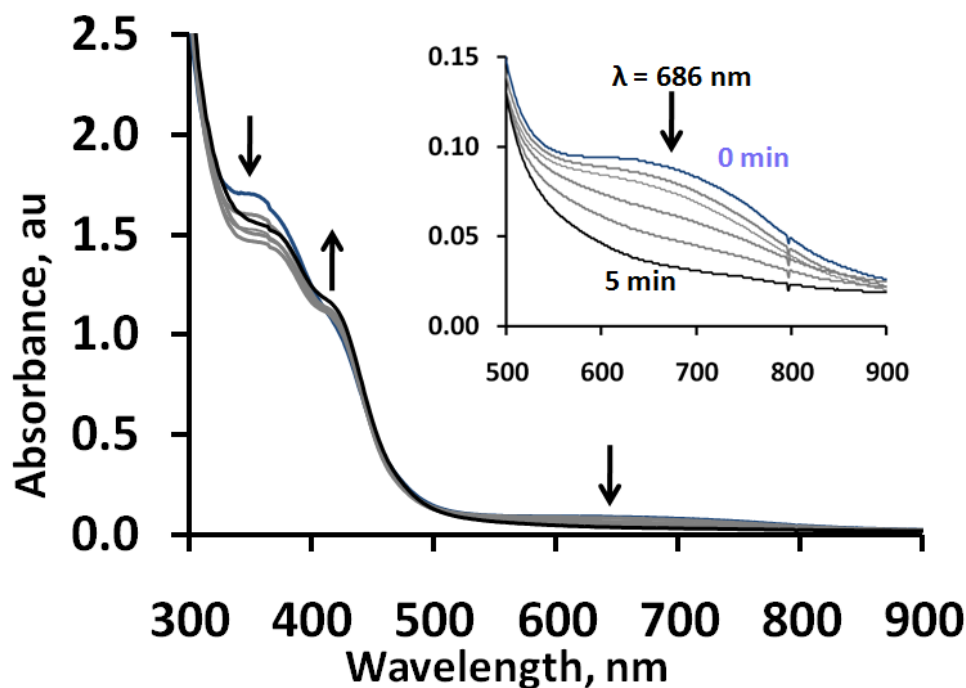


Figure 5.5. Decay spectra of the green reactive intermediate generated from the reaction **6** and *m*-CPBA. Inset: expanded view of 500 – 900 nm showing decay of band at 686 nm.

When 1 equivalent *m*-CPBA is reacted with complex **6** nothing of happens. Interestingly when 2 equivalents of *m*-CPBA are reacted with $[\text{FeCl}(\text{pz}^{\text{Et}}_4\text{lut})][\text{Cl}]$ in CH_2Cl_2 at 0°C a distinct color change is observed as the reaction solution changes from red to pale yellow in color. When monitored by absorption spectroscopy (**Figure 5.6**), the decay of the band at 358 nm is observed upon warming of the solution to room

temperature. While the spectra of the oxidized species is certainly different than that of the starting material (**Figure 5.6**) there are no bands in the characteristic region (600-900 nm) of iron(IV) oxo species despite the change in color to pale yellow upon oxidation. When ≈ 3 equivalents of 9,10-dihydroanthracene are added to the reaction mixture the hydrogen abstraction product anthracene is observed in the GC-MS showing that some conversion does occur ($\approx 17\%$).

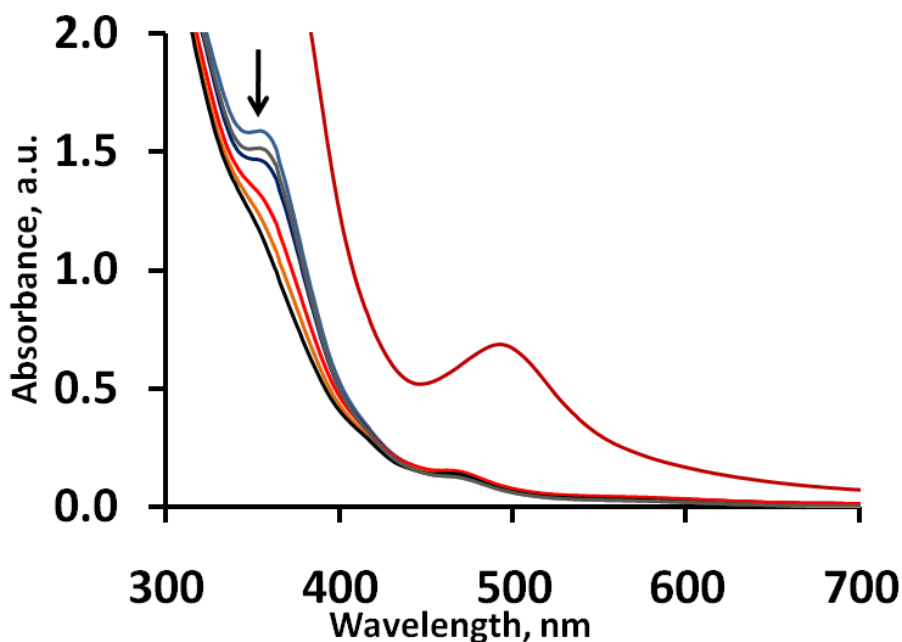


Figure 5.6. Absorption spectrum of the reaction between $[\text{FeCl}(\text{pz}_4\text{Et}_2\text{lut})][\text{Cl}]$ and 2 equivalents *m*-CPBA. Starting material in CH_2Cl_2 is shown on the same plot in brick red.

When excess *m*-CPBA is added to a methanol solution of the complex $[\text{Fe}(\text{Sol})(\text{pz}_4\text{Et}_2\text{lut})][\text{BF}_4]_2$ a color change occurs. However, this change is much slower than either of the other two reactions and the solution does not change to yellow but instead the color disappears. The reaction between **7** and *m*-CPBA occurs much slower even at room temperature compared to the reactions between *m*-CPBA and **1**, **3** and **6**. While the other reaction solutions ($[\text{FeCl}(\text{pz}_4\text{lut})][\text{BAR}^{\text{F}}_4]$ and $[\text{FeCl}([\text{pz}_4\text{Et}_2\text{lut})][\text{Cl}]$)

change color instantly as soon as the oxidant is added even at low temperatures; this reaction occurs slowly within 5 minutes of the addition of oxidant as shown in **Figure 5.7** below. While the solubility has been increased it is difficult to say whether the lifetime of the intermediate species has been increased and further work needs to be done.

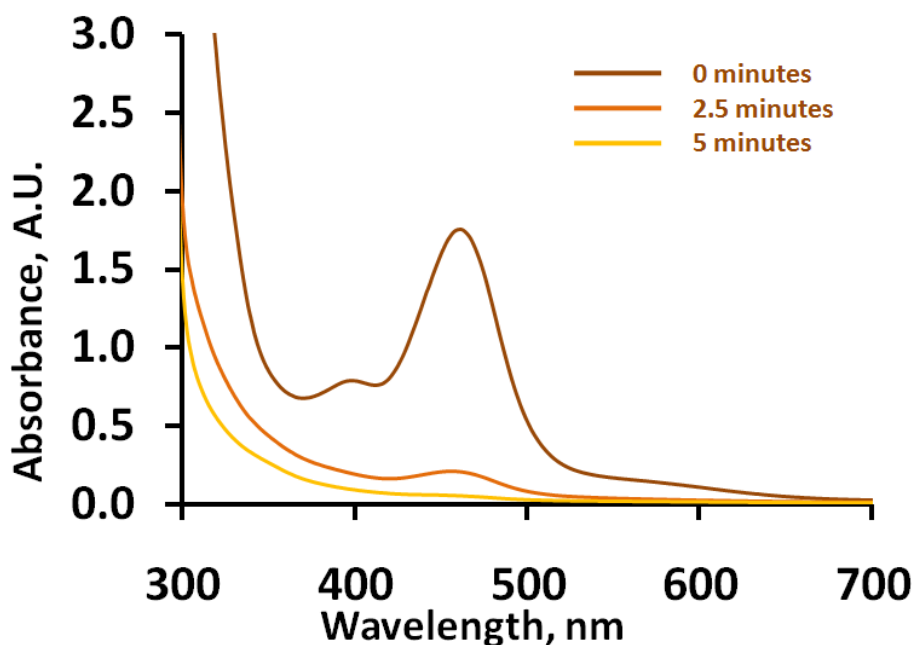


Figure 5.7. Reaction between $[\text{Fe}(\text{Sol})(\text{pz}_4\text{Et}_2\text{lut})][\text{BF}_4]_2$ and excess *m*-CPBA in methanol.

Summary and Conclusions. The reactivity of four new iron(II) complexes has been investigated using absorption spectroscopy to monitor the reactions. Simple axial substitution of tetrafluoroborate salts occurs for only derivatives without 3-methyl pyrazoles possible using $[\text{NEt}_3\text{Bz}][\text{Cl}]$. Reactions between the $[\text{FeCl}(\text{pz}_4\text{lut})][\text{BAr}^{\text{F}}_4]$ complex and strong nucleophilic bases leads to brown insoluble decomposition products which might be due to possible deprotonation of the ligand. In fact reactions between pz_4lut and $^n\text{BuLi}$ followed by quenching with ethyl iodide gives the methyne substituted derivative that when complexed to iron(II) display increased solubility. All newly

synthesized iron(II) complexes display characteristic absorption spectra which allow for easy monitoring by absorption spectroscopy.

After surveying several different oxidants and iron(II) complexes of pz4lut ligands to probe whether any reactive intermediates could be formed, it was found that the combination of *m*-CPBA and [FeCl(pz₄lut)][BAR₄^f] proves the most promising system. In this case a short-lived highly reactive green species is obtained at -30 °C that is capable of converting tri(phenyl)methane to tri(phenyl)methanol. The pz4Et2lut scaffold enjoys increased solubility over the unsubstituted derivative, more over reactions with *m*-CPBA affrds a mixture that is found to convert 9,10-dihydroanthracene to anthracene. Finally, the iron(II) complexes with the pz^{*}₄lut ligand appear unreactive towards chemical oxidants or oxygen atom transfer agents. Clearly further investigations intor reactivity of these complexes are warranted.

Experimental Details

General Considerations. *m*-CPBA, 30 % H₂O₂, THF, Acetonitrile and all transition metal salts were obtained commercially and used as received. Iodosobenzene and [Na][BAR₄^F] were synthesized according to a literature procedure. The synthesis of ligands pz₄lut and pz₄*lut were previously reported in **Chapter 2**. The attempts at oxoferryl generation were performed cooling acetonitrile solutions to -30 °C in a cooling bath and adding an acetonitrile solution containing 2 equivalents of *m*-CPBA. Solvents were dried by conventional procedures and distilled prior to use. Midwest MicroLab, LLC, Indianapolis, Indiana 45250, performed all elemental analyses. Melting point determinations were made on samples contained in glass capillaries using an Electrothermal 9100 apparatus and are uncorrected. ¹H and ¹³C NMR spectra were recorded on a Varian 300 MHz or 400 MHz spectrometer. Chemical shifts were referenced to solvent resonances at δ_H 1.94 and δ_C 1.39 for CD₃CN, δ_H 3.31 and δ_C 49.15 for CD₃OD and δ_H 7.26 and δ_C 77.23 for CDCl₃. UV-visible and NIR spectra were recorded using Shimadzu UV-1600/17pp or Jasco V-570 instruments.

[Fe(THF)(pz₄lut)][BF₄]₂. 0.300 g (0.81 mmol) of pz₄lut in a schlenk flask was dissolved in THF (1 x 10 mL) while 0.276 g (0.82 mmol) of [Fe(H₂O)₆][BF₄]₂ in a separate schlenk flask was dissolved in THF (1 x 10 mL). The pz₄lut solution was transferred via cannula and the flask rinsed with an additional amount of THF (1 x 10 mL) and transferred. A yellow precipitate immediately formed. The THF was filtered off via cannula and the solid was allowed to dry under vacuum 0.281 g (52 %) of a yellow powder. Mp, 300-305 °C decomp. Anal. Calcd. (obsd.) for C₂₃H₂₅B₂F₈FeN₉O: C, 41.05 (40.71); H, 3.74 (3.68); N, 18.73 (18.93).

[Fe(H₂O)(pz^{*}₄lut)][BF₄]₂•THF. 0.250 g (0.52 mmol) of pz^{*}₄lut ligand was added to a 100 mL schlenk flask along with THF (1 x 10 mL) via syringe. To a separate 100 mL schlenk flask was added 0.174 g (0.52 mmol) of [Fe(H₂O)₆][BF₄]₂ along with THF (1 x 10 mL) via syringe. The pz^{*}₄lut solution was transferred via cannula to produce a yellow precipitate immediately. The THF was then filtered off via cannula and the yellow solid washed with Et₂O (3 x 10 mL) and dried under vacuum overnight to give 0.281 g (74 %) of the desired product as a yellow powder. Mp, 315-320 °C decomp. Anal. Calcd. (obsd.) for C₃₁H₄₃B₂F₈FeN₉O₂: C, 46.36 (46.77); H, 5.40 (5.76); N, 15.70 (14.27). μ_{eff} (Evans, CD₃OD, 298 K); 3.05 μ_{B} . ¹H NMR (CD₃CN) δ_{H} 62.79, 45.75, 20.74, 4.97, 3.33, 3.12, -0.85, -3.69. UV-Vis (CH₃CN) λ_{max} , nm (ϵ , M⁻¹, cm⁻¹), 360 (269), 844 (7).

[Fe(CH₃CN)(pz₄lut)][BF₄]₂. 0.103 g (15.0 mmol) of [FeTHF(pz₄lut)][BF₄]₂ was dissolved in acetonitrile (1 x 15 mL). The solution immediately turned deep red/orange in color. Solvents were removed by vacuum distillation to give 0.087 g (89 %) of a deep red/orange solid. X-ray quality crystals were grown by vapor diffusion of THF into a concentrated acetonitrile solution. Mp, 288-290 °C decomp. Anal. Calcd. (obsd.) for C₂₁H₂₀B₂F₈FeN₁₀: C, 39.29 (38.53); H, 3.14 (3.16); 21.82 (19.47). ¹H NMR (CD₃CN) δ_{H} 8.43 (m, 8H), 8.24 (s, 2H), 8.22 (br s, 3H), 6.68 (t, J = 2, 4H), 1.96 (s, 3H). UV-Vis (CH₃CN) λ_{max} , nm (ϵ , M⁻¹, cm⁻¹), 294 (10 750), 292 (7 550), 378 (1 682), 422 (3 200).

[FeCl(pz₄lut)][BAr^F₄]. A solution of 0.350 g (0.60 mmol) of [FeCl(pz₄lut)][Cl] dissolved in 25 mL methanol was combined with a solution of 0.803 g (0.60 mmol) [Na][BAr^F₄] in 15 mL of dichloromethane. Upon mixing an orange/red solution and a white precipitate (NaCl) formed. After stirring for 30 min the colorless insoluble fraction

was removed by filtration. The solvent was then removed by vacuum distillation to give 0.907 g (85 %) of $[\text{Fe}(\text{Cl})(\text{pz}_4\text{lut})][\text{BAr}^{\text{F}}_4]$ as a red/orange solid.

pz₄Et₂lut. To a 250 mL Schlenk flask was added 4.86 g (13.1 mmol) of pz₄lut along with THF (1 x 25 mL). A cold bath was added, and the reaction solution was allowed to equilibrate for approximately 15 minutes. 16.5 mL (26.2 mmol) of ⁿBuLi in hexanes was added to a 25 mL THF solution containing 4.83 g (13.1 mmol) of pz₄lut via syringe and the solution immediately turned dark brown in color. The reaction was allowed to stir at -78 °C for 1 hr, then 3.2 mL (39.3 mmol) of ethyl iodide was added via syringe. After the addition of ethyl iodide, the mixture was slowly warmed to room temperature and was stirred overnight. 250 mL of water was then added and the reaction was extracted with CH₂Cl₂ (3 x 50mL), and the organic fraction was dried over MgSO₄ and concentrated to give a brown oil. The product was eluted on SiO₂ with 1:2 acetone:hexanes (*R*_f = 0.48) to give 4.36 g (78 %) of pz₄Et₂lut as a white powder after removing solvent and after recrystallization from boiling Et₂O. Mp, 109-111 °C. ¹H NMR (CDCl₃) δ_H 7.67 (t, *J* = 8 Hz, 1H, 4-py), 7.58 (dd, *J* = 0.5, 2 Hz, 4H, 3-pz), 7.36 (dd, *J* = 0.5, 2 Hz, 4H, 5-pz), 6.81 (d, *J* = 8, 2H, 3,5-py), 6.24 (dd, *J* = 0.5, 2 Hz, 4H, 4-pz), 3.09 (q, *J* = 7 Hz, 4H, -CH₂), 0.90 (t, *J* = 7 Hz, 6H, -CH₃). ¹³C NMR (CDCl₃) δ_C 157.9, 140.2, 137.8, 130.4, 122.1, 105.8, 84.9, 32.8, 9.0. UV-Vis (CH₃CN) λ_{max}, nm (ε, M⁻¹, cm⁻¹), 294 (10 750), 292 (7 550), 378 (1 682), 422 (3 200).

[FeCl(pz^{Et}₄lut)][Cl]•CH₂Cl₂•H₂O. A stirred solution of 0.400 g (0.93 mmol) of pz₄Et₂lut along in CH₂Cl₂ (10 mL) was transferred via cannula to a stirred solution of 0.118 g (0.93 mmol) of FeCl₂ in MeOH (10 mL). The flask containing pz₄Et₂lut was rinsed with additional CH₂Cl₂ (5 mL) and transferred. Upon mixing, the reaction

solution became deep red in color. After the solution had been stirred for 15 h, the solvent was removed in vacuo to give a deep red solid. Washing with Et₂O (3 x 10 mL), drying under vacuum for 4 h to give 0.437 g (85 %) of [FeCl(pz^{Et}₄lut)][Cl] as a deep red metallic solid. Mp, 160-165 °C decomp. Anal. Calcd. (obsd.) for C₂₄H₃₁Cl₄FeN₉O: C, 43.86 (43.31); H, 4.45 (4.31); N, 19.18 (18.85). ¹H NMR (CD₃OD) δ 7.73 (t, *J* = 9 Hz, 1H), 7.51 (s, 4H), 7.43 (s, 4H), 6.82 (d, *J* = 9 Hz, 2H), 6.24 (s, 4H), 3.01 (q, *J* = 7 Hz, 4H), 0.78 (t, *J* = 7 Hz, 6H). UV-Vis (MeOH) λ_{max}, nm (ε, M⁻¹, cm⁻¹), 294 (10 750), 292 (7 550), 378 (1 682), 422 (3 200).

[Fe(H₂O)(pz₄Et₂lut)][BF₄]₂. A solution of 0.200 g (0.47 mmol) of pz₄Et₂lut in 10 mL THF was added to a stirred solution of 0.158 g (0.47 mmol) [Fe(H₂O)₆][BF₄]₂ in 10 mL of THF and a brown precipitate formed within 30 seconds of stirring. After the mixture had stirred 30 min and the insoluble solid was collected by filtration, and was washed with Et₂O (3 x 10 mL), and was dried under vacuum. The reaction was allowed to stir for 30 minutes, and the solid collected by filtration. The solid was then washed with Et₂O (3 x 10 mL), collected by filtration and allowed to dry under vacuum to give the desired complex 0.192 g (70 %) as a brown/yellow solid. Mp, 170-176 °C. decomp. Anal. Calcd. (Obsd.) for C₂₇H₃₉B₂F₈FeN₉O: C, 49.20 (38.38); H, 5.96 (4.35); N, 19.13 (16.58).

Chapter 6: Boron Complexes of 2,6-dipyrzoly-4-X-Anilines.

Introduction. There is a longstanding interest in developing new brightly-emitting fluorophores for fundamental interest and for a variety of useful applications, from sensors and display technology to biomedical imaging. We recently reported on the synthesis and properties of a series of fluorescent dyes based on the diphenylboron complexes of pyrazolylanilines, or BORAZANs (**Figure 6.1**) of the type $\text{Ph}_2\text{B}(\text{pzAn}^{\text{X}})$ where pz is a pyrazolyl, An is aniline and superscript X is the substituent at the para-

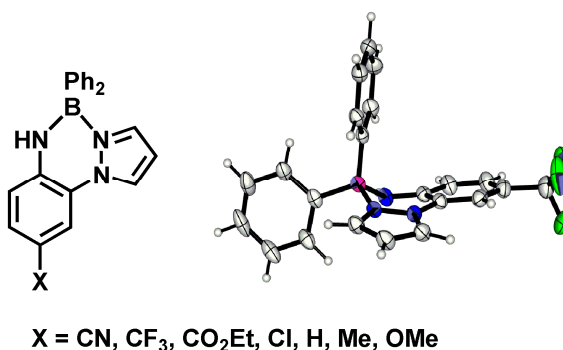


Figure 6.1. The BORAZAN dye framework and representative solid state structure of $\text{Ph}_2\text{B}(\text{pzAn}^{\text{CF}_3})$.

aniline ring. The emission color, intensity, and reactivity of the fluorescent dyes can be tuned in a regular way by varying the para- aniline substituent. For instance, the cyano derivative gave the most intense blue emission ($^{\text{em}}\lambda_{\text{max}}(\text{toluene}) = 452 \text{ nm}$, $\Phi_{\text{F}}(\text{toluene}) = 0.81$) and was the most stable toward solvolysis with protonated solvents such as water or

alcohols. The methoxy derivative gave much less intense yellow green emission ($^{\text{em}}\lambda_{\text{max}}$ (toluene) = 522nm, Φ_{F} (toluene) = 0.07) and readily decomposed in such protic media.

The quantum yields of emission were greatly reduced in Lewis Basic solvents compared to hydrocarbon solvents (and the dyes were also found to undergo rapid dynamic processes giving more symmetric conformations in solution (nominally C_s symmetric) than found in the solid state (C_1 -symmetric)). We conjectured that the dynamic solution processes may be related to the low quantum yield of emission and the high reactivity. That is, if boron-pyrazolyl ring dissociation occurred, the integrity of the dye would be compromised resulting in lower quantum yields and the resulting three-coordinate boron may provide a pathway for degradation. In order to test this hypothesis, we have modified the dye structure by putting an additional pyrazolyl ring at the 6-position of the aniline (**Figure 6.2**). Such a substitution was designed with the intent of kinetically stabilizing the dye by effectively doubling the rate of boron-pyrazolyl bond formation should boron-pyrazolyl dissociation occur in solution. Moreover, with such a

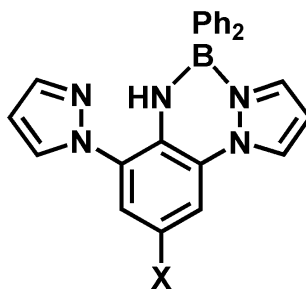
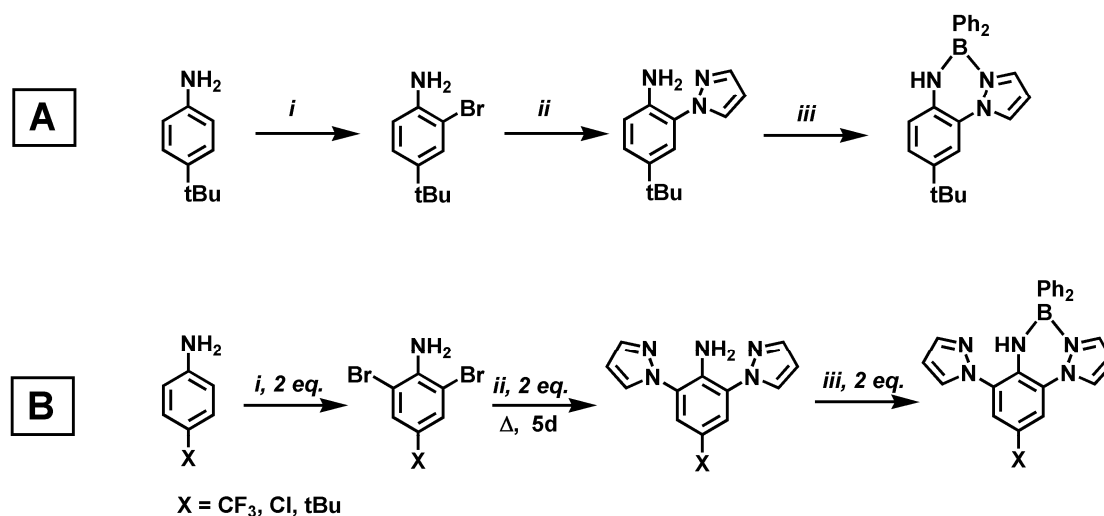


Figure 6.2. General structure of BORAZANs described in this work.

substitution pattern any dynamic processes would be easily detected by NMR, as the pyrazolyl rings would be magnetically inequivalent in a static structure, such as in **Figure 6.2**, but would be equivalent if exchange occurred. We report here on the successful

implementation of this structural modification for enhancing the performance of BORAZAN dyes.

Results & Discussion. The BORAZAN dyes were prepared according to the methods illustrated in **Scheme 6.1**. The compound, $\text{Ph}_2\text{B}(\text{pzAn}^{\text{tBu}})$ (**Scheme 6.1a**) was prepared (for comparison purposes) as described previously for the original BORAZANs: by monobromination of the tert-butyraniline followed by copper- catalyzed N-arylation reaction between pyrazole and 2-bromoaniline via Buchwald^{60a} and Taillefer's^{60b-e} methodology and subsequent reaction of the 2-pyrazolylaniline with triphenylboron. BORAZAN dyes based of the type $\text{Ph}_2\text{B}(\text{pz}_2\text{An}^{\text{X}})$ ($\text{X} = \text{CF}_3$, Cl, ^tBu) were prepared by an analogous route but by first dibromination of the appropriate aniline. The copper-catalyzed coupling reaction required longer reaction times to afford the desired $\text{H}(\text{pz}_2\text{An}^{\text{X}})$ in reasonable yield. The ensuing reaction with triphenylboron provided the desired monoboryl- derivatives with the elimination of benzene.⁶¹ The BORAZANs



Scheme Key: *i*) $(\text{NBu}_4)(\text{Br}_3)$ or Br_2 , 0°C , 2:1 $\text{MeOH}:\text{CH}_2\text{Cl}_2$; *ii*) pyrazole, 4 K_2CO_3 , dimethylethylenediamine, 10 mol% CuI , xylenes, reflux 2d; *iii*) BPh_3 , toluene, reflux 12 h.

Scheme 6.1. Preparation of BORAZAN dyes.

are insoluble in hexanes, those based on $\text{pz}_2\text{An}^{\text{X}}$ are modestly soluble in benzene, and all are soluble in toluene, halocarbons, and polar Lewis basic solvents (THF, CH_3CN , DMF). The compound $\text{Ph}_2\text{B}(\text{pzAn}^{\text{tBu}})$ rapidly decomposes (over the period of minutes) in alcohols, as found previously for $\text{Ph}_2\text{B}(\text{pzAn}^{\text{X}})$ ($\text{X} = \text{Me}, \text{MeO}$), but $\text{Ph}_2\text{B}(\text{pz}_2\text{An}^{\text{X}})$ ($\text{X} = \text{CF}_3, \text{Cl}, \text{tBu}$) persist over days in this type of solvent. In addition, the dipyrazolyl BORAZANs appear indefinitely air stable in the solid or in solution, in stark contrast to their mono-pyrazolyl counterparts which decompose by hydrolysis over time even in the solid state. As further testament to the improved stability of the dyes, the dipyrazolyl derivatives can survive flash chromatography on silica gel, a procedure that immediately annihilates the monopyrazolyl BORAZANs.

Solid State. The molecular structures of four derivatives $\text{Ph}_2\text{B}(\text{pzAn}^{\text{tBu}})$, and $\text{Ph}_2\text{B}(\text{pz}_2\text{An}^{\text{X}})$ ($\text{X} = \text{CF}_3, \text{Cl}, \text{tBu}$) have been determined by single crystal X-ray diffraction. A representative structure of $\text{Ph}_2\text{B}(\text{pz}_2\text{An}^{\text{CF}_3})$ is given in **Figure 6.3**.

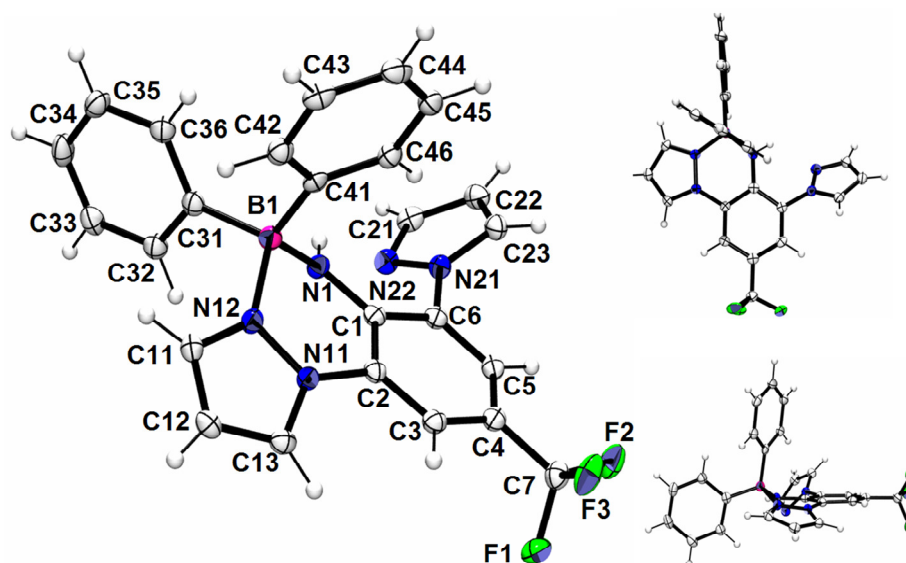


Figure 7.3. Molecular Structure of $\text{Ph}_2\text{B}(\text{pz}_2\text{An}^{\text{CF}_3})$ with atom labeling (left) with alternate views (right). Ellipsoids are shown at the 50% probability level.

Selected intramolecular geometric features of the structurally characterized compounds are summarized in **Table 6.1**. Each of the structurally characterized derivatives possesses C_1 (rather than C_s) symmetry due to puckering of the six-member chelate ring (in a pseudo half-chair conformation), distorted tetrahedral boron, and pyrazolyl ring twisting (best measured by the C(3)C(2)-N(11)N(12) torsion angle of **Figure 6.3**, for instance). As with previously reported members of the BORAZANs, the average B-N distance (1.57 Å) is 0.05 Å shorter than the average B-C distance (1.62 Å) regardless of the substitution pattern along the dye framework. Given the half chair conformation of the chelate ring, the B-C bond of the axial phenyl is detectably longer (1.62-1.64 Å) than that of the equatorial phenyl (1.61-1.62 Å), as found in **Table 6.1**. The longer B-C (axial) bond may presumably arise from its closer proximity to and its participation in an antibonding interaction with the aniline moiety (observed in the HOMO, see Calculations section). Also in each derivative, the B-N(pz) bond is longer (1.61-1.62 Å) than the corresponding B-N (aniline) bond (1.52-1.53 Å), as observed previously and as expected for a dative interaction. The previously reported BORAZANs, exhibited a correlation between intramolecular geometric features and electronic properties of *para*- aniline substituents (delineated by the Hammett parameter, σ_R , for instance). That is, the more electron-withdrawing *para*- aniline substituents gave rise to a greater degree of planarity between the pyrazolyl, aniline, and chelate rings, a result of resonance stabilization that imparts greater “quinoidal” character to the aniline moiety (thereby reducing the stereochemical influence of the aniline nitrogen lone pair). The structural parameters of $\text{Ph}_2\text{B}(\text{pz}_2\text{An}^{\text{CF}_3})$ and $\text{Ph}_2\text{B}(\text{pz}_2\text{An}^{\text{Cl}})$ are in compliance with previous findings, although the correlation is weaker in the current cases. Thus, the aniline nitrogen approaches

Compound	Ph ₂ B(pzAn ^{tBu})	Ph ₂ B(pz ₂ An ^{CF₃})	Ph ₂ B(pz ₂ An ^{Cl})	Ph ₂ B(pzAn ^{tBu})
B-N(1), Å	1.523	1.531	1.522	1.527
B-N(12), pz (Å)	1.612	1.620	1.616	1.605
B-C (ax) (Å)	1.624	1.629	1.635	1.620
B-C (eq) (Å)	1.612	1.619	1.610	1.618
HN-C(1) (Å)	1.368	1.353	1.365	1.371
Σ ∠'s about N(1)	351.57	356.53	356.66	352.69
C(1)-C(2) (Å)	1.410	1.415	1.407	1.402
C(2)-C(3) (Å)	1.395	1.380	1.387	1.400
C(3)-C(4) (Å)	1.386	1.388	1.382	1.389
C(4)-C(5) (Å)	1.405	1.389	1.383	1.399
C(5)-C(6) (Å)	1.377	1.380	1.379	1.386
C(6)-C(1) (Å)	1.401	1.419	1.411	1.414
C(4)-C(7) (Å)	1.530	1.487	---	1.531
C(2)-N(11) (Å)	1.431	1.431	1.430	1.432
C(6)-N(21) (Å)	---	1.423	1.421	1.424
N(1)••N(11) (Å)	2.423	2.439	2.438	2.441
⊥B••(An) ^a (Å)	0.713	0.666	0.702	0.420
(N ₁ BN ₁₂) ^b -(An) (°)	44.71	40.62	40.46	30.51
C(3)C(2)-N(11)N(12) (°)	167.79	169.60	169.21	178.72
C(1)C(2)-N(11)N(12) (°)	16.46	13.81	13.60	7.66
N(11)C(2)-C(1)N(1) (°)	5.70	6.98	4.02	1.88
mpl(B-pz) ^c -(An) (°)	20.60	17.89	16.22	14.06
mpl(pz)-(An) (°)	---	47.73	48.74	49.30
See Figure 1 for atom labeling. Also: pz = pyrazolyl; An = Aniline; (An) = mean plane of C ₆ N aniline ring; mpl(pz) = mean plane of pyrazolyl ring. ^a Distance of normal vector between mean aniline plane and boron. ^b Angle between plane defined by N(1), B(1), N(12) and (An). ^c B-pz = boron-bound pz				

Table 6.1. Selected Bond Distances and Angles for Ph₂B(pzAn^{tBu}), Ph₂B(pz₂An^{CF₃}), Ph₂B(pz₂An^{Cl}), and Ph₂B(pzAn^{tBu}).

planarity ($\Sigma\angle$'s about nitrogen = 357°) in both $\text{Ph}_2\text{B}(\text{pz}_2\text{An}^{\text{CF}_3})$ and $\text{Ph}_2\text{B}(\text{pz}_2\text{An}^{\text{Cl}})$. In $\text{Ph}_2\text{B}(\text{pzAn}^{\text{CF}_3})$ the nitrogen is more pyramidal ($\Sigma\angle$'s about nitrogen = 351°),⁶¹ which provides one indication that replacing an *ortho*-hydrogen with a pyrazolyl has a resonance stabilizing effect. Moreover, the amino-carbon bond N(1)-C(1) distance in $\text{Ph}_2\text{B}(\text{pz}_2\text{An}^{\text{CF}_3})$ (1.353 Å) is shorter than both $\text{Ph}_2\text{B}(\text{pz}_2\text{An}^{\text{Cl}})$ (1.365 Å) and $\text{Ph}_2\text{B}(\text{pzAn}^{\text{CF}_3})$ (1.365 Å) indicative of greater double bond character in the former. The degree of coplanarity between boron-bound pyrazolyl and the aniline rings is best measured by the C(3)C(2)-N(11)N(12) torsion angle of **Figure 6.3** (pyrazolyl ring twisting) since there are a number of ligand distortions that contribute to the dihedral between the mean planes of the two heterocycles, as discussed previously. As such, the degree of coplanarity increases in the order: $\text{Ph}_2\text{B}(\text{pzAn}^{\text{CF}_3})$ (167.9°) < $\text{Ph}_2\text{B}(\text{pz}_2\text{An}^{\text{Cl}})$ (169.2°) < $\text{Ph}_2\text{B}(\text{pz}_2\text{An}^{\text{CF}_3})$ (169.6°). The torsion angles of the latter two are considerably greater (more coplanar) than the corresponding torsion angles involving the free pyrazolyl C(5)C(6)-N(21)N(22) (**Figure 6.3**); $\text{Ph}_2\text{B}(\text{pz}_2\text{An}^{\text{Cl}})$ (131.6°) < $\text{Ph}_2\text{B}(\text{pz}_2\text{An}^{\text{CF}_3})$ (130.1°). Concomitant with the trend of increasing (boron-bound) pyrazolyl-aniline coplanarity, the chelate ring puckering becomes less pronounced. The perpendicular distance between boron and the mean plane of the aniline rings decreases in the order $\text{Ph}_2\text{B}(\text{pzAn}^{\text{CF}_3})$ (0.762 Å) > $\text{Ph}_2\text{B}(\text{pz}_2\text{An}^{\text{Cl}})$ (0.702 Å) > $\text{Ph}_2\text{B}(\text{pz}_2\text{An}^{\text{CF}_3})$ (0.666 Å). Again, the substitution of the *ortho*-hydrogen on aniline for a pyrazolyl ring would appear to diminish the stereochemical influence of the lone pair on the aniline nitrogen, perhaps through resonance stabilization (*vide infra*). The structural effect of *ortho*-pyrazolyl substitution causing greater coplanarity between (boron-bound)pyrazolyl and aniline rings and a lesser chelate ring puckering compared to *ortho*-hydrogen substitution

persists for $\text{Ph}_2\text{B}(\text{pz}_2\text{An}^{\text{tBu}})$ and $\text{Ph}_2\text{B}(\text{pzAn}^{\text{tBu}})$, but these compounds exhibit pronounced flattening of the three fused rings (chelate, pyrazolyl, anilile), an anomalous structural feature compared to all other structurally characterized derivatives. Specifically, the planarity of the aniline nitrogen (sum of angles about N1) increases from 352° for $\text{Ph}_2\text{B}(\text{pzAn}^{\text{tBu}})$ to 353° for $\text{Ph}_2\text{B}(\text{pz}_2\text{An}^{\text{tBu}})$, values that are greater than 344° for $\text{Ph}_2\text{B}(\text{pzAn}^{\text{Me}})$ and even 351° for $\text{Ph}_2\text{B}(\text{pzAn}^{\text{CF}_3})$ but are less than 352° and 353° found for $\text{Ph}_2\text{B}(\text{pz}_2\text{An}^{\text{Cl}})$ and $\text{Ph}_2\text{B}(\text{pz}_2\text{An}^{\text{CF}_3})$, respectively. Similarly, the chelate ring puckering (measured as the perpendicular distance between boron and the mean aniline plane) and pyrazolyl ring twisting (C(3)C(2)-N(11)N(12) torsion, ideally 180° for coplanarity) decreases on traversing from $\text{Ph}_2\text{B}(\text{pzAn}^{\text{tBu}})$ (0.713 \AA , 167.8°) to $\text{Ph}_2\text{B}(\text{pz}_2\text{An}^{\text{tBu}})$ (0.420 \AA , 178.7°); both values are lower (the latter, substantially) than all other structurally characterized derivatives. Given that the electronic properties of a *tert*-butyl substituent are not expected to (and in fact do not, vide infra) deviate significantly from that of a methyl substituent (for instance, compare primitive Hammett parameters, $\sigma_p = -0.09$ for ^tBu , $\sigma_p = -0.06$ for Me),⁶² it is likely that molecular packing influences the intramolecular geometry. For $\text{Ph}_2\text{B}(\text{pz}_2\text{An}^{\text{tBu}})$, the boron-bound pyrazolyl participates in more noncovalent intermolecular interactions than in all other derivatives. As can be seen in **Figure 6.4**, the *tert*-butyl and both the free and boron-bound pyrazolyl groups extensively

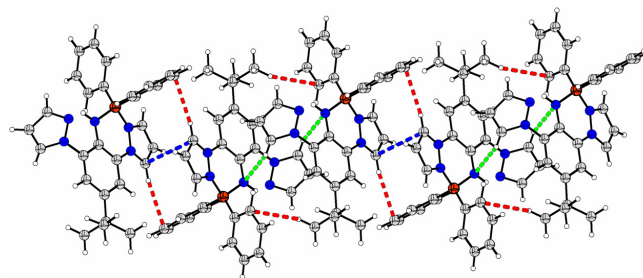


Figure 6.4. Polymeric chain of $\text{Ph}_2\text{B}(\text{pz}_2\text{An}^{\text{tBu}})$ molecules organized along the *a*-axis as a result of π - π (blue dashed lines), CH- π (red dashed lines) and CH-N (green lines).

participate in organizing the supramolecular structure into polymeric chains along the crystallographic *a*-axis. Concerted CH- π (pyrazolyl donor, phenyl acceptor) and π - π (pyrazolyl-pyrazolyl) interactions associate molecules into dimers, in a manner reminiscent of a quadruple phenyl embrace⁶³ or quadruple pyrazolyl embrace.⁶³ The “dipyrazolyl-diphenyl embrace” in the current example is constructed such that there is a π - π interaction between pyrazolyls (blue dashed lines **Figure 6.4**). The centroid-centroid distance of 4.264 Å, the dihedral angle between the mean planes, α , of 0.0°, and the displacement angle, β , (measuring the angle that the centroids of rings are offset from normality) of 28.1° are in the accepted ranges.⁶³ In addition, the CH- π component of the embrace occurs between the acidic hydrogen donor at the 5-position of the pyrazolyl ring and the axial boron-phenyl acceptor. The geometry of the interaction involving C(13)H(13)-centroid[C(3X-3X)] (3.005 Å, 138.0°) is expanded but is still within the accepted range. The dimers are further associated into polymeric chains by weak CH-N interactions that occur between the acidic hydrogen on the 5-position of the pyrazolyl and the aniline nitrogen lone pair of neighboring dimers where the C(23)H(23)-N(1) distance and angle (2.618 Å, 151.8°) are typical for such an interaction. A set of archetypal CH- π interactions⁶⁴ involving the *tert*-butyl hydrogen donors and the equatorial boron-bound phenyl acceptor (C(1X)H(1X)---centroid[C(3X-3X)] = 2.774 Å, 133.9°; red dashed lines above and below the green in **Figure 6.4**) also support the polymeric chain. The supramolecular structure of Ph₂B(pzAn^{tBu}) is that of corrugated sheets (in the bc-plane) composed of three types of noncovalent interactions: a quadruple phenyl embrace involving boron-phenyl groups, CH- π interactions involving *tert*-butyl hydrogen donors and aniline ring acceptors, as well as weak CH- π interactions involving acidic pyrazolyl

hydrogen donors and ‘axial’ boron-bound phenyl acceptors. Since the boron-bound pyrazolyls of other complexes are not involved in as many non-covalent interactions as $\text{Ph}_2\text{B}(\text{pz}_2\text{An}^{\text{tBu}})$ or $\text{Ph}_2\text{B}(\text{pzAn}^{\text{tBu}})$, their metrical parameters may more reliably reflect the intramolecular electronic effects of *para*- aniline substitution than these latter two derivatives.

NMR. The solution NMR spectra of all BORAZANs [either $\text{Ph}_2\text{B}(\text{pzAn}^{\text{X}})$ or $\text{Ph}_2\text{B}(\text{pz}_2\text{An}^{\text{X}})$] clearly show dynamic processes occur such that solution structures appear to have higher than C_1 symmetry, the symmetry obtained from either solid state structural studies or from computational studies (*vide infra*). For instance, only one set of resonances for phenyl ring hydrogens is observed for all the BORAZANs even though, based on the solid state structures, two sets are expected (one set each for ‘axial’ and ‘equatorial’ phenyls). We previously attributed this observation to a low energy ring-flipping process, that was fast on the NMR time-scale even at -80°C in toluene- d_8 , a process we still favor after considering the results of variable temperature NMR studies on the $\text{Ph}_2\text{B}(\text{pz}_2\text{An}^{\text{X}})$ series of compounds which showed only one set of phenyl hydrogen resonances at -80°C . With the $\text{Ph}_2\text{B}(\text{pz}_2\text{An}^{\text{X}})$ series ($\text{X} = \text{CF}_3, \text{Cl}, \text{tBu}$), variable temperature studies also indicate that exchange occurs between otherwise inequivalent boron-bound and ‘free’ pyrazolyl rings. A portion of the ^1H NMR spectra of $\text{Ph}_2\text{B}(\text{pz}_2\text{An}^{\text{tBu}})$ in the region showing the resonance(s) for the hydrogen(s) at the 4-position of the pyrazolyl at various temperatures is shown as a representative example in **Figure 6.5**. At -80°C there are two resonances for 4-pyrazolyl hydrogens at 5.94 and at 5.36 ppm. Comparisons of chemical shifts of the 4-pyrazolyl hydrogen resonances in $\text{Ph}_2\text{B}(\text{pz}_2\text{An}^{\text{tBu}})$ with those of the free ligands $\text{H}(\text{pzAn}^{\text{tBu}})$ ($\delta_{\text{H}} = 6.11$) $\text{H}(\text{pz}_2\text{An}^{\text{tBu}})$ ($\delta_{\text{H}} =$

6.12) and the monopyrazolyl derivative $\text{Ph}_2\text{B}(\text{pzAn}^{\text{tBu}})$ ($\delta_{\text{H}} = 5.53$) establish that the lower field resonance is due to the free pyrazolyl while the higher field resonance is for the boron-bound resonance. On warming to 0°C there is a constant upfield shift in both

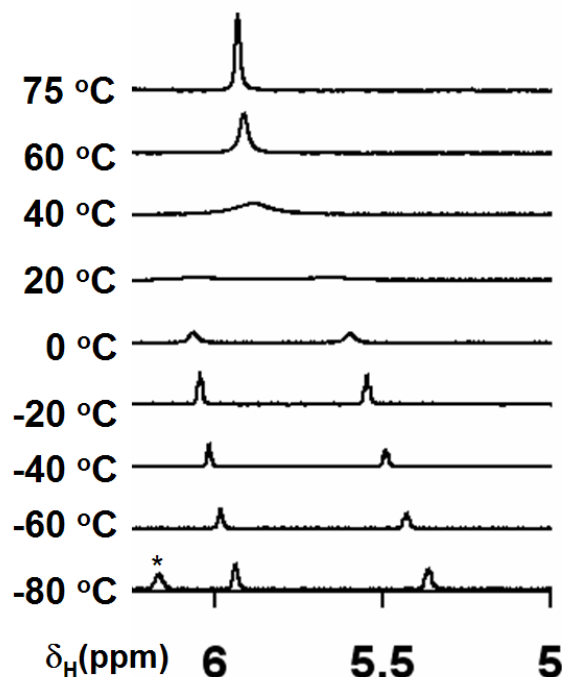


Figure 7.5. The 4-pyrazolyl region of the ^1H NMR spectra for a toluene- d_8 solution of $\text{Ph}_2\text{B}(\text{pz}_2\text{An}^{\text{tBu}})$ acquired at various temperatures. The (*) indicates the resonance for resonances. Above 0°C the resonances broaden and coalesce at 30°C , and above the coalescence temperature the single exchange-averaged resonance sharpens. The activation barriers for (and, hence, the rate of) exchange varies in a regular way with the electron-donating character of the *para*-aniline substituent, as summarized in **Table 6.2**. The more electron-donating substituent gives rise to lower activation barriers and faster rates of exchange. As the activation barrier for exchange falls in line with the expected bond strength of a B-N dative interaction,⁶⁵ the mechanism for pyrazolyl exchange, presumably, involves pyrazolyl bond dissociation, as in **Figure 6.6**. In this context

Compound	T _c (K)	$\Delta\delta$ (Hz) ^a	k _c (s ⁻¹) ^b	ΔG^\ddagger (kcal/mol) ^c
Ph ₂ B(pz ₂ An ^{CF₃})	343	132	586.46	15.8
Ph ₂ B(pz ₂ An ^{Cl})	318	152	675.32	14.5
Ph ₂ B(pz ₂ An ^{tBu})	303	232	1030.75	13.6

^aChemical shift difference in the absence of exchange ^brate constant at coalescence temperature $k_c = \pi\Delta\nu(2)^{-1/2}$. ^c $\Delta G^\ddagger = 4.57(T_c)[10.32 + \log(T_c/k_c)]$ as in reference 68.

electron-withdrawing *para*-aniline substituents render the aniline nitrogen electron-deficient and the nitrogen lone pair is less able to stabilize three-coordinate boron by conjugation with the empty p-orbital on boron. The effect is to induce more Lewis acidic boron and more stable boron-pyrazolyl bonds.

Computational Studies. To facilitate the ensuing discussion of the electronic properties of the BORAZANs, density functional calculations (B3LYP/6-31G*, SPARTAN06)⁶⁶ were performed the free ligands H(pzAn^{tBu}), H(pz₂An^X), and the boron derivatives, Ph₂B(pz_nAn^X) (n = 1,2; X = CF₃, Cl, ^tBu), using Ab Initio (HF/321-G) energy-minimized structures. The HOMO and LUMO for representative ligands, H(pz_nAn^{CF₃}) (n = 1, 2) and their corresponding BORAZANs Ph₂B(pz_nAn^{CF₃}) (n = 1, 2) are given in **Figure 6.7**. A comparison of energy levels for a more extensive set of frontier orbitals [LUMO(+4) to HOMO(-4)] for the remaining compounds are provided in **Figure 6.7**. For all, the HOMO is mainly the non-bonding representation of the aniline-centered pi-system, encompassing the aniline's nitrogen-centered lone pair. There is also a significant (pi-antibonding) contribution from the *para*-aniline substituent's orbitals to the HOMO. Following the convention established from the

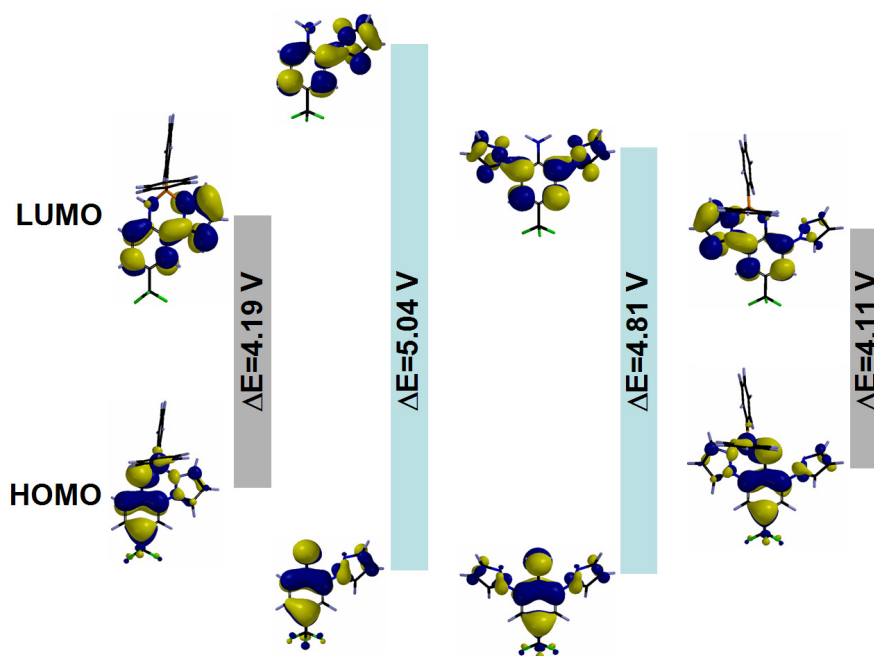


Figure 6.7. HOMO (bottom) and LUMO (top) for (from left to right): $\text{Ph}_2\text{B}(\text{pzAn}^{\text{CF}_3})$, $\text{H}(\text{pzAn}^{\text{CF}_3})$, $\text{H}(\text{pz}_2\text{An}^{\text{CF}_3})$, $\text{Ph}_2\text{B}(\text{pz}_2\text{An}^{\text{CF}_3})$ from density functional calculations (B3LYP/6-31G*). Vertical scale represents relative energy. Gas phase HOMO-LUMO gap energy (ΔE) from calculations is given for ligands (blue) and BORAZANs

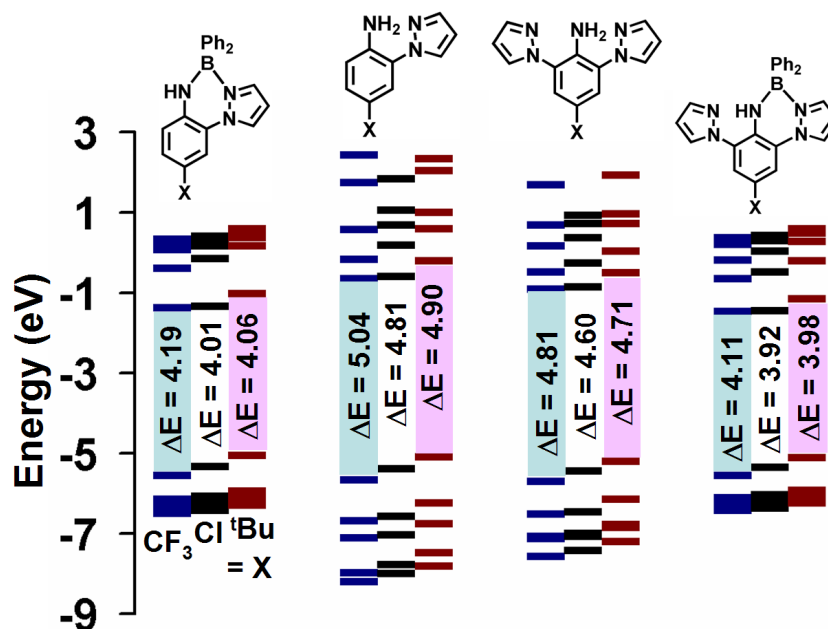


Figure 6.8. Comparison of the energy levels of frontier orbitals [LUMO(+4) to HOMO(-4)] for $\text{H}(\text{pz}_n\text{An}^X)$ ($n = 1, 2$) and corresponding BORAZANs $\text{Ph}_2\text{B}(\text{pz}_n\text{An}^X)$ ($n = 1, 2$) where $X = \text{CF}_3$, Cl, and $t\text{Bu}$ for each compound type.

seminal work of Kasha and Rawls on the photophysics of aniline derivatives,⁶⁷ it is convenient to refer to the HOMO (and other frontier orbitals containing significant contributions from the conjugated aniline lone pair) as a π_L (pi-lone-pair) to provide a distinction from a pure π orbital. Deviations from aniline non-planarity such as twisting of the H_2N -aryl moiety about C-N bond (or other distortions) change the photophysics of the molecule by affording more non-bonding character to the nitrogen lone pair. The LUMO of each compound is π^* in character and spans the pi-systems of both the aniline and the pyrazolyl rings with only a small contribution from the aniline nitrogen's conjugated p-orbital. For the $H(pz_nAn^X)$ ($n = 1,2$) ligands, the HOMO(-4) to HOMO(-1) orbitals are π -bonding, the virtual orbitals LUMO (+1) to LUMO(+3) are π^* anti-bonding, while the LUMO(+4) and higher are σ^* anti-bonding. In the $Ph_2B(pz_nAn^X)$ ($n = 1,2$), orbital contributions from the diphenylboron moiety distinguish the BORAZANs from the ligands. The HOMO(-1) to HOMO(-4), are essentially four linear combinations of boron-phenyl π -orbitals; the next-lowest pzAn-based π_L -orbital is HOMO(-5). The corresponding four π^* orbitals include contributions from both the pzAn and diphenylboryl moieties and constitute the virtual orbitals LUMO(+1) to LUMO(+5).

Examination of the relative energies of the frontier orbitals for the twelve compounds in **Figure 6.8** reveals a number of trends. When comparing the relative energy of the HOMO of a given $H(pzAn^X)$ ligand with that for its corresponding BORAZAN (**Figures 6.7 and 6.8**), the latter is destabilized owing to an antibonding pi-interaction between the boron-bound carbons and the aniline nitrogen's p-orbital that is not present in the former. There is a stabilization of the HOMO with an increase in electron-withdrawing character of the aniline's *para*- substituent. On replacing the ortho-

hydrogen with a pyrazolyl, there is also a small stabilization of the HOMO that arises in an expected fashion owing to the increase in conjugation with the pi-system of the new pyrazolyl group. This increase in conjugation for the dipyrazolyl system causes a significant stabilization of the LUMO, which results in an overall smaller HOMO/LUMO energy gap compared to the monopyrazolyl systems. As with the mono-pyrazolyl systems the destabilization of the HOMO is greater than the stabilization of the LUMO on changing *para*-aniline substituents, which provides an additional basis for tuning the electronic properties of the BORAZAN dyes. It is important to note that the *tert*-butyl substituent affords molecular orbitals in the expected energy range, thus, as was addressed in the structural discussion, hence, the anomalous structural behavior of derivatives with this substituent is not predicted to be electronic in origin, based on calculations.

Electrochemistry. As aniline derivatives are well known electron donors BORAZAN derivatives were previously found to be electroactive, the electrochemistry of CH₃CN solutions of the new ligands and BORAZANs were examined by cyclic voltammetry. The electrochemical data are collected in **Table 6.3** while representative voltammograms for H(pz₂An^{CF₃}) and Ph₂B(pz₂An^{CF₃}) are found in **Figure 6.9**. All compounds exhibited irreversible oxidation, where the reported potentials are those for the anodic wave observed at a scan rate of 0.100 V/s; the cathodic wave is either absent or noticeably less intense than expected. For each series of ligands and BORAZANs, the oxidation becomes more favorable with increasing electron donating character of the *para*- aniline substituent, in accord with the calculations that show a destabilization of the HOMO for this substitution and with previous findings. Thus, for the BPh₂(pz₂An^X)

Compound	Oxid. (V)	Red. (V)	Ref
H(pzAn ^{CF₃})	1.23	---	2
H(pzAn ^{Cl})	1.01	---	2
H(pzAn ^{tBu})	0.88	---	2
H(pz ₂ An ^{CF₃})	1.41	-2.60	b
H(pz ₂ An ^{Cl})	1.24	-2.50	b
H(pz ₂ An ^{tBu})	1.01	---	b
Ph ₂ B(pzAn ^{CF₃})	1.04	-2.39	2
Ph ₂ B(pzAn ^{Cl})	0.84	-2.41	2
Ph ₂ B(pzAn ^{tBu})	0.74	-2.64	b
Ph ₂ B(pz ₂ An ^{CF₃})	1.13	-2.43	b
Ph ₂ B(pz ₂ An ^{Cl})	1.10	-2.58	b
Ph ₂ B(pz ₂ An ^{tBu})	0.86	-2.65	b

^aVersus Ag/AgCl scan rate of 100 mV/s in CH₃CN with NBu₄(PF)₆ as supporting electrolyte. ^bThis work

Table 6.3. Summary of Electrochemical Data for H(pzAn^X), H(pz₂An^X) ligands (X = CF₃, Cl, ^tBu) and their diphenylboron derivatives.

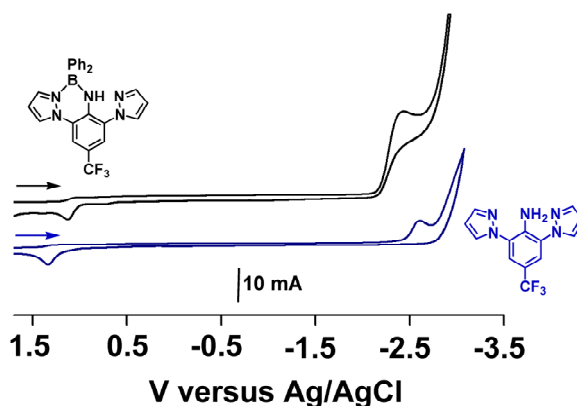


Figure 6.9. Cyclic Voltammograms (100 mV/s) of CH₃CN solutions of H(pz₂An^{CF₃}) (blue, bottom) and Ph₂B(pz₂An^{CF₃}) (black, top) with NBu₄PF₆ as supporting

series, the oxidation potentials decrease $X = {}^t\text{Bu}$ ($E_{\text{pa}} = 0.86 \text{ V}$) $< X = \text{Cl}$ ($E_{\text{pa}} = 1.10 \text{ V}$) $< X = \text{CF}_3$ ($E_{\text{pa}} = 1.13 \text{ V}$). Also in agreement with calculations and earlier results, the oxidations of the BORAZAN complexes are more favorable than those for the free ligands because there is a destabilization of the HOMO brought about by antibonding interactions with the σ - orbitals of the boron-bound carbons. The dipyrazolyl derivatives (both free ligands and BORAZAN complexes) are more difficult to oxidize than the mono pyrazolyl analogues. Thus, the oxidation potentials for the series $\text{Ph}_2\text{B}(\text{pz}_2\text{An}^X)$ [$X = \text{CF}_3$ (1.13 V), Cl (1.10 V), ${}^t\text{Bu}$ (0.86 V)] are higher than the corresponding potentials for the $\text{Ph}_2\text{B}(\text{pzAn}^X)$ series [$X = \text{CF}_3$, (1.04 V), Cl (0.84 V), ${}^t\text{Bu}$ (0.74 V)]. While this result is surprising on first inspection, considering the expected inductive effects of replacing hydrogen with a more electron-donating pyrazolyl, this trend was correctly predicted by the calculations, which showed that the origin is due to stabilization of the HOMO via conjugation with the pi-orbitals of the second pyrazolyl.

Electronic Spectra. The electronic (absorption/emission) spectra of the newly prepared $\text{H}(\text{pz}_n\text{An}^X)$ ligands and $\text{Ph}_2\text{B}(\text{pz}_n\text{An}^X)$ ($n = 1,2$; $X = \text{CF}_3$, Cl, ${}^t\text{Bu}$) compounds parallel those of the previously reported mono-pyrazolyl ($n = 1$; $X = \text{CF}_3$, Cl) derivatives. A summary of the electronic properties are collected in **Table 6.4**. An overlay of the absorption spectra for $\text{H}(\text{pz}_n\text{An}^{\text{CF}_3})$ ligands and $\text{Ph}_2\text{B}(\text{pz}_n\text{An}^{\text{CF}_3})$ ($n = 1,2$) is provided in **Figure 6.10** for reference. The electronic absorption spectrum of each $\text{H}(\text{pz}_n\text{An}^X)$ ($n = 1,2$) ligand consists of three bands for π - π^* transitions⁶⁶; one high- intensity, high-energy band at ca. 230 nm ($\epsilon \approx 20,000$), a second less intense band at ca. 250 ($\epsilon \approx 7000$) nm (in some cases this band occurs as a shoulder to the high-energy band), and a low-energy, low-intensity band for the π_{L} - π^* (HOMO-LUMO) transition above about 300 nm

	Electronic Absorption	Emission	
Compound	$\lambda_{\max}^{\text{abs}}$ (nm), ϵ ($\text{M}^{-1}\text{cm}^{-1}$)	$\lambda_{\max}^{\text{em}}$ (nm)	$\Phi_{\text{F}}(\text{toluene})$, $\Phi_{\text{F}}(\text{CH}_3\text{CN})$
H(pzAn ^{CF₃})	234 (21000), 259 (8600), 305 (3700)	---	---
H(pzAn ^{Cl})	233 (24,000), 255 (9,600), 317 (4,700)	---	---
H(pzAn ^{tBu})	234 (35649), 305 (7510)	---	---
H(pz ₂ An ^{CF₃})	241 (7900), 265 (1900), 317 (1600)	---	---
H(pz ₂ An ^{Cl})	240 (37219), 265 (6923), 329 (6553)	---	---
H(pz ₂ An ^{tBu})	246 (17824), 316 (6995)	---	---
Ph ₂ B(pzAn ^{CF₃})	248 (31000), 288 (13000), 358 (4700)	468	0.63, 0.49
Ph ₂ B(pzAn ^{Cl})	249 (32000), 289 (7800), 375 (6600)	481	0.44,
Ph ₂ B(pzAn ^{tBu})	245 (21607), 371 (3251)	495	0.33, 0.03
Ph ₂ B(pz ₂ An ^{CF₃})	252 (30000), 292 (6500), 323 (6400)	474	0.75, 0.55
Ph ₂ B(pz ₂ An ^{Cl})	251 (26767); 297 (2629); 388 (5460)	493	0.53,
Ph ₂ B(pz ₂ An ^{tBu})	247 (28505), 380 (5706)	502	0.46, 0.16

Table 6.4. Electronic properties of H(pz_nAn^X) and Ph₂B(pz_nAn^X) (n = 1,2; X = CF₃, Cl, ^tBu) compounds from spectroscopic measurements.

($\epsilon \approx 3000$). As indicated from the calculations, the energies of all the absorption bands of the dipyrazolyl derivatives are red-shifted with respect to the monopyrzazolyl derivatives. With the BORAZANs, each band undergoes both hyper- and bathochromic

shifts a new high energy band (presumably for the π - π^* transitions involving the boron-phenyl groups) appears as a shoulder near 200 nm.

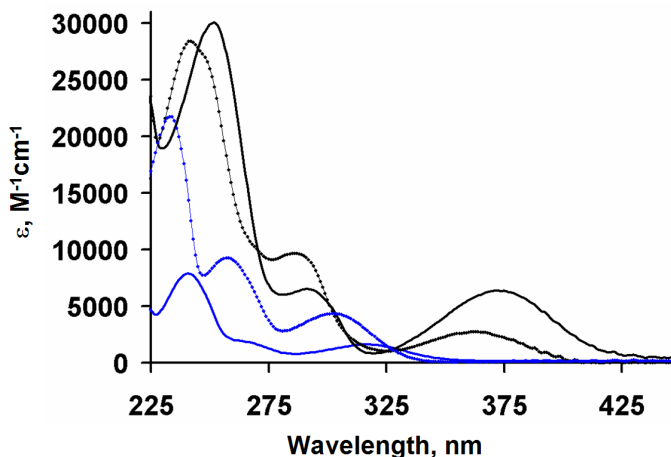


Figure 6.10. Overlay of electronic absorption spectrum of $\text{H}(\text{pzAn}^{\text{CF}_3})$ (dotted blue line), $\text{H}(\text{pz}_2\text{An}^{\text{CF}_3})$ (solid blue line), $\text{Ph}_2\text{B}(\text{pzAn}^{\text{CF}_3})$ (dotted black line), and $\text{Ph}_2\text{B}(\text{pz}_2\text{An}^{\text{CF}_3})$ (solid black line) in CH_2Cl_2 .

The ligands are not emissive under irradiation with UV-light but the BORAZANs exhibit intense emission (either in the solid state or in hydrocarbon or halocarbon solution) that varies from blue for derivatives with electron-withdrawing trifluoromethyl *para*- aniline substituents to green for the *tert*-butyl derivatives (**Figure 6.11**). Previous excited-state lifetime measurements established the fluorescent nature (ns lifetimes) of emission. As with the previously reported mono-pyrazolyl derivatives $\text{Ph}_2\text{B}(\text{pzAn}^{\text{X}})$ ($\text{X} = \text{CN}, \text{CF}_3, \text{CO}_2\text{Et}, \text{Cl}, \text{Me}, \text{OMe}$), the emission of the di-pyrazolyl derivatives $\text{Ph}_2\text{B}(\text{pz}_2\text{An}^{\text{X}})$ ($\text{X} = \text{CF}_3, \text{Cl}, \text{}^t\text{Bu}$) exhibit a regular red-shift of emission with increasing electron-donating character of the *para*- aniline substituent. Thus, the emission maximum of $\text{Ph}_2\text{B}(\text{pz}_2\text{An}^{\text{X}})$ occurs at 474, 493, and 505 nm for $\text{X} = \text{CF}_3, \text{Cl}, \text{}^t\text{Bu}$, respectively. The quantum yields of emission diminish regularly along the series $\text{X} = \text{CF}_3, \text{Cl}, \text{}^t\text{Bu}$ (0.75, 0.53, 0.46

respectively) in accord with the energy gap law which indicates that quantum yields for emission will decrease with lower energy emission.⁶⁷ After considering the implications of the energy gap law, there is a remarkable improvement in the quantum yields of emission of $\text{Ph}_2\text{B}(\text{pz}_2\text{An}^{\text{X}})$ ($\text{X} = \text{CF}_3$, Cl, ^tBu) versus the corresponding mono-pyrazolyl derivatives $\text{Ph}_2\text{B}(\text{pzAn}^{\text{X}})$. Despite the fact that di-pyrazolyl derivatives $\text{Ph}_2\text{B}(\text{pz}_2\text{An}^{\text{X}})$ ($\text{X} = \text{CF}_3$, Cl, ^tBu) exhibit red-shifted emission compared to the corresponding mono-pyrazolyl derivatives $\text{Ph}_2\text{B}(\text{pzAn}^{\text{X}})$, the former enjoy a 10-20% increase in fluorescence quantum yield (**Table 6.4**) with respect to the latter. Since the Stokes shift ($6000 \pm 500 \text{ cm}^{-1}$) is slightly smaller for the dipyrazolyl derivatives compared to that observed for the mono- pyrazolyl derivatives (Stokes shift $6400 \pm 500 \text{ cm}^{-1}$), we tentatively attribute the improvement in quantum yield to the kinetic stabilization of the dye framework brought about by the additional pyrazolyl (increasing the amount of chelated boron).

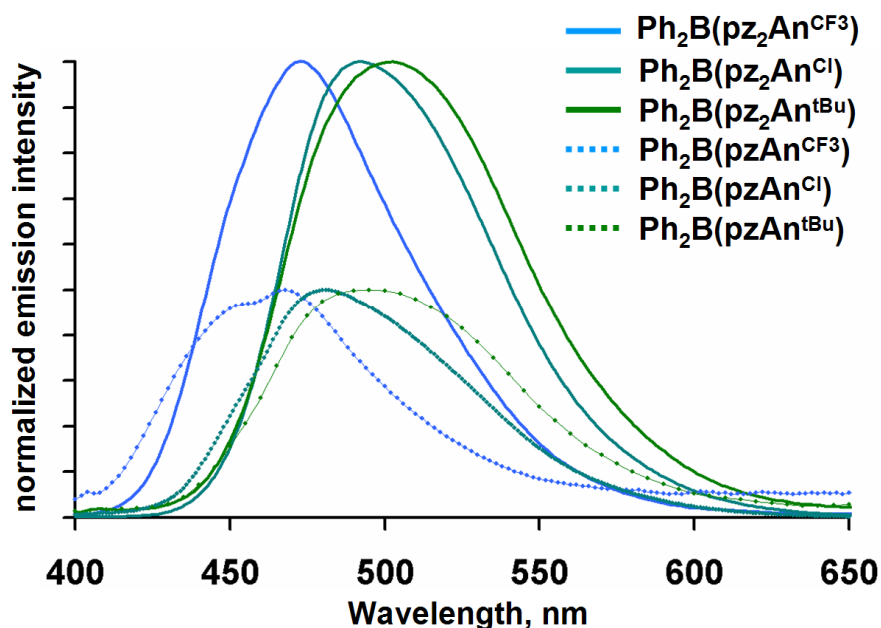


Figure 6.11. Overlay of normalized emission spectra of $\text{Ph}_2\text{B}(\text{pz}_2\text{An}^{\text{X}})$ (solid lines) and $\text{Ph}_2\text{B}(\text{pzAn}^{\text{X}})$ (dashed lines, arbitrarily set to half-intensity of dipyrazolyl derivatives) where ($\text{X} = \text{CF}_3$, blue; Cl, cyan; ^tBu , green).

Conclusions. Three examples of 2,6-dipyrzolyylanilnes $H(pz_2AnX)$ ($X = CF_3, Cl, ^tBu$) have been prepared by exploiting copper-catalyzed amination reactions between pyrazole and 2,6-dibromoaniline. The reaction chemistry of these derivatives with triphenylboron afforded $Ph_2B(pz_2An^X)$ with chelated diphenylboryl moieties, as indicated from X-ray structural studies. The *tert*-butyl derivative exhibits a highly-organized supramolecular structure that is very different than other structurally related compounds of this class. In $Ph_2B(pz_2An^{tBu})$, the boron-bound pyrazolyl is involved in a concerted set of non-covalent CH- π and π - π interactions termed the “dipyrzolyl diphenyl embrace”, that is structurally similar to the known quadruple phenyl or quadruple pyrazolyl embrace. These new highly emissive compounds exhibit a number of adventitious properties compared to the first generation of BORAZAN fluorescent dyes, $Ph_2B(pzAn^X)$, that have only one pyrazolyl group on the heterocyclic ligand scaffold. The emission is color tunable from blue for the derivative with an electron-withdrawing $-CF_3$ *para*-aniline substituent to the green for the related *tert*-butyl substituent. Even though the emission of the di-pyrazolyl derivatives is lower energy than those of the mono-pyrazolyl analogues, the former displays higher luminescence quantum yields than the latter. Moreover, the di-pyrazolyl derivatives enjoy a significant increase in stability towards solvolysis than the mono-pyrazolyl derivatives. Both of the above properties are thought to arise from a kinetic stabilization of the dye framework since the additional pyrazolyl leads to an increase in the rate of boron-pyrazolyl bond formation and should dissociation occur. In fact, such dissociation was easily detected by variable temperature NMR spectroscopic studies of toluene solutions of C_1 -symmetric $Ph_2B(pz_2An^X)$ since the resonances for ‘free’ and boron-bound pyrazolyis undergo exchange. The rates of boron-pyrazolyl dissociation decrease (hence,

the stability of the chelate ring increases) in the order ${}^t\text{Bu} > \text{Cl} > \text{CF}_3$, an order that may be indicative of the anticipated (in)ability of the aniline to stabilize a three-coordinate boron by conjugation between the aniline lone pair and the empty p-orbital on boron.

General Procedure for Ligand Syntheses. A mixture of the desired dibromoaniline (1 equiv), pyrazole (2.4 equiv), K_2CO_3 (4.2 equiv), 40 mol % N,N'-dimethylethylenediamine, and 10-20 mL of *p*-xylenes were degassed by three freeze/pump/thaw cycles. Under a nitrogen blanket, 10 mol % CuI was added, and the resulting mixture was subject to two more freeze/pump/thaw cycles. The mixture was heated under nitrogen at reflux for 5 days (until starting materials were no longer detected by TLC). After cooling to room temperature, 100 mL of H_2O and a few crystals of EDTA- H_4 were added to facilitate workup. The mixture was then extracted with three 100 mL portions of CH_2Cl_2 which were combined and dried over $MgSO_4$ and filtered. The solvent was removed by rotary evaporation to leave oily residues. The residues were purified by column chromatography by using 4:1 hexanes:ethyl acetate as the eluent for all cases (R_f ca. 0.4, SiO_2 plate), except for the trifluoromethyl derivative, for which 1:1 hexanes:dichloromethane was the eluent (R_f ca. 0.4, SiO_2 plate). After column chromatography, all products were initially isolated as oils but could be crystallized by layering dichloromethane solutions with hexanes.

H(pz₂An^{CF₃})₃. With 5.17 g (16.2 mmol) 2,6-dibromo-4-trifluoromethyl-aniline and 2.65 (39 mmol) pyrazole, 1.70 g (36 %) of H(pz₂An^{CF₃})₃ was obtained as a white crystalline solid. Mp, 89-91 °C. Anal. Calcd. (found) for $C_{13}H_{10}F_3N_5$: C, 53.24 (53.48); H, 3.44 (3.23); N, 23.88 (24.05). 1H NMR (C_6D_6) δ_H 7.50 (d, J = 1.7 Hz, 2H), 7.09 (s, 2H), 6.88 (dd, J =2.5 Hz, 2H), 6.64 (s, 2H), 5.98 (t, J =2.2 Hz, 2H). ^{13}C NMR (C_6D_6) δ_C 140.93, 139.77, 130.00, 127.09, 126.45, 119.49, 117.48, 117.04, 106.79. UV-vis (CH_2Cl_2) λ_{max} , nm (ϵ , $M^{-1} cm^{-1}$) 241 (7893), 267 (1794), 317 (1602).

H(pz₂An^{Cl}). With 5.90 (20.6 mmol) 2,6-dibromo-4-chloro-aniline and 3.38 g (49.6 mmol) pyrazole, 0.661 g (12 %) of H(pz₂An^{Cl}) was obtained as white crystalline blocks. Mp, 104-105 °C. Anal. Calcd. (found) for C₁₂H₁₀ClN₅: C, 55.50 (55.22); H, 3.88 (3.53); N, 26.97 (27.14). ¹H NMR (C₆D₆) δ_H 7.51 (d, *J*=1.6 Hz, 2H), 6.94 (dd, *J*= 0.6, 2.5 Hz, 2H), 6.83 (s, 2H), 6.19 (s, 2H), 5.99 (t, *J*=2.1 Hz, 2H). ¹³C NMR (C₆D₆) δ_C 140.89, 135.68, 129.87, 128.16, 127.93, 122.68, 120.10. UV-Vis (CH₂Cl₂) λ_{max}, nm (ε, M⁻¹ cm⁻¹) 240 (37219), 265 (6923), 329 (6553).

H(pz₂An^{tBu}). With 9.50 g (31 mmol) 2,6-dibromo-4-tertbutyl-aniline and 5.08 g (74.6 mmol) pyrazole, 4.78 g (55 %) of H(pz₂An^{tBu}) was obtained as a brown crystalline solid. Mp, 112-114 °C. Anal. Calcd. (found) for C₁₆H₁₉N₅: C, 68.30 (68.55); H, 6.81 (7.09); N, 24.89 (24.62). ¹H NMR (C₆D₆) δ_H 7.63 (d, *J*=1.7 Hz, 2H), 7.24 (d, *J*=2.4 Hz, 2H), 7.08 (s, 2H), 6.12 (t, *J*=2.0 Hz), 5.75 (s, 2H), 1.09 (s, 9H). ¹³C NMR (C₆D₆) δ_C 141.19, 139.89, 135.71, 130.48, 128.50, 121.36, 106.94, 34.26, 31.64. UV-vis (CH₂Cl₂) λ_{max}, nm (ε, M⁻¹ cm⁻¹) 245 (32,251), 371 (4,853). Emission (nm, CH₂Cl₂) λ_{max}, 495.

General Procedure for Syntheses of Diphenylboron Derivatives. Under nitrogen, an equimolar mixture of triphenylboron and the desired 2,6-di(pyrazolyl)aniline in 20-30 mL of toluene were heated at reflux overnight. After cooling, solvent was removed by vacuum distillation to leave a glassy residue. Next, 25 mL of dried hexanes were added, and the mixture was heated under nitrogen with stirring to leave the desired compound as a powder. After cooling to room temperature, the mixture was separated by cannula

filtration. The insoluble component was dried under vacuum. Additional crops of the BORAZAN could be obtained from the hexane-soluble components after concentration and cooling to give a precipitate that is collected by filtration and dried, as above.

Ph₂B(pz₂An^{CF₃})₃. A mixture of 0.501 g (1.7 mmol) H(pz₂An^{CF₃}) and 0.428 g (1.7 mmol) BPh₃ afforded 0.586 g (82 %) of Ph₂B(pz₂An^{CF₃})₃ as a colorless solid. Mp, 173-174 °C decomp. Anal. Calcd. (found) for C₂₅H₁₉BF₃N₅: C, 65.67 (65.33); H, 4.19 (3.92); N, 15.32 (15.01). ¹H NMR (300 MHz, C₆D₆, 22°C): δ = 7.50 (m, 5H, *o*-Ph and H₅-pz free), 7.36 (d, *J* = 2 Hz, 1H, H₅-pzB), 7.27 (m, *J* = 8 Hz, 4H, *m*-Ph), 7.16 (m, *J* = 7, 1 Hz, 2H, *p*-Ph), 7.03 (s, 1H), 6.89 (br d, *J* = 2 Hz, 2H, H₃-pzB + NH), 6.72 (s, 1H), 6.29 (d, *J* = 3 Hz, 1H, H₃-pz free), 5.92 (pseudo t, *J* = 2 Hz, 1H, H₄-pz free), 5.46 (pseudo t, *J* = 3 Hz, 1H, H₄-pzB) ppm. ¹H NMR (400 MHz, C₇D₈, 20°C): δ = 7.49 (s, 1H, H₅-pz free), 7.42 (d, *J* = 8 Hz, 4H, *o*-Ph), 7.34 (s, 1H, H₅-pzB), 7.22 (t, *J* = 8 Hz, 4H, *m*-Ph), 7.13 (t, *J* = 8 Hz, 2H, *p*-Ph), 7.04 (s, 1H), 6.91 (d, *J* = 2 Hz, 1H), 6.89 (d, *J* = 2.1 Hz, 1H, H₃-pzB), 6.79 (s, 1H), 6.43 (s, 1H), 6.29 (d, *J* = 3 Hz, 1H, H₃-pz free), 5.95 (pseudo t, *J* = 2 Hz, 1H, H₄-pz free), 5.48 (pseudo t, *J* = 3 Hz, 1H, H₄-pzB) ppm. ¹H NMR (400 MHz, C₇D₈, 80°C): δ = 7.35 (br m), 7.24 (br s), 7.17 (br m), 7.09 (br m), 7.00 (br s), 5.84 (br s). ¹³C NMR (75 MHz, C₆D₆, 22°C): δ = 141.21, 140.60, 135.25, 133.30, 129.49, 127.75, 127.18, 126.86, 122.49, 119.15, 112.31, 107.01, 106.80 ppm. ¹¹B NMR (128 MHz, C₆D₆, 22°C): δ = -0.3 (ω_{1/2} = 233 Hz) ppm. ¹⁹F NMR (376 MHz, C₆D₆, 22°C): δ = -60.6 S-9 ppm. UV/Vis (nm, CH₂Cl₂): λ_{max}, (ε, M⁻¹cm⁻¹) = 252 (30,016), 292 (6,500), 372 (6,359). Emission (nm, CH₂Cl₂) λ_{max} = 474.

Ph₂B(pz₂An^{Cl}). A mixture of 0.253 g (0.96 mmol) H(pz₂An^{Cl}) and 0.278 g (1.1 mmol) BPh₃ afforded 0.256 g (69 %) of Ph₂B(pz₂An^{Cl}) as a green solid. Mp, 227-230 °C decomp. Anal. Calcd. (found) for C₂₄H₁₉BClN₅: C, 68.03 (68.22); H, 4.52 (4.42); N, 16.53 (16.81). ¹H NMR (300 MHz, C₆D₆, 22°C): δ = 7.61 (m, 4H), 7.37 (t, *J* = 7 Hz, 1H), 7.29 (t, *J* = 1 Hz, 1H), 7.27 (t, *J* = 2 Hz, 1H), 7.25 (d, *J* = 1 Hz, 2H), 6.99 (d, *J* = 16 Hz, 2H), 6.83 (s, 1H), 6.49 (d, *J* = 19 Hz, 2H), 6.03 (br s, 1H), 5.56 (br s, 1H) ppm. ¹H NMR (400 MHz, C₇D₈, 50°C): δ = 7.42 (m, 4H), 7.34 (br s, 1H), 7.22 (t, *J* = 7 Hz, 4H), 7.16 (t, *J* = 1 Hz, 1H), 7.12 (t, *J* = 1 Hz, 1H), 6.90 (d, *J* = 1.9 Hz, 2H), 6.71 (br s, 1H), 6.42 (br s, 2H), 5.95 (br s, 1H), 5.58 (br s, 1H) ppm. ¹H NMR (400 MHz, C₇D₈, 50°C): δ = 5.93 (m, 4H), 5.74 (t, *J* = 7 Hz, 5H), 5.68 (t, *J* = 3 Hz, 1H), 5.66 (t, *J* = 3 Hz, 1H), 5.64 (t, *J* = 2 Hz, 1H), 5.41 (br s, 2H), 5.16 (br s, 3H), 4.35 (br s, 3H) ppm. ¹³C NMR (75 MHz, C₆D₆, 22°C): 137.61, 134.04, 128.21, 127.25, 117.43, 107.26 ppm. ¹¹B NMR (128 MHz, C₆D₆, 22°C): δ = -0.3 (ω_{1/2} = 292 Hz) ppm. UV/Vis (nm, CH₂Cl₂): λ_{max}, (ε, M⁻¹cm⁻¹) = 251 (26,768); 289sh (3,528); 388 (5,460). Emission (nm, CH₂Cl₂) λ_{max} = 493.

Ph₂B(pz₂An^{tBu}). A mixture of 0.50 g (1.7 mmol) H(pz₂An^{tBu}) and 0.50 g (2.1 mmol) of BPh₃ afforded 0.58 g (74 %) of Ph₂B(pz₂An^{tBu}) as a green solid. Mp, 217-219 °C. Anal. Calcd. (found) for C₂₈H₂₈BN₅: C, 75.51 (75.25); H, 6.34 (6.52); N, 15.72 (15.98). ¹H NMR (300 MHz, C₆D₆, 22°C): δ = 7.61 (d, *J* = 6.8 Hz, 4H), 7.28 (t, *J* = 7.2 Hz, 4H), 7.19 (m, 2H), 7.01 (br s, 2H), 6.76 (br s, 2H), 6.55 (s, 1H), 6.04 (br s, 2H), 5.59 (br s, 2H), 1.06 (s, 9H) ppm. ¹H NMR (400 MHz, C₇D₈, 20°C): δ = 7.50 (m, 4H), 7.22 (t, *J* = 7 Hz, 5H), 7.14 (t, *J* = 1 Hz, 1H), 7.12 (t, *J* = 2 Hz, 1H), 7.09 (br s, 3H), 6.49 (br s, 1H), 5.87 (d, *J* = 92 Hz, 4H), 1.07 (s, 9H) ppm. ¹H NMR (400 MHz, C₇D₈, 80°C): δ = 7.39 (m, 4H),

7.34 – 7.10 (m, 9H), 6.24 (br s, S-10 2H), 5.91 (br s, 3H), 3.51 (br s, 1H), 1.06 (s, 9H) ppm. ^{13}C NMR (75 MHz, C_6D_6 , 22°C): 136.86, 136.17, 134.13, 128.18, 127.08, 107.08, 34.19, 31.64 ppm. ^{11}B NMR (128 MHz, C_6D_6 , 22°C): $\delta = -0.1$ ($\omega_{1/2} = 529$ Hz) ppm. UV/Vis (nm, CH_2Cl_2): λ_{max} , (ϵ , $\text{M}^{-1}\text{cm}^{-1}$) = 247 (28,505), 380 (5,706). Emission (nm, CH_2Cl_2) $\lambda_{\text{max}} = 502$

Chapter 7: Nickel Complexes of a New NN Pincer Ligand.

Introduction. Over the course of the past decade there has been a surge in the research dealing with “pincer” type ligands (**Figure 7.1**). As the surge in research has continued; the focus has shifted from mere curiosity and chemically interesting species to these complexes having specific applications in catalysis, synthesis as well as materials science.⁷⁰ Only recently has the non-innocent redox behavior of these ligands been considered a source of the fascinating chemistry performed by some of these species.⁷¹ Some of the unique electro- and photochemical properties of these “pincer” ligands and their transition metal complexes has been highlighted in the work done by the Peters, Mindiola and Milstein groups.^{72a-f} While transition metals are the most heavily studied both main group (Al, Ge) and late transition (Rh, Pd, Re, Ir) metals all have been reported.¹

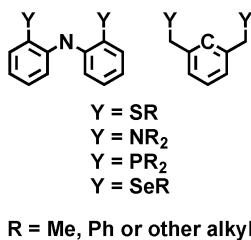


Figure 7.1. Commonly studied “pincer” type ligands.

Generally speaking, there are symmetric pincer type ligands as well as unsymmetrical pincer type ligands; with the symmetric type being the more commonly studied. **Figure 7.1** (above) displays the commonly reported symmetric type pincer

ligands: YCY and YNY. Where $Y = SR, NR_2, PR_2, S_R$; where $R =$ alkyl group and Y can be any combination of the two.⁷⁰ The electronic properties as well as sterics of the ligand can be tuned by varying the Y as well as R group on the ligand. One of the lesser reported type of pincer ligands (which will be the focus of this work reported here) is that of the symmetric NNN type where all three donors are nitrogen based which is introduced below.⁷⁰

Recently our group has reported on the NNN type pincer ligand shown below in **Figure .2** and its Rhenium(I) analogue that showcases its unique electronic properties.⁷³ This previously unreported system has numerous advantages owing to its nearly limitless and easily-accessible structural variants. Doing so allows one to take advantage of the well known fact that arylamines are electron donors.⁷⁴ Which allows for the tuning of electronic properties through the para-position as well as tuning of sterics without affecting electronics through substitution along the pyrazole backbone.⁷⁵

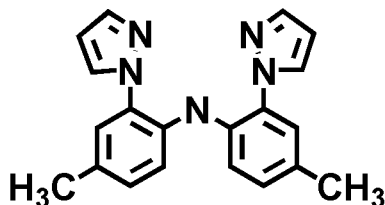
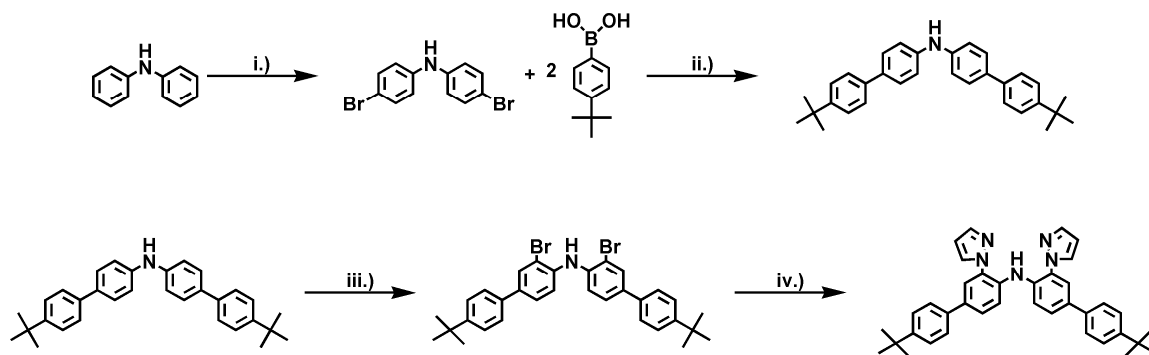


Figure 7.2. Recently reported NNN type pincer ligand by our group.

We were interested to see if it was possible to substitute at the *para* position of the phenyl ring using simple reaction chemistry instead of using commercially available phenyls and if so what are its properties with nickel complexes. This chapter reports the details on the synthesis of a new ligand prepared by simple reaction chemistry and its properties with nickel(II) and nickel(III) complexes characterized by spectroscopic methods such as electrochemistry, EPR and absorption spectroscopy.

Results. The synthesis of the new ligand **L₁** utilizes both Suzuki coupling⁷ and copper(I) catalyzed coupling reaction first reported by Taillifer⁷⁷ and Buchwald⁷⁸ between aryl bromides (prepared from literature procedures)⁶⁰ and pyrazole as shown below in **Scheme 7.1**. The first steps include bromination of diphenylamine with *n*-bromosuccinimide and then utilizing Sonogashira coupling with 4-*tert*-butylphenyl boronic acid to obtain the desired diarylamine as a colorless solid in moderate yield (~ 53 %) after chromatographic separation on silica gel with 4 : 1 hexane : dichloromethane. The desired ligand can then be synthesized via a direct two step synthesis by first *ortho*-bromination of the starting material with two equivalents of Br₂ in MeOH/CH₂Cl₂. The bromination reaction proceeds quickly (within 1 h) to give NH(*o*-Br-4-*t*bu-biphenyl)₂. Finally, the copper(I) catalyzed reaction, using a large excess of pyrazole (3.5 eq) and K₂CO₃ (3.5 eq) to obtain the desired product in moderate yields (~ 50 %) after chromatographic separation on silica gel with 8 : 1 hexanes : ethyl acetate.



Scheme 7.1. Synthetic route to new ligand **L₁**. i.) 2 NBS, 0 °C, DMF, 3 h. ii.) 5 mol % Pd(0), 2 M aq. K₂CO₃, toluene/MeOH, 80 °C, 20 h. iii.) 2 Br₂, 1:1 MeOH/CH₂Cl₂, 0 °C, 1 h. iv.) 3.5 HPz, 3.5 K₂CO₃, 10 mol % CuI, 40 mol % DMED, xylenes, 3 d.

The nickel(II) (charge neutral) complex was synthesized according the **Scheme 7.2** shown below and were characterized in solution. Starting with nickel(II) chloride

hexahydrate in methanol and refluxing it with two equivalents of ligand (**L**₁) for 30 minutes and then adding two equivalents of tetra-ethyl ammonium hydroxide afforded the desired nickel(II) complex as a brown air stable solid almost quantitatively (~ 94 %) after gravity filtration and rinsing with methanol (3 x 10 mL). Unfortunately, numerous attempts to grow x-ray quality crystals (from layering a concentrated dichloromethane solution with hexanes) failed and at best would give frail needles that would decompose once removed from the solvent. Further attempts at crystallization included the synthesis of the nickel(III) derivative by oxidation of the nickel(II) complex with ferrocenium tetrafluoroborate (~ 70 %) as green air stable solid (**Scheme 7.2**). However, numerous attempts to crystallize this derivative also failed; only yielding frail needles that diffracted poorly.

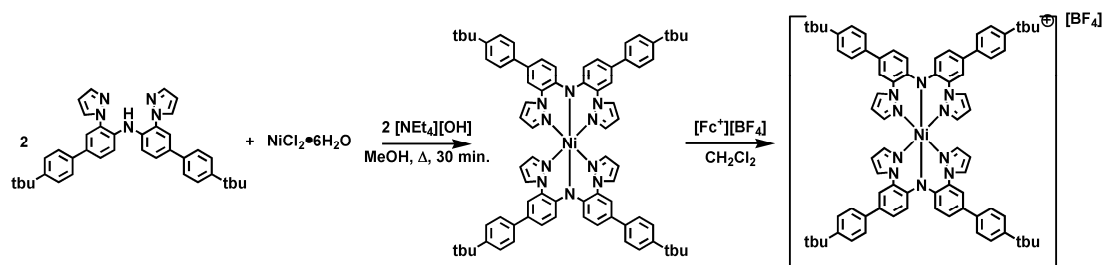


Figure 7.2. Synthesis of nickel(II) and nickel(III) complexes.

Electrochemistry. Diarylamines are well known to exhibit irreversible oxidation waves; as evident in a number of nitroxide•ONAr₂ radical species produced by chemical oxidation reactions in work by Rajca and others⁷⁹ More recently, our group has prepared a series of non-innocent di(2-pyrazolyl)amine pincer ligands that have varying substituents in the *para*- position of the aryl ring. We have shown that the oxidation potential (while irreversible) can be varied in a regular way by changing the inductive

power (i.e. electron withdrawing or electron donating groups) of the *para*- substituent on the aryl ring as shown below in **Figure 7.3**. Interestingly, it was found that substitution along the pyrazole backbone has little to no effect on the oxidation potential regardless of the substituent.

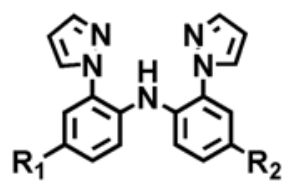
 $R_1 = R_2 = \text{Me}$ $R_1 = R_2 = 4\text{-tbu-phenyl}$ $R_1 = R_2 = \text{CF}_3$	R_1	R_2	$E_{pc} \text{ (V)}$
	Me	Me	1.03 ^a
	<i>t</i> -tbu-phenyl	<i>t</i> -tbu-phenyl	1.08, 1.46 ^b
	CF ₃	CF ₃	1.52 ^a

Figure 7.3. Electrochemical data of substituted di(2-pyrazolyl)amine pincer ligands. ^a = unpublished reference, ^b = this work.

The cyclic voltammogram for both **L**₁ and [Ni(**L**₁)₂] (in CH₂Cl₂) is shown below in **Figure 7.4**. As can be seen from the figure below; the ligand shows two irreversible oxidations and no reductions (not shown) in the negative potential range ($E_{pc} = 1.08 \text{ V}$ and 1.46 V vs Ag/AgCl) which fit in with the expected electron donating capabilities of the phenyl rings being less electron donating than the methyl groups but more so than the trifluoromethyl groups.⁸⁰ A second oxidation also becomes visible as expected due to the second set of aryl rings attached at the *para* position of the aryl rings.

Upon complexation to nickel(II) the electrochemical behavior of the ligand changes as these oxidation waves become quasi reversible in nature and also experience a shift to a lower oxidation potential. A quasi reversible Ni^{II/III} oxidation wave also becomes evident upon scanning the potential range. The $E_{1/2}$ for the Ni^{II/III} is 0.27 V vs Ag/AgCl; while the values for the next two ligand based oxidations are as follows: 0.52

V and 1.41 V vs Ag/AgCl. Compared to the previously reported nickel(II) complex by our group these oxidations are less favorable than $-\text{CH}_3$, $-\text{CH}_3$ (1st oxidation $E_{1/2} = 0.18$ V, 2nd oxidation $E_{1/2} = 0.45$ V) but more favorable than $-\text{CF}_3$, $-\text{CF}_3$ ($E_{1/2} = 0.79$ V, 1.06 V).⁵ Again, the shift in values is to be expected considering the poorer electron donating ability of the phenyl rings compared to the methyl groups but stronger than trifluoromethyl groups in the *para* position.

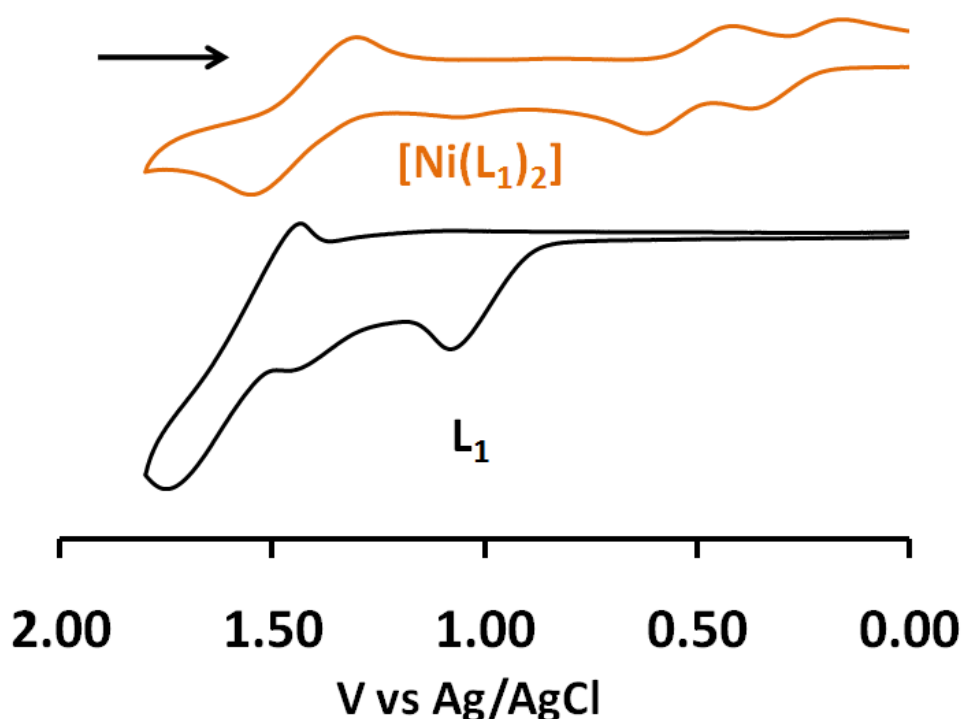


Figure 7.4. Cyclic voltammograms of L_1 (bottom) and $[\text{Ni}(\text{L}_1)_2]$ (top) in CH_2Cl_2 with 0.1 mM $[\text{NBu}_4][\text{PF}_6]$; scan rate = 100 mvs.

Solution Properties. The electronic absorption spectrum for the free ligand (L_1 in CH_2Cl_2) is shown below in **Figure 7.5**; while the spectra for both the $[\text{Ni}(\text{L}_1)_2]$ and $[\text{Ni}(\text{L}_1)_2][\text{BF}_4]$ (in CH_2Cl_2) are shown below in **Figure 7.6 & 7.7**. The spectrum of L_1 contains two transitions most likely and $\pi-\pi^*$ in nature based on our previous studies^{ref} (228 (70 910), 238sh (55 825), 342 (54 089)).

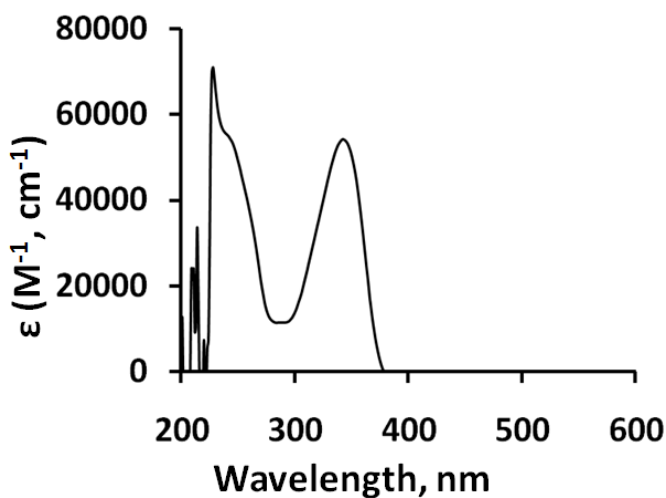


Figure 7.5. Electronic absorption spectrum of L_1 in CH_2Cl_2 .

Upon complexation to Nickel(II) an orange solid is formed to give $[Ni(L_1)_2]$. The complex is orange in solution and is intensely colored and gives solution magnetic moments substantially higher ($4.43 \mu_B$) than the spin only value ($2.82 \mu_B$). Two other complexes synthesized by our group; the $-CH_3$, $-CH_3$ substituted derivative as well as the $-CH_3$, $-CN$ derivative also give solution magnetic moments higher than the spin only value ($4.52 \mu_B$ for $-CH_3$, $-CH_3$ and $4.17 \mu_B$ for $-CH_3$, $-CN$). The increased solution magnetic moment is most likely due to a significant amount of orbital contribution. Therefore using the modified formula to account for orbital contributions $\mu_{eff} = \sqrt{4s(s+1) + l(l+1)}$ the expected value becomes $4.52 \mu_B$ which agrees well with the experimental values obtained for all complexes.

The absorption spectrum of $[Ni(L_1)_2]$ in dichloromethane shows four bands; two of high intensity ($\epsilon > 50,000 \text{ M}^{-1} \text{ cm}^{-1}$) and two lower intensity bands ($\epsilon < 1000 \text{ M}^{-1} \text{ cm}^{-1}$) 250 (105 523), 416 (98 257), 532 (815), 853 (255) similar to other nickel(II) complexes.⁸¹

While the metal is high spin d^8 and has $d \leftarrow d$ electronic transitions they are most likely obscured by the high intensity bands centered at 853 nm (which is most likely a low energy $\pi^* \leftarrow \pi$ transition) and 532 nm. If the intensities of the bands are ignored and the transitions are assumed to be obscured by the low energy $\pi^* \leftarrow \pi$ transition the ligand field parameter Δ_o can still be calculated based on the position of the lowest energy band at 853 nm giving a $\Delta_o \approx 11,723 \text{ cm}^{-1}$.

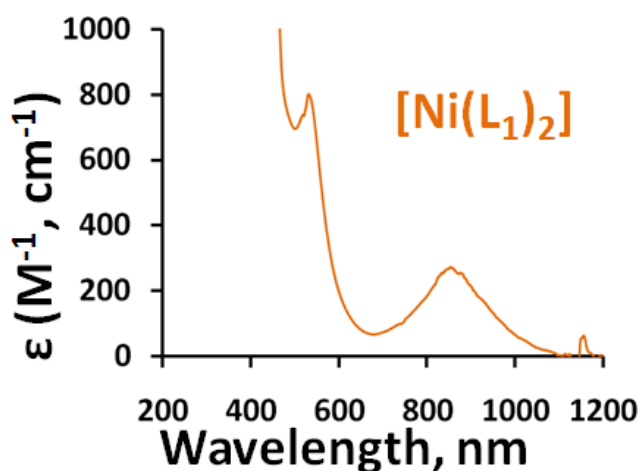


Figure 7.6. Absorption spectra of $[\text{Ni}(\text{L}_1)_2]$ in CH_2Cl_2 .

Upon oxidation of $[\text{Ni}(\text{L}_1)_2]$ with ferrocenium tetrafluoroborate the color of the complex changes from orange to an intense dark green. The complex gives a solution magnetic moment consistent with the oxidized product and three unpaired electrons of $3.97 \mu_B$ which agrees well with the spin only moment of $3.87 \mu_B$. The presence of nickel(III) is also confirmed by EPR measurements obtained at 70 K and 10 K as discussed below. The electronic absorption spectra of the oxidized species shows presence of three additional bands similar to other nickel(III) complexes¹³: two of low intensity ($\epsilon < 6,000 \text{ M}^{-1} \text{ cm}^{-1}$) and three high intensity ($\epsilon > 10,000 \text{ M}^{-1} \text{ cm}^{-1}$); 254 (96

293), 350sh (34 580), 404 (55 203), 602 (5 854), 725sh (5 804), 854 (16 210). While the nickel(III) center is confirmed no transitions for the $d \leftarrow d$ transitions are directly observed and are mostly likely obscured by the high intensity transitions at 602 nm, 725 nm, and 548nm which are most likely charge transfer in nature (ligand to metal) based on intensity.

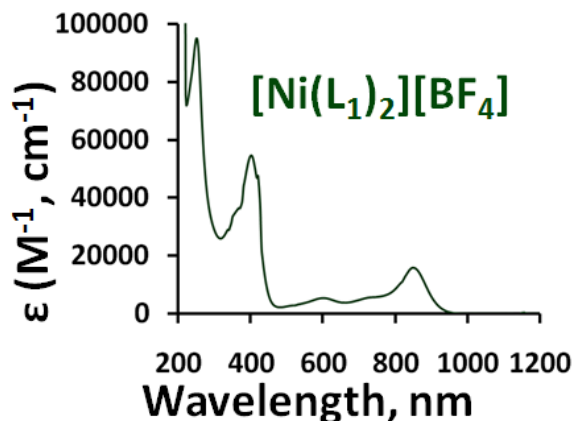


Figure 7.7. Electronic absorption spectra of $[\text{Ni}(\text{L}_1)_2][\text{BF}_4]$ in CH_2Cl_2 .

Electron Paramagnetic Resonance. The frozen glass EPR spectra were obtained as additional confirmation of the spin states. The complex $[\text{Ni}(\text{L}_1)_2]^{2+}$ is EPR silent as expected due to the large zero field splitting as is common for high spin d^8 non kramer's ($S = 1$) complexes giving further support to the Ni^{2+} oxidation state despite the large magnetic moment. The EPR spectra of $[\text{Ni}(\text{L}_1)_2][\text{BF}_4]$ was obtained as a frozen glass (70 K, 10 K) in CH_2Cl_2 . The spectra for $[\text{Ni}(\text{L}_1)_2][\text{BF}_4]$ at 70 K and 10 K are shown below in **Figure 7.8** each consisting of three components at 70 K and 10 K signals belonging to the same component are marked with asterisks (red, black) while the impurity is marked with blue. The high temperature component (black) experiences a

decrease in signal intensity upon cooling to 10 K while the low temperature component (red) experiences an increase upon cooling to 10 K. Both the high and low temperature

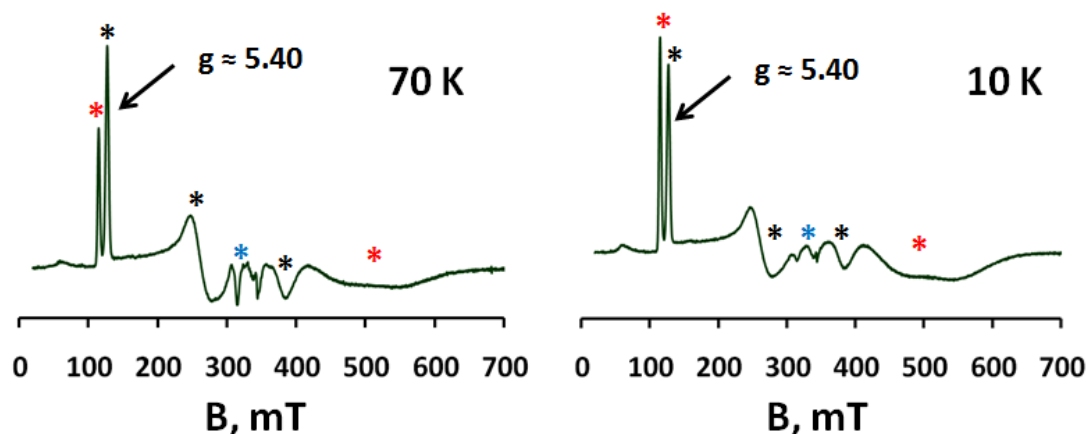


Figure 7.8. EPR spectra of Frozen glass solutions 70 K (left) and 10 K (right) of $[\text{Ni}(\text{L}_1)_2][\text{BF}_4]$.

components belong to the same species which is the desired Ni^{3+} . However, due to the symmetry of the ligand the D value becomes negative therefore flipping the ground and excited states so that the $m_s = +3/2$ becomes the ground state and $m_s = +1/2$ is the low lying excited state which is easily populated at 70 K and therefore explains the decrease in signal intensity at 10 K and the signal increase for the $m_s = +3/2$ component at 10 K. This is further supported by simulations of each component at 70 K and 10 K shown below in **Figure 7.9**. Finally, the experimental spectrum at 70 K can be simulated by using the average parameters of $g_{\parallel} = 2.093$, $g_{\perp} = 2.089$, $E/D = 0.241$, $D = -10 \text{ cm}^{-1}$ shown below in **Figure 7.10** further supporting a $m_s = +1/2$ and $m_s = +3/2$ component.

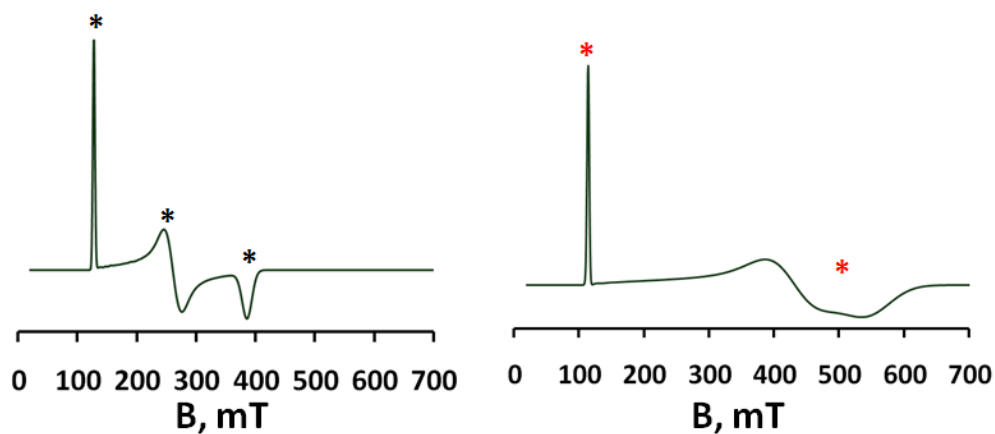


Figure 7.9. Simulations of $m_s = +1/2$ component with $g_{\parallel} = 2.093$, $g_{\perp} = 2.073$, $E/D = 0.237$, -10 cm^{-1} (left) and $m_s = +3/2$ component with $g_{\parallel} = 2.093$, $g_{\perp} = 2.105$, $E/D = 0.245$, $D = -10 \text{ cm}^{-1}$ (right).

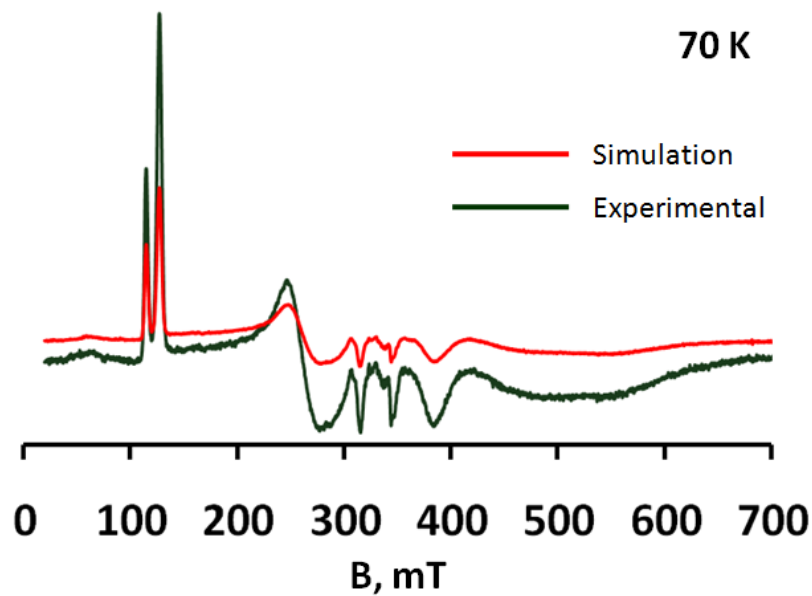


Figure 7.10. Simulated and experimental spectra of $[\text{Ni}(\text{L}_1)_2][\text{BF}_4]$ at 70 K using average parameters.

Summary. Two new nickel complexes have been synthesized using a newly prepared ligand by substitution at the *para* position of the phenyl rings using simple reaction chemistry. Both $[\text{Ni}(\text{L}_1)_2]$ and $[\text{Ni}(\text{L}_1)_2][\text{BF}_4]$ have been characterized spectroscopically and display characteristics consistent with high spin d^8 ($[\text{Ni}(\text{L}_1)_2]$) and d^7 ($[\text{Ni}(\text{L}_1)_2][\text{BF}_4]$) as confirmed by solution magnetic moments as well as EPR spectroscopy. EPR measurements show that $[\text{Ni}(\text{L}_1)_2][\text{BF}_4]$ contains a negative D value owing to the symmetry about the nickel(III) center and therefore has a ground state of $m_s = +3/2$ and a low lying excited state of $m_s = +1/2$. However, we were unable to obtain crystal structures of either complex due to the high solubility of the complexes giving frail needles that poorly diffract at best. Electrochemical measurements show that the new ligand complex is slightly harder to oxidize than the previously synthesized $-\text{CH}_3$, $-\text{CH}_3$ substituted product owing to the stronger electron donating ability of the methyl groups over the phenyl groups in the *para* position. Due to the ease of substitution at the *para* position the potential for several new derivatives to be synthesized remains high.

General Considerations. Diphenyl amine, 4-tBu phenyl boronic acid, bromine, pyrazole, and all transition metal halides were obtained commercially and were used as received. The compound p-(dibromodiphenyl amine) was prepared according to a literature method.¹³ Solvents were dried by conventional procedures and distilled prior to use, except where noted. Midwest MicroLab, Indiana 45250, performed all elemental analyses. Melting point determinations were made on samples contained in glass capillaries using an Electrothermal 9100 apparatus and are uncorrected. ¹H and ¹³C NMR spectra were recorded on a Varian 300 MHz spectrometer. Chemical shifts were referenced to solvent resonances at δ_{H} 7.27 and δ_{C} 77.23 for CDCl₃ and δ_{H} 5.32 and δ_{C} 53.1 for CD₂Cl₂. Uv-visible and NIR spectra were recorded using Shimadzu UV-1600/1700 or Jasco V-570 instruments. EPR spectral measurements were obtained using a Bruker ELEXSYS E600 equipped with an ER4116DM cavity resonating at 9.63 GHz, an Oxford Instruments ITC503 temperature controller and ESR-900 helium flow cryostat. The EPR spectra were recorded with 100 kHz field modulation.

4-tBu(biphenylamine). To an oven dried schlenk flask was added 2.00 g (6.1 mmol) of bis(4-bromophenyl)amine along with 0.367 (5 mol %) of palladium (0). Toluene (1 x 25 mL) was then added via syringe and the solution was degassed for 15 minutes. To a sepearte 100 mL schlenk flask was added 2.39 g (13.4 mmol) of 4-tert-butylphenyl boronic acid along with methanol (1 x 10 mL) via syringe and transferred slowly via cannula to the main reaction flask. 2.0 M aq. K₂CO₃ (1 x 10 mL) was then added via syringe and the reaction was heated at 80 °C for 20 h. After 20 h. the reaction was allowed to cool and the layers were separated and the aqueous layer was extracted with toluene (3 x 25 mL). The organic fractions were combined, dried over MgSO₄ and

concentrated to give an oily residue. Chromatographic separation using silica gel with 4:1 hexanes:dichloromethane as an eluent afforded crude 4-tBu(biphenylamine) as a colorless powder (4.18 g, 53 %) from the third band ($R_f = 0.33$ SiO₂ plate). Further crops were obtained by flushing the column with pure dichloromethane to obtain a yellow solid which was triturated with diethyl ether to give colorless powder. Mp, 229-232 °C. ¹H NMR (CDCl₃) δ_H 7.51 (dd, $J = 8, 13$ Hz, 12 H), 7.18 (d, $J = 8$ Hz, 4 H), 5.83 (br s, 1H, N-H), 1.39 (s, 18 H, -tBu). ¹³C NMR (CDCl₃) δ_C 149.7, 142.2, 138.1, 133.9, 127.9, 126.3, 125.8, 118.1, 34.6, 31.5.

4-tBu(dibromobiphenylamine). 1.69 g (3.91 mmol) of tertbutylbenzenediphenyl amine was added to a 250 mL 3 neck round bottom flask along with dichloromethane (1 x 75 mL) along with methanol (1 x 15 mL). The flask was then placed into an ice bath and allowed to equilibrate for approximately 15 minutes. 0.45 mL of Br₂ (7.83 mmol) in dichloromethane (1 x 15 mL) and methanol (1 x 15 mL) was then added slowly via an addition funnel. The reaction was then allowed to stir 1 hour at 0 °C. After 1 hour saturated aqueous sodium thiosulfate (1 x 150 mL) was added and the orange color disappeared. The organic layer was separated and dried over magnesium sulfate and concentrated. A yellow/green oily solid was obtained and adsorbed onto SiO₂ and eluted with 4:1 hexane : dichloromethane. 1.66 g (70 %) of a white crystalline solid was obtained. Mp, 146-150 °C. ¹H NMR (CDCl₃) δ_H 7.86 (d, $J = 2$ Hz, 2H), 7.47 (m, 12H), 6.56 (br s, 1H), 1.39 (s, 18H). ¹³C NMR (CDCl₃) δ_C 150.5, 138.9, 136.6, 135.7, 131.6, 126.7, 131.6, 126.7, 126.4, 125.9, 118.1, 114.6, 34.7, 31.5.

di(2-pyrazolyl-4-tbu-biphenyl)amine. To an oven dried 250 mL schlenk flask was added 2.61 g (4.4 mmol) of dibromo compound along with 1.06 g (15.4 mmol) of

pyrazole and 2.16 g (15.4 mmol) of potassium carbonate. The flask was then backfilled and evacuated with N_2 (3x). 0.15 mL of 1,3-diaminopropane along with distilled xylenes (1 x 5 mL) was added via syringe. The flask was covered in foil and a reflux condenser was attached. The reaction was allowed to reflux and monitored by TLC. After 1 day no product formation was observed and further amounts of reactants were added. After 2 days minimal product formation was observed and again further amounts of reactants were added. Finally, after 3 days no starting material remained. The reaction was allowed to cool and water (1 x 30 mL) was added. The reaction mixture was then extracted with dichloromethane (3 x 25 mL) dried over $MgSO_4$ and concentrated. The brown oily substance was adsorbed onto SiO_2 and eluted with 8 : 1 hexanes : ethyl acetate to give a 1.22 g (49 %) of a green/yellow powder. Mp, 137 – 140 °C. 1H NMR ($CDCl_3$) δ_H 8.96 (br s, N-H), 7.78 (t, J = 3 Hz, 4H, $H_{3,5}$ -pz), 7.53 (m, 14H), 6.49 (t, J = 3Hz, 2H, H_4 -pz), 1.38 (s, 18H, tBu). ^{13}C NMR ($CDCl_3$) δ_C 150.3, 140.8, 137.1, 135.9, 133.9, 130.6, 130.1, 126.7, 126.3, 125.9, 123.7, 118.9, 106.9, 34.6, 31.4

$[Ni(L_1)_2] \cdot MeOH \cdot H_2O$. To an oven dried 100 mL schlenk flask was added 0.500 g (0.88 mmol) of Pz ligand along with 0.105 g (0.44 mmol) of $NiCl_2 \cdot 6H_2O$. Methanol (1 x 20 mL) was then added and a condenser was attached and the the mixture was allowed to reflux for 30 minutes. After 30 minutes 0.527 g (2 eq) of $[NEt_4][OH]$ was added. The vial was then rinsed with additional methanol (1 x 5 mL) and transferred. Upon addition of the tetraethyl ammonium hydroxide the reaction mixture turned green and then a brown precipitate formed. The reaction was allowed to stir for an additional 30 minutes. After 30 minutes the reaction was allowed to cool to room temperature and the brown solid was collected by gravity filtration and rinsed with methanol (2 x 5 mL). 0.494 g (94

%) of a brown powder was obtained. Mp, 330-340°C. Anal. Calcd. (obsd.) for $C_{77}H_{82}N_{10}NiO$: C, 74.69 (74.69); H, 6.67 (6.11); N, 11.31 (11.42). μ_{eff} (evans) (CD_2Cl_2 , 295.15 K): 4.43 μ_B . 1H NMR (CD_2Cl_2) δ_H 50.22, 33.88, 20.20, 8.50, 7.41, 7.02, 5.95, 1.30. Uv-Vis (CH_2Cl_2) λ_{max} , nm (ϵ , M^{-1} , cm^{-1}), 250 (105 523), 416 (98257), 532 (815), 853 (255).

$[Ni(L_1)_2][BF_4] \cdot MeOH$. To an oven dried 100 mL schlenk flask was added 0.200 g (0.17 mmol) of orange nickel complex. The flask was then evacuated and backfilled with N_2 (3x). Dichloromethane (1 x 20 mL) was then added via syringe to produce a deep orange solution. To another oven dried 100 mL schlenk flask was added 0.047 g (0.17 mmol) of ferrocenium tetrafluoroborate. The flask was evacuated and backfilled with N_2 (3x). Dichloromethane (1 x 20 mL) was then added via syringe to produce a deep blue solution. The ferrocenium solution was then transferred via cannula to the flask containing nickel complex. Upon transfer the nickel solution turned deep green in color. Upon completion of the transfer the flask was rinsed with an additional amount of dichloromethane (1 x 15 mL). The reaction was allowed to stir for 1 hour at room temperature. After 1 hour the solution was removed in vacuo. The residue green solid was washed with acetonitrile (1 x 10 mL) to remove any unreacted starting material. The solvent was then removed and the green residue was washed with hexanes (3 x 10 mL) to remove ferrocene. 0.150 g (70 %) of a fine green powder was obtained. Mp, 350-360 °C. decomp. Anal. Calcd. (obsd.) for $C_{77}H_{80}N_{10}NiBF_4O$: C, 70.76 (69.57); H, 6.17 (5.87); N, 10.72 (10.10). μ_{eff} (evans) (CD_2Cl_2 , 295.15 K): 3.97 μ_B . Uv-Vis (CH_2Cl_2) λ_{max} , nm (ϵ , M^{-1} , cm^{-1}), 254 (96293), 350sh (34580), 404 (55203), 602 (5854), 725sh (5804), 854 (16210).

BIBLIOGRAPHY

- 1.) Grohmann, A. *Adv. Inorg. Chem.* **2004**, 56, 179.
- 2.) Grohmann, A. *Dalton Trans.* **2010**, 39, 1432.
- 3.) DeMott, J. C.; Basul, F.; Kilgore, U. J.; Foxman, B. M.; Huffman, J. C.; Ozerov, V.; Mindiola, D. J. *Inorg. Chem.* **2007**, 46, 6721 and references therein.
- 4.) Huan, J.-S.; Xie, J.; Fui, S. C. F.; Fang, G.-S.; Zhu, N.; Che, C.-M. *Inorg. Chem.* **2008**, 47, 5727.
- 5.) Morin, T. J.; Bennett, B.; Lindeman, S. V.; Gardinier, J. R. *Inorg. Chem.* **2008**, 47, 7468.
- 6.) (a) The, K. I.; Peterson, L. K. *Can. J. Chem.* **1973**, 51, 422. (b) The, K. I.; Peterson, L. K.; Kiehlmann, E. *Can. J. Chem.* **1973**, 51, 2448. (c) Peterson, L. K.; Kiehlmann, E.; Sanger, A. R.; The, K. I. *Can. J. Chem.* **1974**, 52, 2367.
- 7.) Reger, D. L.; Watson, R. P.; Smith, M. D. *Inorg. Chem.* **2006**, 45, 10077.
- 8.) (a) Reger, D. L.; Watson, R. P.; Gardinier, J. R.; Smith, M. D. *Inorg. Chem.* 2004, 43, 6609. (b) Reger, D. L.; Gardinier, J. R.; Semeniuc, R. F.; Smith, M. D. *Dalton Trans.* **2003**, 1712.
- 9.) Khlobystov, A. N.; Blake, A. J.; Champress, N. R.; Lemonovskii, D. A.; Majouya, A. G.; Zyk, N. V.; Schröder, M. *Coord. Chem. Rev.* **2001**, 222, 155.
- 10.) (a) Reger, D. L.; Gardinier, J. R.; Elgin, J. D.; Smith, M. D.; Hautot, D.; Long, G. J.; Grandjean, F. *Inorg. Chem.* **2006**, 45, 8862. (b) DeBari, H.; Zimmer, M. *Inorg. Chem.* **2004**, 43, 3344.
- 11.) (a) Miras, H.N.; Wilson, E.F.; Cronin, L. "Unraveling the Complexities of Inorganic and Supramolecular Self-Assembly in Solution with Electrospray and Cryospray Mass Spectrometry" *Chem. Commun.* **2009**, 1297-1311. (b) Reger, D.L.; Semeniuc, R.F.; Rassolov, V.; Smith, M.D. "Supramolecular Structural Variations with Changes in Anion and Solvent in Silver(I) Complexes of a Semirigid, Bitopic Tris(pyrazolyl)methane Ligand." *Inorg. Chem.* **2004**, 43, 537. and references.

- 12.) (a) Valentini, M.; Pregosin, P. S.; R  gger, H. *Organometallics* **2000**, *19*, 2551. (b) Reger, D. L.; Gardinier, J. R.; Pellechia, P. J.; Smith, M. D.; Brown, K. J. *Inorg. Chem.* **2003**, *42*, 7635.
- 13.) Dymock, K.; Palenik, G. J. *Acta. Cryst. B* 1974, *30*, 1364.
- 14.) Heeg, M. J.; Kroener, R.; Deutsch, E. *Acta Crystallogr. Sect C: Struct. Commun.* **1985**, *41*, 684.
- 15.) (a) Costas, M.; Mehn, M. P.; Jensen, M. P.; Que, L., Jr. *Chem. Rev.* **2004**, *104*, 939, and references cited therein. (b) Kaizer, J.; Klinker, E. J.; Oh, N. Y.; Rhode, J.-U.; Song, W. J.; Stubna, A.; Kim, J.; M  nck, E.; Nam, W.; Que, L., Jr. *J. Am. Chem. Soc.* **2004**, *126*, 472. (c) Jonas, R. T.; Stack, T. D. P. *J. Am. Chem. Soc.* **1997**, *119*, 8566.
- 16.) (a) Kui, S. C. F.; Fang, G.-S.; Zhu, N.; Chem, C.-M. *Inorg. Chem.* **2008**, *47*, 5727. (b) Canty, A. J.; Minchin, N. J.; Skelton, B. W.; White, A. H. *J. Chem. Soc., Dalton Trans.* **1986**, 2205.
- 17.) (a) Klein Gebbink, R. J. M.; Jonas, R. T.; Goldsmith, C. R.; Stack, T. D. P. *Inorg. Chem.* **2002**, *41*, 5633. (b) de Vries, M. E.; La Crois, R. M.; Roelfes, G.; Kooijman, H.; Spek, A. L.; Hage, R.; Feringa, B. L. *Chem. Commun.* **1997**, 1549.
- 18.) (a) Freedman, D. E.; Jenkins, D. M.; Iavarone, A. T.; Long, J. R. *J. Am. Chem. Soc.* **2008**, *130*, 2884. (b) Wong, E. L.-M.; Fang, G.-S.; Che, C.-M.; Zhu, N. *Chem. Commun.* **2005**, 4578.
- 19.) L  pez, J. P.; Heinemann, F. W.; Prakash, R.; hess, B. A.; Horner, O.; Jeandey, C.; Oddou, J.-L.; Latour, J.-M.; Grohmann, A. *Chem.-Eur. J.* **2002**, *8*, 5709.
- 20.) For instance, see: (a) Zhao, N.; Bullinger, J. C.; Van Stipdonk, M. J.; Stern, C. L.; Eichhorn, D. M. *Inorg. Chem.* **2008**, *47*, ASAP. (b) Zhao, N.; Van Stipdonk, M. J.; Bauer, C.; Campana, C.; Eichhorn, D. M. *Inorg. Chem.* **2007**, *46*, 8662.
- 21.) (a) Luening, U.; Baumstark, R.; Peters, K.; Von Schnering, H. G. *Liebigs Ann. Chem.* **1990**, *2*, 129. (b) Steenland, M. W. A.; Lippens, W.; Herman, G. G.; Goeminne, A. M. *Bull. Soc. Chim. Belges* **1993**, *102*, 239.
- 22.) (a) Reger, D. L.; Grattan, T. C.; Brown, K. J.; Little, C. A.; Lamba, J. J. S.; Rheingold, A. L.; Sommer, R. D. *J. Organomet. Chem.* **2000**, *607*, 120. (b) Reger, D. L.; Watson, R. P.; Gardinier, J. R.; Smith, M. D.; Pellechia, P. J. *Inorg. Chem.* **2006**, *45*, 10077. (d) Reger, D. L.; Watson, R. P.; Smith, M. D.; Pellechia, P. J. *Organometallics* **2006**, *25*, 743. (e) Reger, D. L.; Watson, R. P.; Smith, M. D.; Pellechia, P. J. *Organometallics* **2005**, *24*, 1544. (f) Reger, D. L.; Watson, R. P.; Gardinier, J. R.; Smith, M. D. *Inorg. Chem.* **2004**, *43*, 6609.

- 23.) Chanaka, D.; De Alwis, L.; Schultz, F. A. *Inorg. Chem.* **2003**, *42*, 3616, and references cited therein.
- 24.) Robinson, K.; Gibbs, G. V.; Ribbe, P. H. *Science* **1971**, *172*, 567.
- 25.) Bebbink, R. J. M. K.; Jonas, R. T.; Goldsmith, C. R.; Stackk, T. D. P. *Inorg. Chem.* **2002**, *41*, 4633.
- 26.) (a) Figgis, B. N.; Hitchman, M. A. *Ligand Field Theory and Its Applications*; Wiley-VCH: New York, 2002. (b) Lever, A. B. P. *Inorganic Electronic spectroscopy*; Elsevier: New York, 1968.
- 27.) Hendrich, M. P.; Debrunner, P. G. *Biophys. J.* 1989, *56*, 489.
- 28.) Que, L. *Physical Methods in Bioinorganic Chemistry*. University Science Books: Sausalito, CA, 2000.
- 29.) Crabtree, R. H. *The Organometallic Chemistry of the Transition Metals*. Wiley, New Jersey, 2005.
- 30.) For example: (a) Pickens, S. R.; Artell, A. E. *Inorg. Chem.* **1980**, *19*, 15. (b) Fujii, H.; Dou, Y.; Zhou, A.; Yoshida, T.; Ikeda-Saito, M. *J. Am. Chem. Soc.* **1998**, *120*, 8251.
- 31.) Takano, S.; Yano, Y.; Tagaki, W. *Chem. Lett.* **1981**, 1177-1180.
- 32.) Schmidt, S.; Heinemann, F. W.; Ghromann, A. *Eur. J. Inorg. Chem.* **2000**, 1657.
- 33.) Hegetschweiteg, K.; Mass, O.; Zimmer, A.; Geue, R. J.; Sargeson, A. M.; Harmer, J.; Schweiger, A.; Buder, I. Scwitzgtelbel, G.; Reiland, V.; Frank, W. *Eur. J. Inorg. Chem.* **2003**, 1340.
- 34.) Higgs, T.C.; Carrano, C. J. *Inorg. Chem.* **1997**, *36*, 291.
- 35.) Ren, X.; Alleyne, B. D.; Djurovich, P. I.; Adachi, C.; Tsyba, I.; Bau, R.; Thompson, M. E. *Inorg. Chem.* **2004**, *43*, 1697.
- 36.) Sheu, S.-C.; Tien, M.-J.; Cheng, M.-C.; Ho, T.-I.; Peng, S.-M.; Lin, Y.-C.; *J. Chem. Soc., Dalton Trans.* **1995**, 3503.
- 37.) Balarugan, V.; Mukherjee, R. *Inorg. Chim. Acta.* **2006**, *359*, 1376.
- 38.) Peisach, J.; Blumberg, W. E. *Arch. Biochem. Biophys.* **1974**, *165*, 691
- 39.) (a) Drago, R. S. *Physical Methods In Chemistry*; Saunders: Philadelphia, 1977; p 648-649; (b) Lever, A. B. P. *Inorganic Electronic Spectroscopy*; Elsevier: New York, 1968.

- 40.) Long, G. J.; Grandjean, F.; Reger, D. L. *Top. Curr. Chem.* **2004**, 233, 91.
- 41.) (a) Adediran, M.; Ayo, O. B.; Trans. Met. Chem. 1991, 16, 348. (b) Pettirari, C.; Marchetti, F.; Cingolani, A.; Leoresi, D.; Colapietro, M.; Marquadonna, S. *Polyhedron* 1998, 17, 4145. (c) The, K. I.; Peterson, L. K. *Can. J. Chem.* **1973**, 51, 422.
- 42.) (a) Pearce, J. N.; Moore, T. E. *American Chemical Journal*; (b) Rhode, I.; Vogt, E.; *Z. Physik. Chem.* **1932**, B15, 353; (c) Kiss, A.; Richter, M. *Z. Physik. Chem.* **1940**, A187, 211.
- 43.) (a) Costas, M.; mehn, M. P.; Jensen, M. P.; Que, L., Jr. *Chem. Rev.* **2004**, 104, 939, and references cited therein. (b) Kaizer, J.; Klinker, E. J.; Oh, N. Y.; Rohde, J.-U.; Song, W. J.; Stubna, A.; Kim, J.; Münck, E.; Nam, W.; Que, L., Jr. *J. Am. Chem. Soc.* **2004**, 126, 472. (c) Jonas, R. T.; Stack, T. D. P. *J. Am. Chem. Soc.* **1997**, 119, 8566.
- 44.) Chanaka, D.; De Alwis, L.; Schultz, F. A. *Inorg. Chem.* **2003**, 42, 3616, and references cited therein.
- 45.) Matu-ura, M.; Tani, F.; Naruta, Y. *J. Am. Chem. Soc.* **2002**, 124, 1941.
- 46.) Reger, D. L.; Gardinier, J. R.; Elgin, J. D.; Smith, M. D.; Hautot, D.; Long, G. J.; Grandjean, F. *Inorg. Chem.* **2006**, 45, 8862. (b) De Bari, H.; Zimmer, M. *Inorg. Chem.* **2004**, 43, 3344.
- 47.) (a) Little, B. F.; Long, G. J.; *Inorg. Chem.* **1978**, 17, 3401. (b) Wroblewski, J. T.; Long, G. J. *Inorg. Chim. Acta*, **1978**, 30, 221.
- 48.) Shenoy, G. K.; Wagner, F. E.; Kalvius, G. M. in *Mössbauer Isomer Shifts*, Shenoy, G. K.; Wagner, F. E., Eds., North-Holland, Amsterdam, (1978) p. 49.
- 49.) (a) Reger, D. L.; Elgin, J. D.; Smith, M. D.; Grandjean, F.; Rebbouh, L.; Long, G. J. *Polyhedron*, **2006**, 25, 2616. (b) Reger, D. L.; Gardinier, J. R.; Elgin, J. D.; Smith, M. D.; Hautot, D.; Long, G. J.; Grandjean, F. *Inorg. Chem.*, **2006**, 45, 8862 (c) Reger, D. L.; Gardinier, J. R.; Bakbak, S.; Gemmill, W.; Smith, M. D.; Rebbouh, L.; Grandjean, F.; Shahin, A. M.; Long, G. J. *J. Amer. Chem. Soc.*, **2005**, 127, 2303. (d) Reger, D. L.; Gardinier, J. R.; Smith, M. D.; Shahin, A. M.; Long, G. J.; Rebbouh, L.; Grandjean, F. *Inorg. Chem.*, **2005**, 44, 1852.
- 50.) Ingalls, R. *Phys. Rev.*, **1964**, A133, 787.
- 51.) Coonors, K. A. *Binding Constants*; Wiley: New York, 1987.
- 52.) Likussar, W.; Boltz, D. F. *Anal. Chem.* **1971**, 43, 1265.

- 53.) (a) Gebbink, R. J. M. K.; Jonas, R. T.; Goldsmith, C. R.; Stack, T. D. P. *Inorg. Chem.* **2002**, *41*, 4633. (b) Ortega-Villar, N.; Ugalde-Saldívar, V. M.; Muñoz, C.; Ortiz-Frade, L. A.; Alvarado-Rodriguez, J. G.; Real, J. A.; Moreno-Esparza, R. *Inorg. Chem.* **2007**, *46*, 7285.
- 54.) Hendrich, M. P.; Debrunner, P. G. *Biophys. J.* **1989**, *56*, 489.
- 55.) Figgis, B. N.; Hitchman, M. A. *Ligand Field Theory and Its Applications*; Wiley-VCH: New York, 2002.
- 56.) Que, L., Jr.; Ho, R. Y. N. *Chem. Rev.* 1996, *96*, 2607.
- 57.) For example: (a) Lubben, M.; Meetsma, A.; Wilkinson, E. C.; Feringa, B.; Que, L., Jr. *Angew. Chem. Int. Ed. Engl.* 1995, *34*, 1512. (b) Rhode, J.-U.; In, J. H.; Lim, M. H.; Brennessel, W. W.; Bukowski, M. R.; Stubna, A.; Münk, E.; Nam, W.; Que, L., Jr. *Science* 2003, *299*, 1037. (c) Lim, M. H.; Rhode, J.-U.; Stubna, A.; Bukowski, M. R.; Costas, M.; Ho, R. Y. N.; Münk, E.; Nam, W.; Que, L., Jr. *Proc. natl. Acad. Sci. U.S.A.* 2003, *100*, 3665.
- 58.) Kaizer, J.; Klinker, E. J.; Oh, N. Y.; Rohde, J.-U.; Song, W. J.; Stubna, A.; Kim, J.; Münck, E.; Nam, W. Que, L., Jr. *J. Am. Chem. Soc.* 2004, *126*, 472.
- 60.) (a) Antilla, J. C.; Baskin, J. M.; Barder, T. E.; Buchwald, S. L. J. *Org. Chem.* **2004**, *69*, 5578. (b) Cristau, H.-J.; Cellier, P. P.; Spindler, J.-F.; Taillefer, M. *Eur. J. Org. Chem.* **2004**, *69*, 5578. (c) Taillefer, M.; Xia, N.; Oulai, A. *Angew. Chem., Int. Ed.* **2007**, *46*, 934. (d) Christau, H.-J.; Cellier, P. P.; Spindler, J.-F.; Taillefer, M. *Chem. Eur. J* **2004**, *10*, 5607. (e) See, also, Linley, J. M.; McRobbie, I. M.; Meth-Cohn, O.; Suschitzky, H. *J. Chem. Soc. Perkin Trans.* **1980**, *4*, 982.
- 61.) Liddle, B. J.; Silva, R. M.; Morin, T. J.; Macedo, F. P.; Shukla, R.; Lindeman, S. V.; Gardiner, J. R. *J. Org. Chem.* **2007**, *72*, 5637.
- 62.) Isaacs, N. *Physical Organic Chemistry*, 2nd ed.; Longman Scientific and Technical: Essex, 1995; Chapter 4.
- 63.) (a) Dance, I. *Dalton* **1996**, 3755. (b) Dance, I. *Chem. Euro. J.* **1996**, 2481.
- 64.) Braga, D.; Grepioni, F. Tedesco, E. *Organometallics* **1998**, *17*, 2669.
- 65.) (a) LeTourneau, H. A.; Birsch, R. E.; Korbeck, G.; Radkiewicz-Poutsma, J. L. *J. Phys. Chem. A* **2005**, *109*(51), 12014-12019. (b) Fisher, L.; Holme, T. *J. Comp. Chem.* **2001**, *22*(9), 913-922.
- 66.) Shao, Y.; et. al. *Phys. Chem. Chem. Phys.* **2006**, *8*, 3172.

- 67.) As these author's point out, an $n \rightarrow \pi^*$ transition in hindered aromatic amines or in N-heterocycles refers to electronic transitions from the lone pairs occupying orbitals orthogonal to the π -system (as found in pyridine, for instance) to the appropriate π -system orbital.
- 68.) (a) Caspar, J. V.; Sullivan, B. P.; Kober, E. M.; Meyer, T. J. *Chem. Phys. Lett.* **1982**, 91 (2), 91. (b) Penner, A. P.; Siebrand, W.; Zgierski, M. Z. *J. Chem. Phys.* **1978**, 69 (12), 5496. (c) Englman, R.; Jortner, J. *Mol. Phys.* 1970, 18 (2), 14
- 69.) Kessler, H. *Angew. Chem. Int. Ed. Engl.* **1970**, 9, 219.
- 70.) Morales-Morales, D.; Jensen, C. M. *The Chemistry of Pincer Compounds*; Elsevier: Amsterdam, 2007.
- 71.) Albrecht, M.; van Koten, G. *Angew. Chem. Int. Ed.* **2001**, 40, 3750-3781.
- 72.) (a) Harkins, S. B.; Peters, J. C. *Inorg. Chem.* **2006**, 45, 4316. (b) Mazzeo, M.; Lambert, M.; Massa, A.; Scettri, A.; Pellecchia, C.; Peters, J. C. *Organometallics* **2008**, 27, 5741. (c) Adhikari, D.; Mossin, S.; Bassuli, F.; Dible, B. R.; Chipara, M.; Fan, H.; Huffman, J. C.; Meyer, K.; Mindiola, D. *Inorg. Chem.* **2008**, 47, 10479. (d) Bailey, B. C.; Hongjun, F.; Huffman, J. C.; Baik, M-H; Mindiola, D. J. *J. Am. Chem. Soc.* **2006**, 128, 6798. (e) Feller, M.; Ben-Ari, E.; Gupta, T.; Shimon, L. J. W.; Leitun, G.; Diskin-Posner, Y.; Weirer, L.; Milstein, D. *Inorg. Chem.* **2007**, 46, 10479. (f) Ben-Ari, E.; Leitun, G.; Shimon, L. J.; Milstein, D. J. *J. Am. Chem. Soc.* **2006**, 128, 15390.
- 73.) Wanniarachchi, S.; Liddle, B. J.; Toussaint, J.; Lindeman, S. V.; Bennett, B.; Gardinier, J. R. *Dalton Trans.* **2010**, 39, 3167.
- 74.) For example see: Louie, J.; Hartwig, J. F. *J. Am. Chem. Soc.* **1997**, 119, 11695 and references therein.
- 75.) Liddle, B. J. Thesis Ph.D. Marquette University, Milwaukee, WI, February, 2009.
- 76.) Ishow, E. Brosseau, A.; Clavier, G.; Nakatani, K.; Pansu, R. B.; Vachon, J-J.; Tauc, P.; Chauvat, D.; Mendonca, C. R.; Piovesan, E. *J. Am. Chem. Soc.* **2007**, 129, 8970.
- 77.) Antilla, J.-C.; Baskin, J. M.; Barder, T. E.; Buchwald, S. L. *J. Org. Chem.* **2004**, 69, 5578.
- 78.) (a) Cristau, H.-J.; Cellier, P. P.; Spindler, J.-F.; Taillefer, M. *Eur. J. Org. Chem.* (b) Cristau, H.-J.; Cellier, P. P.; Spindler, J.-F.; Taillefer, M. *Eur. J. Org. Chem.* 2004, 695. (c) Taillefer, M.; Xia, N.; Ouali, A. *Angew. Chem. Int. Ed.* 2007, 46, 934. (d) Christau, H.-J.; Cellier, P. P.; Spindler, J.-F.; Taillefer, M. *Chem Eur. J.* 2004, 10, 5607.
- 79.) Rajca, A.; Vale, M.; Rajca, S. *J. Am. Chem. Soc.* **2008**, 130, 9099.

- 80.) Hansch, C.; Leo, A.; Taft, R. W. *Chem. Rev.* **1991**, *91*, 165.
- 81.) Adhikari, D.; Mossin, S.; Basuli, F.; Huffman, J. C.; Szilagyi, R. K.; Meyer, K.; Mindiola, D. J. *J. Am. Chem. Soc.* **2008**, *130*, 367.